Dissertation
submitted to the
Combined Faculties for the Natural Sciences and for Mathematics
of the Ruperto-Carola University of Heidelberg, Germany
for the degree of
Doctor of Natural Sciences

presented by
Diploma Physicist Verena Fiedler
born in Freiburg i. Br.

Oral examination: 19th December 2007

Atmospheric SO_2:
Global Measurements using Aircraft-Based CIMS

Referees:	Prof. Dr. Frank Arnold
	Prof. Dr. Klaus Pfeilsticker

Atmospheric SO_2:
Global Measurements using Aircraft-Based CIMS.

Aircraft based measurements of tropospheric sulfur dioxide, SO_2, have been carried out during four campaigns in South America (TROCCINOX), Australia (SCOUT-O3), Europe (INTEX/MEGAPLUME) and Africa (AMMA). SO_2 has been measured by chemical ionization mass spectrometry (CIMS), permanently online calibrated with isotopically labelled SO_2. The measurement method is described thoroughly in this work and the measured data are presented. Moreover, the data of the different regions are compared in general and typical air mass situations with SO_2 enhancement are shown. A detailed analysis of four SO_2 pollution plume cases emphasizes the main features: long-range transport, SO_2 from metal smelters/volcanoes or from biomass burning. The SO_2 measurements are analyzed in the light of simultaneously measured trace gas, particle and meteorological data. Air mass trajectory models (FLEXPART or HYSPLIT) are employed for a determination of the pollution origin. Further going evaluations with the aerosol model AEROFOR complete the analyses and point out, that the measured SO_2 mole fractions are sufficient to explain new particle formation and growth. Finally, a first comparison of the measured SO_2 to results from a global circulation model (ECHAM) with implemented sulfur chemistry showed a significant underestimation of the measured SO_2 mole fraction by the model in the free troposphere.

Atmosphärisches SO_2:
Globale Messungen mit einem flugzeug-getragenen CIMS-Gerät

Flugzeug-getragene Messungen von troposphärischem Schwefeldioxid, SO_2, wurden während 4 verschiedenen Messkampagnen in Südamerika (TROCCINOX), Australien (SCOUT-O3), Europa (INTEX/MEGAPLUME) und Afrika (AMMA) durchgeführt. SO_2 wurde mittels Chemischer Ionisations Massenspektroskopie (CIMS) gemessen, permanent online geeicht mit isotopisch markiertem SO_2. Die Messmethode wird ausführlich in dieser Arbeit beschrieben und die gewonnenen Daten werden vorgestellt. Desweiteren werden die Daten der verschiedenen Regionen verglichen und typische Luftmassensituationen mit erhöhtem SO_2 gezeigt. Eine detaillierte Analyse von vier verschiedenen Verschmutzungsplumes greift die Punkte Ferntransport, SO_2 aus Metall-Verhüttung/Vulkanen und Verbrennung von Biomasse auf. Die SO_2 Messungen werden mit Blick auf simultan gemessene Spurengas-, Partikel- und Wetterdaten analysiert. Luftmassentrajektorien (FLEXPART oder HYSPLIT) werden genutzt, um die Herkunft der Verschmutzung zu bestimmen. Weiterführende Auswertungen mit dem Aerosolmodell AEROFOR vervollständigen die Analysen und zeigen auf, dass die gemessenen SO_2 Molfraktionen ausreichen, um die Bildung neuer Parikel und deren Wachstum zu erklären. Abschliessend zeigt ein erster Vergleich des gemessenen SO_2 mit Ergebnissen eines globalen Zirkulationsmodells (ECHAM) mit implementierter Schwefelchemie, dass die gemessenen SO_2 Molfraktionen in der freien Troposphäre durch das Modell signifikant unterschätzt werden.

Contents

Chapter 1

Introduction

Sulfur dioxide, SO_2, is an important trace gas in the atmosphere. It is part of a wide variety of chemical reactions and it is the precursor of atmospheric sulfuric acid, H_2SO_4. Sulfuric acid moreover is the most important known aerosol nucleation precursor so far. SO_2 therefore has an impact on the Earth's aerosol inventory.

Aerosol particles principally influence human life in many different ways. In a global view they might contribute to climate change due to their major role in atmospheric chemistry and their ability to interact directly with solar and infrared terrestrial radiation fields [Ramanathan et al., 2001, Harshvardhan et al., 2002, Garrett et al., 2002].

Furthermore they take a major part in the formation of cloud condensation nuclei (CCN) [Menon and Saxena, 1998].

Humans can also directly be affected by SO_2 and aerosols. SO_2 is a poisonous gas, that harms the lungs and the whole respiratory system and might even contribute to cardiovascular diseases [Sunyer et al., 2003a, Sunyer et al., 2003b]. Aerosols may cause harm through inhalation as well [Stieb et al., 2002, Wichmann and Peters, 2000, Kim, 2000], especially small, i.e. freshly nucleated, particles, as they can penetrate extremely deeply into the lungs, which can finally lead to breathing diseases or even lung cancer.

In order to understand, predict and finally prevent such effects a detailed investigation of the sources and growth mechanisms of aerosol particles and their precursors is needed.

SO_2 as well as other trace gases including NO, NOy, CO, O_3 and Aerosol parameters have recently been measured for the first time simultaneously in many different regions of the world, i.e. Europe, South America, Australia and Africa, during several measurement campaigns. The SO_2 measurements were carried out by the Atmospheric Physics Group of the Max-Planck-Institute for Nuclear Physics in close cooperation with the German Aerospace Center (DLR). The applied measurement technique was chemical ionization mass spectrometry (CIMS) with permanent in-flight calibration.

The content of this work builds up as follows: In **Chapter 2** the principles of SO_2-chemistry and the main features of aerosol theory will be presented. **Chapter 3** will concentrate on a detailed presentation of the applied SO_2 measurement technique CIMS and its advantages compared to other existent or former SO_2 measurement methods. In this context also the specific realization of the setup for aircraft measurements, which has been used now for all recent measurement campaigns, will be explained.

Chapter 4 will describe the different mainly EU funded projects during which the SO_2 measurements took place and will name their main objectives.

The following three chapters eventually will concentrate on the analysis of the obtained data. Firstly **Chapter 5** will provide a principle comparison of the results at the four different measurement sites with emphasis on general features and air mass origin. In **Chapter 6** four SO_2 pollution plume case studies will be presented: the detection of copper smelter exhaust in Brazil, long range SO_2 transport from middle America to Europe, long range transport from Asia to Europe and the detection of biomass burning pollution in central Africa. These four examples will be discussed in detail and additional analyses e.g. with the aerosol nucleation model AEROFOR will be employed. Thirdly a first attempt to validate the sulfur module of the general circulation model ECHAM will be shown in **Chapter 7**.

Finally **Chapter 8** will point out the conclusions of this thesis and an outlook will identify the perspectives and will describe the future work which is planned.

Chapter 2

Atmospheric Sulfur Chemistry and Aerosol Theory

This chapter deals with atmospheric sulfur chemistry, emphasizing on SO_2, and the impact of sulfur compounds on aerosol formation and nucleation.

2.1 Sulfur Chemistry

Sulfur is present in the Earth's atmosphere at a total volume mixing ratio of less than 1 ppmv[1] [Seinfeld and Pandis, 2006]. Nevertheless, the influence of sulfur containing compounds on chemical reactions and especially particle formation is definitely high, and therefore it affects even climate in a not negligible way.

2.1.1 Atmospheric Sulfur Compounds

Table 2.1 shows the main atmospheric sulfur compounds, as well as their average lifetimes and a typical average mixing ratio.

Most of these compounds, H_2S, CH_3SCH_3 (DMS), CS_2 and OCS stem from natural sources, i.e. emissions from certain species of algae in the ocean or from plants and bacteria in soil. In an oxic environment, i.e. in the presence of oxygen, bacteria form amino acids and proteins by reducing sulfates to sulfides. Anaerobic bacteria use sulfate for respiration which leads to the formation of H_2S in an anoxic environment, i.e. in the absence of oxygen. DMS is emitted by marine plankton, OCS stems from trees or soils.

---

[1] parts per million by volume=10^{-6} mol/mol

Name	**Formula**	**Average Lifetime**	**Mean pptv Clean Continental**	**Mean pptv Polluted Continental**	**Mean pptv Free Troposphere**
Hydrogen Sulfide (Gas)	H_2S	2 days	15-340	0-800	1-13
Dimethyl Sulfide (Gas)	CH_3SCH_3	0.5 days	7-100	2-400	< 2
Carbon Disulfide (Gas)	CS_2	1 week	15-45	80-300	< 5
Carbonyl Sulfide (Gas)	OCS	7 years	510	520	510
Sulfur Dioxide (Gas)	SO_2	2-10 days	70-200	100-10000	30-260
Sulfuric Acid (Gas)	H_2SO_4	1 hour	< 0.1	0.004-0.4	< 0.1
Sulfate Ion (Aerosol)	SO_4^{2-}	5 days	10-120	100-10000	5-70

Table 2.1: Main Sulfur-Containing Compounds in the Atmosphere, Average Lifetimes and Typical Average Mixing Ratios [Seinfeld and Pandis, 2006].

Further oxidation products of all these compounds may act either as main components or as condensation nuclei in aerosols. The long average lifetime of OCS for example makes a transportation of this compound up into the stratosphere very probable, where it is oxidized to sulfuric acid (H_2SO_4). This is the source for a stratospheric aerosol layer, the so-called Junge-layer [Junge, 1961]. The main natural sulfur dioxide (SO_2) source are volcanoes, and these emissions also often inject SO_2 up into the stratosphere. But volcanic emission only count for about 10% of the total SO_2 emissions. SO_2 may also be an oxidation product of the above mentioned biogenic sulfur compounds, but the biggest source, around 90% of the total SO_2 burden, are anthropogenic emissions like fossil fuel combustion and biomass burning. **Figure 2.1** gives a rough overview of the atmospheric sulfur cycle.

Gaseous sulfuric acid is created from sulfur dioxide in reactions with OH radicals and water [Reiner and Arnold, 1993, Reiner and Arnold, 1994]. Due to its low saturation vapor pressure, it condenses very easily onto existent particles and forces their growth. Moreover, sulfuric acid is considered to be the most important vapor concerning nucleation and new particle formation and directly affects climate in this way. All aerosol types (sulfates, organics, mineral dust, sea salt) intercept incoming sunlight, and reduce the energy flux arriving at the Earth's surface, thus producing a cooling. The earth's albedo (i.e. the percentage of solar radiation that is reflected back from the earth to space) is increased. Aerosols also contribute to long-wave heating, as infrared radiation from the earth's surface is reflected back by the particles, which results in a positive, heating, effect. Nevertheless the cooling

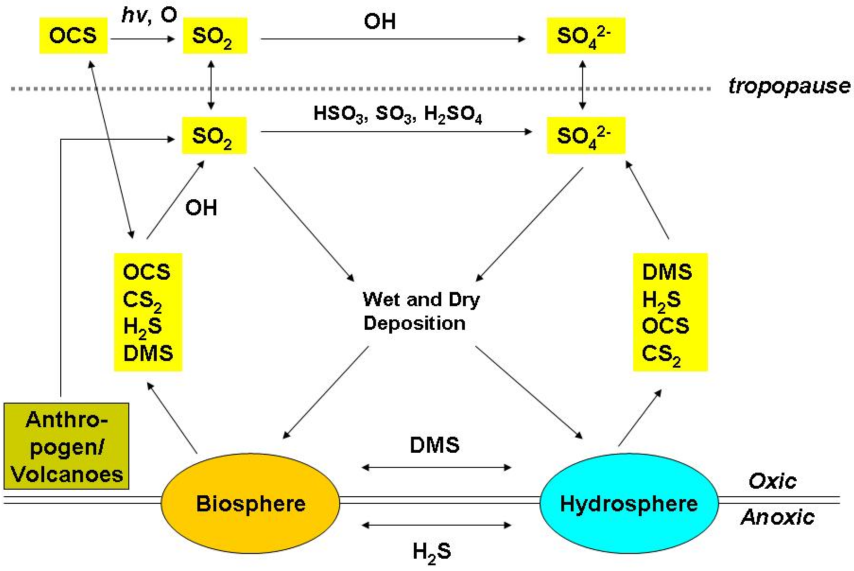

Figure 2.1: Schematic overview of the simplified atmospheric sulfur cycle.

effect of aerosols on the climate seems to prevail by far. **Figure 2.2** shows the radiative effects of several atmospheric compounds. Sulfur contributes here to columns sulphate and cloud albedo effect ([IPCC, 2007]).

In addition to this direct radiative effects, there are several indirect effects, that are only poorly quantified yet, but all those indirect effects result in a cooling: more aerosols produce more and smaller droplets in a cloud, making it more reflective. Moreover smaller droplets are less likely to coagulate into raindrops and thus the lifetime of clouds is extended, again increasing the earth's albedo. All these points show that aerosols and their precursors SO_2 and H_2SO_4 have a strong influence on climate change, they quasi oppose the climate warming by CO_2 and other greenhouse gases and seem to keep the warming effect to a moderate extent. **Figure 2.3** shows the development of the CO_2 and SO_2 emissions from the year 1850 until 2000 and gives a prognosis for the further development till the year 2100. As can be seen, the SO_2 emissions will go down in this prognosis very soon, assuming more and more the use of sulfur free fuels and cleaner combustion processes, whereas the CO_2 emissions are still likely

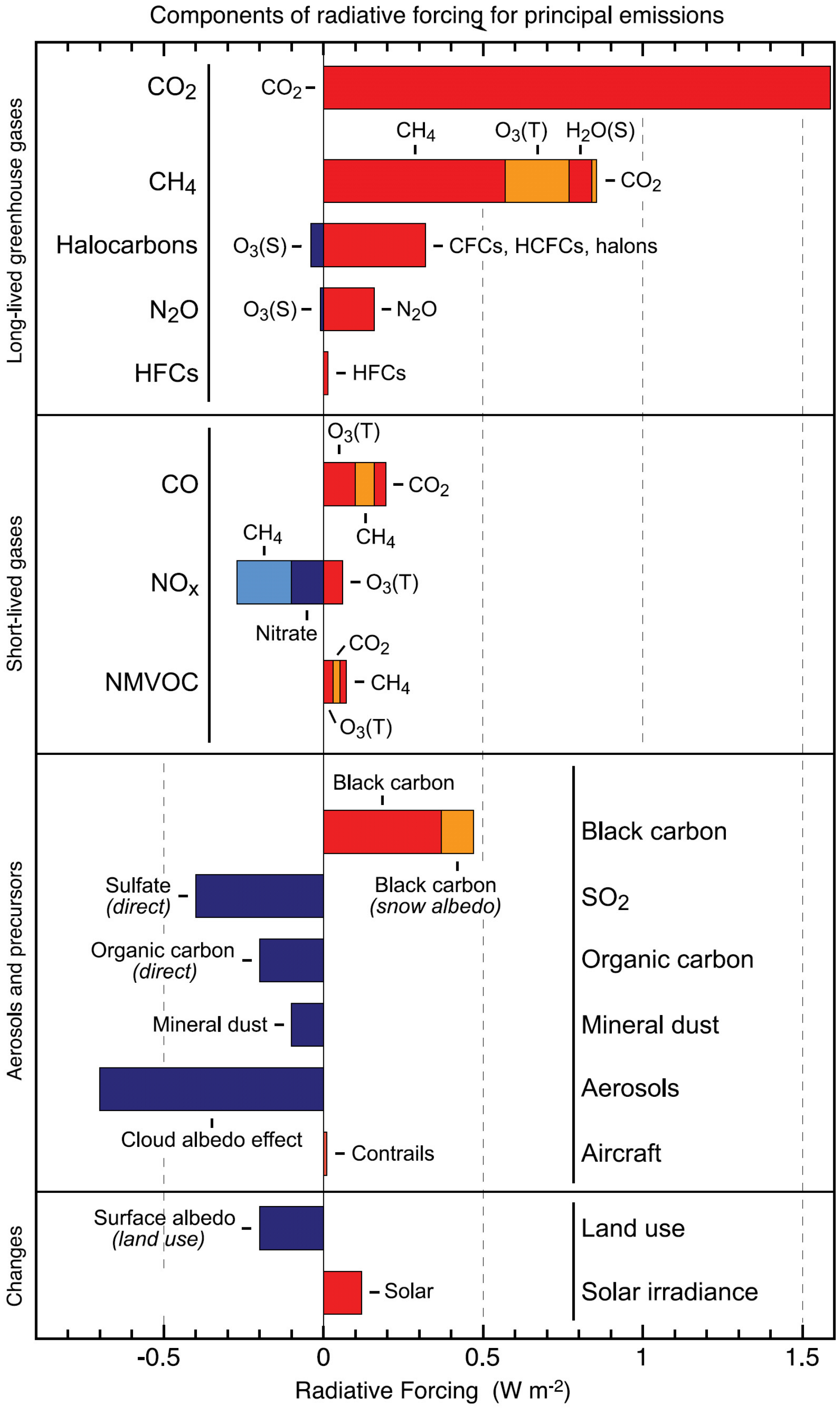

Figure 2.2: Radiative forcing effects of several atmospheric species. Sulfur species and aerosols mainly contribute to negative, cooling effects in the columns sulfate and cloud albedo effect. (S) indicates stratospheric, (T) tropospheric substances [IPCC, 2007].

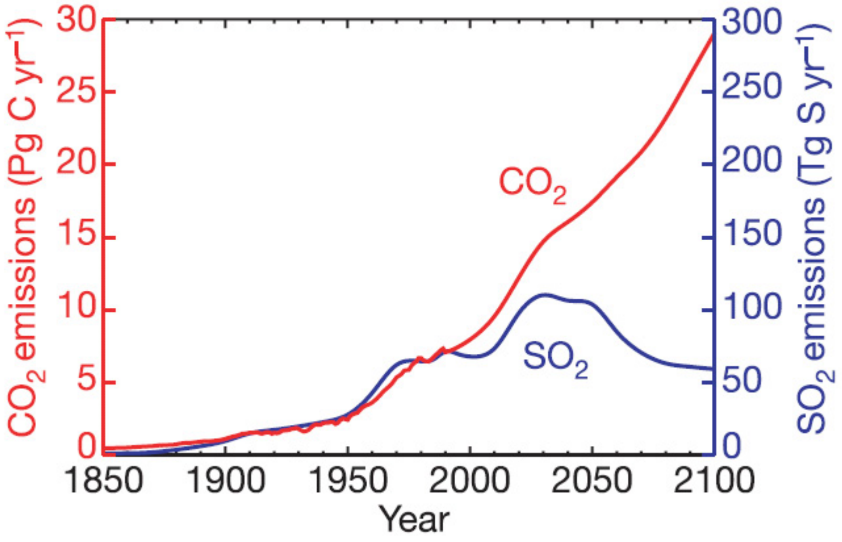

Figure 2.3: Historical CO_2 and SO_2 emissions in 10^{15} gram carbon and 10^{12} gram sulfur per year from 1850 - 2000, followed by projected values to the year 2100 from the IPCC SRES[25] A2 scenario [Andreae et al., 2005].

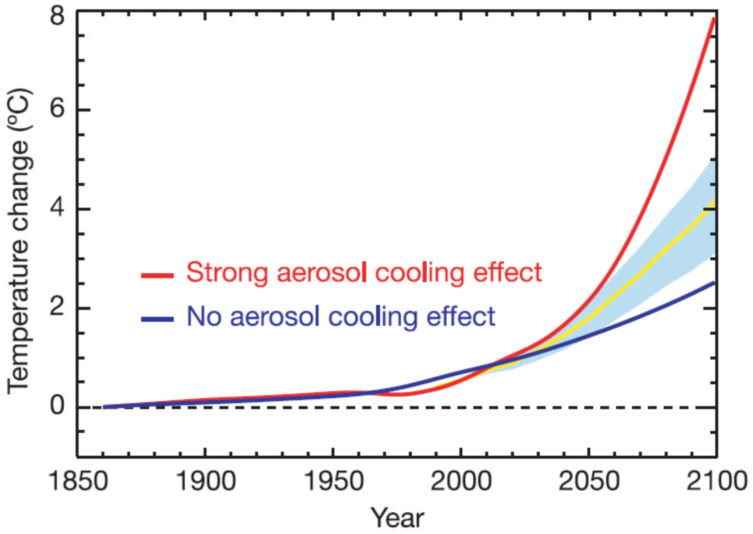

Figure 2.4: Predicted temperature change for two extreme cases: Red curve: Assumption of a strong cooling effect by aerosols today. Its reduction together with an reduction of SO_2 emissions will lead to a strong temperature increase by 8° in the year 2100. Blue curve: Temperature increase if no aerosol cooling effect is assumed for today's atmosphere. The shaded area indicates the range of temperature increase prognoses of the IPCC 2001 report. [Andreae et al., 2005].

to increase.

If we now assume a today's strong cooling effect of aerosols, that will be reduced together with the reduction of SO_2 emissions, one has to expect an even stronger warming of the earth's climate in future years (red curve in Figure 2.4) than most of the climate models predict (blue shaded area in Figure 2.4) [Andreae et al., 2005].

Conclusively one can say that investigations of SO_2 concentrations in the atmosphere are really important and a not negligible contribution to the actual climate debate.

At this place it is just to mention that e.g. the nobel laureate Paul Crutzen already started thinking about the possibilities to oppose the climate change technically with injections of SO_2 into the stratosphere [Crutzen, 2006]. The injections should built up a stratospheric aerosol layer, that could serve as a shield against the solar radiation. However, in my opinion one should be really careful with such proposals. Side effects, that will occur in such a complex system as the atmosphere, might not be predictable in advance.

2.1.2 Atmospheric SO_2

As mentioned above about 90% of the atmospheric sulfur dioxide stems from anthropogenic combustion processes, ship exhaust for example contains up to 5% of sulfur compounds, kerosine 350 ppmM[2] and normal diesel fuel between 5 and 50 ppmM. Further SO_2 is produced by power plants, biomass burning and metal smelter industry. **Figure 2.5** shows the EDGAR inventory (Emission Database for Global Atmospheric Research), an estimate of the world's total anthropogenic sulfur dioxide emissions [Olivier et al., 1994, van Aardenne et al., 2001]. SO_2 emissions are given as color code in Gigagrams per year. The highest pollution originates from highly industrialized countries like the USA, Europe, India and Asia. The sulfur emission source strength is regionally quite different. And also the future development of the emissions differs regionally a lot. As the fuel sulfur content in Europe and the US is reduced more and more, a reduction of the sulfur emissions in those regions in the next years can be expected, whereas the sulfur production in India and Asia will grow in coming years probably to a great extent.

---

[2] parts per million by mass

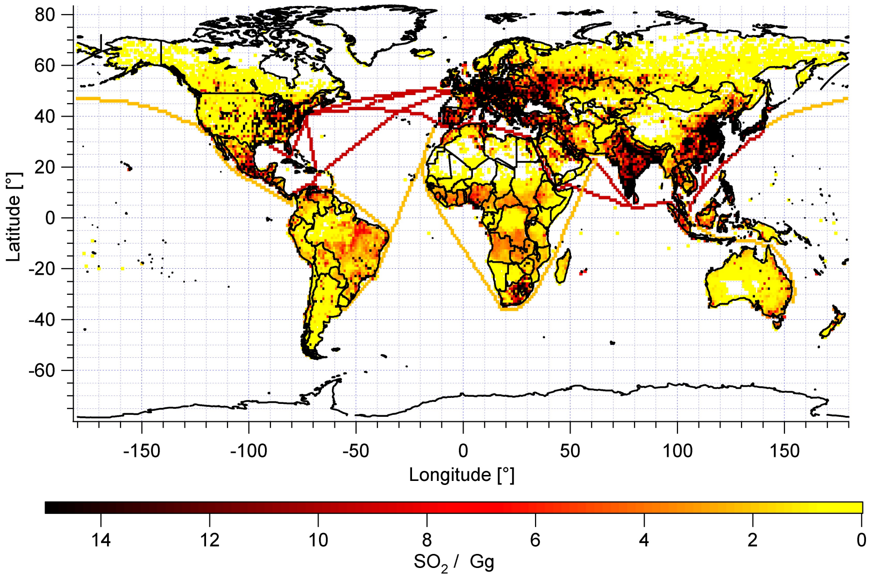

Figure 2.5: EDGAR inventory: Sulfur dioxide emission estimates for the year 2000, including combustion processes, biomass burning and ship trails as color code in Gigagrams (Gg) per year.

Sulfur dioxide reacts under tropospheric conditions via both gas and aqueous-phase processes and is removed from the atmosphere via dry and wet deposition.

In the gas phase the dominant reaction is oxidation by the OH radical, the so-called Stockwell-Calvert-Mechanism [Stockwell and Calvert, 1983].

$$\mathrm{SO_2 + \cdot OH + M \longrightarrow HSO_3\cdot + M},\ k_1 = 9\cdot 10^{-13}\mathrm{cm^3 s^{-1}} \tag{2.1}$$

$$\mathrm{HSO_3\cdot + O_2 \longrightarrow SO_3 + HO_2\cdot},\ k_2 = 4.3\cdot 10^{-13}\mathrm{cm^3 s^{-1}} \tag{2.2}$$

$$\mathrm{SO_3 + H_2O + M \longrightarrow H_2SO_4 + M}. \tag{2.3}$$

In this reaction the temperature and pressure dependent step (2.1) is limiting (the indicated value for k is for a temperature of 295 K and a pressure of $1.0\cdot 10^5$ Pa). There are two possible pathways, how H_2SO_4 could be formed from SO_3 and water [Reiner and Arnold, 1993, Reiner and Arnold, 1994, Kolb et al., 1994, Lovejoy et al., 1996].

$$\mathrm{SO_3 + 2H_2O \longrightarrow H_2SO_4 + H_2O} \tag{2.4}$$

$$\mathrm{SO_3(H_2O) + H_2O \longrightarrow H_2SO_4 + H_2O}. \tag{2.5}$$

Although the rate constant of reaction (2.3) is not exactly known so far, it is definitely smaller than k_1 [Finlayson-Pitts and Pitts, 2000].

The OH radical which is necessary for the upper reaction is in the troposphere mainly formed by the photolysis of ozone:

$$\mathrm{O_3 + h\nu \longrightarrow O(^1D) + O_2}, \ (\lambda \ \leq \ 310 \text{ nm}) \tag{2.6}$$

$$\mathrm{O(^1D) + H_2O \longrightarrow 2 \cdot OH}, \ k = 2.2 \cdot 10^{-10} \mathrm{cm^3 s^{-1}} \tag{2.7}$$

$$\mathrm{O(^1D) + M \longrightarrow O(^3P) + M}. \tag{2.8}$$

Ozone is photolyzed into oxygen and an excited O in singlet D state. 90 % of these excited oxygen atoms lose their energy through collisions with other molecules (M in step (2.8)) and usually recombine to oxygen [Finlayson-Pitts and Pitts, 2000]. About 10 % collide with water molecules which leads to OH formation according to reaction (2.7).

Other sources of OH are the photolysis of nitrous acid HONO and hydrogen peroxide H_2O_2. Due to its high reactivity, the OH-radical has only a lifetime of about 1 s under atmospheric conditions. Consequently, OH chemistry stops almost completely during nighttime. Then another reaction becomes an important sink for SO_2, the reaction with the methyl peroxy radical, $CH_3O_2\cdot$:

$$\mathrm{CH_3O_2 \cdot + SO_2 \longrightarrow CH_3O \cdot + SO_3} \tag{2.9}$$

SO_3 again forms sulphuric acid following reaction (2.3).

Furthermore SO_2 can be solved in water droplets. Oxidants like H_2O_2 produce H_2SO_4 in the liquid phase from this SO_2. New theories came up recently, that SO_2 could also be emitted again from water droplets while freezing, if not converted to H_2SO_4 before [Clegg and Abbatt, 2001].

More details on sulfur chemistry can be found in [Finlayson-Pitts and Pitts, 2000] and very nicely and clear in [Wayne, 2000].

Concluding an estimation of the half life of SO_2 in the upper troposphere with respect to the chemical reaction (2.1) and with the assumption of a constant OH concentration. The time derivative of the SO_2 concentration is

$$\frac{d[\mathrm{SO_2}]}{dt} = -k[\mathrm{SO_2}][\mathrm{OH}] \tag{2.10}$$

which leads to

$$\ln{[\mathrm{SO_2}]} = -k[\mathrm{OH}]t \tag{2.11}$$

and

$$[\mathrm{SO_2}](t) = [\mathrm{SO_2}](0) \cdot e^{-k[\mathrm{OH}]t} \tag{2.12}$$

The half life is then determined as follows:

$$\begin{aligned} 0.5 &= e^{-k[\mathrm{OH}]\tau_{1/2}} && (2.13)\\ \Rightarrow \ln 2 &= k[\mathrm{OH}] \cdot \tau_{1/2} && (2.14)\\ \Rightarrow \tau_{1/2} &= \frac{\ln 2}{k[\mathrm{OH}]} && (2.15) \end{aligned}$$

If we consider a cloud free sky and a diurnally averaged OH concentration of $1 \cdot 10^6$ cm^{-3} [Logan et al., 1981], we get, with the rate coefficient $k \approx 10^{-12}$ cm^{3}s^{-1},

$$\begin{aligned} \tau_{1/2} &= \frac{\ln 2}{1 \cdot 10^{-6}} && (2.16)\\ &\approx 0.693 \cdot 10^6 \text{ s} = 192.5 \text{ h} \approx 8 \text{ days} && (2.17) \end{aligned}$$

After about 8 days a SO_2 concentration in the upper troposphere is reduced to its half. So a ground emission of e.g. 1 ppbv SO_2, that is transported by convection fast into the upper troposphere, can travel there for several days. After 8 days the mole fraction would still be 500 pptv, which could then be measured by our instruments.

2.2 Aerosol Theory

There are in principle two mechanisms for the formation of new particles in the atmosphere:

- Through homogeneous, heterogeneous or ion induced nucleation of originally gaseous compounds, especially H_2SO_4, NH_3 and water, which coagulate and condense then onto preexistent particles.
- Through dispersion of dust or sea salt spray and water droplets.

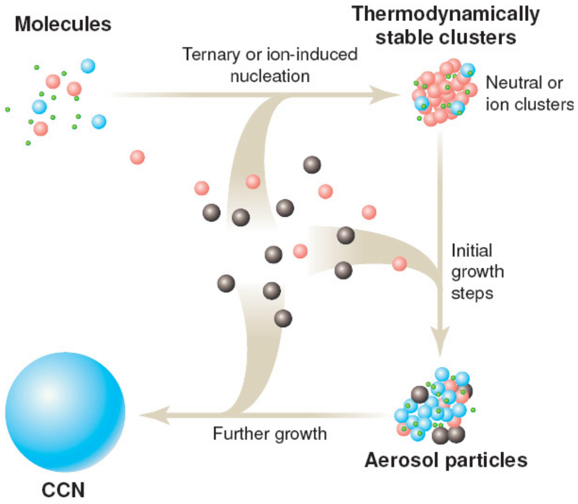

Figure 2.6: Illustration of the process of nucleation via binary, ternary or ion induced nucleation and further growth up to cloud condensation nuclei (CCN) [Kulmala, 2003].

Sulfuric acid plays an important role for the first point. Here we need to distinguish between 4 different pathways [Seinfeld and Pandis, 2006]:

- Homomolecular Homogeneous Nucleation: Only one type of molecules forms clusters through coagulation directly from the gas phase. This process requires such a high supersaturation of the condensable species, that it usually does not build up in the free troposphere.

- Heteromolecular Homogeneous Nucleation: Two or more types of molecules form clusters through coagulation from the gas phase. The most important formation pathways known so far are binary nucleation of H_2SO_4 and water and ternary nucleation of H_2SO_4, NH_3 and water.

- Heterogeneous Nucleation: Condensation of one or more condensable species onto the surface of preexistent water droplets or particles.

- Ion Induced Nucleation: Accumulation of (charged or polarized) molecules on existent ions. This mechanism matters the most in the stratosphere and upper troposphere.

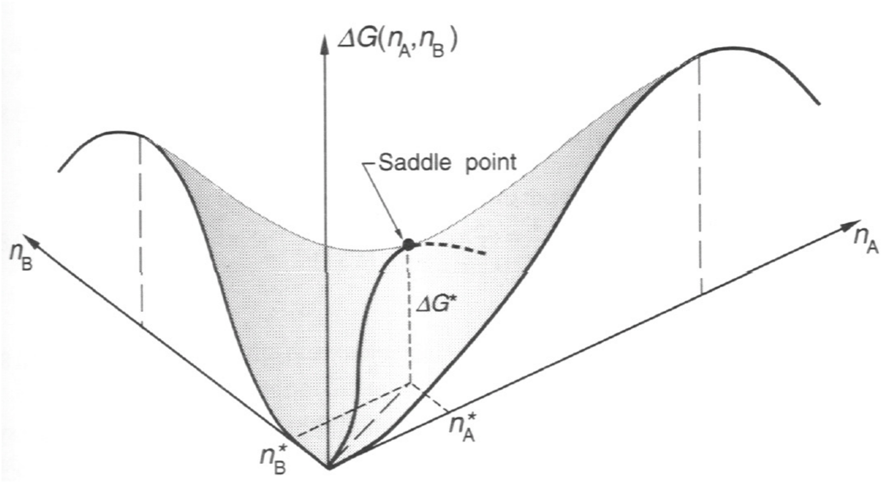

Figure 2.7: Saddle shaped free energy surface ΔG for binary cluster formation as function of the number of molecules type A, n_A, and the number of molecules type B, n_B. [Seinfeld and Pandis, 2006].

Figure 2.6 illustrates the formation of new particles via nucleation and the creation of cloud condensation nuclei (CCN) with all the effects mentioned above.

Nucleation theory itself is a very complex matter and can be presented here only fragmentarily. As an example the nucleation rate of classical binary nucleation theory will be derived very briefly. All other theories follow the same pattern, just starting from different Gibbs free energies.

Classical binary nucleation theory was first used by Flood, Volmer, Neumann, Döring and Reiss [Flood, 1934, Volmer, 1939, Neumann and Döring, 1940, Reiss, 1950]. They noted that a growing binary cluster can be thought of as moving on a saddle-shaped free energy surface, the saddle point corresponding to the critical cluster (critical cluster size means the size from which the cluster starts to be stable). **Figure 2.7** shows this saddle-shaped surface for binary homogeneous nucleation. The change of the Gibbs free energy of formation of a spherical binary liquid cluster from the vapor phase is [Reiss, 1950]:

$$\Delta G = n_1 \Delta\mu_1 + n_2 \Delta\mu_2 + 4\pi r^2 \sigma \tag{2.18}$$

with n_i being the number of the i'th species in the cluster, $\Delta\mu_i$ being the change of the chemical potential of species i between the vapor phase and the liquid phase, r being the radius of the cluster and σ the surface tension.

The total number n_i can be written as

$$n_i = n_i^s + n_i^b \tag{2.19}$$

where n_i^s indicates the number of surface molecules and n_i^b the number of interior ("bulk") molecules.

The saddle point on the free energy surface can be found setting

$$\left(\frac{\partial \Delta G}{\partial n_i}\right)_{n_j} = 0 \tag{2.20}$$

and this leads to the following two equations (by using the Gibbs-Duhem equation)

$$n_1^b d\mu_1^l + n_2^b d\mu_2^l = 0 \tag{2.21}$$

$$n_1^s d\mu_1^l + n_2^s d\mu_2^l + A d\sigma = 0 \tag{2.22}$$

and furthermore to the binary Kelvin equation:

$$\Delta\mu_i + \frac{2\sigma\nu_i}{r^*} = 0 \tag{2.23}$$

(ν_i are the partial molecular volumes: $n_1\nu_1 + n_2\nu_2 = \frac{4}{3}\pi r^3$).

So we find for the radius and the free energy of formation of the critical cluster:

$$r^* = -\frac{2\sigma\nu_i}{\Delta\mu_i} \tag{2.24}$$

$$\Delta G^* = \frac{4}{3}\pi r^{*2}\sigma \tag{2.25}$$

From there the nucleation rate J can be derived:

$$J = R_{ave} F Z \exp\left(-\Delta G^*/kT\right) \tag{2.26}$$

with R_{ave} being the average condensation rate, F is the number of molecular species in the vapor, Z is the Zeldovich non equilibrium factor (a numerical correction [Stauffer, 1976]), k is the Boltzmann constant and T the temperature.

In detail this derivation is far more complex, but a complete and detailed derivation can be found in [Seinfeld and Pandis, 1998].

The main removal mechanisms for aerosol particles in the atmosphere are dry and wet deposition. Particles, especially large ones, are settling down in the gravitational field of the earth (dry deposition) or are washed out (”scavenged”) by rain (wet deposition). Both mechanisms lead to a change in the shape of the particle number distribution (smaller particles are ”caught” by bigger ones, the distribution is shifted to higher particle diameters) and finally this reduces the total number of particles [Seinfeld and Pandis, 1998, Laakso et al., 2003]. Also coagulation reduces the number of particles, but preserves the total mass of the aerosol.

Chapter 3

Sulfur Dioxide Measurement Method

Typical mixing ratios of atmospheric SO_2 lie in the ppbv[1] or even pptv[2] range. These low concentrations make the measurements a real challenge to the experimentalists. This chapter will present the measurement method CIMS (Chemical Ionization Mass Spectrometry) that has been developed in our work group and its theoretical background. The advantages compared to former methods will be pointed out and the practical setup during four aircraft measurement campaigns will be described.

3.1 Measurement Method

3.1.1 Former Measurement Methods

First in situ measurements of atmospheric SO_2 were provided by [West and Gaeke, 1956] in the 1950'ties and by [Georgii and Jost, 1964, Jaeschke et al., 1976] in the 1960'ties. Both used a filter sampling technique and the chemiluminescence reaction of potassium permanganate ($KMnO_4$) and sulfur as detection. In the 70'ties followed [Maroulis et al., 1980, Thornton et al., 1986] with flame-photometric methods and ion chromatography. Since 1990 mass spectrometry has been used, e.g. by [Bandy et al., 1993, Thornton et al., 1997]. **Table 3.1** lists some technical data of these different measurement methods. Obviously, the main disadvantage of all methods is the very low time resolution of 3 to 40 minutes. Especially

---

[1] parts per billion by volume, i.e. 10^{-9} mol/mol

[2] parts per trillion by volume, 10^{-12} mol/mol

Technique	**Measured Substances**	**SO_2 detection limit pptv**	**Time Resolution**	**Reference**
Filter Chemiluminescence	SO_2	26± 50%	5-20 min	[Meixner and Jaeschke, 1981]
Filter Ion Chromatography	SO_2	10± 20%	15-40 min	[Ferek and Hegg, 1993]
Chemiluminescence	SO_2	30± 20%	3 min	[Meixner and Jaeschke, 1981]
Gas chromatograph flame photometry	OCS,H_2S, CS_2,SO_2,DMS	20± 25%	3 min sample every 12 min	[Thornton et al., 1986]
Gas chromatograph mass spectrometry	OCS,H_2S, CS_2,SO_2,DMS	10± 5%	3 min sample every 12 min	[Bandy et al., 1993]

Table 3.1: Atmospheric Sulfur Measurement Techniques. Data from an SO_2 measurement technique intercomparison paper [Gregory et al., 1993].

if aircraft measurements are considered, e.g. 10 minutes correspond typically to a flown distance of 100 km, if the airplane flies with 600 km/h. This resolution is actually so bad, that only statements about mean mole fractions over those distances can be made. Smaller pollution plumes for example need a much higher time resolution for detection.

A comparison of these different measurement techniques can be found in [Gregory et al., 1993].

3.1.2 Chemical Ionization

3.1.2.1 Principle

Sulfur dioxide is measured by our group via chemical ionization mass spectrometry (CIMS). The method bases on an ion molecule reaction firstly proposed by [Möhler et al., 1992, Möhler and Arnold, 1992] and further investigated by [Seeley et al., 1997, Reiner et al., 1998]. The principle of this measurement method is to convert the neutral trace gas molecules into charged and therefore detectable product ions through a highly efficient ion molecule reaction [Speidel et al., 2007]. Typical rate coefficients of such reactions lie around $10^{-9}\text{cm}^3\text{s}^{-1}$ compared to $10^{-11}\text{cm}^3\text{s}^{-1}$ in the case of a fast reaction between neutral molecules.

Figure 3.1 depicts a schematic CIMS setup. The main components are a flowreactor, an ion source and a mass spectrometer for the ion detection. Atmospheric air with the trace substance of interest A is pumped into the flowreactor, an approximately 30 cm long 4 cm in diameter stainless steal tube. With an ion source (in this work a gas discharge source,

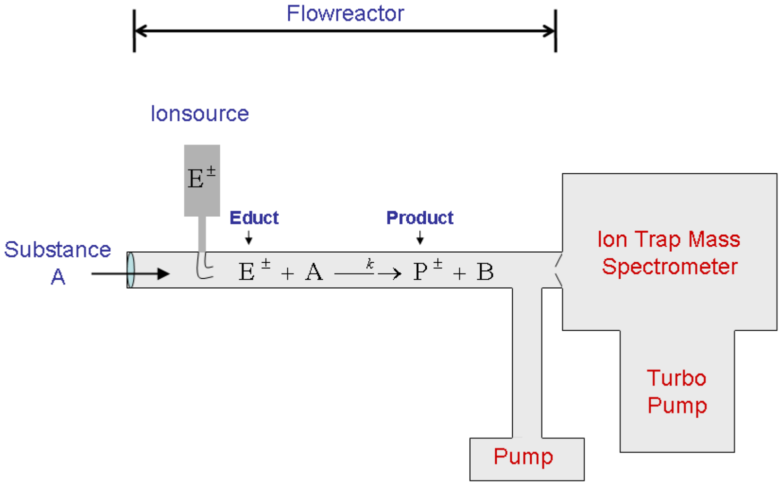

Figure 3.1: Principle scheme of a CIMS apparatus.

but also a radioactive Polonium source could be used) so-called educt ions $E^{\pm}$ are produced and injected into the main air stream of the flowreactor. There they undergo the following reaction with the trace gas A, leading to product ions $P^{\pm}$ and a neutral product B:

$$E^{\pm} + A \xrightarrow{k} P^{\pm} + B \tag{3.1}$$

The time derivative of the educt ion concentration is

$$\frac{d}{dt}[E^{\pm}] = -\frac{d}{dt}[P^{\pm}] = -k[E^{\pm}][A] \tag{3.2}$$

Assuming only a negligible reduction of [A] by this reaction ($[A](t)=[A]_0=$constant), equation (3.2) can be directly integrated to

$$[E^{\pm}] = [E^{\pm}]_0 \cdot e^{-k[A]t} \tag{3.3}$$

The total charge needs to be preserved ($[P^{\pm}]+[E^{\pm}]=$const.), consequently one gets a similar formula for the product ion concentration.

$$[P^{\pm}] = [E^{\pm}]_0 \cdot (1 - e^{-k[A]t}) \tag{3.4}$$

Dividing equation (3.4) by equation (3.3) and solving for [A] we get the so-called **ACIMS-Formula**[3]

$$[\mathrm{A}] = \frac{1}{k \cdot t_{IMR}} \ln \left(1 + \frac{[\mathrm{P}^{\pm}]}{[\mathrm{E}^{\pm}]}\right) \tag{3.5}$$

The concentration of the neutral substance A can finally be determined by measuring the product and educt ion concentrations, if the rate constant k and the reaction time t_{IMR} is known.

This reaction scheme will become more complicated if the educt ions react with several types of molecules.

$$\mathrm{E}^{\pm} + \mathrm{A}_i \longrightarrow \mathrm{P}_i^{\pm} + \mathrm{B_i} \tag{3.6}$$

Then the **Parallel-ACIMS-Formula** needs to be used.

$$[\mathrm{A}_i] = \frac{1}{k \cdot t} \cdot \frac{[\mathrm{P}_i^{\pm}]}{\sum_{j=1}^{n}[\mathrm{P}_j^{\pm}]} \cdot \ln \left(1 + \frac{\sum_{j=1}^{n}[\mathrm{P}_j^{\pm}]}{[\mathrm{E}^{\pm}]}\right) \tag{3.7}$$

As this formula is not necessary for sulfur dioxide measurements the reader is referred to [Wollny, 1998] for a detailed derivation.

3.1.2.2 Measurements of sulfur dioxide by CIMS

In the concrete case of atmospheric sulfur dioxide measurements an ion molecule reaction with CO_3^- ions is employed [Möhler et al., 1992]. The SO_2 molecules react in two steps with CO_3^- ion water clusters forming SO_5^- ion water clusters and CO_2.

$$\mathrm{CO_3^-(H_2O)}_n + \mathrm{SO_2} \xrightarrow{k_n} \mathrm{SO_3^-(H_2O)}_m + \mathrm{CO_2} + (n-m)\mathrm{H_2O} \tag{3.8}$$

$$\mathrm{SO_3^-(H_2O)}_m + \mathrm{O_2} \xrightarrow{k_m} \mathrm{SO_5^-(H_2O)}_p + (m-p)\mathrm{H_2O} \tag{3.9}$$

The rate constants k_n of reaction (3.8) depend on the number of water ligands and range from $0.6 \cdot 10^{-9}$ cm^3s^{-1} in wet air (n=5) to $0.9 \cdot 10^{-9}$ cm^3s^{-1} in dry air (n=0) with a maximum of $1.6 \cdot 10^{-9}$ cm^3s^{-1} in between (n=1) [Seeley et al., 1997]. Reaction (3.8) is followed by the

---

[3] the A in ACIMS stands for active, i.e. the educt ions are produced artificially in an ion source. There also exists the method PACIMS (PA=passive), which employs naturally occurring ions as educt ions.

rapid reaction (3.9) of the SO_3^--clusters with O_2, which is available in excess. The rate coefficients k_m for reaction (3.9) are about a factor of 30 smaller ($5 \cdot 10^{-11}$ cm^3s^{-1}) than the k_n [Möhler et al., 1992].

The CO_3^- ions (mass 60 amu) and the SO_5^- ions (mass 112 amu) can then be detected e.g. as in our case with an ion trap mass spectrometer. A typical mass spectrum is shown in **Figure 3.2**.

The ACIMS-formula (3.5) yields:

$$[SO_2] = \frac{1}{k \cdot t} \cdot \ln(1+R) \tag{3.10}$$

with

$$R = \frac{[SO_5^-]}{[CO_3^-]} = \frac{[112]}{[60]} \tag{3.11}$$

being the ratio of the ion count rates of mass 112 and mass 60.

$$k = \sum_{n=0}^{5} k_n \frac{[CO_3^-(H_2O)_n]}{[CO_3^-]_{tot}} \tag{3.12}$$

is the effective weighted rate coefficient for reaction (3.8) and t is the reaction time.

As the reaction coefficients k_n are strongly depending on the number of ligand water molecules involved in this reaction and therefore strongly depending on the water vapor mole fraction or relative humidity of the investigated air mass, the calculation of the effective rate coefficient k is difficult and complicated and its accuracy depends on the accuracy of the humidity measurements, which are unfortunately slow and inaccurate [Speidel et al., 2007, Nau, 2004].

It is obvious that moreover the error of the whole measurements depends besides the accuracy of the detections of educt and product ions directly on the accuracy of the rate constant k and the reaction time t. Especially the rate constant with its strong water vapor dependence makes a distinct determination of the SO_2 mixing ratio difficult. Another error source are store and release effects along the sampling line. Depending on temperature and humidity, SO_2 might condense onto the surface of the sampling line, being released again e.g. at lower humidities. To enhance the accuracy of the measurements and to avoid the calculation of the rate constant k and the reaction time t the following calibration method is applied.

3.1.2.3 Permanent Online-Calibration with isotopically labelled SO_2

Isotopically labelled SO_2 (i.e. SO_2 with ^{34}S instead of ^{32}S) is added permanently to the trace gas flow during measurements. The heavy molecule then undergoes the same reactions as the lighter one at the same temperature and humidity conditions. The knowledge of the exact SO_2 mole fraction in the added calibration gas so allows a direct correlation of the peak height of the mass 114 ($^{34}SO_5^-$) in the measured mass spectrum to the added SO_2 mole fraction, which can then also be used for calculating the atmospheric SO_2 mole fraction from the peak height of mass 112 ($^{32}SO_5^-$). **Figure 3.3** shows a typical mass spectrum with the additional calibration peak at mass line 114. Here it has to be taken into account, that the isotopically labelled standard is not completely pure, it also contains traces of ^{32}S. Likewise, the atmospheric SO_2 contains a certain percentage of heavy sulfur [Bandy et al., 1993].

$$[112] = K_{as}C_s + K_{aa}C_a \tag{3.13}$$

with K_{as} being the percentage of ^{32}S in the standard and K_{aa} the percentage of ^{32}S in ambient air and C_s the concentration of the standard and C_a the ambient SO_2 concentration. Similar

$$[114] = K_{ss}C_s + K_{sa}C_a \tag{3.14}$$

with K_{ss} the percentage of ^{34}S in the standard and K_{sa} the percentage of ^{34}S in ambient air. This formula can be solved for C_a and an expression for the SO_2 mole fraction is obtained.

$$[SO_2] = C_a = C_s \cdot \frac{K_{ss}R - K_{as}}{K_{aa} - K_{sa}R} \tag{3.15}$$

with

$$R = [112]/[114] \tag{3.16}$$

being the ratio of the background corrected ion mass peak intensities.

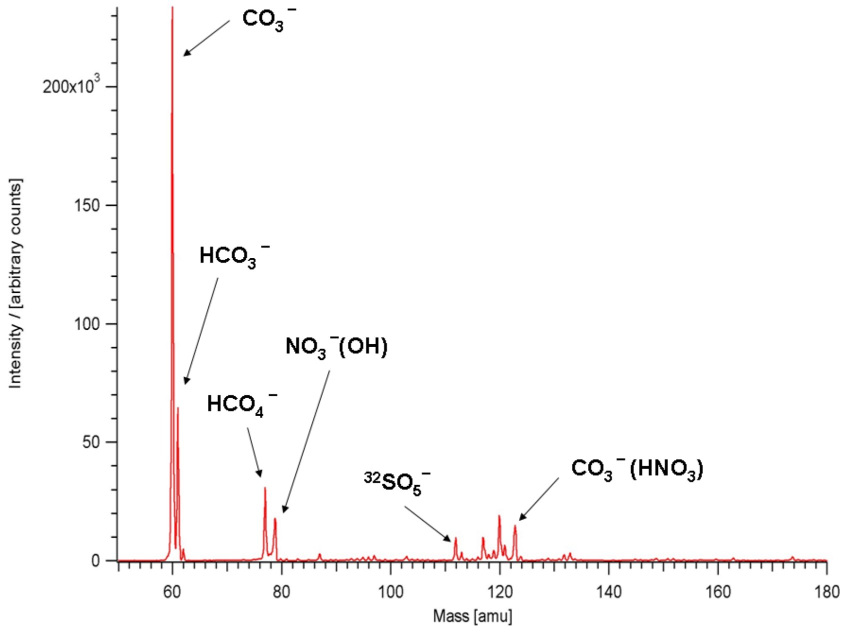

Figure 3.2: Typical mass spectrum for SO_2 measurements.

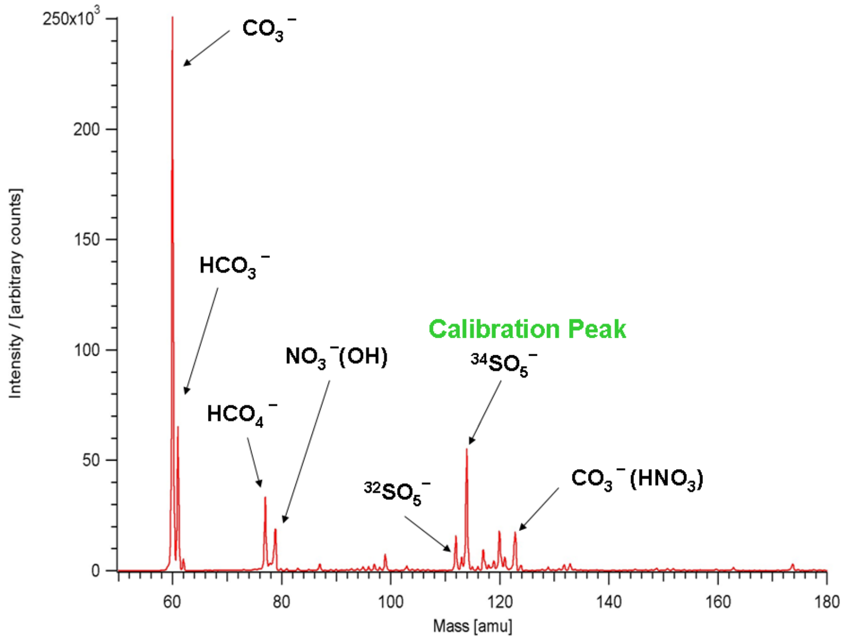

Figure 3.3: Typical mass spectrum for SO_2 measurements with addition of isotopically labelled SO_2.

At this place it is just to mention, that principally the HNO_3 mole fraction is measured simultaneously to SO_2. The reaction of the HNO_3 molecule (mass 63 amu) with the CO_3^- ions leads to the formation of a product ion with mass 123 ($CO_3^-(HNO_3)$), which can be detected by the mass spectrometer (view **Figures 3.2** and **3.3**). So far there does not exist a calibration for HNO_3 yet, which is the reason that this thesis focuses only on SO_2. Recently, first attempts of a HNO_3 calibration have been made and will be presented in [Nau, 2008]. In the following case studies (chapter 6) sometimes also a rough estimation of the HNO_3 mole fraction is shown by using the upper SO_2 calibration also for HNO_3 (this means in formula (3.15) just replacing R by R' =[123]/[114]).

3.1.3 Ion Detection

3.1.3.1 Quadrupole Ion Trap Mass Spectrometry - Theory

The quadrupole mass filter was first proposed by W. Paul 1953 [Paul and Steinwedel, 1953, Paul and Raether, 1955, Paul et al., 1958]. The new invention was a mass spectrometer which used only electric fields for mass selection. Previously, mass spectrometers used magnetic fields which made the instruments usually heavy and unwieldy.

When a single ion experiences a quadrupole field, there is no space charge due to the presence of other charged particles and the field is then said to be ideal. In this case the potential ϕ at any point (x, y, z) within the field is called harmonic and may be expressed by the relationship

$$\phi = \frac{\phi_0}{r_0^2}(\lambda x^2 + \sigma y^2 + \gamma z^2) \tag{3.17}$$

where ϕ_0 is the applied electric potential, λ, σ and γ are weighting constants for the x, y and z coordinates and r_0 is a device dependent constant.

The applied potential is a combination of a radio frequency potential $V \cos \omega t$ and a direct current potential U:

$$\phi_0 = U - V \cos \omega t \tag{3.18}$$

with $\omega = 2\pi f$ (f the frequency of the field in Hz).

Equation (3.17) must satisfy Laplace´s equation:

$$\Delta\phi = 0 \tag{3.19}$$

This leads to the following condition, that has to be satisfied in all kind of quadrupole devices:

$$\lambda + \sigma + \gamma = 0 \tag{3.20}$$

or in trivial case $\phi_0 = 0$.

The force in x-direction experienced by an ion of mass m and charge e and likewise the forces in y- and z-direction may be expressed as

$$F_x = ma = m\frac{d^2x}{dt^2} = -e\frac{\partial \phi}{\partial x} \tag{3.21}$$

where a is the acceleration of the ion.

Substituting equation (3.18) for ϕ_0 in equation (3.17) and differentiating with respect to x, y and z yields the potential gradients. Furthermore this leads to the equations of motion of a single charged positive ion in an electric quadrupole field.

$$\frac{d^2x}{dt^2} + \frac{2\lambda e}{mr_0^2}(U - V\cos\omega t)x = 0 \tag{3.22}$$

$$\frac{d^2y}{dt^2} + \frac{2\sigma e}{mr_0^2}(U - V\cos\omega t)y = 0 \tag{3.23}$$

$$\frac{d^2z}{dt^2} + \frac{2\gamma e}{mr_0^2}(U - V\cos\omega t)z = 0. \tag{3.24}$$

By introducing the dimensionless parameter $\xi = \omega t/2$ this equation can be transformed to the following expression, the **Mathieu-equation**:

$$\frac{d^2u}{d\xi^2} + (a_u - 2q_u\cos 2\xi)\mu \cdot u = 0 \tag{3.25}$$

with u representing x, y or z, μ representing λ, σ or γ, respectively and

$$a_u = \frac{8eU}{mr_0^2\omega^2} \qquad \mathit{and} \qquad q_u = \frac{4eV}{mr_0^2\omega^2} \tag{3.26}$$

This equation was originally solved by Mathieu who was investigating the motions of a vibrating membrane. So the solutions are well known and can be found in literature, e.g. [Mathieu, 1868, McLachlan, 1947].

A three-dimensional quadrupole ion trap (see schematic **Figure 3.4**) is built of a hyperboloid ring electrode and two hyperboloid end-cap electrodes. The derivation of the formulas

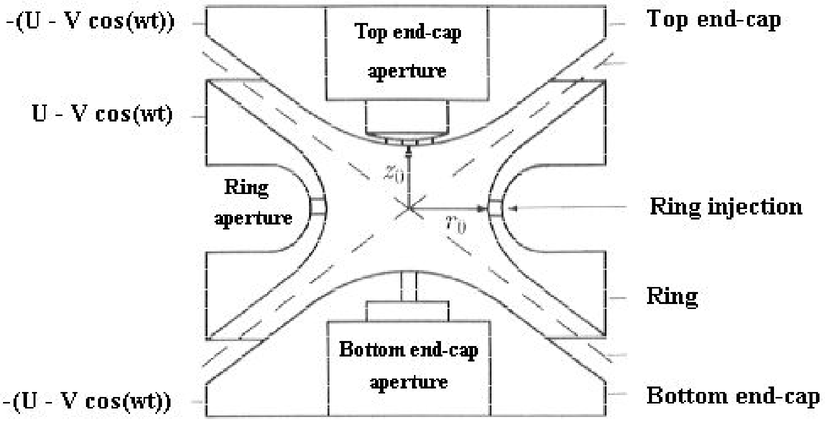

Figure 3.4: Principle structure of a Paul ion trap.

for the ion trap is analogue to the upper derivation but it is appropriate to solve the equations in cylindrical coordinates $((x,\, y,\, z) \rightarrow (r,\, \theta,\, z);\; x = r\cos\theta,\; y = r\sin\theta,\; z = z)$. This leads to the following equations of motion:

$$\frac{d^2z}{dt^2} - \frac{4e}{mr_0^2}(U - V\cos\omega t)z = 0 \tag{3.27}$$

$$\frac{d^2r}{dt^2} + \frac{2e}{mr_0^2}(U - V\cos\omega t)r = 0 \tag{3.28}$$

And with the substitutions $\xi = \omega t/2$ and

$$a_z = -2a_r = \frac{-16eU}{m\omega^2 r_0^2} \qquad and \qquad q_z = -2q_r = \frac{-8eV}{m\omega^2 r_0^2} \tag{3.29}$$

the Mathieu equation (3.25) is obtained again.

Furthermore, considering the boundary conditions $\phi(r_0, 0, 0) = \phi(0, r_0, 0) = \phi_0$ and $\phi(0, 0, z_0) = -\phi_0$ this leads to a condition for the physical shape of the trap:

$$r_0^2 = 2z_0^2 \tag{3.30}$$

Depending only on the two parameters a and q stable and unstable solutions of the Mathieu equations can be calculated, which determines if an ion can be kept inside the trap. A graphical representation of stable solutions and the stability region near the origin is shown in **Figure 3.5**.

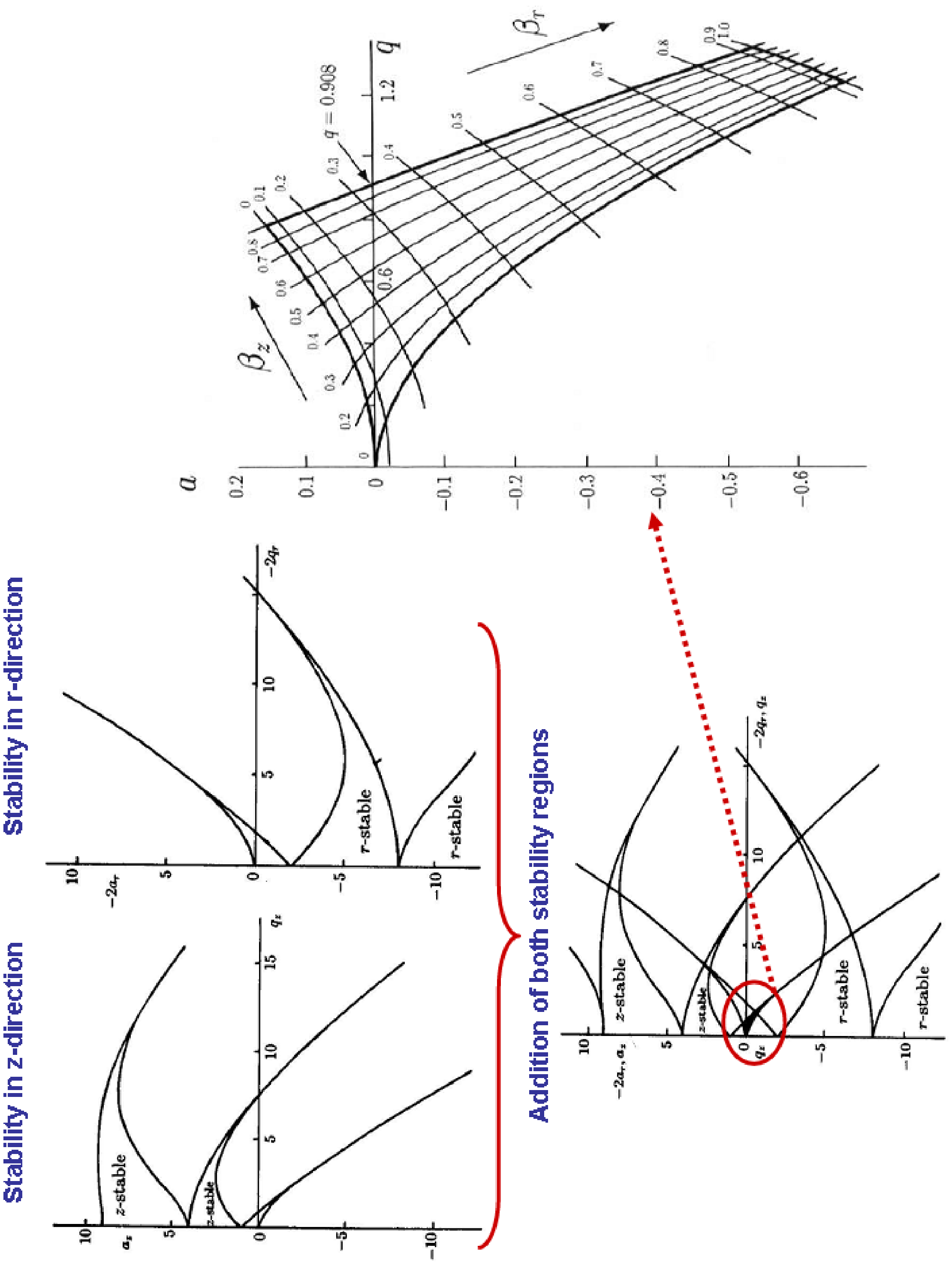

Figure 3.5: Graphical representation of stable solutions of the Mathieu equation for the three-dimensional quadrupole ion trap plotted in (a, q) space, i.e. in z- and r- direction (left panels). The resulting operational stability region near the origin is shown on the right side. Graphics by [March and Hughes, 1989].

A very good introduction to quadrupole ion trap mass spectrometry gives the book by R. March and R. Hughes [March and Hughes, 1989].

3.1.3.2 Ion Trap Mass Spectrometry (ITMS)

Our CIMS-apparatus is equipped with a commercial ion trap mass spectrometer, LCQ, fabricated by Thermo Finnigan. The original instrument was constructed for the analysis of liquids. The so-called electro-spray unit was removed and replaced by an adapter for KF40 tubes, i.e. a 40 mm in diameter stainless steal tubing. **Figure 3.6** gives a schematic view of the interior of the mass spectrometer and **Figure 3.7** shows the interior on a photograph. Through a front orifice of 0.015 cm in diameter a part of the gas sample is soaked into the octapole region of the instrument, differentially pumped by a turbo molecular pump (TMP, 200 liters/s). The main gas stream is pumped directly through the exhaust tube by an additional rotary pump (7 liters/s). In the exhaust tube humidity, temperature and pressure of the sample is measured. The ion stream in the instrument is focused by two octapoles and the inter-octapole lens. Afterwards ions are injected into the ion trap for about 250 ms (the ion injection time). This ion injection time is manually variable, depending on the kind of measurement: for substances with very low concentrations, one would employ longer injection times to collect a higher number of ions.

Under operating conditions the pressure in the flow reactor and therefore in front of the front orifice was kept constantly at 70 hPa. At the first pumping stage downstream of the inlet orifice the pressure was about 10^{-1} Pa and at the second pumping stage smaller than 10^{-3} Pa. The electric potential of the trap is kept in such a way, that all masses have stable orbits (**Figure 3.8**, left side), prescribed by the Mathieu equations. Inside the trap, helium is used as damping gas to slow down the ions ("kinetic cooling") and to displace molecules that could disturb the measurements like water molecules. This is also the reason, why not the $SO_5^-(H_2O)$ clusters are visible in our measurement, but only the SO_5^- ion. The H_2O ligands are stripped of in the trap. Next the electric potential of the trap is changed so that the orbits for one ion mass after each other become unstable in axial direction (**Figure 3.8**, right side). The ions are ejected from the trap and impinge with high energy on a conversion

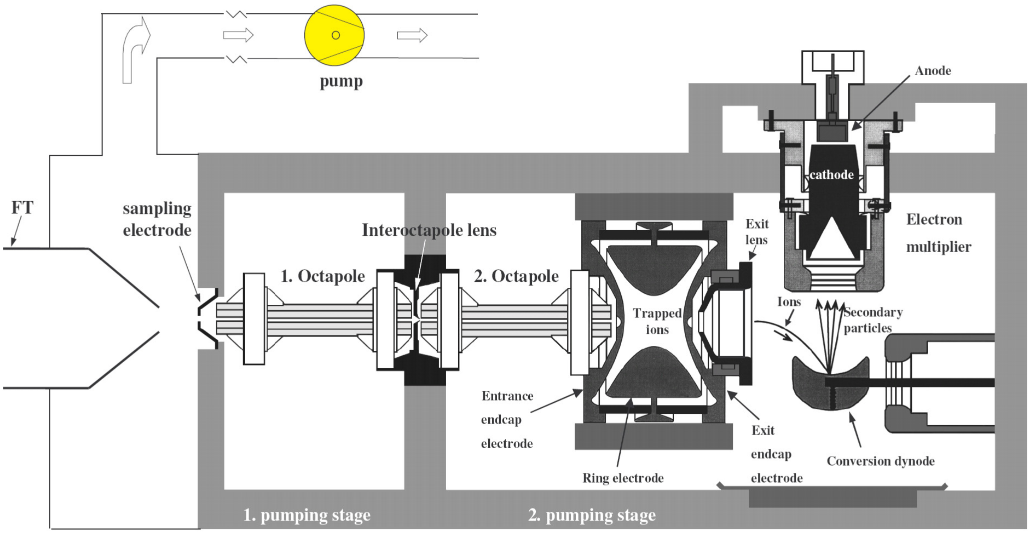

Figure 3.6: Schematic view of the structure of the ion trap mass spectrometer [Hanke, 1999].

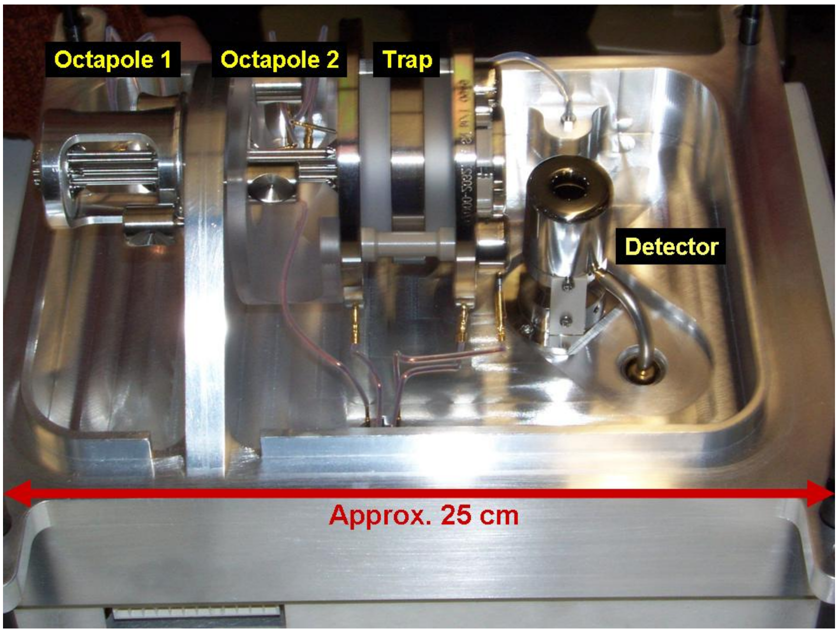

Figure 3.7: Photograph of the interior of the ion trap mass spectrometer.

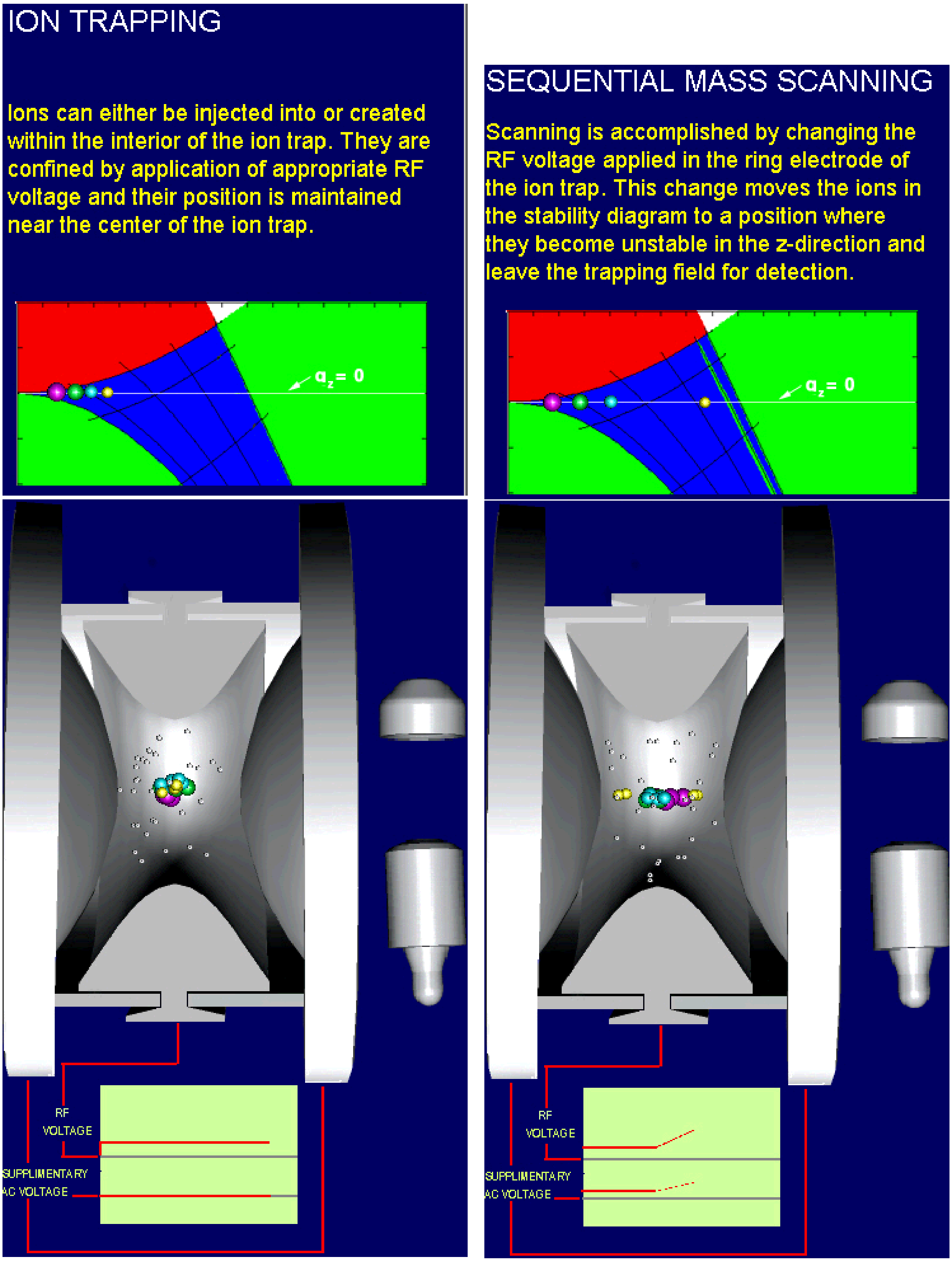

ION TRAPPING

Ions can either be injected into or created within the interior of the ion trap. They are confined by application of appropriate RF voltage and their position is maintained near the center of the ion trap.

SEQUENTIAL MASS SCANNING

Scanning is accomplished by changing the RF voltage applied in the ring electrode of the ion trap. This change moves the ions in the stability diagram to a position where they become unstable in the z-direction and leave the trapping field for detection.

Figure 3.8: Mass storage (left) and selection (right) via change of the electrical potential in the trap. In the upper part the Mathieu stability diagram [graphics by Finnigan].

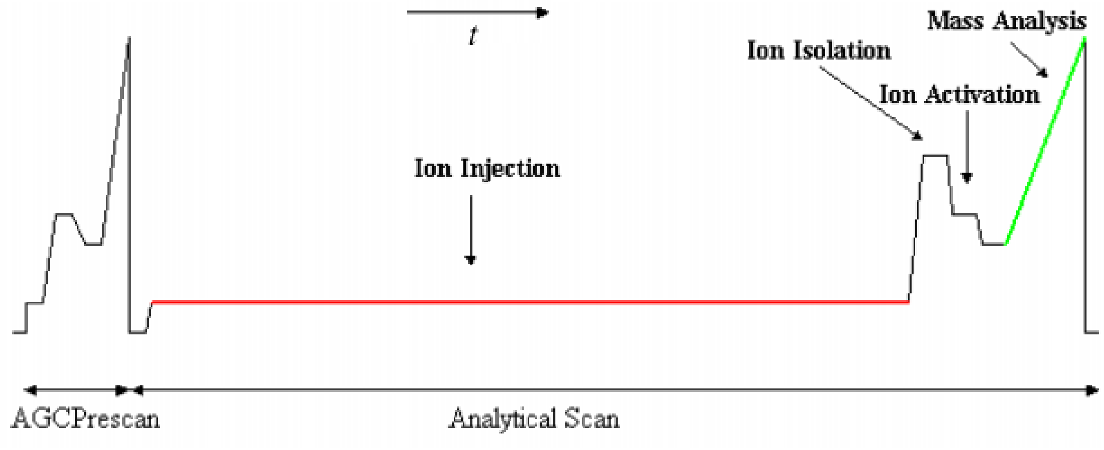

Figure 3.9: The AGC triggered order of a mass scan. By a prescan an ideal ion injection time is determined, which leads to an ideal amount of ions in the trap [graphics by Finnigan].

dynode, where secondary particles are emitted. The conversion dynode has a voltage of ±15 kV, the polarity depending on the measurement mode. For measurements of negative ions the polarity is positive and positive ions are emitted, for negative ions the polarity is negative and negative ions and electrons are emitted. The secondary particles are then focused and collected by an electron multiplier (Voltage ±1080 V, negative in the negative ion mode), where they strike the inner walls and eject further electrons. This leads at the end of the multiplier to a measurable current, which is proportional to the number of secondary particles initially emitted. This current is finally measured by an electrometer.

By a system called Automatic Gain Control (AGC) the collection of a sufficient number of ions is ensured, **Figure 3.9**. By the AGC prescan (duration 0.2 ms), the ion concentration in the gas stream is roughly checked and from there an ideal ion injection time is determined. The above explained manual choice of an ion injection time just gives an upper limit. The AGC helps a lot to determine the ideal injection time by limiting the amount of ions in the trap. Too few ions in the trap would cause a large statistical error to the measurement, too many ions would also disturb the measurement by ion-ion interactions in the trap.

Moreover, a first smoothing for the data is already provided during measurement by the choice of a number of so-called microscans. The number of microscans simply means, that in each microscan the ions are injected into the trap and analyzed as usual, the ion count rates of all microscans are added and divided by the number of microscans. We usually worked with a microscan number of 5, which results in a total time resolution of the measurement of about 1 second.

3.1.4 Error Calculation and Detection Limit

3.1.4.1 Error Calculation

The error of the measurements comprises several parts: the error of the SO_2 standard concentration in the gas bottle, the error of the mass flows through the mass flow controllers, the error of the total flow through the whole system as well as statistical errors. Therefore the error calculation follows the Gaussian error propagation principle. Further errors as the error of the ion residence time in the flow reactor or the error of the rate coefficient k are already taken into account by the use of the isotopically labelled calibration, view sections 3.1.2.2 and 3.1.2.3. The calculation values differed somewhat from campaign to campaign, as e.g. the standard in the bottle differs or a flow was changed. But the principle calculation scheme was always the same. The calculation for SCOUT-O3 (campaign description view chapter 4) will be presented here as example. **Table 3.2** lists the main uncertainties that have to be considered for the error calculation.

The SO_2 mole fraction is calculated as follows:

$$[\mathrm{SO_2}] = \frac{\Phi_{SO_2}}{\Phi_{tot}} \cdot \mathrm{S}_{conc} \cdot \frac{K_{ss}\mathrm{R} - K_{as}}{K_{aa} - K_{sa}\mathrm{R}} =: \frac{\Phi_{SO_2}}{\Phi_{tot}} \cdot \mathrm{S}_{conc} \cdot \mathrm{X} \tag{3.31}$$

with Φ_{SO_2} the mass flow of the calibration gas, Φ_{tot} the total mass flow through the measurement system, S_{conc} the calibration gas mole fraction in the standard bottle, R the ratio of the ion count rates of mass 112 and mass 114 and the K_{ii} the factors of the Bandy formula (3.15) from above. The exact values can be found in **Table 3.2**.

The relative error of the SO_2 mole fraction is then

$$\left(\frac{\sigma_{[\mathrm{SO_2}]}}{[\mathrm{SO_2}]}\right)^2 = \left(\frac{\sigma_{\Phi_{SO_2}}}{\Phi_{SO_2}}\right)^2 + \left(\frac{\sigma_{\Phi_{tot}}}{\Phi_{tot}}\right)^2 + \left(\frac{\sigma_{\mathrm{S}_{conc}}}{\mathrm{S}_{conc}}\right)^2 + \left(\frac{\sigma_{\mathrm{X}}}{\mathrm{X}}\right)^2 \tag{3.32}$$

with

$$\left(\frac{\sigma_{\Phi_{SO_2}}}{\Phi_{SO_2}}\right)^2 = 0.01^2 \tag{3.33}$$

$$\left(\frac{\sigma_{\Phi_{tot}}}{\Phi_{tot}}\right)^2 = 0.033^2 \tag{3.34}$$

$$\left(\frac{\sigma_{\mathrm{S}_{conc}}}{\mathrm{S}_{conc}}\right)^2 = 0.1^2 \tag{3.35}$$

For the calculation of σ_X, the error of the "Bandy-factor", some further information is needed. The number N of ions counted, considered 5 microscans (view last paragraph of previous section) and a signal amplification of 1000 by the electron multiplier, is

$$\mathrm{N} = \frac{\mathrm{n}}{5} \cdot 1000 \tag{3.36}$$

The statistical error of n and accordingly the statistical error of N is

$$\sigma_\mathrm{n} = \sqrt{\mathrm{n}} \tag{3.37}$$

$$\Rightarrow \quad \sigma_\mathrm{N} = 200 \cdot \sqrt{\mathrm{n}} = 200 \cdot \sqrt{\frac{\mathrm{N}}{200}} \tag{3.38}$$

$$\Rightarrow \quad \sigma_\mathrm{N}^2 = 200 \cdot \mathrm{N} \tag{3.39}$$

Now σ_X can be calculated as follows:

$$\sigma_\mathrm{X}^2 = \left(\frac{\partial \mathrm{X}}{\partial \mathrm{R}}\right)^2 \cdot \sigma_\mathrm{R}^2 \tag{3.40}$$

Type of error	**Factor**	**Value**	**Rel. Error**	**Significance**
Calibration standard in the bottle	S_{conc}	480 ppbv	10%	high
Mass flow controller SO_2	Φ_{SO_2}	10.93 smlm	1%	low
Total mass flow	Φ_{tot}	8.51 slm	3.3%	high
Statistical error of the ion peak height	R	$X112/X114$	$\sqrt{\frac{200}{X112} + \frac{200}{X114}}$	high
Fraction of $^{114}SO_2$ in the standard (SCOUT)	K_{ss}	0.9033	-	no
Fraction of $^{112}SO_2$ in the standard (SCOUT)	K_{as}	0.0967	-	no
Fraction of $^{112}SO_2$ in nature	K_{aa}	0.939	-	no
Fraction of $^{114}SO_2$ in nature	K_{sa}	0.0511	-	no

Table 3.2: Compilation of the most important individual errors of the SO_2 measurements.

$$= \left(\frac{ac - bd}{(c - \mathrm{R}d)^2}\right)^2 \cdot \sigma_{\mathrm{R}}^2 \tag{3.41}$$

with

$$\begin{aligned} a &= K_{ss} \\ b &= K_{as} \\ c &= K_{aa} \\ d &= K_{sa} \end{aligned}$$

and

$$\sigma_{\mathrm{R}}^2 = \mathrm{R}^2 \cdot \left(\left(\frac{\sigma_{X112}}{X112}\right)^2 + \left(\frac{\sigma_{X114}}{X114}\right)^2\right) \tag{3.42}$$

which becomes with formula (3.39)

$$\sigma_{\mathrm{R}}^2 = \mathrm{R}^2 \cdot \left(\frac{200}{X112} + \frac{200}{X114}\right) \tag{3.43}$$

These calculations result in a relative error of X between ±5 and ±50% depending on the fact how close to the detection limit an ion count rate is measured.

$$\left(\frac{\sigma_{\mathrm{X}}}{\mathrm{X}}\right)^2 = \text{from} \quad 0.05^2 \quad \text{to} \quad 0.5^2 \tag{3.44}$$

The error becomes bigger close to the detection limit.

All these factors together give the relative error of the measured mole fraction of SO_2 according to formula (3.32). This error ranges usually between ±5 and ±20% for all measurement campaigns.

$$\frac{\sigma_{[\mathrm{SO_2}]}}{[\mathrm{SO_2}]} = \quad 5 \quad \text{to} \quad 20\% \tag{3.45}$$

3.1.4.2 Detection Limit

During all campaigns the background of the measurements has been determined both by short in-flight background measurements and by comprehensive background measurement at the ground. For these measurements the CIMS apparatus is running with zero air (Nitrogen of purity 5.0 without measurable amounts of SO_2 or HNO_3) to determine the electronic noise of the instrument. If the background of the measurements is known, a detection limit can be calculated.

The definition of the detection limit (DL) in literature is usually

$$\mathrm{DL} = \overline{\mathrm{BG}} + 3\sigma_{BG} \tag{3.46}$$

or sometimes also

$$\mathrm{DL} = \overline{\mathrm{BG}} + 2\sigma_{BG} \tag{3.47}$$

with $\overline{\mathrm{BG}}$ being the arithmetic mean of the background and σ_{BG} its absolute error. As example here again the calculation for SCOUT-O3 is presented. The mean background of the mass lines 112 and 114 without addition of the calibration gas (pure instrumentally caused background) is

$$\overline{\mathrm{BG}_1 X112} = 6227 \text{ counts} \tag{3.48}$$

$$\overline{\mathrm{BG}_1 X114} = 1284 \text{ counts} \tag{3.49}$$

A similar background measurement but with addition of 493 pptv SO_2 calibration gas yields mean background count rates for the mass lines 112 and 114 of

$$\overline{\mathrm{BG}_2 X112} = 13662 \pm 2541 \text{ counts} \tag{3.50}$$

$$\overline{\mathrm{BG}_2 X114} = 72850 \text{ counts} \tag{3.51}$$

with 2541 counts being the standard deviation σ_{BG} of the mean background of mass line 112. After substraction of the mean instrumentally background the count rates reduce to

$$\overline{X112_{cor}} = 7453 \text{ counts} \tag{3.52}$$

$$\overline{X114_{cor}} = 71565 \text{ counts} \tag{3.53}$$

Consequently the 2σ environment of the background

$$\overline{X112_{cor}} + 2\sigma_{BG} = 7453 + 2 \cdot 2541 = 12535 \text{ counts} \tag{3.54}$$

leads to the ratio R

$$\mathrm{R} = \frac{\overline{X112_{cor}} + 2\sigma_{BG}}{\overline{X114_{cor}}} = \frac{12535}{71565} = 0.17516 \tag{3.55}$$

Campaign	**Detection Limit (2σ) / pptv**	**Subtracted background of X112**
ITOP	38	19 pptv
TROCCINOX	30	23 pptv
SCOUT	33	6227 counts (i.e.$\approx$ 40 pptv)
INTEX	13	1022 counts (i.e.$\approx$ 26 pptv)
AMMA	25	1847 counts (i.e.$\approx$ 33 pptv)

Table 3.3: Detection limits and subtracted background values for SO_2 measurements for all four aircraft campaigns and as comparison the values of one former campaign named ITOP.

And this ratio corresponds according to formula (3.15) to a mole fraction of 32.6 pptv. **Table 3.3** lists the detection limits (2σ) and subtracted mean background values (X112) for all four campaigns.

3.1.5 Advantages of the CIMS Method

There are several main advantages of this CIMS SO_2 measurement method compared to the former ones. Firstly, the measurable mixing ratios are very low, in the case of SO_2 around 30 pptv, in case of e.g H_2SO_4 even a few ppqv [Fiedler et al., 2005]. These low detection limits are achievable accompanied by a very high resolution of a second for SO_2 and of around a minute for H_2SO_4, which allows now very fast and accurate SO_2 in situ measurements on aircraft etc. Moreover, the permanent online calibration provides an automatic correction of temperature or pressure changes and possible wall losses. This markedly increases the precision of the measurements. Principally, there are also measurements of many other substances with a similar experimental setup but maybe different ion molecule reactions conceivable: H_2SO_4 was already measured by our group several times [Uecker, 2002, Fiedler, 2004, Fiedler et al., 2005], OH and peroxy radicals [Hanke, 1999], HNO_3 [Umann et al., 2005], HCL, NH_3 etc. A further advantage of the use of an ion trap mass spectrometer is the so-called ion fragmentation mode. In this mode ions with a certain mass can be stored in the trap for a while. These ions can then be excited by collisions with the helium damping gas in the trap until they dissociate into fragments. This can be of great help for the identification of molecular species with high mass numbers.

3.2 Experimental Setup

Figure 3.10 shows a schematic representation of the aircraft CIMS setup for SO_2 measurements. Through the backward showing inlet at the top of the aircraft, air is soaked into the flowreactor tube with a volume flow of approximately 8 standard liters per minute (slm). The inlet is showing backwards to avoid the sampling of water droplets or aerosol particles while flying through clouds, haze and dust. The pressure is kept constant at 70 hPa via an electronic mass flow controller, which is directly controlled by a pressure sensor. While pressure outside of the airplane changes with altitude, conditions are constant in the flow tube. Right ahead of this pressure control, the calibration gas (manufactured by Westfalen Gas, Germany) is added to the main gas stream. In the flowreactor, the air passes first a pressure and temperature sensor, then the ion source, an oxygen gas discharge. This ion source creates free electrons e^-, which attach to atmospheric O_2 forming charged O_2^- and O^-. These ions react further with ozone forming O_3^- and then with CO_2 the CO_3^- educt ions are formed. After an about 20 cm long reaction path, the ions enter the mass spectrometer and are analyzed as mentioned above. In the exhaust tube, a second pressure and temperature measurement is placed and the humidity of the air sample is determined with a dewpoint sensor. A critical orifice in front of the flow tube pump works as additional flow control. Additionally, in **Figure 3.11** a photograph of the aircraft setup for AMMA (campaign explanations see next chapter) is shown.

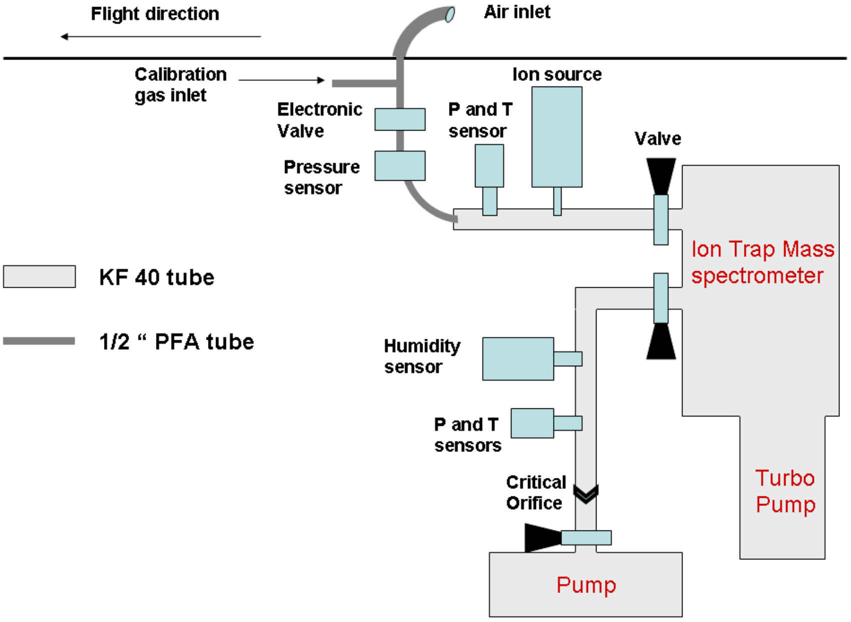

Figure 3.10: Schematic view of the experimental setup: Air inlet in the ceiling of the aircraft, pressure controlled airflow into the mass spectrometer, sensors etc.

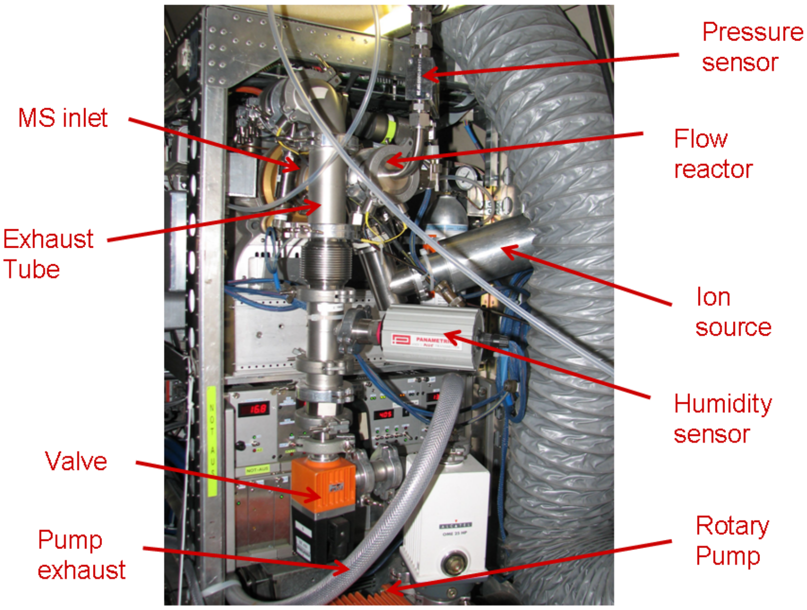

Figure 3.11: Photograph of the aircraft setup for SO_2 measurements during AMMA.

Chapter 4

Measurement Campaigns

Within the framework of this thesis, the instrument was in use for measurements of atmospheric SO_2 in 4 different aircraft measurement campaigns. Campaign starting points were Araçatuba (Brazil), Darwin (Northern Australia), Oberpfaffenhofen (Germany) and Ouagadougou (Burkina Faso, Africa). During the Australian campaign already the transfer flights from Europe to Australia and back were measurement flights. Table 4.1 comprises the dates and the areas covered by measurement flights during the four campaigns and Table 4.2 names the activity coordinators of the different campaigns and informative web pages.

Besides SO_2, other trace gases including NO, NOy, CO, CO_2, O_3 and particles of different size classes have been measured by other instruments deployed on the aircraft as well as standard information like temperature, pressure, humidity, flight level etc. During all campaigns the instruments were installed on the DLR research aircraft Falcon, which has a maximum flight altitude of about 13km and a maximum range of 3-4 hours.

Campaign	**Flights**	**Time**	**Lat Min**	**Lat Max**	**Lon Min**	**Lon Max**
TROCCINOX	5	Feb 2005	−28° S	−19° S	−53° W	−47° W
SCOUT Transfer	14	Nov & Dec 2005				
SCOUT Darwin	9	Nov/Dec 2005	−23° S	−7° S	125° E	135° E
INTEX	11	Mar-May 2006	34° N	53° N	−20° W	12° E
AMMA	5	Aug 2006	4° N	17° N	−8° W	4° E

Table 4.1: List of aircraft campaigns with SO_2 measurements.

Campaign	**Activity Coordination**	**Web Address**
TROCCINOX	U. Schumann, DLR	*www.pa.op.dlr.de/troccinox/*
SCOUT-O3	C. Schiller, FZJ	*www.ozone-sec.ch.cam.ac.uk/scout_o3/*
INTEX	H. Schlager, DLR	*http://cloud1.arc.nasa.gov/intex-b/*
MEGAPLUME	A. Stohl, NILU	*www.eufar.net/experiment/rprojects/specproj.php*
AMMA	J. Polcher, CNRS	*www.amma-eu.org*

Table 4.2: List of aircraft campaigns coordinators and web pages.

4.1 TROCCINOX

The main objectives of the TROCCINOX (**Tro**pical **C**onvection, **C**irrus and **N**itrogen **Ox**ides Experiment) campaign were:

- to improve the knowledge about lightning-produced NOx in tropical thunderstorms by quantifying the produced amounts, by comparing it to other major sources of NOx and by assessing its global impact, and
- to improve the current knowledge on the occurrence of other trace gases (including water vapor) and particles (ice crystal, aerosols and their precursor SO_2) in the upper troposphere and lower stratosphere in connection with tropical deep convection as well as large scale upwelling motions.

The scientific objectives of TROCCINOX were addressed by performing field experiments in the tropics including measurements on different spatial scales. Two research aircrafts, the Russian M55 Geophysica and the DLR Falcon probed the large scale structure of the upper troposphere and lower stratosphere during transfer flights and local flights in Brazil. Takeoff and landing was always in Araçatuba (−21° 8' S, 50° 25' W, 390 m asl). The covered flight area is listed in Table 4.1. SO_2 was measured during five flights between the 5th and the 10th of February 2005 [Schuck, 2006, Schuck et al., 2007, Arnold et al., 2007]. Further information can be found on the campaign web page (view Table 4.2).

Special objectives concerning SO_2 were a better understanding of the influence of deep convection on the SO_2 vertical transport and the influence of South American pollution sources on the SO_2 concentration as well as the role of SO_2 as new particle precursor.

4.2 SCOUT-O3 Tropical

The central aim of the SCOUT-O3 (**S**tratospheric-**C**limate Links with Emphasis **o**n the **U**pper **T**roposphere and Lower Stratosphere) project is to provide scientific knowledge for global assessments on ozone depletion and climate change for the Montreal and Kyoto Protocols. The Montreal Protocol has successfully reduced emissions and atmospheric concentrations of CFCs, which are estimated to return to their pre-ozone hole concentrations by about 2050. The Kyoto Protocol was the first international measure to put a restraint on the rise of carbon dioxide (CO_2) emissions caused by industrialized nations. In detail:

- Better understanding of trace gas and aerosol processes in the upper troposphere and lower stratosphere (UTLS) through modelling and data analysis.

- Lack of knowledge about the tropical stratosphere and upper troposphere is addressed through tropical field campaigns involving aircraft and balloons to investigate detailed mechanisms of air transport from the troposphere to the stratosphere.

Here SO_2 was measured during the 14 transfer flights from Oberpfaffenhofen via Larnaca (Cyprus), Dubai, Hyderabad (India), U-Tapao (Thailand), Brunei to Darwin (Australia) and back the same route with two further stops in Bahrain and Brindisi (Italy). Locally in Australia, we had 9 flights starting from Darwin ($-12°$ 24' S, 130° 54' W, 0 m asl) between the 16th of November and the 5th of December 2005. The flight area is listed in Table 4.1 and the informative web page is marked in Table 4.2.

Concerning SO_2 the region is interesting because of the possibility to investigate deep convection and long range transport from Indonesia, an area with high biomass burning activity.

4.3 SHIPS, INTEX-B, MEGAPLUME

This campaign actually was a mixture of three different campaigns. The first part SHIPS dealt with the investigation of ship exhaust, therefore flights in the English Channel were performed to get ship track measurements as well as ship chasing flights. Ship exhaust measurements are special because of the really high SO_2 mole fractions. The ship measurements are not further investigated in this thesis as this thesis focuses on long range transport and industrial pollution sources of SO_2 and not on traffic, but the overview panels for the ship flights can be found in the appendix.

The second part INTEX-B (**In**tercontinental Chemical **T**ransport **Ex**periment, view also Tables 4.1 and 4.2) aims at the detection of North American pollution plumes that are transported with westerly winds till Europe.

- Quantify the transpacific transport and evolution of Asian pollution to North America and assess its implications for regional air quality and climate.
- Quantify the outflow and evolution of gases and aerosols from Mexico City.
- Investigate the transport of Asian and North America pollution to the eastern Atlantic and assess its implications for European air quality.
- Validate and refine satellite observations of tropospheric composition.
- Map emissions of trace gases and aerosols and relate atmospheric composition to sources and sinks.

Part three, MEGAPLUME (Long-range transport of **mega**city air pollution **plume**s), was a campaign with the objective to detect the pollution plume of the town of Mexico City, which is, depending on the weather situation, transported as well over the Atlantic till Europe. The objectives listed in detail are

- To intercept a North American megacity plume over Europe, preferably the Mexico City plume after it has been characterized extensively by upwind North American aircraft and ground measurements.
- To investigate the degree of chemical processing that has occurred in the plume en route to Europe.
- To estimate the potential impact of such a plume on the chemical composition of the troposphere above Europe.

Obviously, measurements of SO_2 are of interest for all the objectives in INTEX-B and MEGAPLUME.

Flights started either from Oberpfaffenhofen (48° 6' N, 11° 18' E, 520 m asl), Santiago de Compostela (42° 54' N, $-8°$ 24' W, 260 m asl) or Brest (48° 24' N, $-4°$ 24' W, 34 m asl) between the 24th of March 2006 and the 5th of May 2006. The covered flight area can be found in Table 4.1.

4.4 AMMA

The overall objectives of AMMA (**A**frican **M**onsoon **M**ultidisciplinary **A**nalysis) are as follows:

- To improve our understanding of the West African Monsoon and its influence on the physical, chemical and biological environment regionally and globally.
- To provide the underlying science that relates variability of the West African Monsoon to issues of health, water resources, food security and demography for West African nations and defining and implementing relevant monitoring and prediction strategies.
- To ensure that the multidisciplinary research carried out in AMMA is effectively integrated with prediction and decision making activity.

The Falcon measurements here provided information about the composition of the atmosphere over Western Africa and had to investigate convective influence on trace gas transport, lightning NOx production or biomass burning pollution. SO_2 was measured for a better understanding of new particle formation and for mapping the SO_2 pollution over western Africa. The impacts of SO_2 on soot coating and soot hygroscopicity are addressed as well. The airplane was based in Ouagadougou (12° 21' N, $-1°$ 30' W, 316 m asl), the capital of Burkina Faso and the covered flight area is listed in able 4.1. Flights took place from the 4th to the 13th of August 2006.

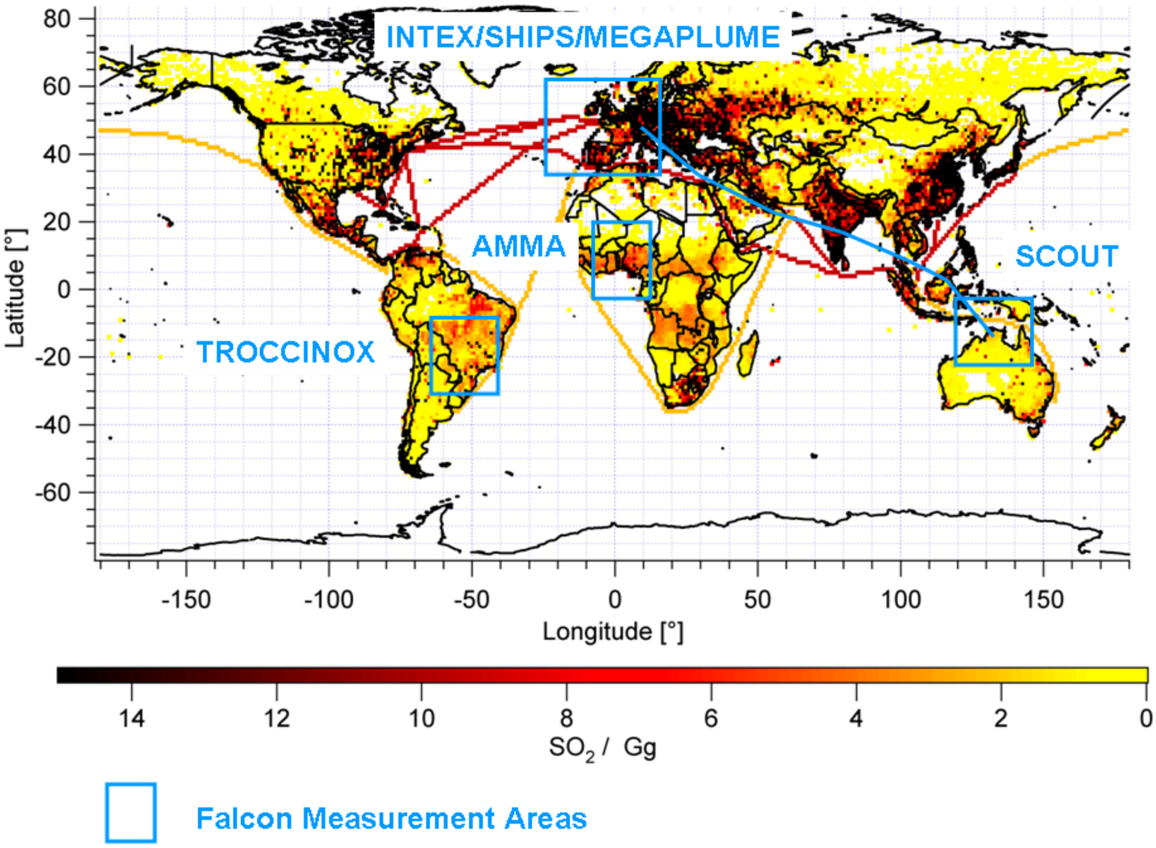

Figure 4.1: EDGAR inventory world map. In blue the Falcon research measurement areas. Dark colors indicate enhanced SO_2 emissions (for the EDGAR inventory view also chapter 2).

Figure 4.1 shows all measurement areas on the EDGAR inventory world map (view also chapter 2). As can be seen, interesting areas for sulfur measurements are covered. Several types of comparisons and analyses are now possible, as areas with similar conditions, like the three tropical regions, can now be compared to the European area. Convective influence could be studied at several places as well as anthropogenic or biogenic influences.

This work will focus now on the one hand on a comparison of different features of all those campaigns, especially on an comparison between tropics and subtropics. On the other hand certain special flights with interesting measurement results will be discussed and further analyses e.g. on new particle formation and nucleation will be added.

Chapter 5

Measurement Data

The SO_2 time series for each flight made during the four campaigns, the trace gas and some meteorological data can be found in **Appendix A**. A discussion of each flight here in detail will not be possible, as it simply would go beyond the scope of this thesis. Instead, this chapter will lie attention on a principle comparison and main features of the data at the four different campaigns. A discussion of interesting pollution plume cases will follow in the next chapter.

5.1 Median Profiles

A good tool for a fundamental comparison is the comparison of median and mean profiles. The mean profile weights all data points of a certain altitude level the same by just adding them and dividing by the total number of data points. The median is the value that divides the data points into two equivalent halves. The number of data points with values bigger than the median is the same as the number of data points with values smaller than the median. If you have e.g. 11 values sorted from the smallest to the biggest, the sixth data point will be the median, as 5 data points have a lower and five data points a larger value. The median has the advantage that extremely high or low values are suppressed. That makes the median especially interesting for atmospheric SO_2 measurements, as the SO_2 mole fraction can vary in a range from a few pptv to several ppbv.

In **Figures 5.1** and **5.2** SO_2 profiles are plotted for the three tropical campaigns in the upper panel and for the European campaign in the lower panel once with linear x-axes

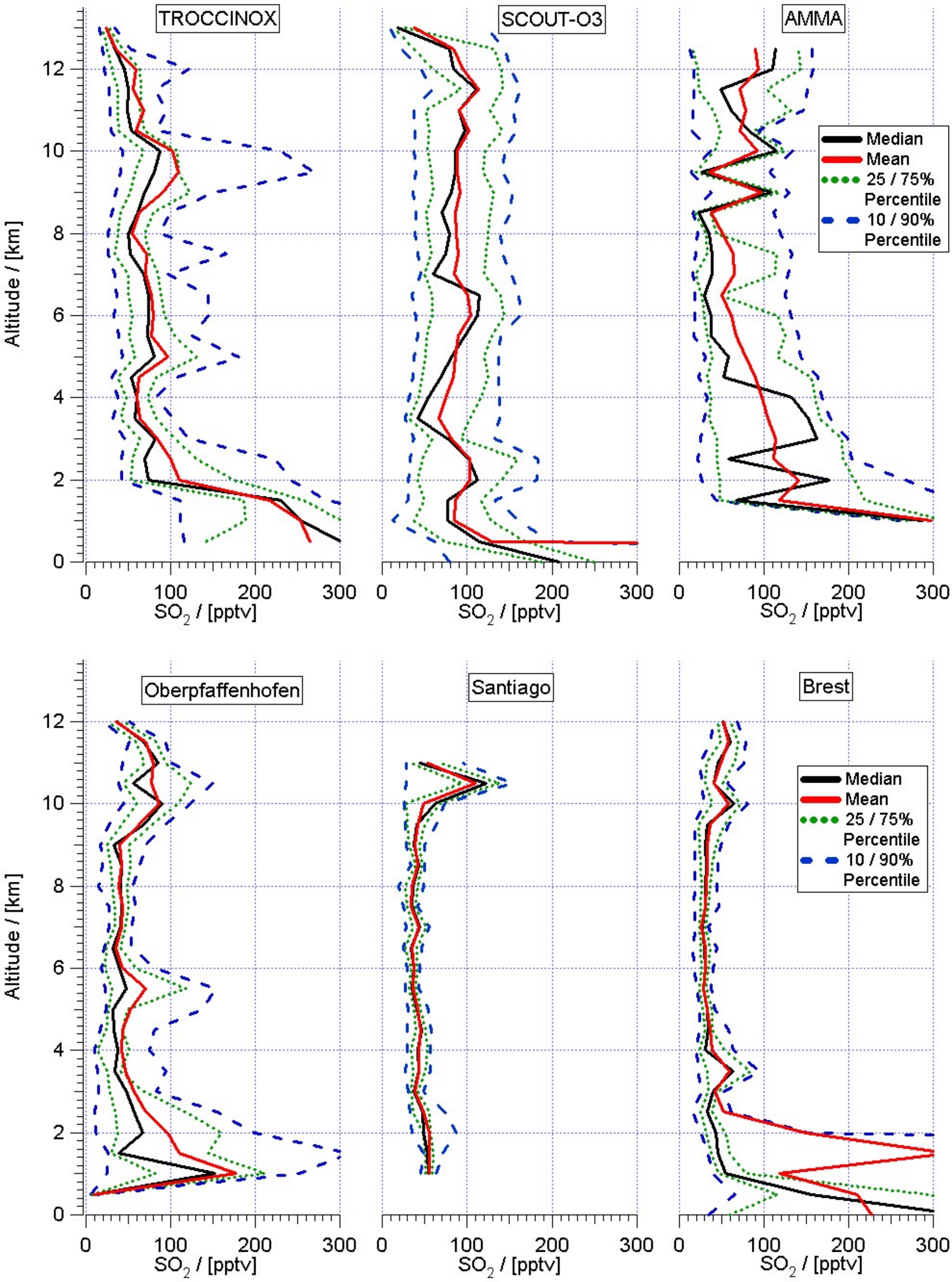

Figure 5.1: Median SO_2 mole fraction profiles of the tropical campaigns (upper panel) and the European campaign (lower panel). Always in red the mean value, in black the median, dotted green the 25% and 75% percentiles and dashed blue the 10% and 90% percentiles.

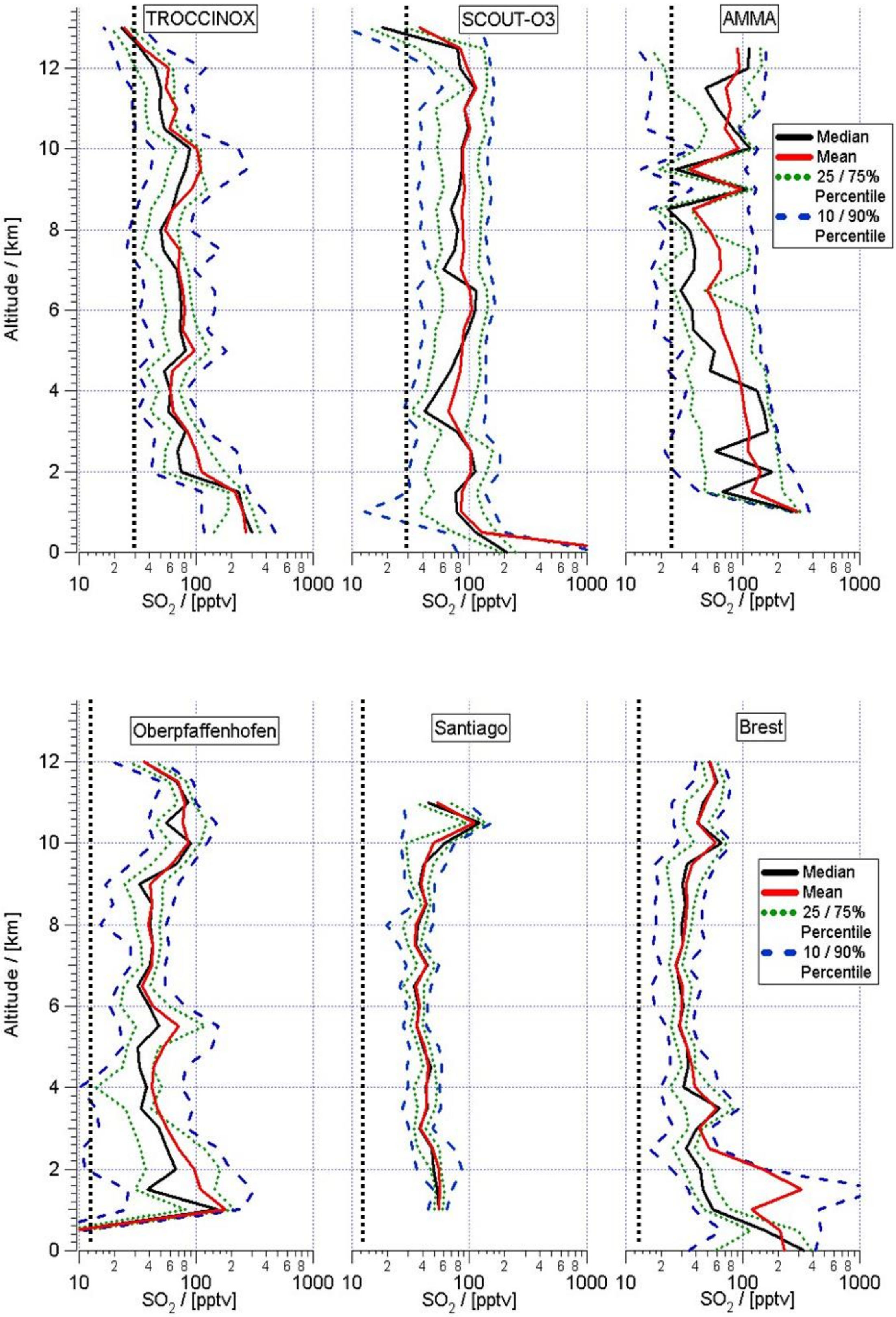

Figure 5.2: Same as Figure 5.1 but with logarithmic x-axes. The black dotted vertical line marks the SO_2 detection limit, which was slightly different for each campaign.

(**Figure 5.1**), once with logarithmic x-axes (**Figure 5.2**). The profiles are always an average of all flights during each campaign and therefore also an average over a time of usually 3-4 weeks. In addition to the mean (red) and median (black) profiles the upper and lower percentiles (10%, 25%, 75% and 90%) are plotted. 10%-percentile e.g. means that 10 percent of the data set lie below that value, 90 percent lie above. Correspondingly the 90%-percentile is the value with 10 percent of the data set lying above that value and 90 percent lying below (25%- and 75%-percentile analogue). The advantage of the median compared to the mean is e.g. visible in the boundary layer profile of Brest. The mean is obviously strongly influenced by a few very high values (visible in the 90% percentile), whereas the median shows a more moderate and therefore more representative increase.

The profile values for the INTEX campaign have been calculated for three different locations (Santiago, Brest and Oberpfaffenhofen), depending on the take off airport of the Falcon.

In **Figure 5.2** the SO_2 measurement detection limit, which was slightly different for each campaign (13-33 pptv), is marked by a black dotted line.

On a first view it is remarkable that all profiles with exception of Santiago show a similar behavior at low altitudes. High mole fractions of several ppbv in the boundary layer, where most of the SO_2 emission sources are located, are followed by a strong decline at the transition between boundary layer and free troposphere, at an altitude between 1-2km. Santiago lies almost at sea level. The "missing" boundary layer in Santiago might be caused by the fact, that the instrument was switched on only at altitudes above 1 km. If one takes only values above 1 km into account, enhanced boundary layer values would e.g. for SCOUT not be detected either.

The median in the free troposphere is mostly quite constant with altitude at all places, but its values in the tropics (70-90 pptv) are markedly higher than the values over Europe (30-40 pptv), (**Figure 5.3**). These higher tropical mean values might be explained by the effective transport of SO_2 in tropical convective systems, by the different sources of SO_2 emissions and by a shorter transport time between source and measurement site. To show

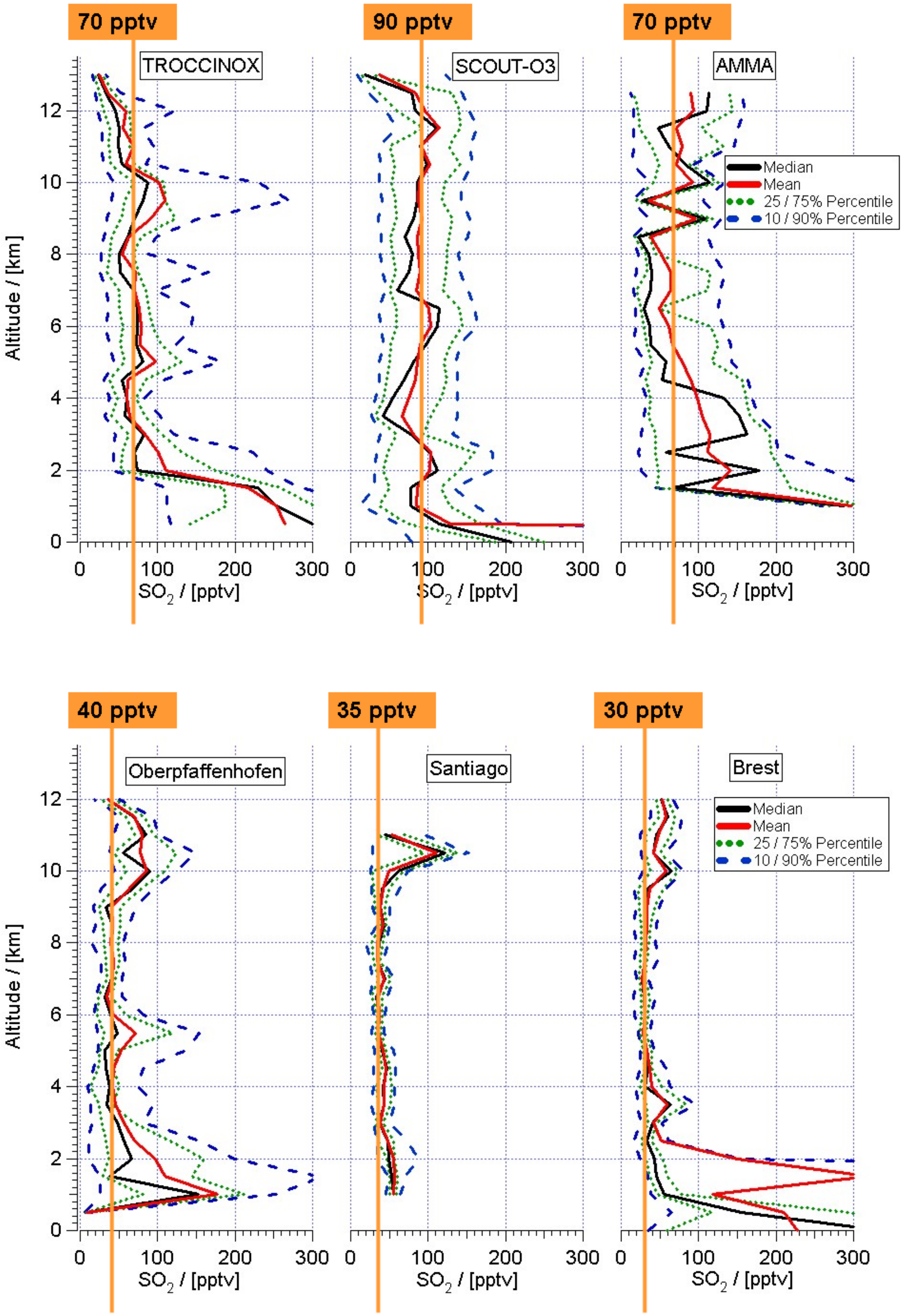

Figure 5.3: Same as Figure 5.1. The orange line gives a rough value for the mean SO_2 mole fraction of the upper troposphere.

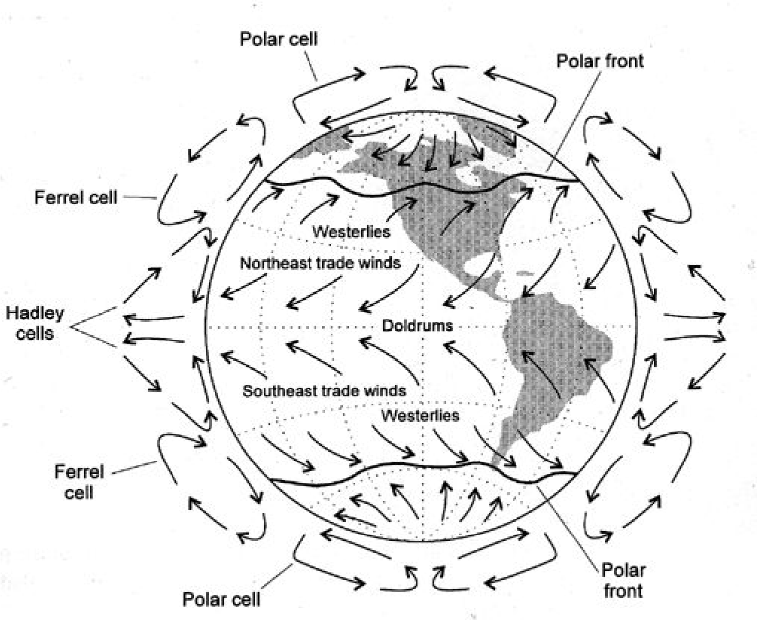

Figure 5.4: Schematic representation of the general global air mass circulation. (Figure after [Seinfeld and Pandis, 1998]).

this thoroughly air mass trajectories have been analyzed.

5.2 SO_2 Rich Air Masses

Europe is influenced mainly by westerly winds. The typical global air mass circulation is represented in **Figure 5.4**. The general pattern of the air circulation is influenced by both thermal circulation (e.g. the updraft of warm tropical air at the equator connected to cool northern air flows to the equator) and Coriolis force. In the temperate regions, between 30° and 60° N, adjacent to the North-East trade winds, the surface winds are westerlies because of the Coriolis force.

Therefore the in western Europe measured SO_2 mostly stems from sources in America or even Asia, that have been transported over the Atlantic ocean in several (usually more than 6) days, which means that a large fraction of the emitted SO_2 has already been scavenged or has been converted to H_2SO_4. The half life of SO_2 with respect to chemical conversion to H_2SO_4 is about 8 days as shown in section 2.1.2. In Brazil, trajectory analyses suggest that the probed air masses with enhanced SO_2 were either influenced by copper smelter or volcano emissions from southern Peru/northern Chile or by emissions from the cities of Sao Paolo and Rio de Janeiro. In both cases the air masses travelled only a few days until they reached the measurement area. In Australia, also influenced by westerlies, most of the flights probed air masses from the North-West, approaching from Indonesia, which is a region with high biomass burning activity. Biomass burning was also an important factor for the African campaign, where air masses stemming from central Africa were probed. **Figures 5.5** and **5.6** comprise such typical trajectories for SO_2 rich air masses during the four different campaigns.

Because of different institutional cooperations, there were different types of trajectory analyses available for the four campaigns. For TROCCINOX and INTEX, model simulations with FLEXPART, a trajectory model by the Norwegian Institute for Air Research (NILU) are used. For SCOUT, backward trajectories have been calculated with the model LAGRANTO by the University of Zurich (ETH). And for AMMA, there exist backward trajectories calculated with the model TM5 by the Royal Netherland Meteorological Institute (KNMI). Even if these different trajectory models are not directly comparable, they provide nevertheless the information about the general pathway and age of the air masses as well as the time air masses travelled from a region with possibly enhanced SO_2 to the measurement area.

The model FLEXPART is a complex lagrangian dispersion model. A bunch of 40000 so called test particles is released at a start point, from where forward or backward calculations are possible. As meteorological basis, FLEXPART uses the data from the European Center for Medium-Range Weather Forecast (ECMWF), e.g. wind fields, temperature, pressure etc. The gridded data has 1x1 degree resolution globally and 0.5x0.5 degree resolution from 90W-20E and 40S-20N. For the test particles diffusion, turbulence and convection is considered. FLEXPART moreover provides further information, as it is coupled to the emission database EDGAR. As emission input for carbon monoxide, nitrogen oxides and sulfur dioxide, the EDGAR version 3.2 for the year 2000 on a 1 x 1 degree grid is used outside North America. Over most of North America, the inventory of Frost and McKeen [Frost et al., 2006] is used. The model treats the trace gases as tracer, but without considering any chemical sources or sinks. Therefore FLEXPART can predict quite well the occurrence of enhanced SO_2, but the

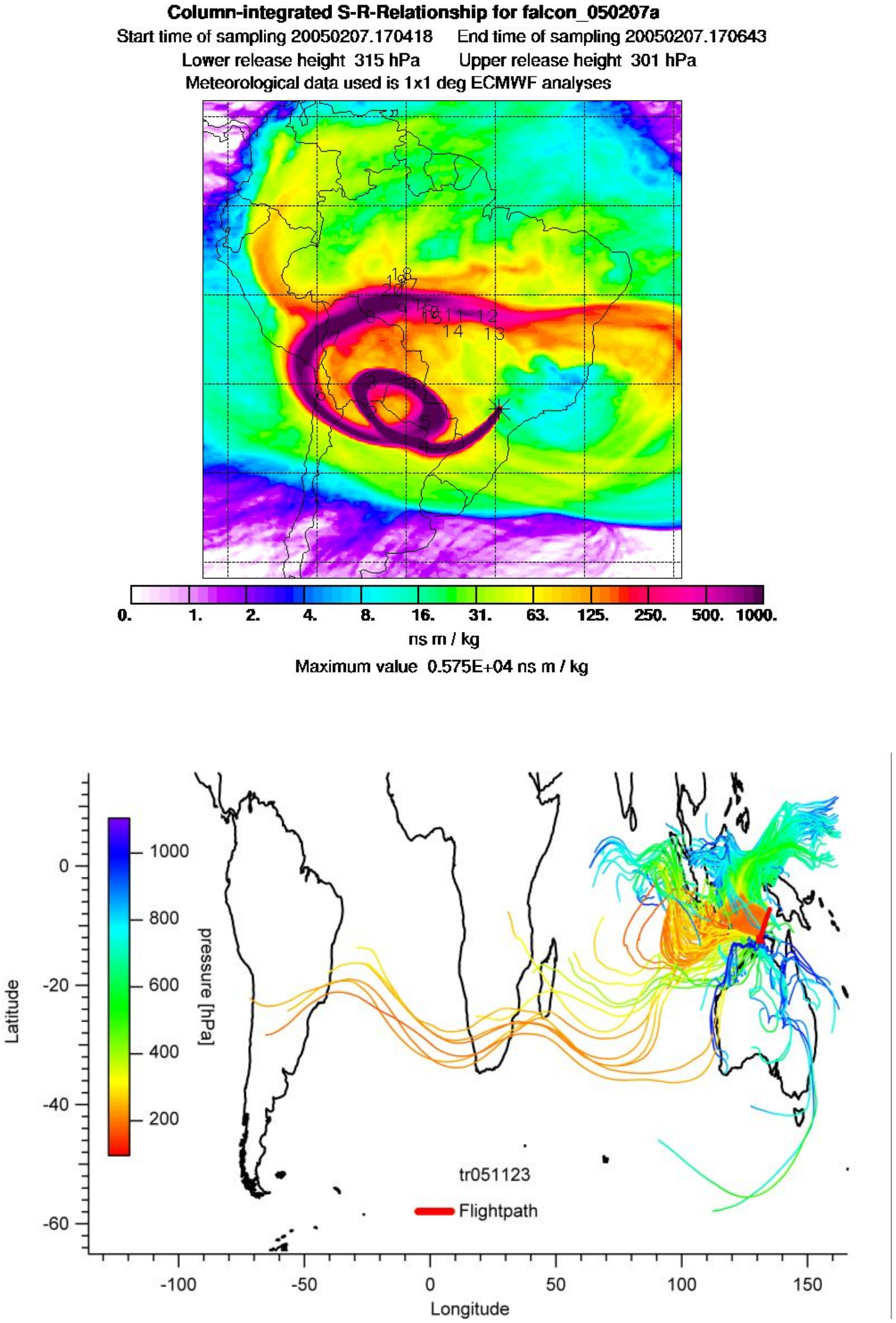

Figure 5.5: Typical trajectories of SO_2 rich air masses during TROCCINOX (upper panel, FLEXPART simulation) and SCOUT (lower panel, LAGRANTO simulation). In the TROCCINOX picture, dark violet colors indicate the central path of the air mass from the measurement area, marked by a star, backward. For the SCOUT trajectory, the color coding indicates the pressure altitude of the trajectories, which go 10 days backward. It can be seen, that mostly air masses originating in the boundary layer of Indonesia have been probed.

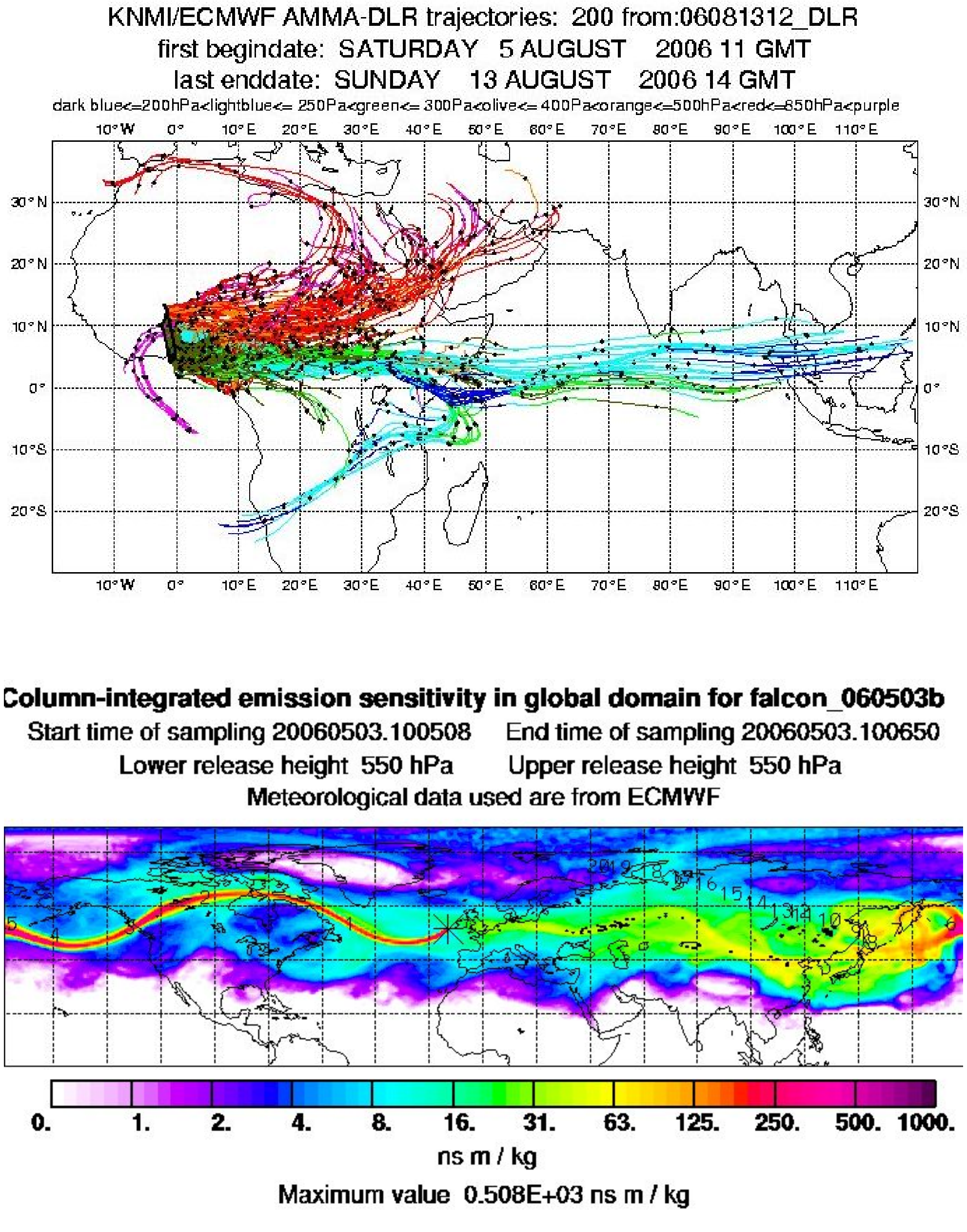

Figure 5.6: Typical trajectories of SO_2 rich air masses during AMMA (upper panel, TM5 simulation) and INTEX (lower panel, FLEXPART simulation). For AMMA, the trajectory pressure is color coded. Air masses stemmed mostly from central Africa, which is a region with high biomass burning activity. The INTEX picture indicates a trajectory origin in central Asia, but with a travel time of more than 10 days, which explains that not so high SO_2 mole fractions have been detected in Europe.

predicted concentrations at the measurement site are usually too high, as no chemical SO_2 removal during transportation is assumed [Stohl et al., 2002, Stohl et al., 2005].

Several different outputs and graphical representations of the model exist. In this work mainly the so-called column residence time is used. This product shows the vertically integrated residence time of the particles. Strictly, this is not a residence time, but the response an emission release of unit source strength would have at the measurement point assuming no chemical transformations, deposition, etc. Briefly, this column residence time plots give as color code a kind of probability for a certain air mass parcel to reach the measurement site. The numbers superimposed on the shading are the days back in time. A second output, which will be used in this work, is the co-called SO_2 source contribution graph. The result is an emission contribution of a certain source in ppbv per square meter to the modelled SO_2 output.

The simpler models LAGRANTO and TM5 just calculate backward trajectories from the ECMWF wind fields, without considering a certain trace gas species or further variables.

Concluding a comparison of our measurements to former measurements. Unfortunately there exist only very few SO_2 measurements of an altitude range comparable to ours. Most measurements only reach up to 5 or 6 km, e.g. [Tu et al., 2003, Tu et al., 2004]. The group around D. Thornton and A. Bandy from Drexel University, Philadelphia, employs gas chromatography/mass spectrometric SO_2 measurements and also uses an isotopically labelled calibration. Their measurement system is well described in [Bandy et al., 1993]. Between 1991 and 1996 they measured SO_2 in altitudes from the ground level up to 12 km at several campaigns (PEM-West A and B, PEM-tropics and ACE1) over the Pacific Ocean [Thornton et al., 1999]. The measured altitude SO_2 profiles during the PEM-West B campaign are plotted in **Figure 5.7**. The measurement region is not directly comparable to ours, as their measurements took only place over the free Pacific ocean. But in general one can say that the range of the data from 10 to 1000 pptv is quite similar to ours.

In [Thornton et al., 1999] also a latitudinal distribution of SO_2 mole fractions has been published. The graphs are presented in **Figure 5.8**. In this figure the SO_2 mole fraction

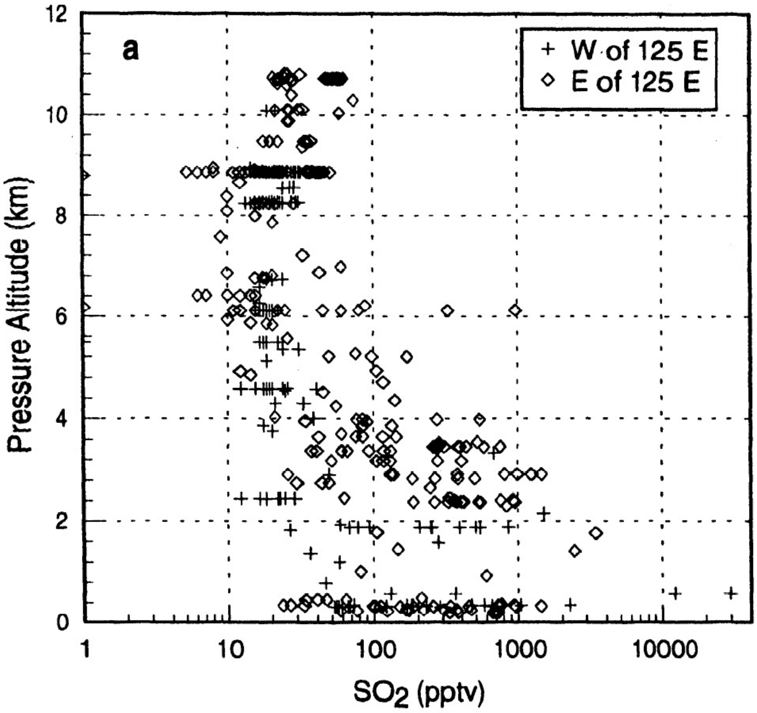

Figure 5.7: Profile of SO_2 measurements over the Pacific by [Thornton et al., 1997] during the PEM-West B campaign. It is distinguished between data points measured west or east of 125° East.

is plotted as a function of latitude for four different altitude regimes ($<$ 0.5 km, 0.5-4 km, 4-8 km, 8-12 km). Our SO_2 measurements are added as colored bars, each campaign in a different color. The boundary layer value is indicated by a colored diamond respectively. The measurements during INTEX, which were mainly taken over the free Atlantic obviously fit quite well into the Pacific data. Also the AMMA data fits quite well. The data from SCOUT and TROCCINOX lies almost constantly higher than the Pacific data. But here it has to be taken into account that the free Pacific on the southern hemisphere is almost completely uninfluenced by anthropogenic pollution sources, whereas the measurements during SCOUT and TROCCINOX took place over continents.

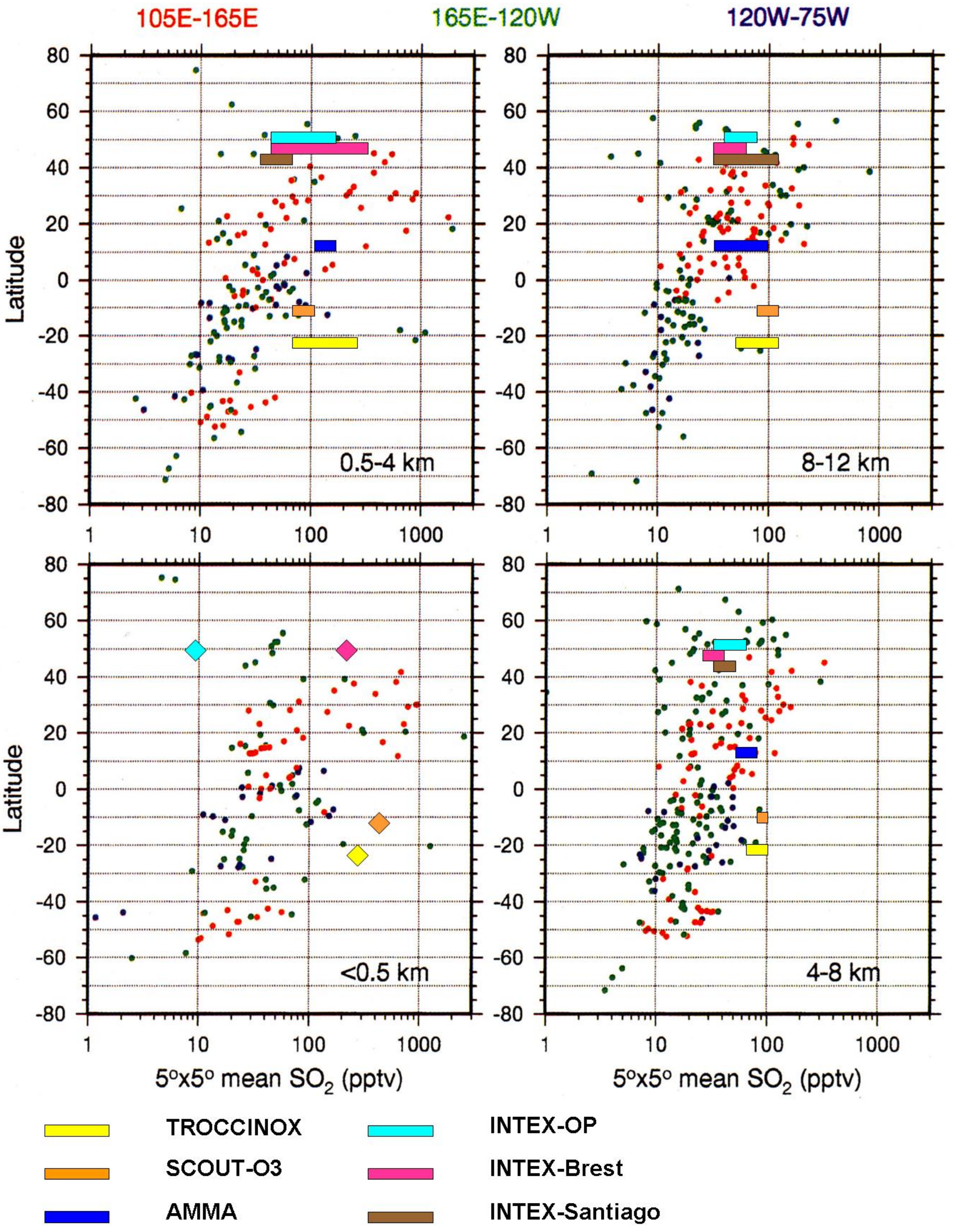

Figure 5.8: Arithmetic mean SO_2 mole fractions as a function of latitude [Thornton et al., 1999]. The four plots correspond to 4 different altitude regimes (< 0.5 km, 0.5-4 km, 4-8 km, 8-12 km). The range of our measurements is added for all campaigns to the figures as colored bars. Our boundary layer value is added as colored diamond.

Chapter 6

SO_2 Pollution Plumes: Case Studies

This chapter will deal with 4 different interesting case studies of SO_2 rich pollution plumes detected during the 4 campaigns: a probably copper smelter or volcano caused SO_2 pollution plume, detected during TROCCINOX over Brazil, a detection of long range transport of SO_2 pollution from middle America to Europe during SCOUT-O3, a very probable industrial pollution plume from East Asia, travelling almost around the whole world eastwards to Europe and detected during the INTEX campaign and last but not least an aged biomass burning pollution plume, detected over the West African Sea during AMMA. The measured plume data will be presented in detail and further going analyses will be shown.

6.1 TROCCINOX Flight 20050207, Copper Smelter Emissions

The TROCCINOX flight made on the 7th of February was a survey flight with two complete vertical profiles in the vicinity of Araçatuba. The flight path is shown in **Figure 6.1**. All TROCCINOX flights with the CIMS instrument aboard the FALCON have already previously been discussed [Schuck et al., 2007]. Here one flight will be discussed in more detail.

A time series of the whole flight is presented in **Figure 6.2**. Trajectories of air masses probed by the FALCON aircraft were calculated using the FLEXPART trajectory model [Stohl et al., 2002, Stohl et al., 2005]. Those trajectories have been analyzed for the most interesting parts of the flight. **Figures 6.3-6.5** comprise those trajectories. As can be seen from **Figure 6.2**, concerning the SO_2 mole fraction there is not much variation during the

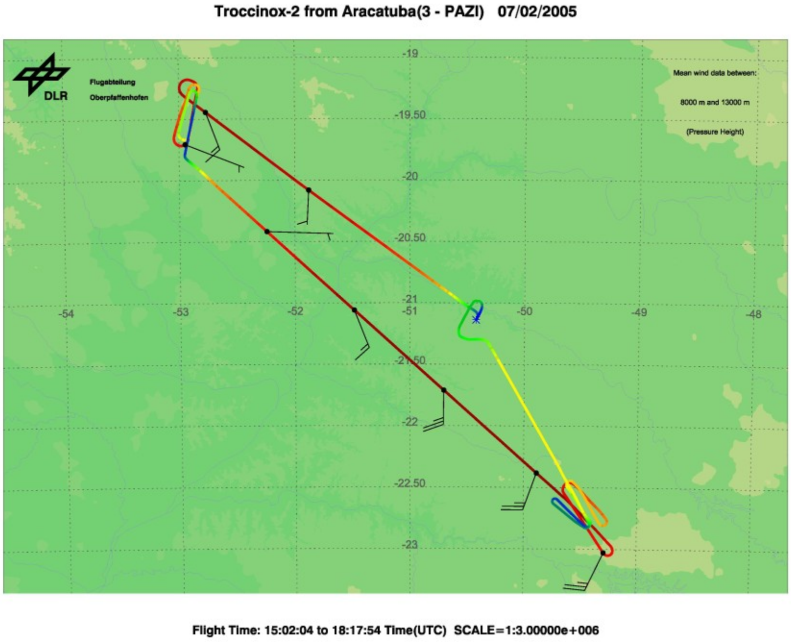

Figure 6.1: Flight path of TROCCINOX flight 20050207. The colors from blue to red roughly indicate the altitude (0 to 12 km). Distance of the wind direction markers is 15 minutes. 1° Longitude corresponds to approximately 100 km, 1° Latitude to 111 km.

first ascend and descend of the flight, the mole fraction is almost constant around 70 pptv. Starting at 15:53 UTC the first profile beginning from an altitude of 11 km was flown down to a lowest altitude of 1 km. At the lowest step of this first descend, when the aircraft dives into the boundary layer, the SO_2 mole fraction reaches peak values of 400 pptv. The corresponding FLEXPART trajectory is plotted with number 1 in **Figure 6.3**. The central air mass was just 3-5 days before passing the area of Sao Paolo and Rio de Janeiro, which explains those high SO_2 values even 5 days later at the measurement site. The strong boundary layer pollution is also visible in high concentrations of accumulation mode and non volatile aerosol particles and in an increase of the CO and NOy mole fractions.

For a better resolution of the following second ascend a zoom of Figure 6.2 is plotted in **Figure 6.6**. After leaving the boundary layer the SO_2 mole fraction first goes back to values below 100 pptv. In this region the main air mass direction is turning from the east to the north (FLEXPART columns number 2 and 3). The air is getting dryer. The other

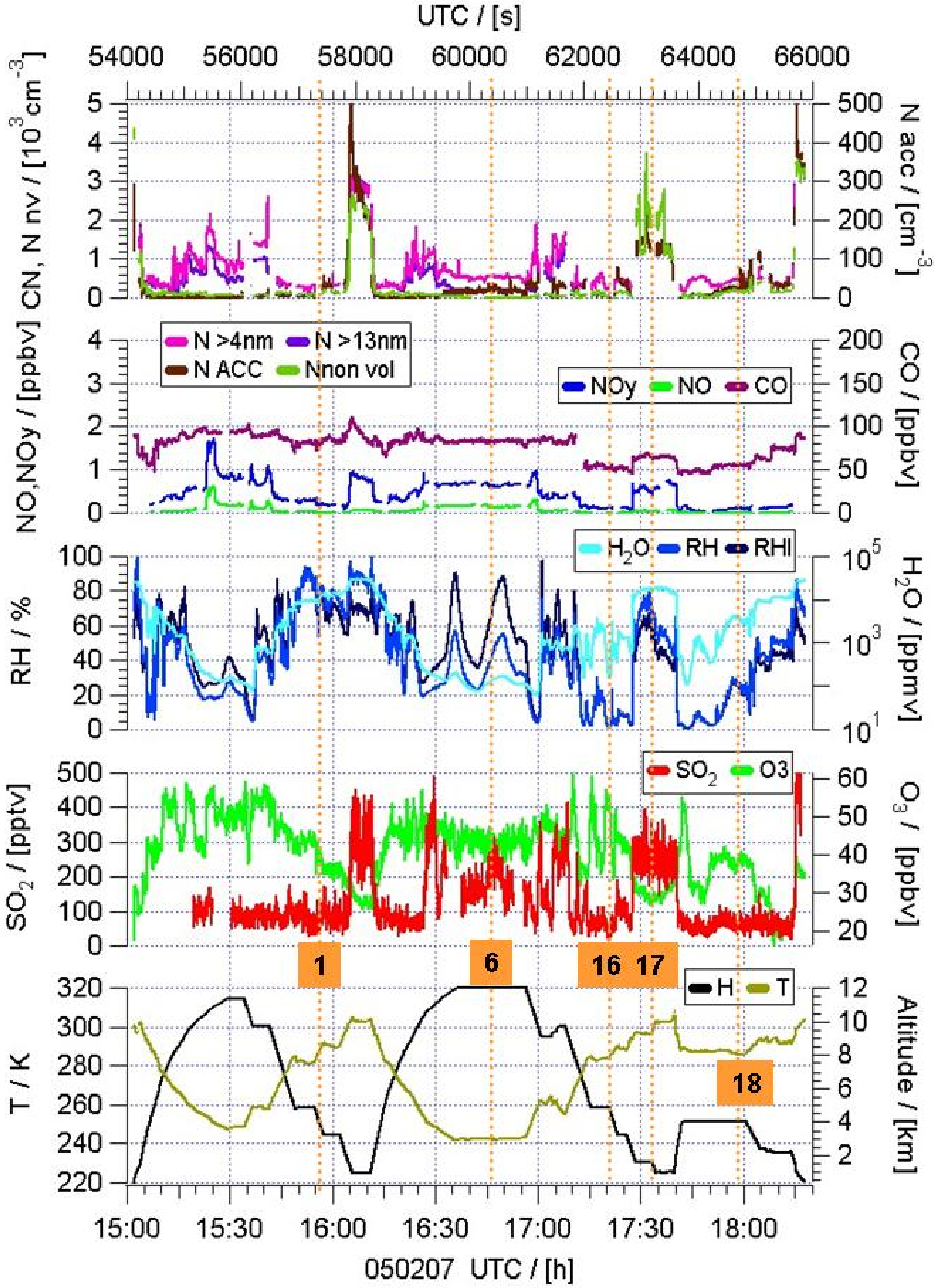

Figure 6.2: Stacked plot of complete time series of measured trace gases and aerosols for flight 20050207. Lowest panel: flight altitude and temperature, above SO_2 and O_3 mole fraction, above H_2O mixing ratio and rel. humidity over water and over ice, above NO, NOy and CO mole fractions, upper panel: particles with diameters larger than 4 and 13 nm, non volatile and accumulation mode particles. In orange points in time with FLEXPART trajectories presented in Figures 6.3-6.5.

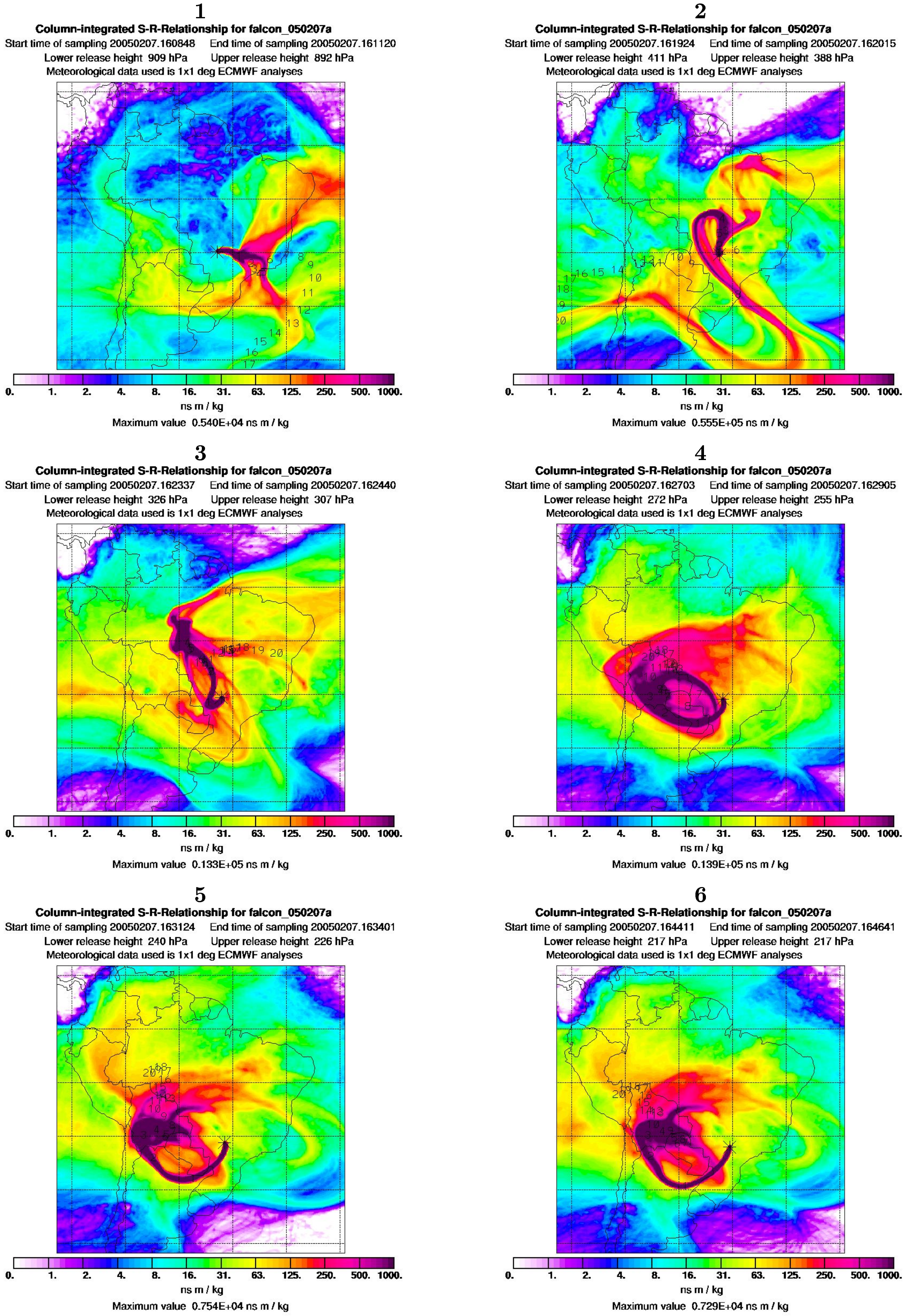

1

Column-integrated S-R-Relationship for falcon_050207a
Start time of sampling 20050207.160848 End time of sampling 20050207.161120
Lower release height 909 hPa Upper release height 892 hPa
Meteorological data used is 1x1 deg ECMWF analyses
Maximum value 0.540E+04 ns m / kg

2

Column-integrated S-R-Relationship for falcon_050207a
Start time of sampling 20050207.161924 End time of sampling 20050207.162015
Lower release height 411 hPa Upper release height 388 hPa
Meteorological data used is 1x1 deg ECMWF analyses
Maximum value 0.555E+05 ns m / kg

3

Column-integrated S-R-Relationship for falcon_050207a
Start time of sampling 20050207.162337 End time of sampling 20050207.162440
Lower release height 326 hPa Upper release height 307 hPa
Meteorological data used is 1x1 deg ECMWF analyses
Maximum value 0.133E+05 ns m / kg

4

Column-integrated S-R-Relationship for falcon_050207a
Start time of sampling 20050207.162703 End time of sampling 20050207.162905
Lower release height 272 hPa Upper release height 255 hPa
Meteorological data used is 1x1 deg ECMWF analyses
Maximum value 0.139E+05 ns m / kg

5

Column-integrated S-R-Relationship for falcon_050207a
Start time of sampling 20050207.163124 End time of sampling 20050207.163401
Lower release height 240 hPa Upper release height 226 hPa
Meteorological data used is 1x1 deg ECMWF analyses
Maximum value 0.754E+04 ns m / kg

6

Column-integrated S-R-Relationship for falcon_050207a
Start time of sampling 20050207.164411 End time of sampling 20050207.164641
Lower release height 217 hPa Upper release height 217 hPa
Meteorological data used is 1x1 deg ECMWF analyses
Maximum value 0.729E+04 ns m / kg

Figure 6.3: FLEXPART trajectories for points in time 1-6 of flight 20050207. This so called column residence time plots give as color code a kind of probability for that air mass parcel to reach the measurement area. More explanations in the text.

7

Column-integrated S-R-Relationship for falcon_050207a

Start time of sampling 20050207.165706 End time of sampling 20050207.165746
Lower release height 246 hPa Upper release height 231 hPa
Meteorological data used is 1x1 deg ECMWF analyses

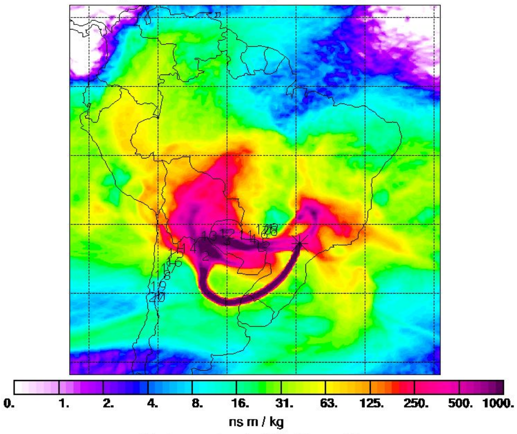

Maximum value 0.570E+04 ns m / kg

8

Column-integrated S-R-Relationship for falcon_050207a

Start time of sampling 20050207.165906 End time of sampling 20050207.165946
Lower release height 297 hPa Upper release height 279 hPa
Meteorological data used is 1x1 deg ECMWF analyses

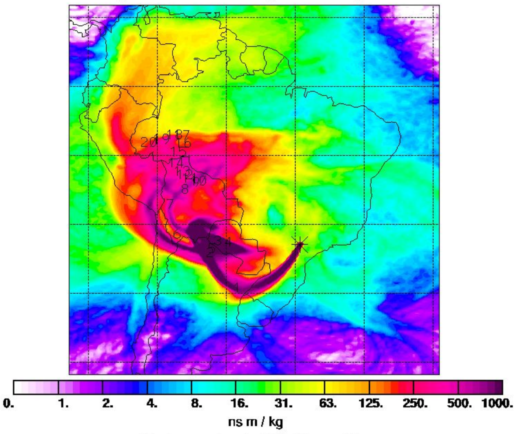

Maximum value 0.580E+04 ns m / kg

9

Column-integrated S-R-Relationship for falcon_050207a

Start time of sampling 20050207.170025 End time of sampling 20050207.170418
Lower release height 315 hPa Upper release height 315 hPa
Meteorological data used is 1x1 deg ECMWF analyses

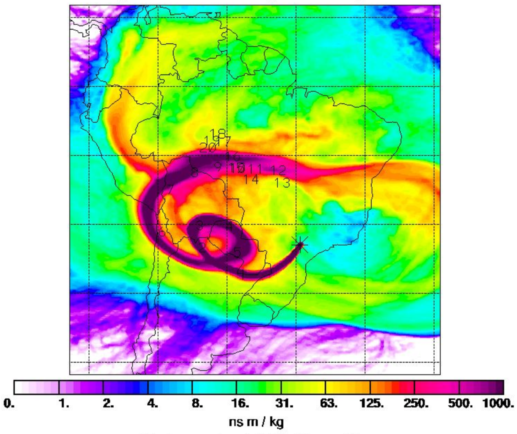

Maximum value 0.604E+04 ns m / kg

10

Column-integrated S-R-Relationship for falcon_050207a

Start time of sampling 20050207.170418 End time of sampling 20050207.170643
Lower release height 315 hPa Upper release height 301 hPa
Meteorological data used is 1x1 deg ECMWF analyses

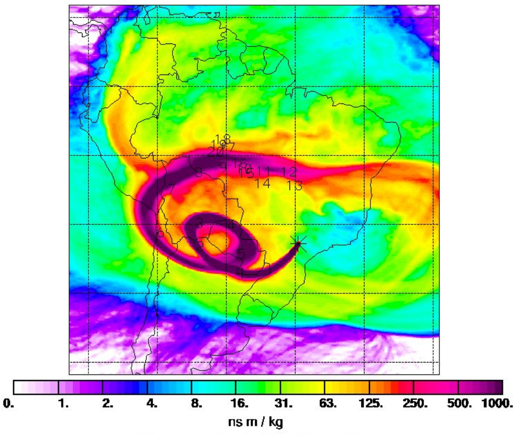

Maximum value 0.575E+04 ns m / kg

11

Column-integrated S-R-Relationship for falcon_050207a

Start time of sampling 20050207.170838 End time of sampling 20050207.170918
Lower release height 340 hPa Upper release height 320 hPa
Meteorological data used is 1x1 deg ECMWF analyses

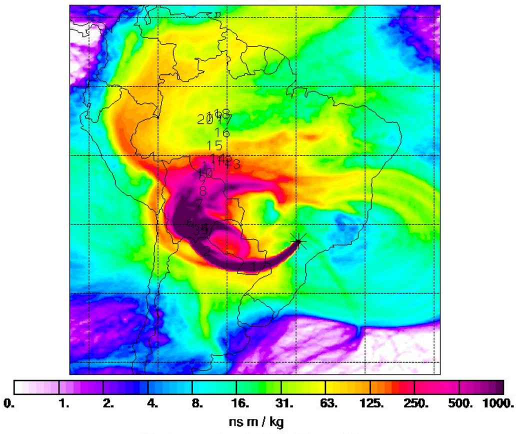

Maximum value 0.161E+05 ns m / kg

12

Column-integrated S-R-Relationship for falcon_050207a

Start time of sampling 20050207.170957 End time of sampling 20050207.171037
Lower release height 382 hPa Upper release height 360 hPa
Meteorological data used is 1x1 deg ECMWF analyses

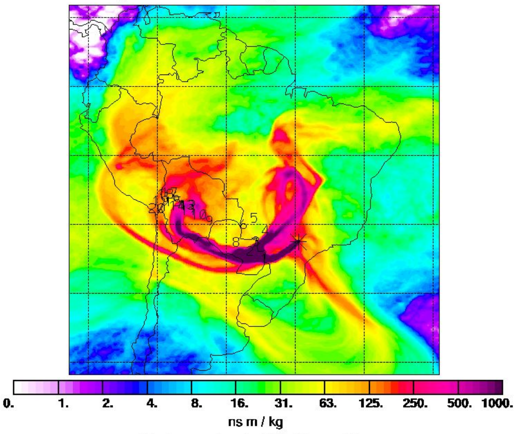

Maximum value 0.748E+04 ns m / kg

Figure 6.4: FLEXPART trajectories 7-12 of flight 20050207.

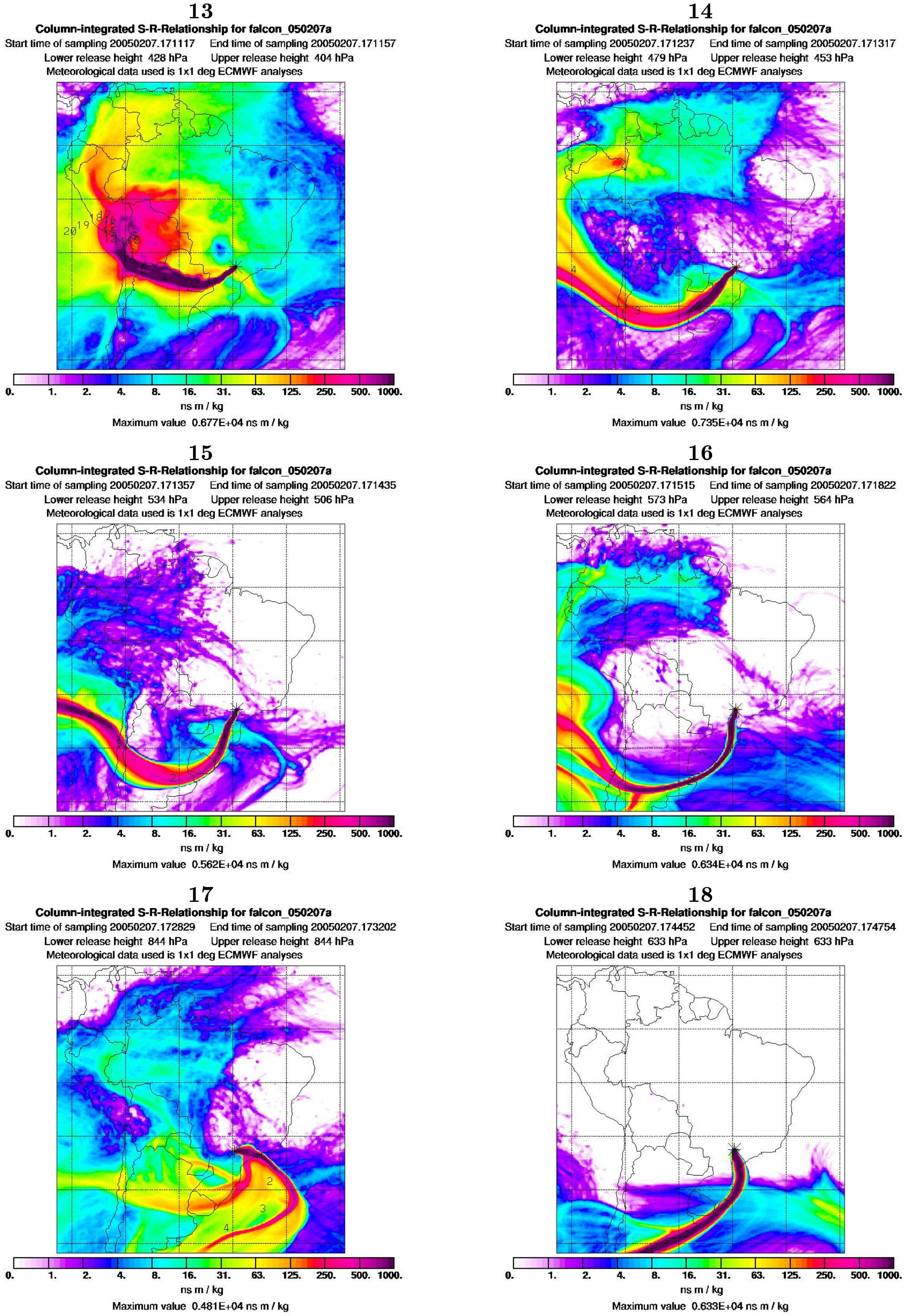

13

Column-integrated S-R-Relationship for falcon_050207a
Start time of sampling 20050207.171117 End time of sampling 20050207.171157
Lower release height 428 hPa Upper release height 404 hPa
Meteorological data used is 1x1 deg ECMWF analyses

Maximum value 0.677E+04 ns m / kg

14

Column-integrated S-R-Relationship for falcon_050207a
Start time of sampling 20050207.171237 End time of sampling 20050207.171317
Lower release height 479 hPa Upper release height 453 hPa
Meteorological data used is 1x1 deg ECMWF analyses

Maximum value 0.735E+04 ns m / kg

15

Column-integrated S-R-Relationship for falcon_050207a
Start time of sampling 20050207.171357 End time of sampling 20050207.171435
Lower release height 534 hPa Upper release height 506 hPa
Meteorological data used is 1x1 deg ECMWF analyses

Maximum value 0.562E+04 ns m / kg

16

Column-integrated S-R-Relationship for falcon_050207a
Start time of sampling 20050207.171515 End time of sampling 20050207.171822
Lower release height 573 hPa Upper release height 564 hPa
Meteorological data used is 1x1 deg ECMWF analyses

Maximum value 0.634E+04 ns m / kg

17

Column-integrated S-R-Relationship for falcon_050207a
Start time of sampling 20050207.172829 End time of sampling 20050207.173202
Lower release height 844 hPa Upper release height 844 hPa
Meteorological data used is 1x1 deg ECMWF analyses

Maximum value 0.481E+04 ns m / kg

18

Column-integrated S-R-Relationship for falcon_050207a
Start time of sampling 20050207.174452 End time of sampling 20050207.174754
Lower release height 633 hPa Upper release height 633 hPa
Meteorological data used is 1x1 deg ECMWF analyses

Maximum value 0.633E+04 ns m / kg

Figure 6.5: FlEXPART trajectories 13-18 of flight 20050207.

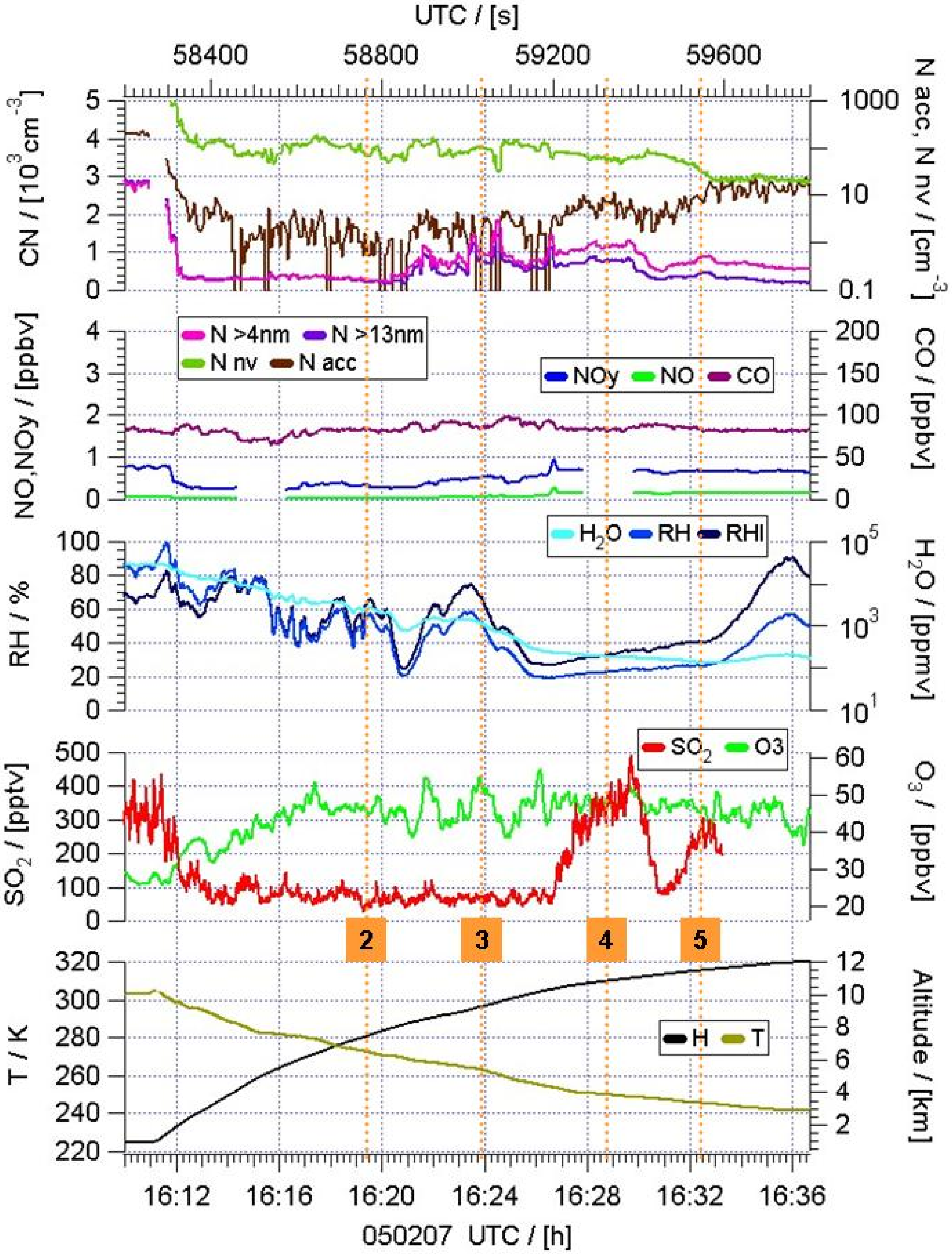

Figure 6.6: Stacked plot of the second ascend of flight 20050207. Explanations same as in Figure 6.2.

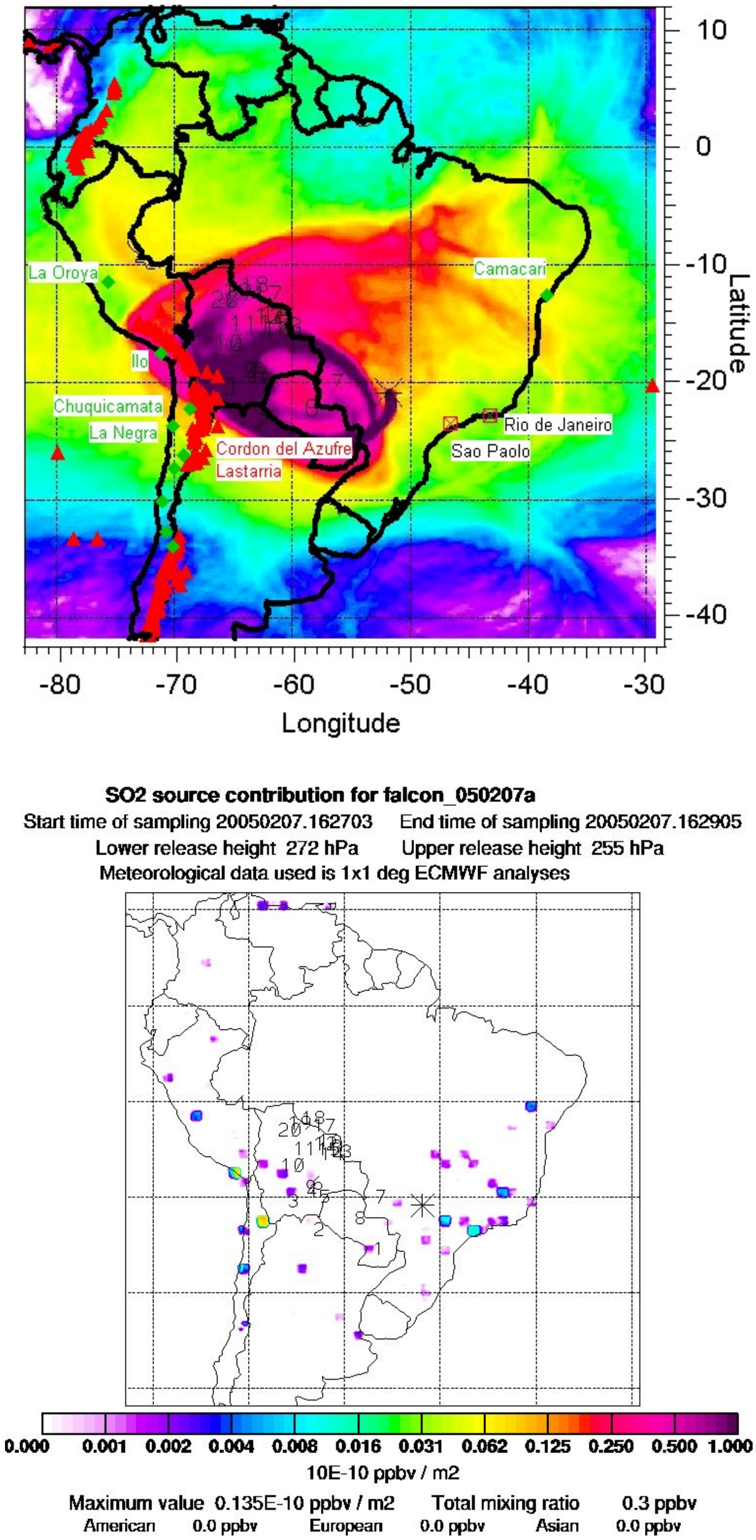

Figure 6.7: The FLEXPART column (upper panel) and source contribution (lower panel) for point 4 of the flight, red triangles are volcanos, green diamonds copper smelters. The names belong to copper smelters, volcanoes or cities. The two most contributing modelled sources fit to the copper smelters Ilo and Chuquicamata.

trace gases do not show any significant changes. Above an altitude of 10 km a SO_2 rich air mass is probed, the mole fraction increasing up to 400 pptv. This first peak is followed at about 11.5 km by a second but smaller peak in the SO_2 mole fraction (200 pptv). Nucleation mode particles (N4, N13) are also enhanced. The FLEXPART trajectories number 4 and 5 show that the air now comes from westerly directions, over a region with high volcanic and copper smelter activities. To proof this, major copper smelters and volcanoes of South America have been plotted together with FLEXPART trajectory 4 in one graph (**Figure 6.7**, upper panel, volcanoes are indicated by red triangles, copper smelters by green diamonds). The volcanoes were all not active during our measurement period, so the smelters seem to be the most probable pollution source and at least two of them lie on the central path of the trajectory, Ilo and Chuquicamata, which both belong to the biggest copper smelters of the world with a copper production of 300000 and 500000 metric tons per year. The FLEXPART source contribution picture (**Figure 6.7**, lower panel) further strengthens this suggestion by pointing to Ilo and Chuquicamata as major sources of the observed elevated SO_2. Nevertheless, a "quiet" activity of the volcanoes Lastarria and Cordon del Azufre in the area (also marked in Figure 6.7) has been reported recently [Froger et al., 2007], so a quiet degassing of volcanoes at least as additional possible SO_2 source cannot completely excluded. The trace gases CO, NO and NOy do not show any changes in their mole fraction and their values are almost typical for remote areas (CO $<$ 100 ppbv, NO $<$ 0.1 ppbv and NOy $<$ 0.4 ppbv). This is a further hint, that the pollution does not stem from a typical combustion process. Metal smelters produce SO_2 by oxidizing sulfur contained in the copper ore (most copper ores are sulfites). If the smelter exhaust is not efficiently filtered large amounts of SO_2 will be released into the atmosphere. However, other pollutants like CO or NO should not be markedly enhanced. The SO_2 emissions from the copper smelters or volcanoes then must have been transported quite efficiently to higher altitudes, mostly by deep convection as indicated by special FLEXPART sensitivity studies. From there the pollution was transported further to the measurement area.

At the highest flight level of 12 km the air mass does not change much, which can be seen from FLEXPART plot number 6, and so does the SO_2 mole fraction, which only slightly varies

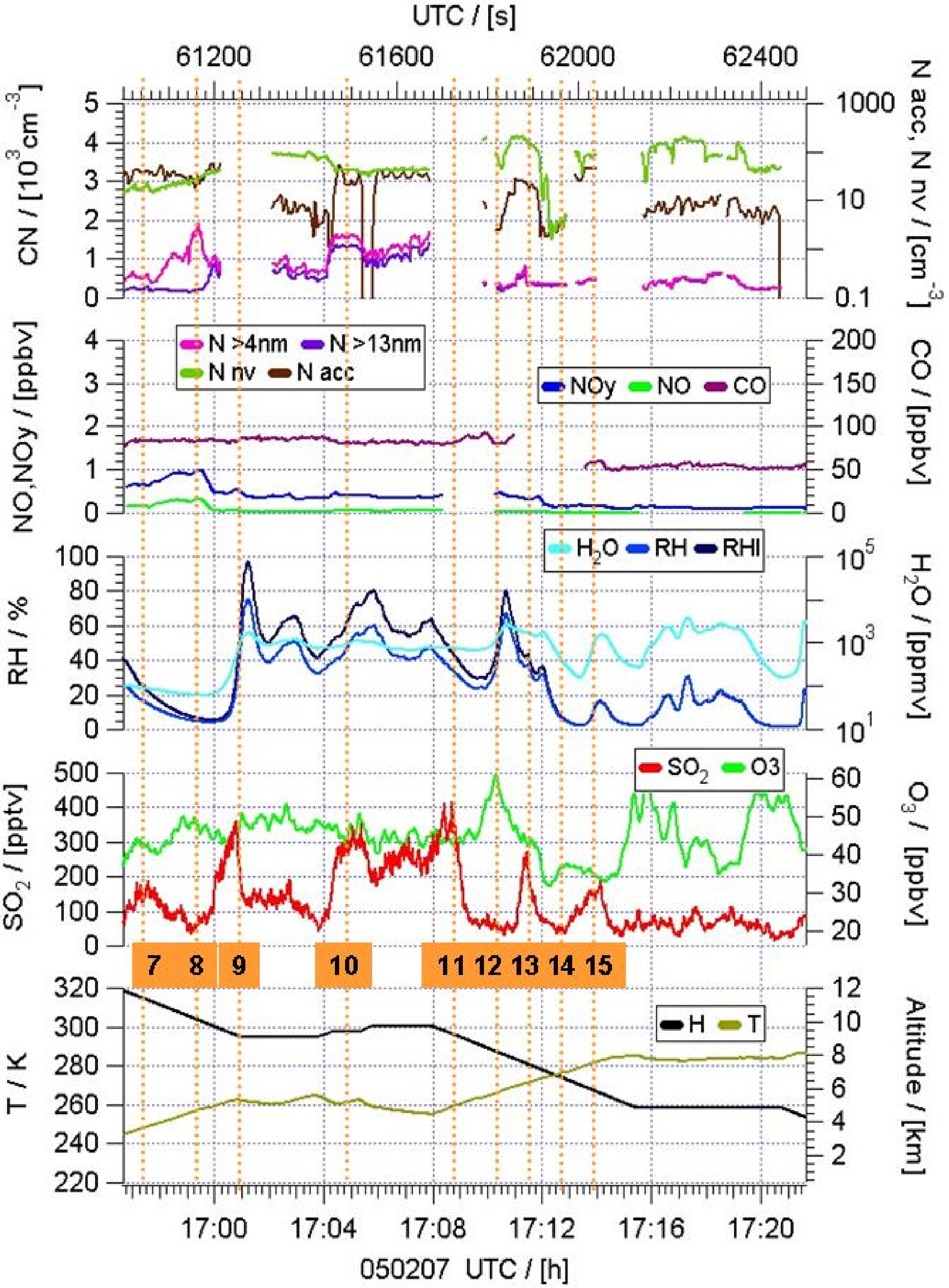

Figure 6.8: Stacked plot of the second descend of flight 20050207. Explanations same as in Figure 6.2.

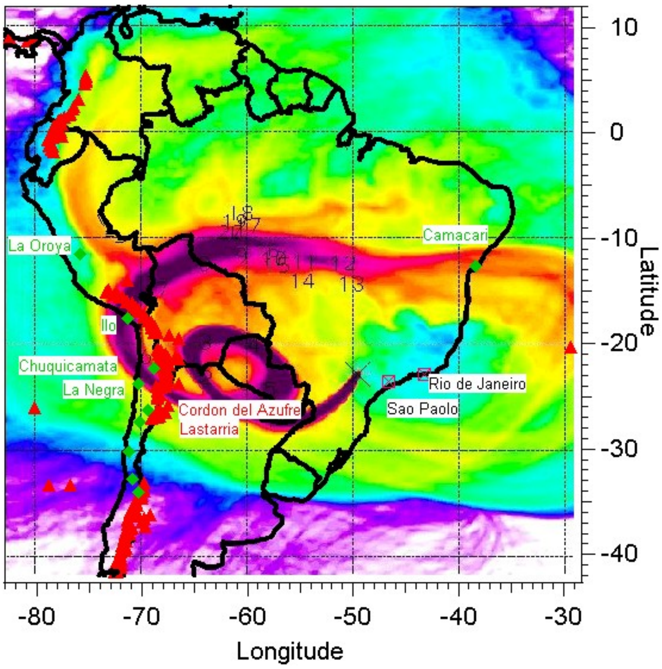

Figure 6.9: The FLEXPART column for point 10 of the flight, red triangles are volcanos, green diamonds copper smelters. The names belong to copper smelters, volcanoes or cities.

around 200 pptv. However, 200 pptv is an already high value for the upper troposphere, but this is not surprising as the air mass still travelled over the copper smelter/volcanic region a few days before.

The second descend is again plotted zoomed in **Figure 6.8**. From the trajectories one can see, that until point number 13 the principle air mass direction stays rather constant, but it is interesting to see, how a slight change in the travel time or in the central path of the air mass results in large variations of the SO_2 mole fraction from 80 to 400 pptv. The travel time the air mass needed from the copper smelter region in southern Peru and northern Chile to the measurement area seems to be the most critical factor controlling the SO_2 mole fraction in the measurement region. A longer travel time means more SO_2 loss due to chemical reactions and deposition and therefore less SO_2 reaches the measurement site. CO and NOy again stay rather constant. The concentration of small particles shows a correlation with the SO_2 mole fraction between point 10 and 11.

For the most polluted part of the flight, after point number 10, the FLEXPART column is

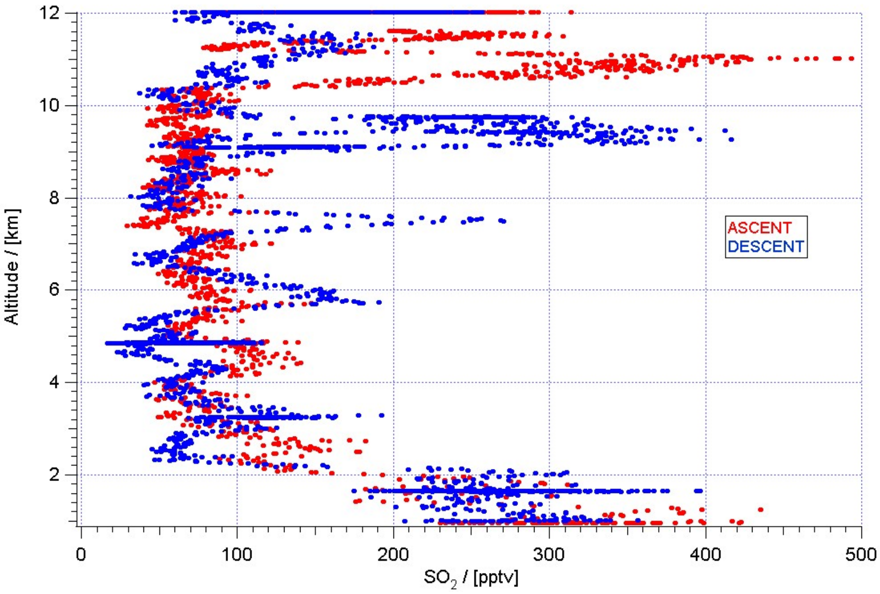

Figure 6.10: Ascent and descent vertical SO_2 profiles of TROCCINOX flight 20050207.

once more plotted in one graph with copper smelters and volcanoes in **Figure 6.9**. Obviously also the smelter La Negra now might contribute to the enhanced SO_2 concentration.

Beginning with point 14 at an altitude of 7 km and with further declining flight altitude the air mass direction changes dramatically, turning to the south and finally coming in a wide bow again from easterly directions over the cities Rio de Janeiro and Sao Paolo. The SO_2 mole fraction in the boundary layer reaches 250 pptv (view **Figure 6.2**).

Finally the SO_2 mole fraction flight profile is plotted in **Figure 6.10**. The ascent is depicted in red, the descent in blue. The different pollution layers at different altitudes can be nicely seen, especially during the descent. Mole fractions of up to nearly 500 pptv SO_2 have been detected. The highly elevated SO_2 can serve as H_2SO_4 precursor and therefore new particle formation can be induced. Simulations with the aerosol nucleation model AEROFOR (view section 6.3 and [Arnold et al., 2007]) have shown, that already SO_2 mole fractions of around 100 pptv can lead to a significant increase in the small particles and further growth of these particles then to a significant increase in the number of cloud condensation nuclei, which finally affects the earth's climate. The particle nucleation topic will be further discussed in the third section of this chapter, in connection to the INTEX pollution plume example.

6.2 SCOUT-O3 Transfer Larnaca-Dubai 20051104, SO_2 Long Range Transport

The second transfer flight of the SCOUT-O3 Tropical campaign started from Larnaca on the island of Cyprus and ended in the emirate Dubai (**Figure 6.11**).

Figure 6.12 shows the measured SO_2 mole fraction and for comparison the concentration of aerosol particles with diameters larger than 5 nm (N5). In the vicinity of both airports, a very strong SO_2 pollution of the boundary layer was observed. But the interesting features of this flight are two enhancements in SO_2 and in particles at an altitude of 10 km between 13:00 and 13:30 UTC and between 14:45 and 15:15 UTC. The SO_2 mole fraction reaches here up to 240 pptv, whereas it goes back to an upper tropospheric background value of 30 pptv between the two maxima.

The particle concentration shows a similar behavior as the SO_2 so both seem to stem from the same pollution source or nucleation occurred during the flight. Unfortunately all particles with diameters bigger than 5 nm have been sampled during SCOUT together in one channel,

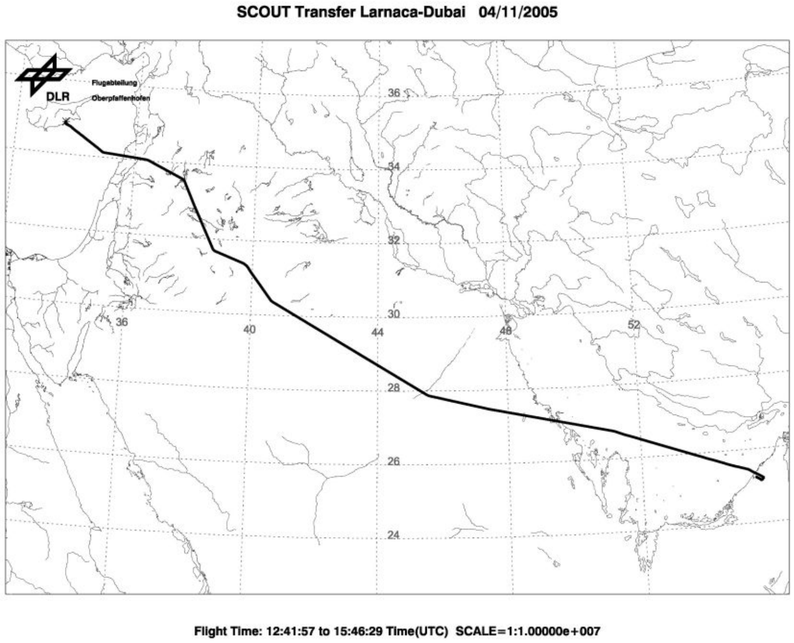

Figure 6.11: Flight path of SCOUT transfer flight 20051104, Larnaca-Dubai.

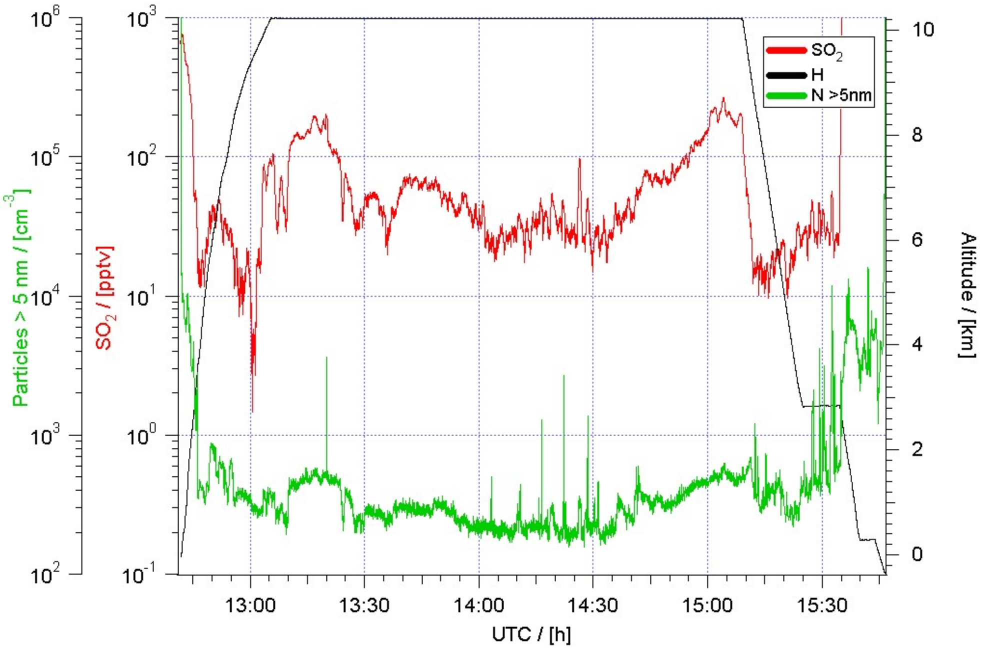

Figure 6.12: Sulfur dioxide and particles time series of flight 20051104.

that means that one has no information about the specific diameter distribution. Usually two samples are taken, one of particles e.g. with diameters larger than 5 nm and one with e.g. diameters larger than 13 nm. From their difference particles with diameters between 5 and 13 nm, freshly nucleated particles, can be determined. The missing second channel here makes a distinction of nucleation mode particles and bigger particles not possible.

The sharp spikes in the particles at 13:20 UTC and between 14:15 and 14:30 UTC are accompanied by similar spikes in NO or in NOy (see overview panel in the appendix), which is a strong hint that these spikes are probably caused by fresh or aged aircraft exhaust trails.

Figure 6.13 is a scatter plot of N5 versus SO_2 for the data points between 13:05 and 15:15 UTC, so for data that has been measured above 10 km. A correlation between particles and SO_2 is clearly visible, a higher SO_2 mole fractions results in a higher H_2SO_4 concentrations and therefore in a higher particle concentration. However, the gradient of the fit curve (orange line in Figure 6.13) is decreasing with increasing particle concentration, the increase in the particle concentration does not go linearly with the SO_2 mole fraction. The reason for this is that more particles mean a bigger surface available for condensation. A higher SO_2 mole

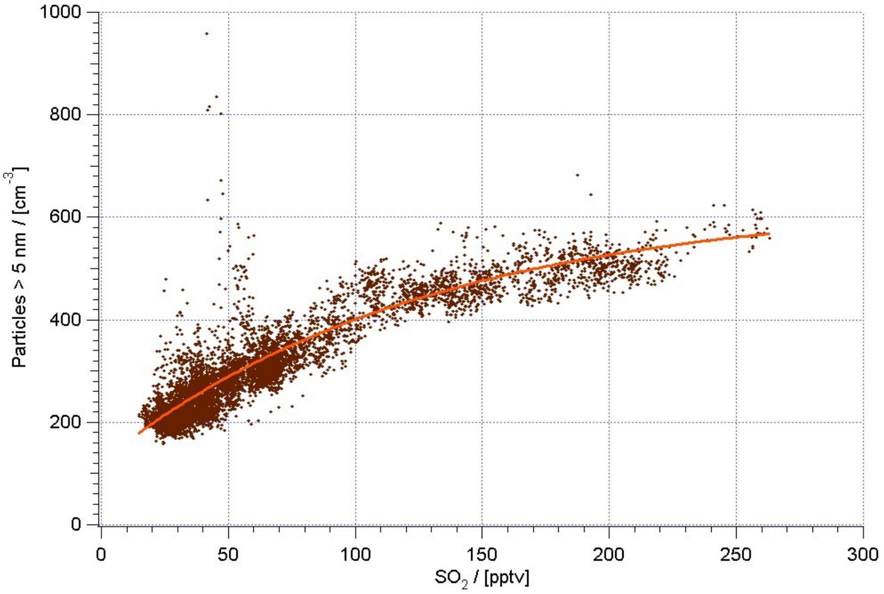

Figure 6.13: Concentration of particles with diameters larger than 5 nm versus SO_2 mole fraction for data points measured above 10 km of flight 20051104.

fraction and thus a higher H_2SO_4 concentration do not necessarily mean more particles. A part of the H_2SO_4 will condense onto the preexistent aerosol, forcing its growth, and will consequently not be available for new particle formation. Moreover, particles also coagulate with each other (self-coagulation), so that the increase in the total number of particles reduces. In this way nucleation somehow limits itself.

Analyzing the corresponding trajectories (calculated with the model LAGRANTO, **Figure 6.14- 6.16**), it seems that pollution transport from middle America is the source of the SO_2 enhancements. For both sections, the trajectories end about 10 days before in the boundary layer of middle America, whereas the trajectories between the enhancements always stayed in altitudes of more than 10 km and made a turn around the world in that time. However, it can not completely be excluded that the pollution stems from sources in Spain, which the trajectories also passed over, but in high altitudes (200 hPa, corresponding to 11-12 km altitude). Therefore deep convection would have been needed to occur over Spain, which is in November less probable.

From the estimation of the SO_2 lifetime with respect to the removal by OH in section

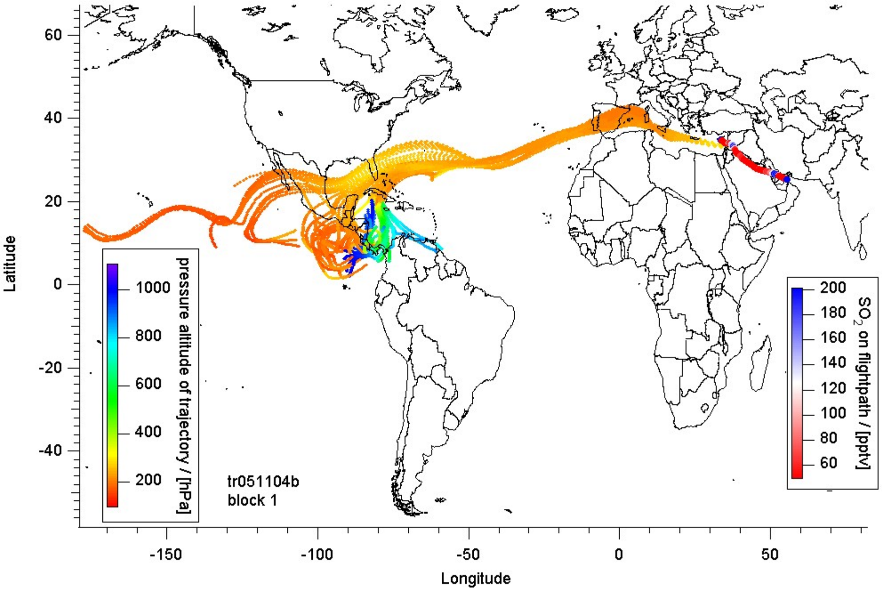

Figure 6.14: LAGRANTO trajectories for flight 20051104. Trajectories ending between 13 and 13:30 UTC on the flight path, so during the first SO_2 increase. Pressure altitude of the trajectories is color coded, as well as SO_2 mole fraction along the flight path.

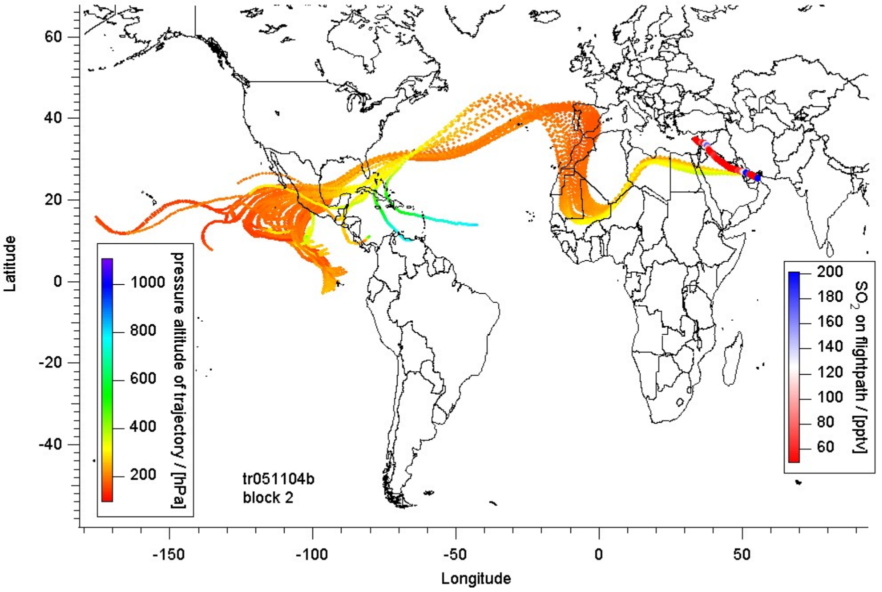

Figure 6.15: LAGRANTO trajectories for flight 20051104. Lower panel: Trajectories ending between 14:45 and 15:15 UTC, during the second SO_2 increase. Pressure altitude of the trajectories is color coded, as well as SO_2 mole fraction along the flight path.

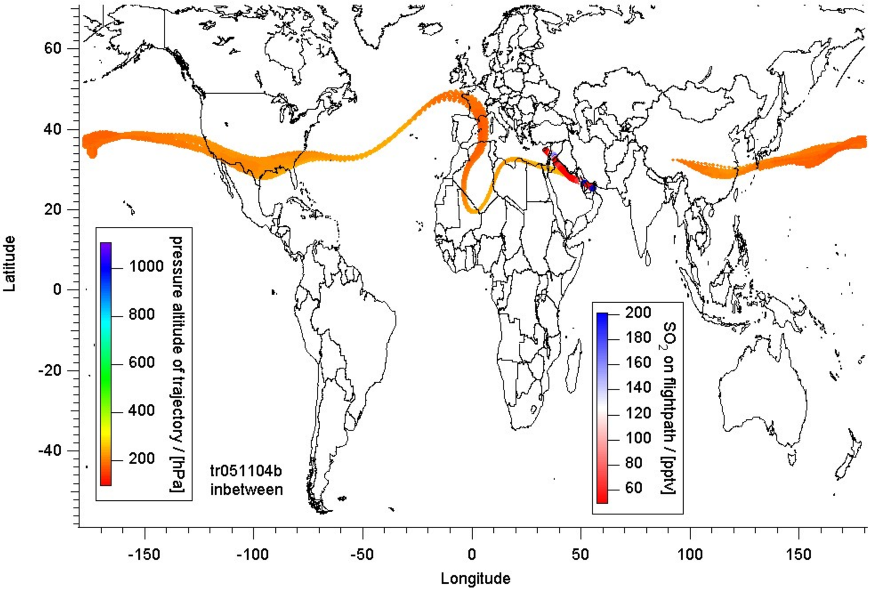

Figure 6.16: LAGRANTO trajectories for flight 20051104. Trajectories ending around 13:45 and 14:30 UTC between the two SO_2 enhancements. Pressure altitude of the trajectories is color coded, as well as SO_2 mole fraction along the flight path.

2.1.2 follows, that the measured 200 pptv need to be multiplied by 2.5 in order to get a reasonable value for the probable SO_2 emission 10 days before. This would mean a mole fraction of 500 pptv SO_2 in the boundary layer of middle America, which is a typical value for polluted regions. For Spain as pollution source region, which was passed only 3 days before the measurements, a SO_2 emission of 270 pptv would be sufficient to explain the measured mole fractions.

6.3 INTEX Flight 20060503b, Asian Emissions

The INTEX flight 20060503b started from Brest in Northern France and the measurements took place over the Atlantic Ocean south and west of Ireland. The flight path is depicted in **Figure 6.17**. The objective was to find and to probe an Asian pollution plume, which had been predicted before by FLEXPART. The complete time series of the flight can be found in the appendix. Between 10:00 and 11:00 UTC one or several pollution plumes were detected as particularly indicated by very markedly elevated SO_2.

Figures 6.18 and **6.19** show this section of the flight more in detail. In **Figure 6.18** the mole fractions of various trace gases (CO, O_3, NO, NOy, HNO_3, SO_2) are plotted. After 10:03 UTC 3 strongly elevated SO_2 peaks are observed with mole fractions of up to 1 ppbv. Also between the peaks the air mass is SO_2 enriched with a mean value of 100 pptv. The SO_2 peaks are accompanied by slight peaks in NOy and CO, but those peaks are less pronounced.

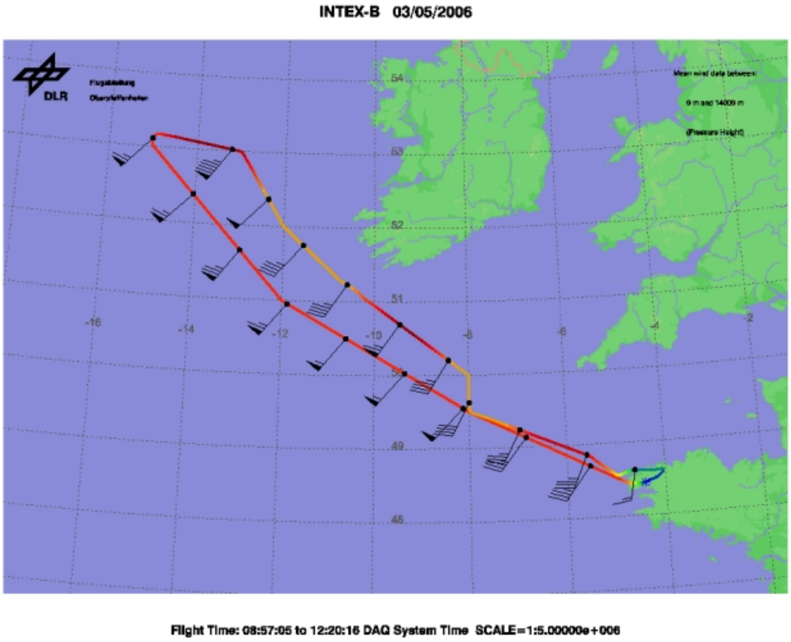

Figure 6.17: Flight path of INTEX flight 20060503. The colors from blue to red roughly indicate the altitude (0 to 7 km). Distance of the wind direction markers is 10 minutes. 1° Longitude corresponds to approximately 70 km, 1° Latitude to 111 km.

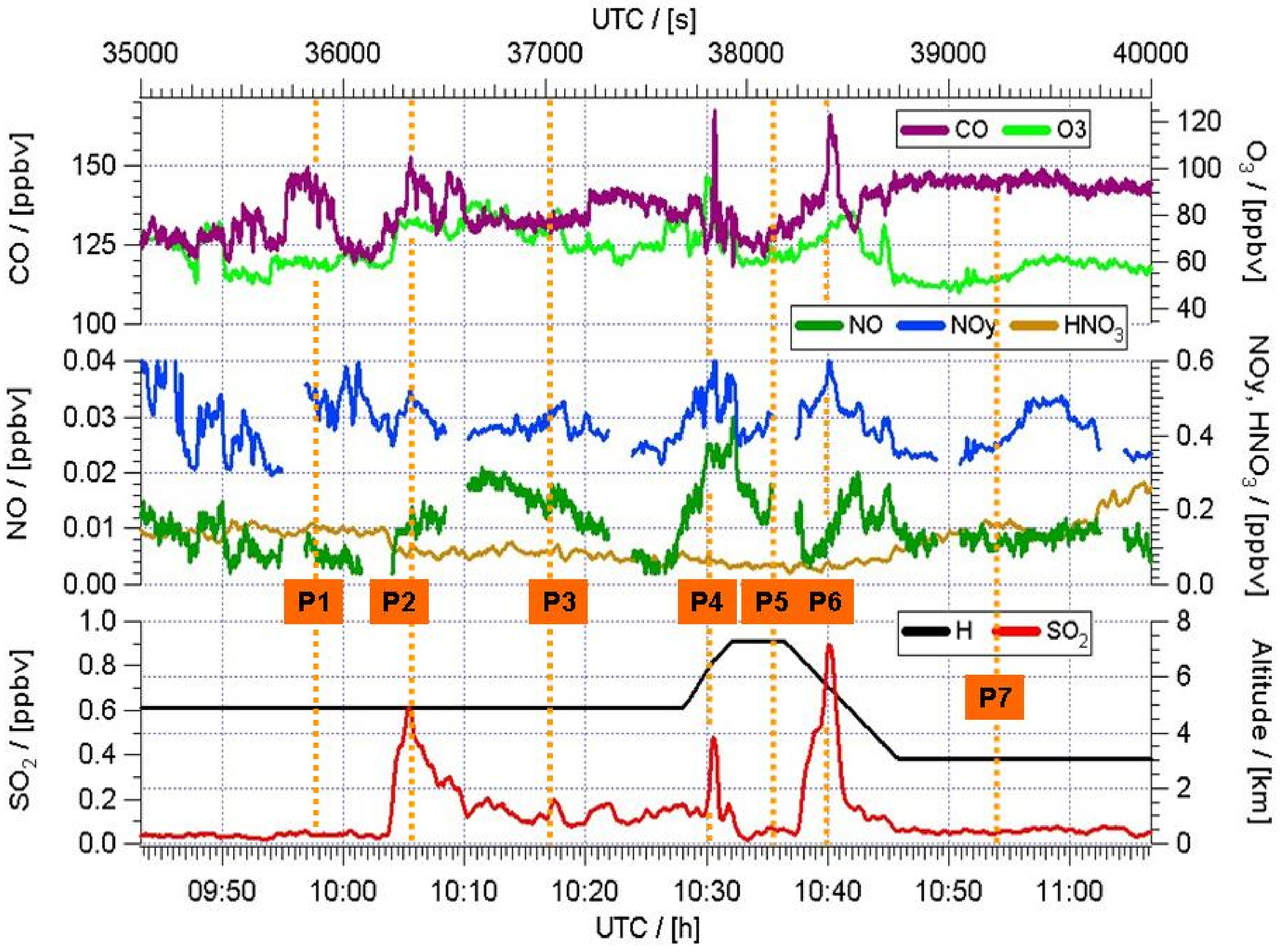

Figure 6.18: Trace gases during the central part of INTEX flight 20060503. Upper panel mole fractions of ozone and CO, middle panel NO,NOy and HNO_3, lower panel SO_2 mole fraction and flight altitude. In orange points in time of FLEXPART trajectories plotted in Figures 6.20-6.22.

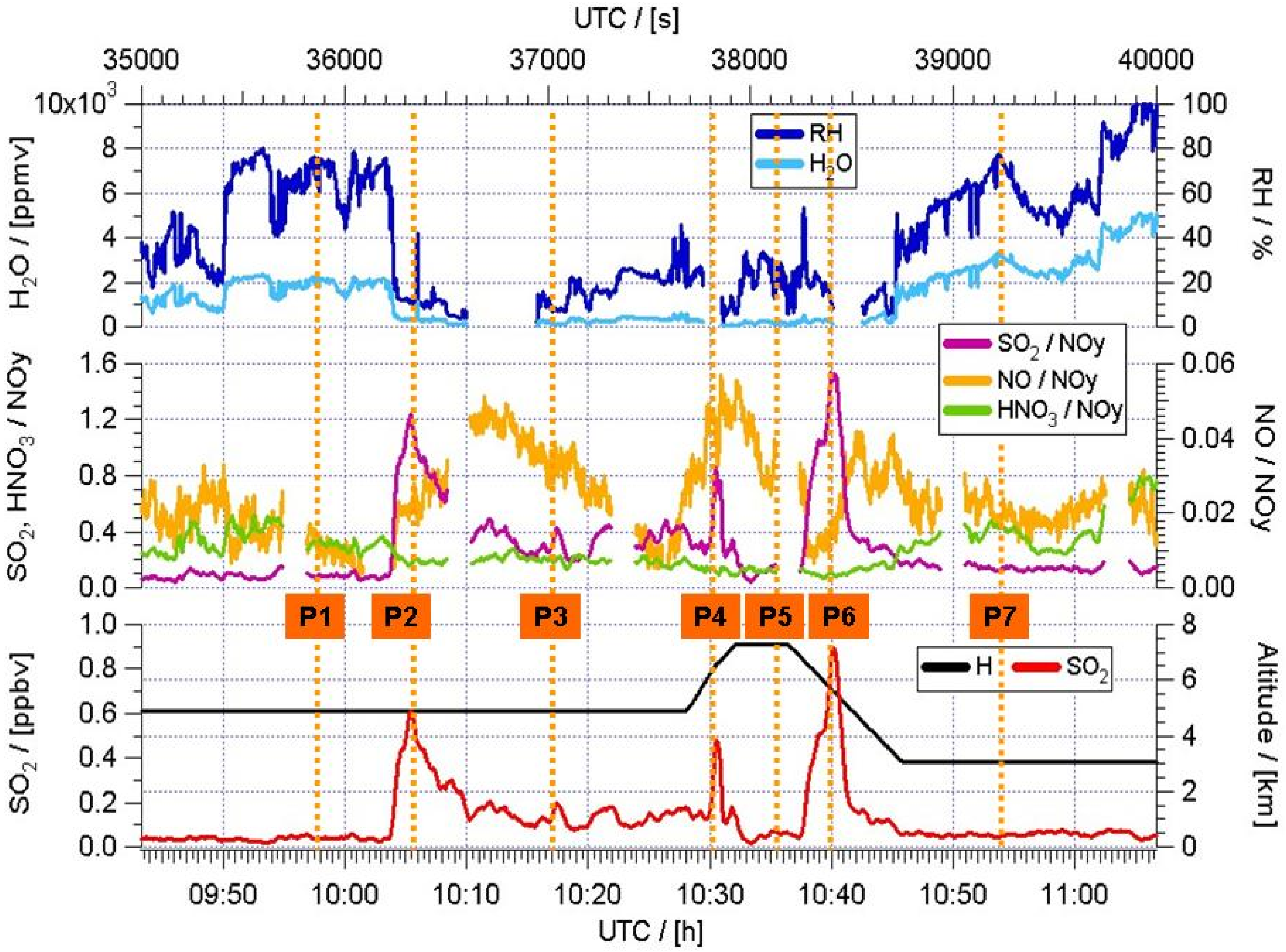

Figure 6.19: Additional data for the central part of INTEX flight 20060503. Upper panel relative humidity and water vapor mixing ratio, middle panel ratios of NO/NOy, H_2SO_4/NOy and HNO_3/NOy, lower panel SO_2 mole fraction and flight altitude. In orange points in time of FLEXPART trajectories plotted in Figures 6.20-6.22.

In **Figure 6.19** additionally relative humidity and water vapor mixing ratio of that flight part as well as the calculated ratios of SO_2 to NOy, of NO to NOy and of HNO_3 to NOy are presented. The enhanced SO_2 is measured in a relatively dry air mass with mean relative humidity values of about 20%, whereas the humidity values before and after that air mass exceed 60%, which is already a hint that a change of the air mass origin occurred at the first SO_2 increase. The calculated NO/NOy ratio shows quite low values (<0.06). For fresh emissions, when no chemical transformation has occurred yet, almost all NOy exists in form of NO and their ratio is close to one. In this flight part the ratio never exceeds 0.06, which means that the originally emitted NO has almost completely been converted to NO_2, PAN and HNO_3. This is a hint, that the air must be aged, the pollution is not fresh. However, the single mole fractions of both NO and NOy are quite low (<0.03 ppbv, <0.6 ppbv) compared to typical middle tropospheric values (several ppbv, see flight overviews in the appendix).

The SO_2/NOy ratio instead shows rather high values (0.2-1.5). Typical fresh emission ratios here lie between 0.1 and 0.2 depending on the source type. The reason might be an effective removal of NOy species (HNO_3 ?). Indeed, the HNO_3 mole fraction (0.1 ppbv, almost constant) and the HNO_3/NOy (0.2) ratio is low.

In order to analyze the possible air mass origin, FLEXPART trajectories [Stohl et al., 2002, Stohl et al., 2005] have been employed. The trajectories (always column residence time in the upper part of the figures and SO_2 source contribution in the lower part) for seven interesting points are plotted in **Figures 6.20-6.23** and their starting points are marked in the time series graphs.

The column residence time figures suggest that the two highest peaks in the SO_2 mole fraction (P2 and P6) both originate 6-8 days before in east and central Asia, whereas most of the other trajectories originate further north or in northern America. The SO_2 source contribution figures also strengthen this impression. However, e.g. trajectory P5 also originates in central Asia with a strong source contribution, but here we do not see a SO_2 enhancement in our measurements. Carbon Monoxide shows the same behavior, peaks at P2 and P6 but actually a local minimum around P5.

P1

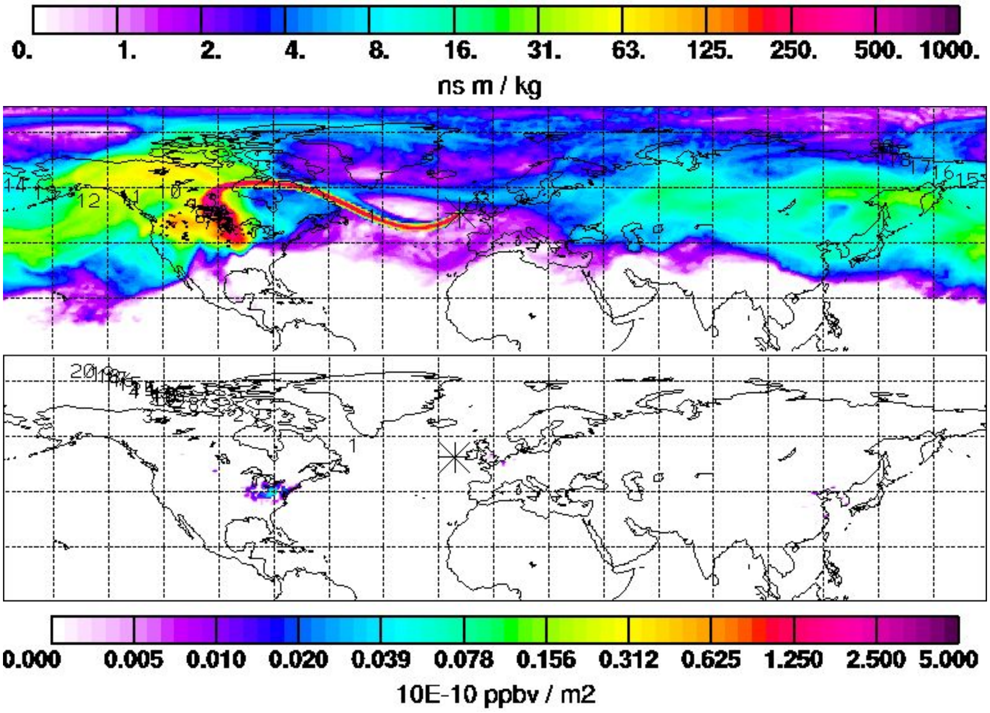

P2

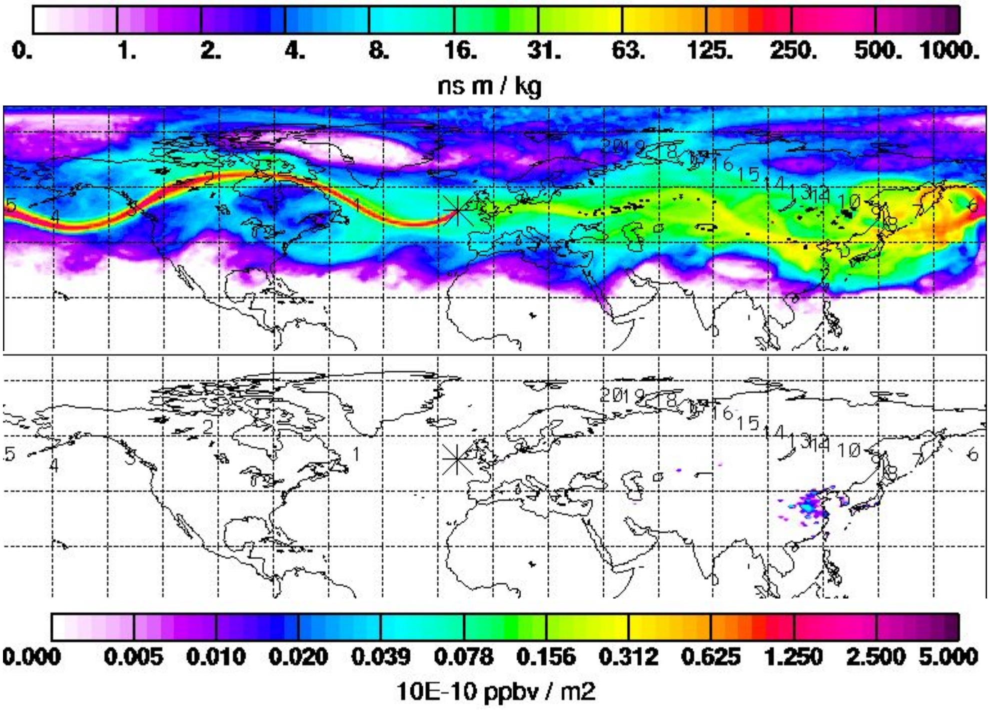

Figure 6.20: FLEXPART results for point 1 and 2 of Figure 6.18. Always in the upper part of the figures (and upper color bars) column residence time, in the lower part of the figures (and lower color bars) SO_2 source contribution.

P3

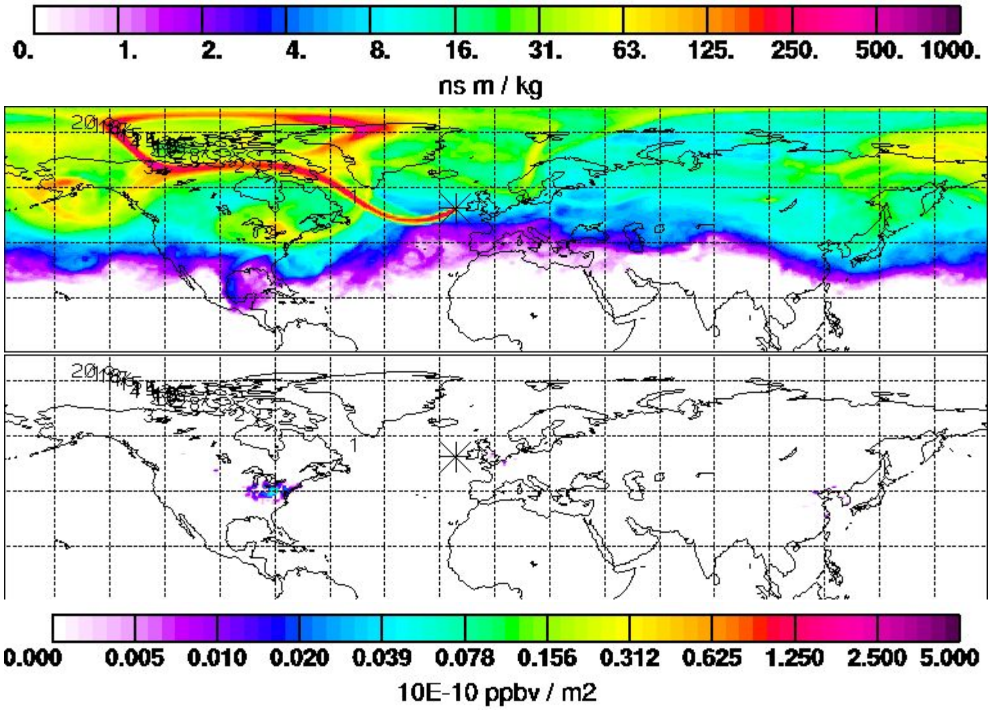

P4

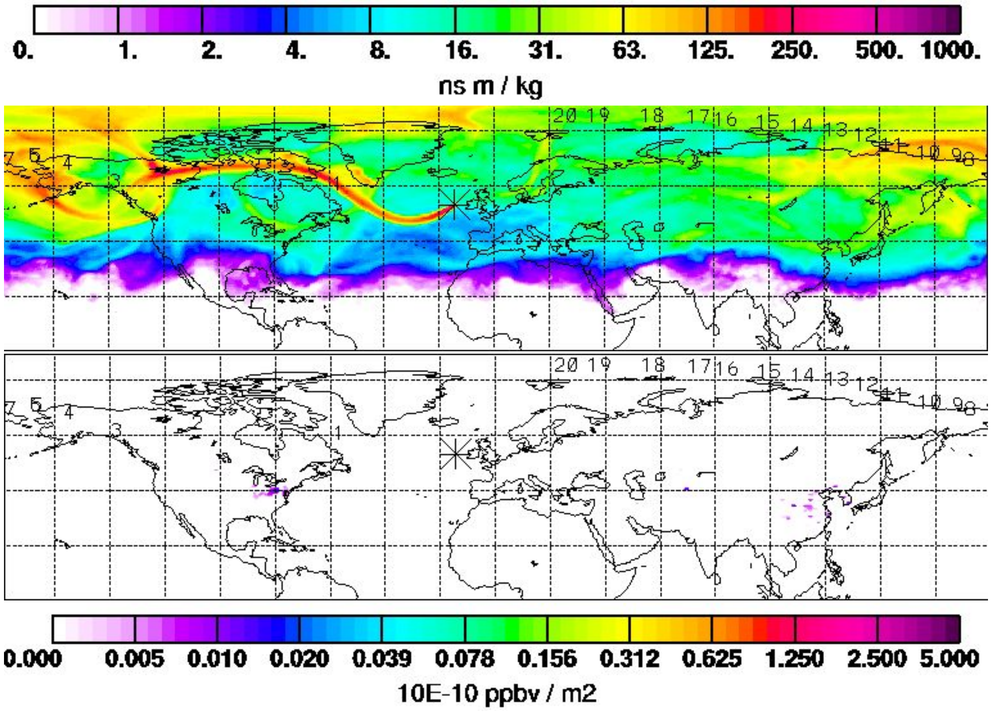

Figure 6.21: FLEXPART results for point 3 and 4 of Figure 6.18. Always in the upper part of the figures (and upper color bars) column residence time, in the lower part of the figures (and lower color bars) SO_2 source contribution.

P5

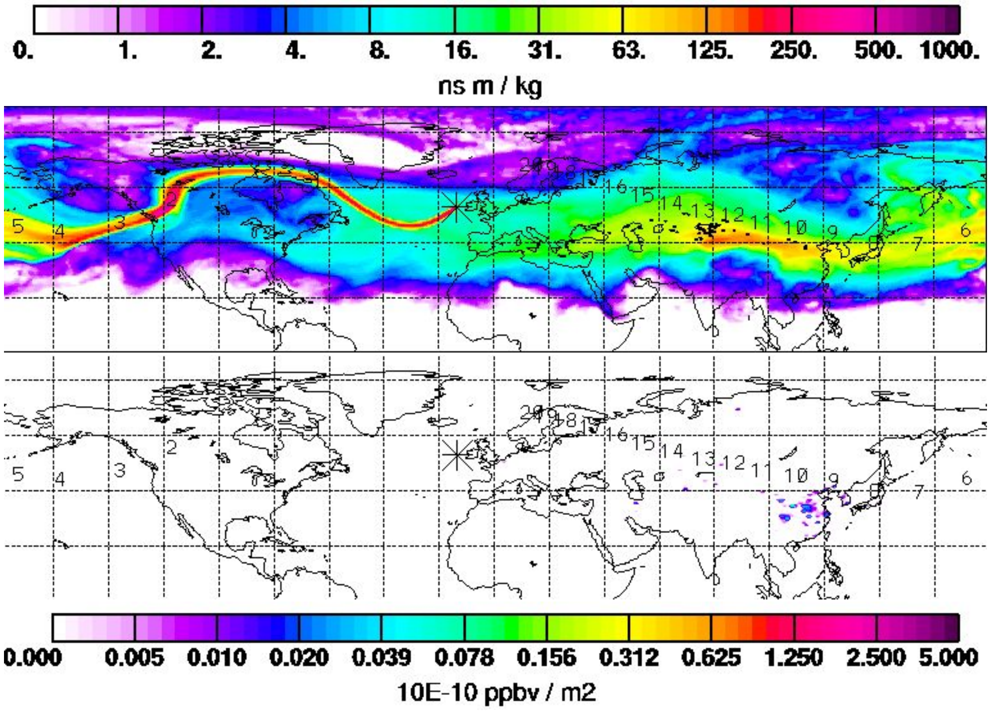

P6

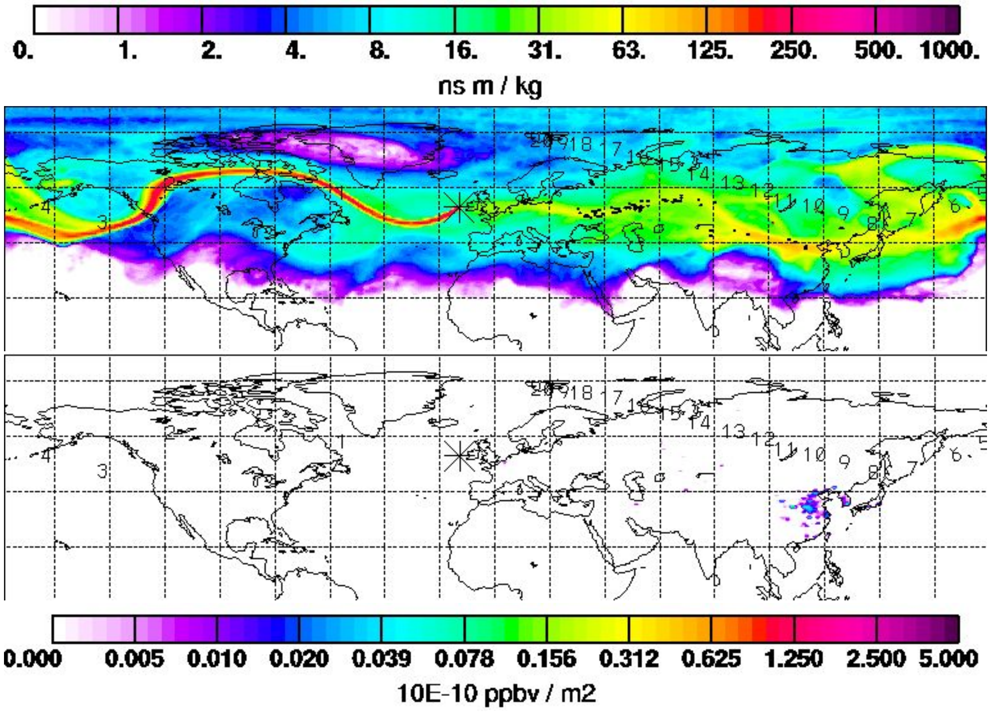

Figure 6.22: FLEXPART results for point 5 and 6 of Figure 6.18. Always in the upper part of the figures (and upper color bars) column residence time, in the lower part of the figures (and lower color bars) SO_2 source contribution.

P7

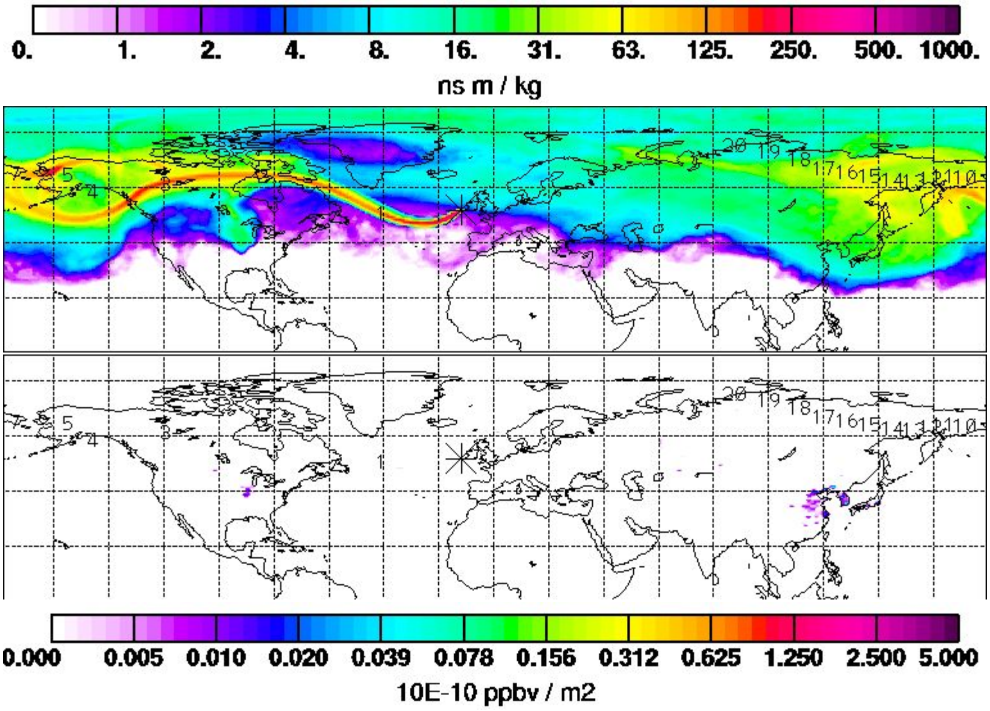

Figure 6.23: FLEXPART results for point 7 of Figure 6.18. In the upper part of the figure (and upper color bar) column residence time, in the lower part of the figure (and lower color bar) SO_2 source contribution.

Figure 6.24 is the FLEXPART age spectrum of the the modelled SO_2 mole fraction. The heights of the vertical bars describe the expected amount of SO_2 transported to the measurement region. The colors indicate the approximate age of the SO_2 polluted air mass. The blue dotted line shows the actual SO_2 mole fraction measurements. As mentioned in chapter 5, FLEXPART does not take into account any chemical sinks, which leads to an overestimation of the SO_2 mole fraction by FLEXPART. As can be seen from **Figure 6.24**, the age of the air mass with enhanced measured SO_2 is 8-12 days and this air mass is interestingly older than the air masses before and after the measured SO_2 enhancement (only 4-7 days). We do not see the modelled SO_2 increases at 10 and 11 UTC in the measurements. The air masses around 10 and around 11 have much higher relative humidities (70% compared to 20% in the older air mass), so it seems possible, that the SO_2 in the humid air mass has been converted to H_2SO_4 due to more OH formation.

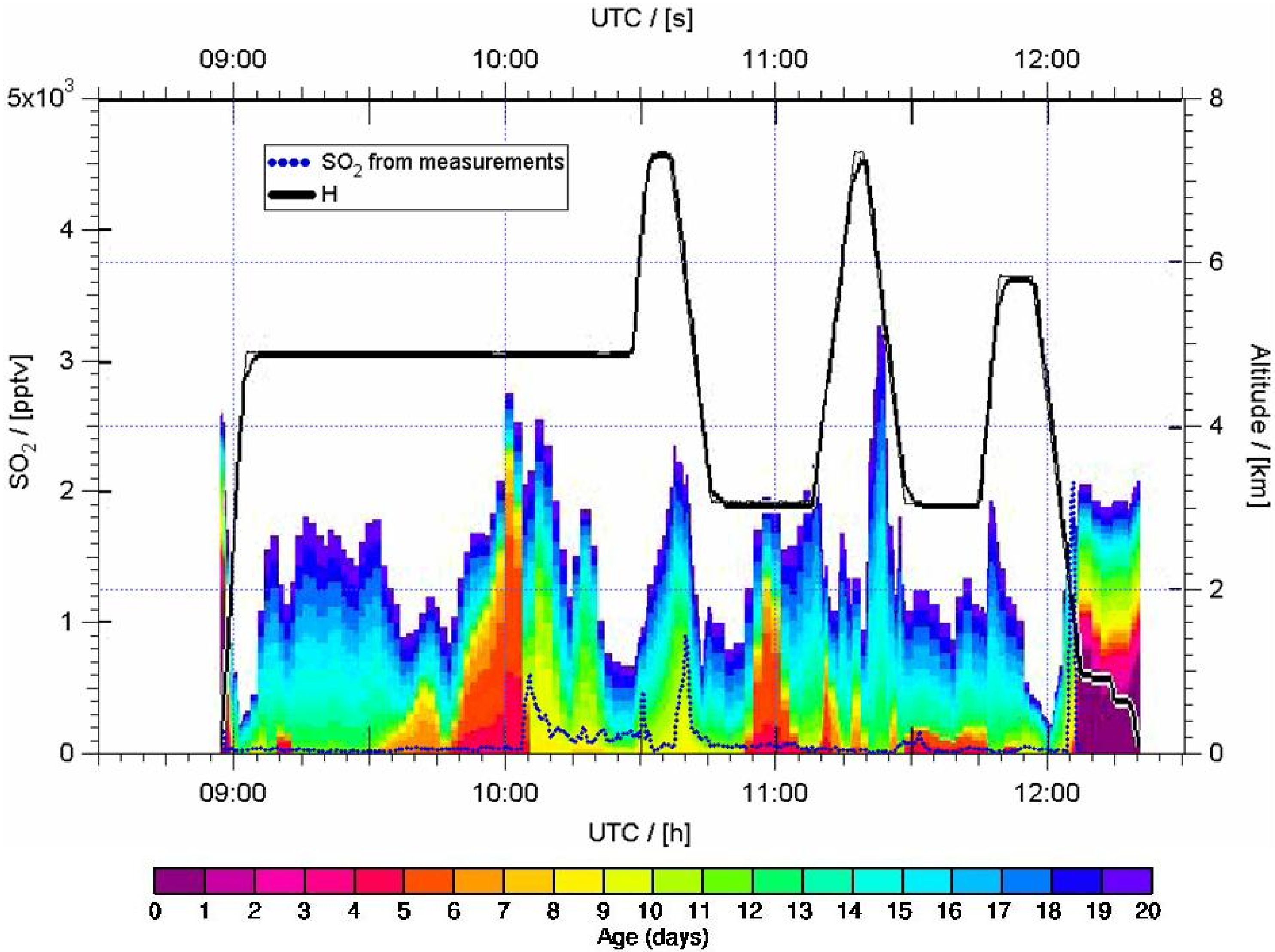

Figure 6.24: FLEXPART SO_2 age spectrum and measured SO_2 mole fraction of INTEX flight 20060503. The vertical bars show the expected mole fraction of SO_2 during the flight, the color code the corresponding age of the air mass.

For the highest peak in the SO_2 mole fraction (P6) simulations with the aerosol nucleation model AEROFOR [Pirjola, 1998, Pirjola and Kulmala, 1998] have been made along the trajectory in cooperation with Liisa Pirjola from the Helsinki Polytechnic University. This model treats aerosol formation by homogeneous binary nucleation of H_2SO_4 and H_2O as well as aerosol growth by H_2SO_4-H_2O condensation and aerosol coagulation. From a prescribed SO_2 and OH concentration the H_2SO_4 concentration is calculated. Further model input needed is an initial particle concentration, humidity and temperature along the trajectory. The model then delivers the homogeneous binary nucleation rate J_{honu}, condensation sink CS, which is principally the inverse H_2SO_4 lifetime, and particle concentrations between 4 and 200 nm.

The particle concentration calculation in the model moreover builds on a bimodal initial particle size distribution, possessing the lognormal parameters

$$\mathrm{N}_1 = 200\ \mathrm{cm}^{-3} \tag{6.1}$$

$$\mathrm{d}_1 = 130\ \mathrm{nm} \tag{6.2}$$

$$\sigma_1 = 1.45 \tag{6.3}$$

and

$$\mathrm{N}_2 = 50\ \mathrm{cm}^{-3} \tag{6.4}$$

$$\mathrm{d}_2 = 250\ \mathrm{nm} \tag{6.5}$$

$$\sigma_2 = 1.9 \tag{6.6}$$

with N_1 the initial particle number concentration in mode 1, d_1 the mean diameter of that mode and σ_1 the standard deviation of the lognormal distribution, N_2, d_2 and σ_2 respectively in mode 2. In our case, four different scenarios have been calculated for point P6. The initial particle concentrations are varied by multiplying the upper values by 0, 1, 2 and 4, resulting in total initial particle concentrations of 0, 250, 500 and 1000 cm^{-3}.

The simulation time is 8.5 days starting at 00:00 UTC on 25th of April 2006, so ending around noon on the 3rd of May 2006, which was the flight measurement day. The initial SO_2 concentration of $5.2 \cdot 10^{10}$ cm^{-3} was chosen in such a way that the final modelled SO_2

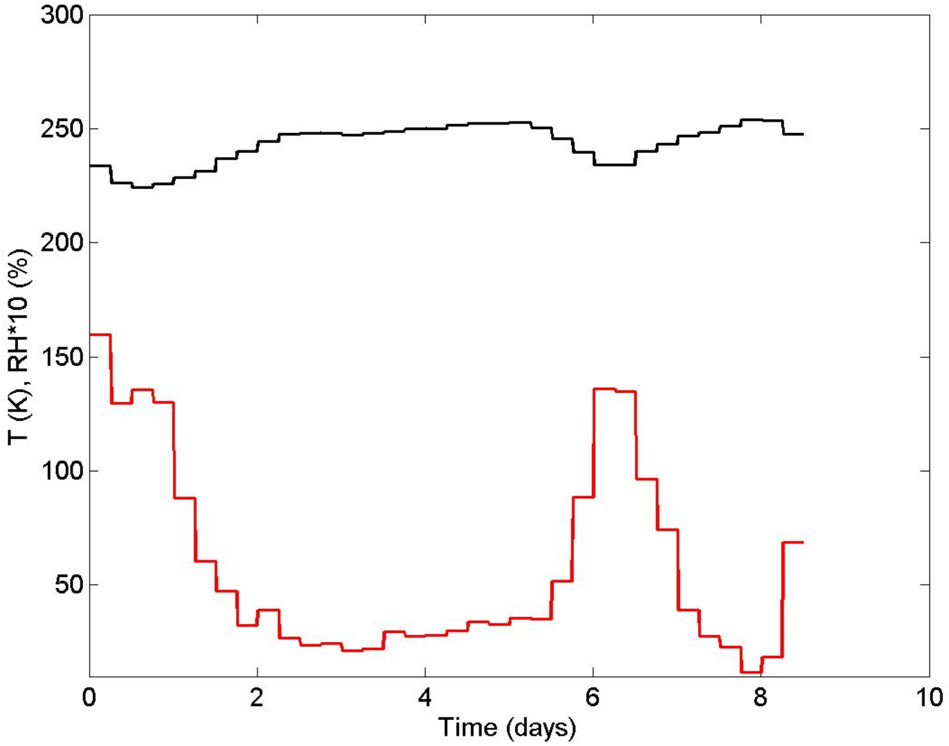

Figure 6.25: AEROFOR simulation input: temperature (black) and relative humidity (red) along FLEXPART trajectory P6.

concentration ($1.3{\cdot}10^{10}$ cm^{-3}) matches the measured SO_2 ($\approx$ 900 pptv). At the beginning of the simulation the trajectory P6 was already lifted to 335 hPa ($\approx$ 8 km). For the OH variation clear sky was assumed with constantly 14 hours of daylight, which is the case for latitudes 45-50, where the FLEXPART trajectory travels the last two days. Before, the trajectory also passes higher latitudes with longer daylight, but this has not been taken into account.

In **Figure 6.25** the model inputs temperature and humidity along the trajectory are plotted. The temperature stays rather constant around 240 K the whole time, humidity varies between 1 and 16% with two maxima at the beginning and on simulation day 6. **Figures 6.26-6.33** eventually depict the actual AEROFOR model simulations.

Figures 6.26 and **6.27** describe the model results for the first scenario without initial particles, so the initial particle concentration is 0. The H_2SO_4 concentration (**Figure 6.26**, lower panel) shows a diurnal variation, following the diurnal variation of OH as expected.

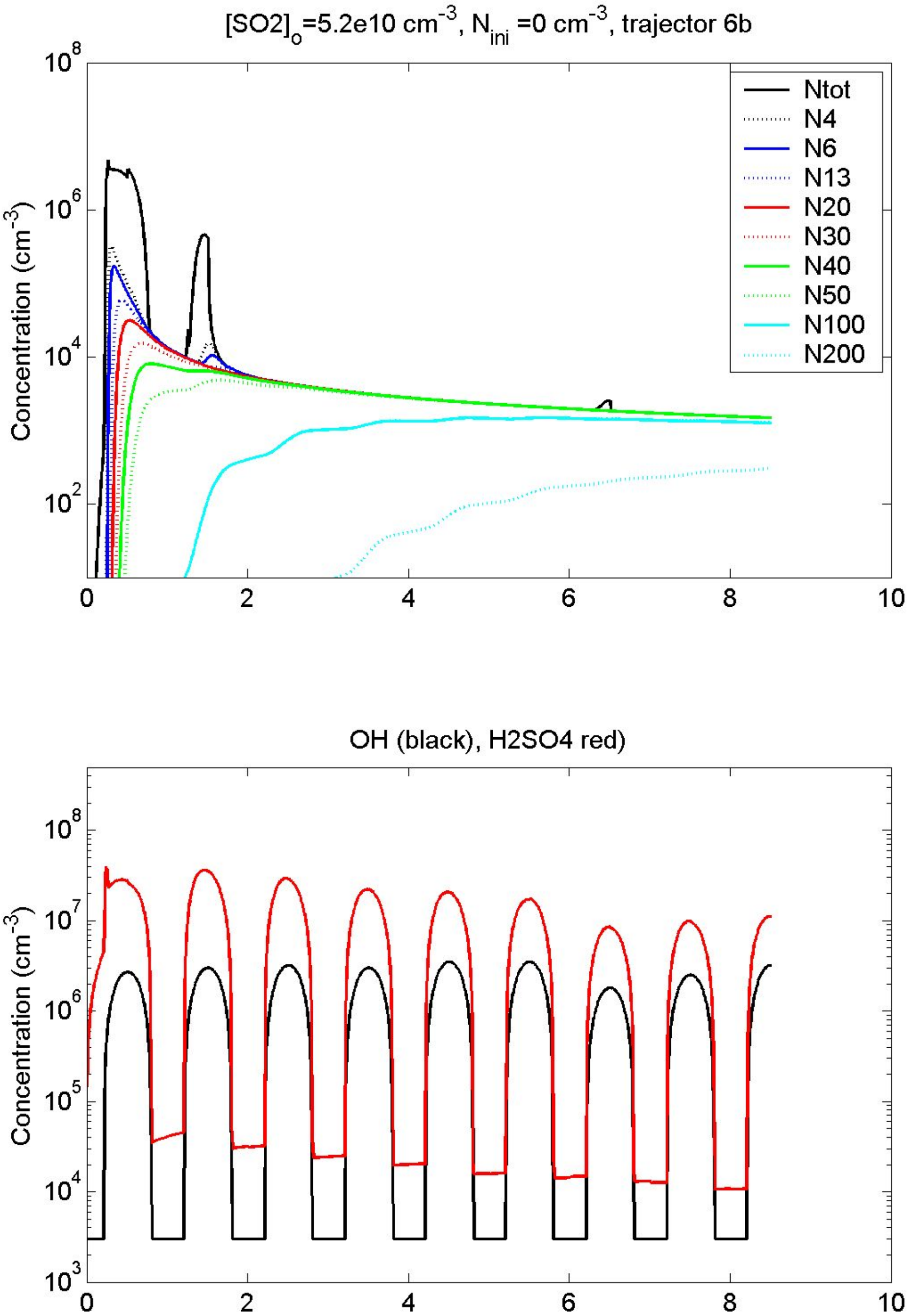

Figure 6.26: AEROFOR simulation scenario 1: no initial particle concentration. Upper panel: particle concentrations of particles of different size classes. Lower panel: modelled OH and H_2SO_4 concentrations.

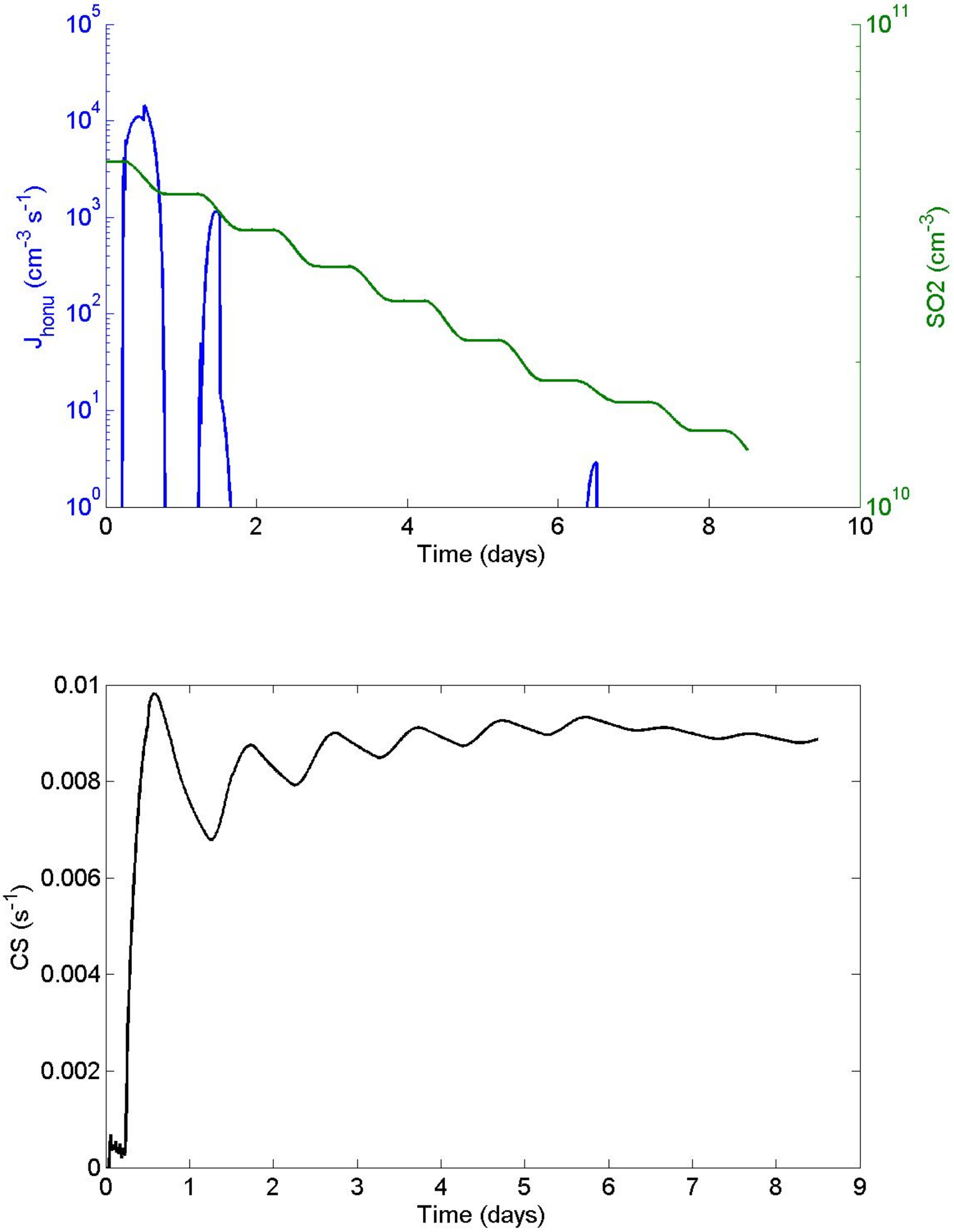

Figure 6.27: AEROFOR simulation scenario 1: no initial particle concentration. Upper panel: homogeneous nucleation rate J_{honu} and SO_2 concentration. Lower panel: condensation sink CS.

Right in the beginning, H_2SO_4 noontime concentrations of $3{\cdot}10^7$ cm^{-3} are reached, which go slightly down each day to finally $9{\cdot}10^6$ cm^{-3}. The homogeneous nucleation rate J_{honu} (**Figure 6.27**, upper panel) shows two strong maxima right in the beginning on day 0 and day 1 (10000 and 1000 cm^{-3} s^{-1}) and a smaller peak on day 6, which corresponds to the local minima in temperature accompanied by local maxima in humidity. Low temperatures and high relative humidities favor new particle formation. The condensation sink CS (**Figure 6.27**, lower panel) starts at 0 s^{-1} as no initial particles exist, but increases immediately to 0.01 s^{-1} simultaneously to the occurring nucleation. During nighttime the CS decreases caused by the decrease in the total particle surface, which results from coagulation and growth of the existing particles. The surface to volume ratio decreases with increasing radius of the particles. So if small particles coagulate to bigger ones the total aerosol surface decreases. That means that the total aerosol surface available for condensational growth decreases during night, if no new particles are formed. All this eventually results in the particle concentrations graphed in **Figure 6.26**, upper panel. A strongly developed increase in the total particle concentration (up to $4{\cdot}10^6$), caused by the two nucleation bursts on day 0 and 1, is followed by a slow decrease of the total particles to a final value of $\approx$ 1000 cm^{-3}. Condensational and coagulational growth of the freshly built particles forms particles with diameters larger than 100 nm already after one day. Particles of these size classes can act as cloud condensation nuclei (CCN) and are therefore available for cloud formation.

Figures 6.28 and **6.29** depict similar graphs for scenario 2, an initial particle concentration of 250 cm^{-3}. Compared to scenario 1, H_2SO_4 concentration and homogeneous nucleation rate show nearly the same behavior. The CS starts at 0.002 s^{-1}, because of the initial particles that are available for condensation already when the simulation starts. The CS maximum value is 0.01 s^{-1}, also the same as in scenario 1. Freshly nucleated particles are formed in the same amount as in scenario one, so there is obviously enough H_2SO_4 available for both, growth of the initial particles and nucleation of new ones. The formation of CCN after 1 day is still enhanced and a final total particle concentration of 1000 cm^{-3} at the measurement site can be expected.

The plots for scenario 3 (initial particle concentration 500 cm^{-3}) are shown in **Figures**

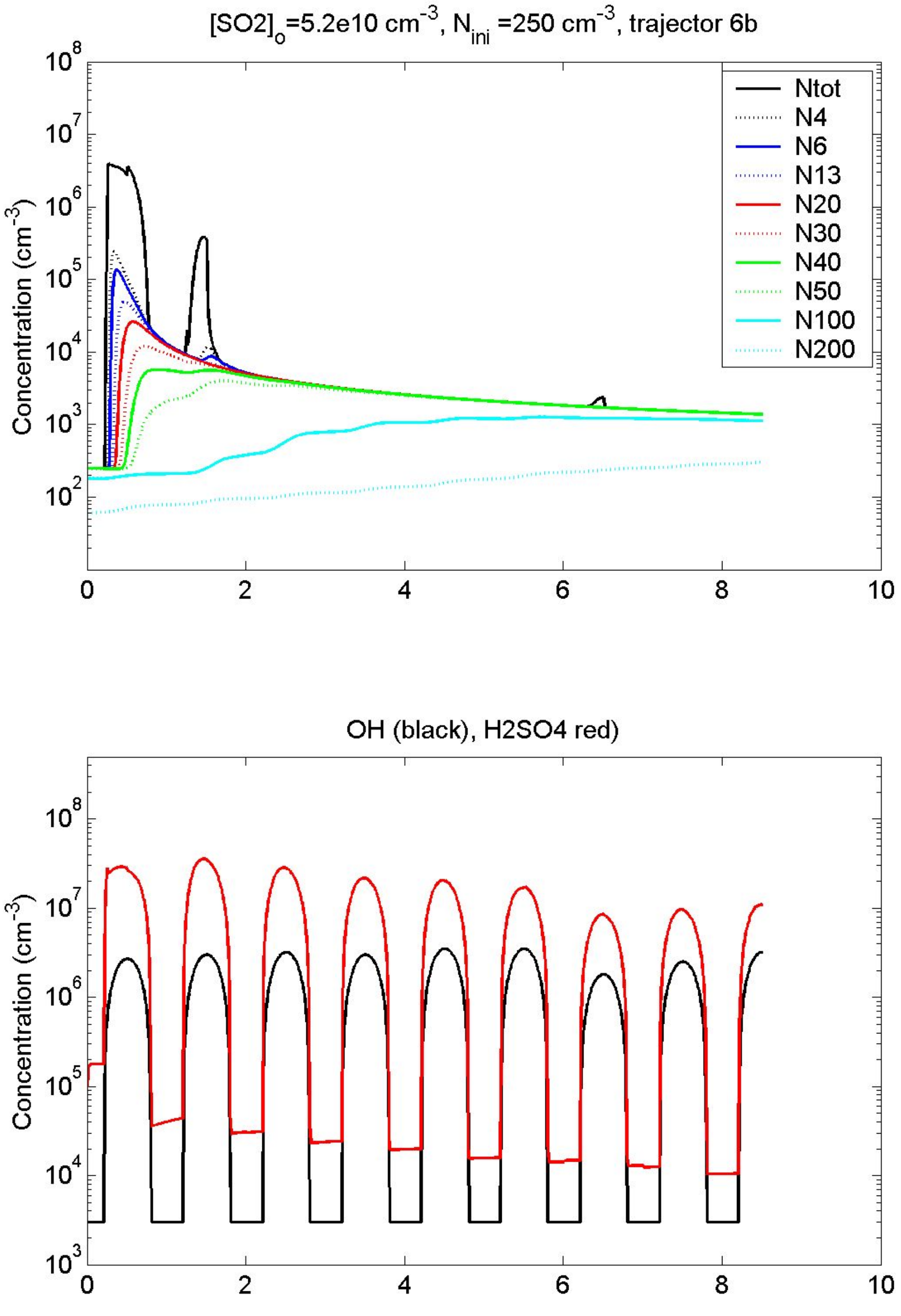

Figure 6.28: AEROFOR simulation scenario 2: initial particle concentration of 250 cm^{-3}. Upper panel: particle concentrations of particles of different size classes. Lower panel: modelled OH and H_2SO_4 concentrations.

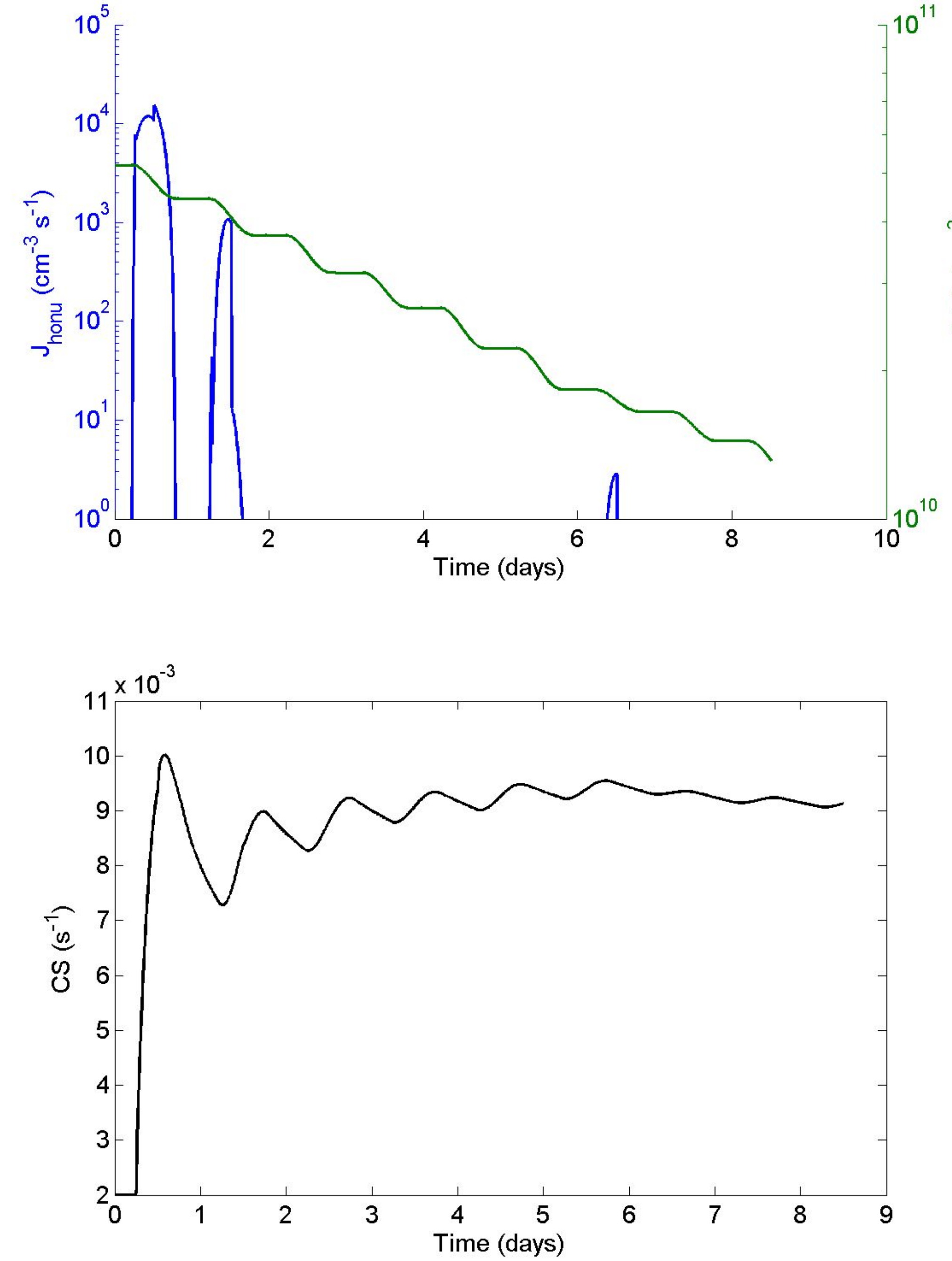

Figure 6.29: AEROFOR simulation scenario 2: initial particle concentration 250 cm^{-3}. Upper panel: homogeneous nucleation rate J_{honu} and SO_2 concentration. Lower panel: condensation sink CS.

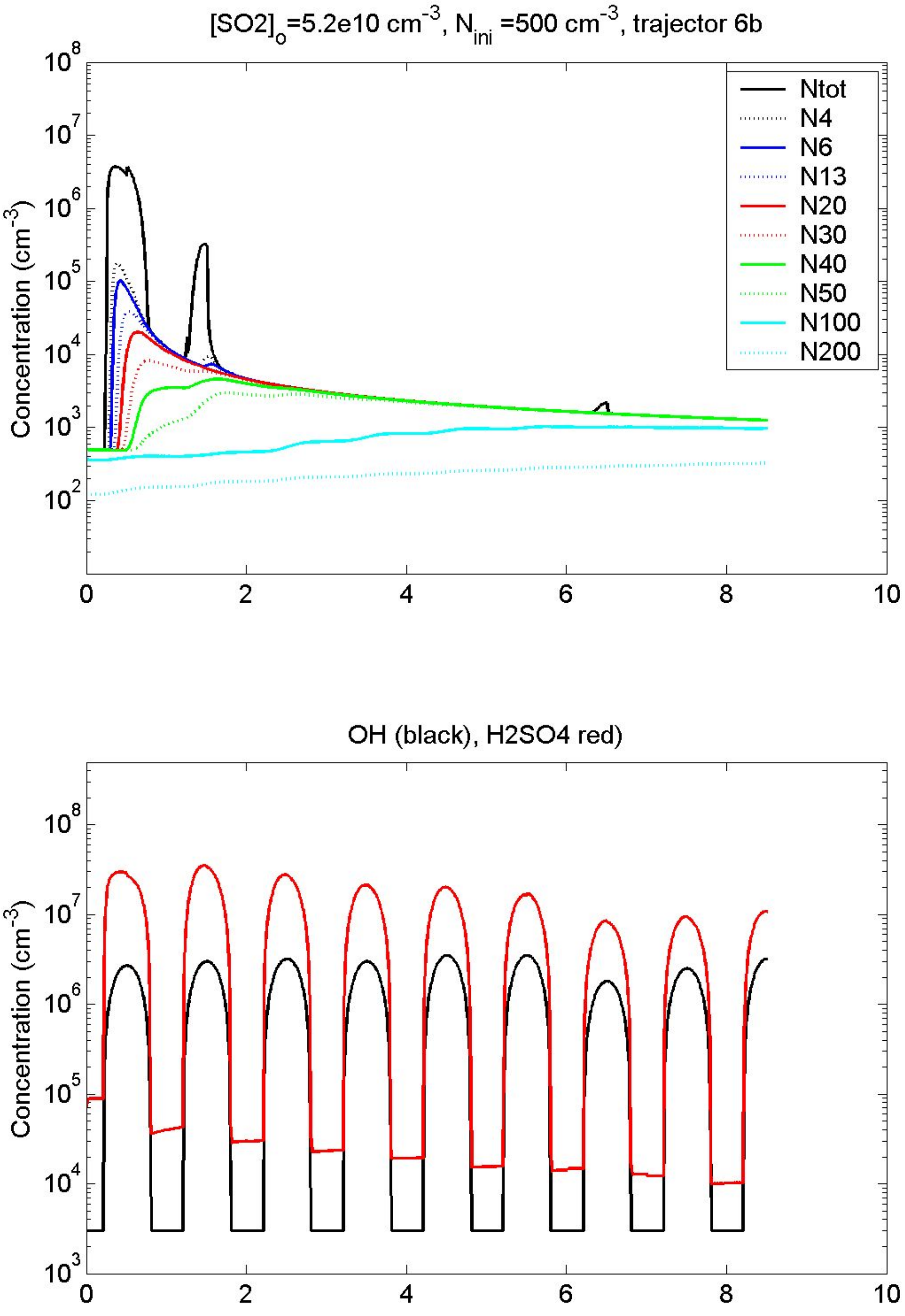

Figure 6.30: AEROFOR simulation scenario 3: initial particle concentration 500 cm^{-3}. Upper panel: particle concentrations of particles of different size classes. Lower panel: modelled OH and H_2SO_4 concentrations.

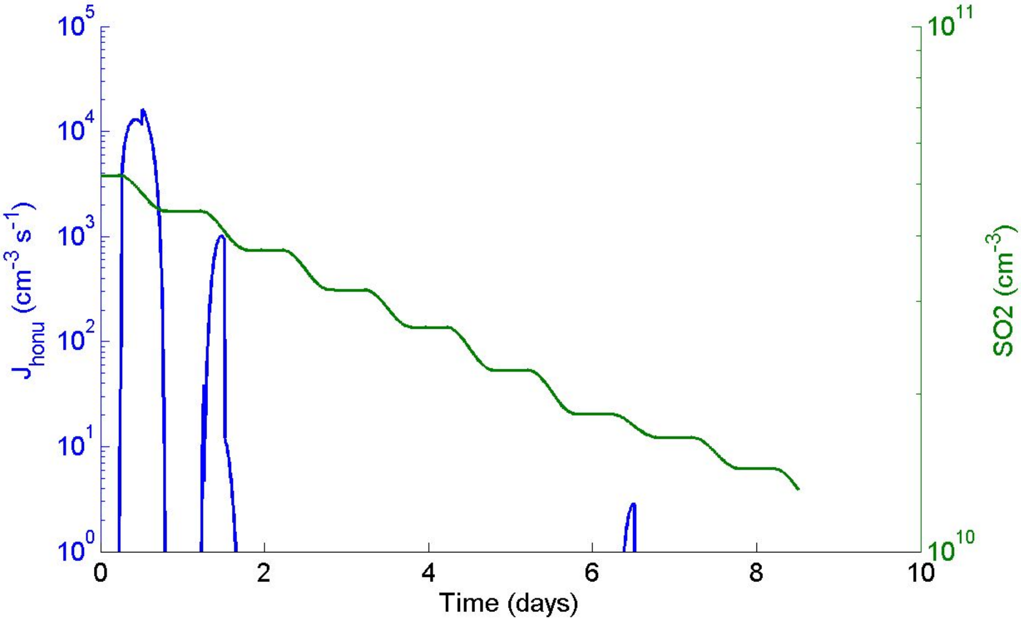

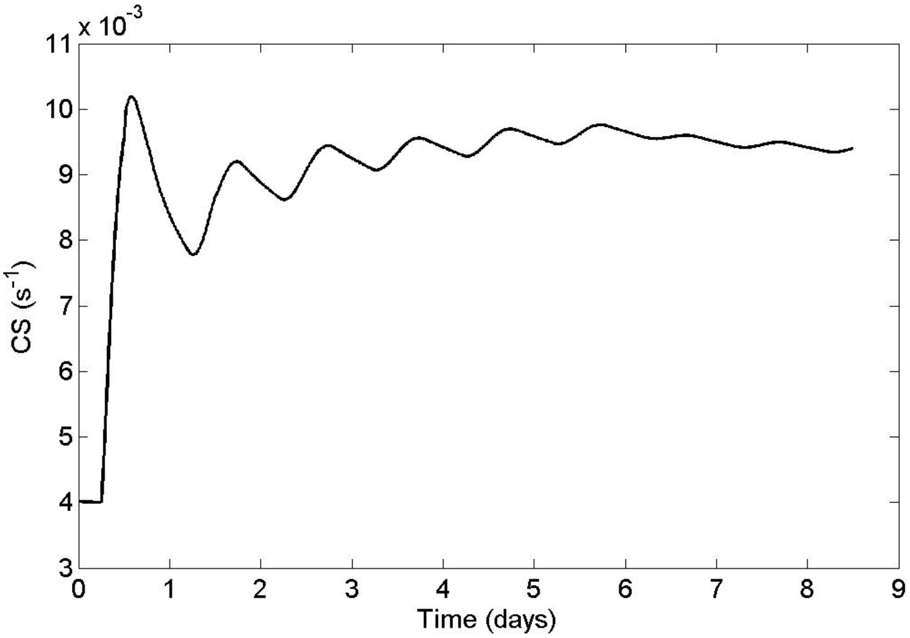

Figure 6.31: AEROFOR simulation scenario 3: initial particle concentration 500 cm^{-3}. Upper panel: homogeneous nucleation rate J_{honu} and SO_2 concentration. Lower panel: condensation sink CS.

6.30 and **6.31**. The higher initial particle concentration again has no substantial influence on the H_2SO_4 concentration and the nucleation rate, but the higher CS (starting at 0.004 s^{-1} and 0.01 s^{-1} in maximum) influences the growth of the particles in the size classes N50, N100 and N200. The growth starts slightly later than in scenario 1 and the total increase in the number concentration of CCN is less developed. Nevertheless the final concentration of CCN reaches in the sum of initial and freshly formed particles again 1000 cm^{-3}.

The fourth scenario eventually starts with the assumption of 1000 cm^{-3} as initial particle concentration, which was the modelled final value in the other 3 scenarios. The H_2SO_4 concentration development stays still the same, the nucleation rate on day 0 either, but on day 1 J_{honu} is slightly lowered. The condensation sink is further increasing and lies all the time above 0.009 s^{-1} with a maximum of 0.015 s^{-1}. The increase in the total particle concentration on day 0 and 1 is still enormous, but the growth in all size classes is now markedly suppressed. So the H_2SO_4 concentration seems still to be high enough for new particle formation, but a large amount of H_2SO_4 will be already consumed by condensation onto the initial particles, so that not much H_2SO_4 is left for condensation on the newly formed ones. The final concentration of CCN is approximately 800 cm^{-3}.

Typical measured particle concentrations lie in the range of 500 cm^{-3}, in very polluted cases also 2000-4000 cm^{-3} can be reached (view flight overviews in the appendix or Figure 6.12). So at least scenario 3 is quite realistic.

A fifth scenario would have maybe been interesting, namely with such a high initial particle concentration (e.g. 2000 cm^{-3}), that no nucleation occurred at all due to a complete removal of the condensable gases by condensation onto preexistent aerosol.

Conclusively one can say, that without an extraordinarily high initial particle concentration the observed SO_2 and the deduced H_2SO_4 led to a significant increase in particles with diameters larger than 50 nm, which can act as cloud condensation nuclei. This is already the case for only one example of SO_2 pollution transport. Assuming many similar events in the atmosphere, this formation of CCN might have a significant influence on climate by favoring cloud formation and by extending the lifetime of clouds and therefore tend to contribute to increase the earth's albedo.

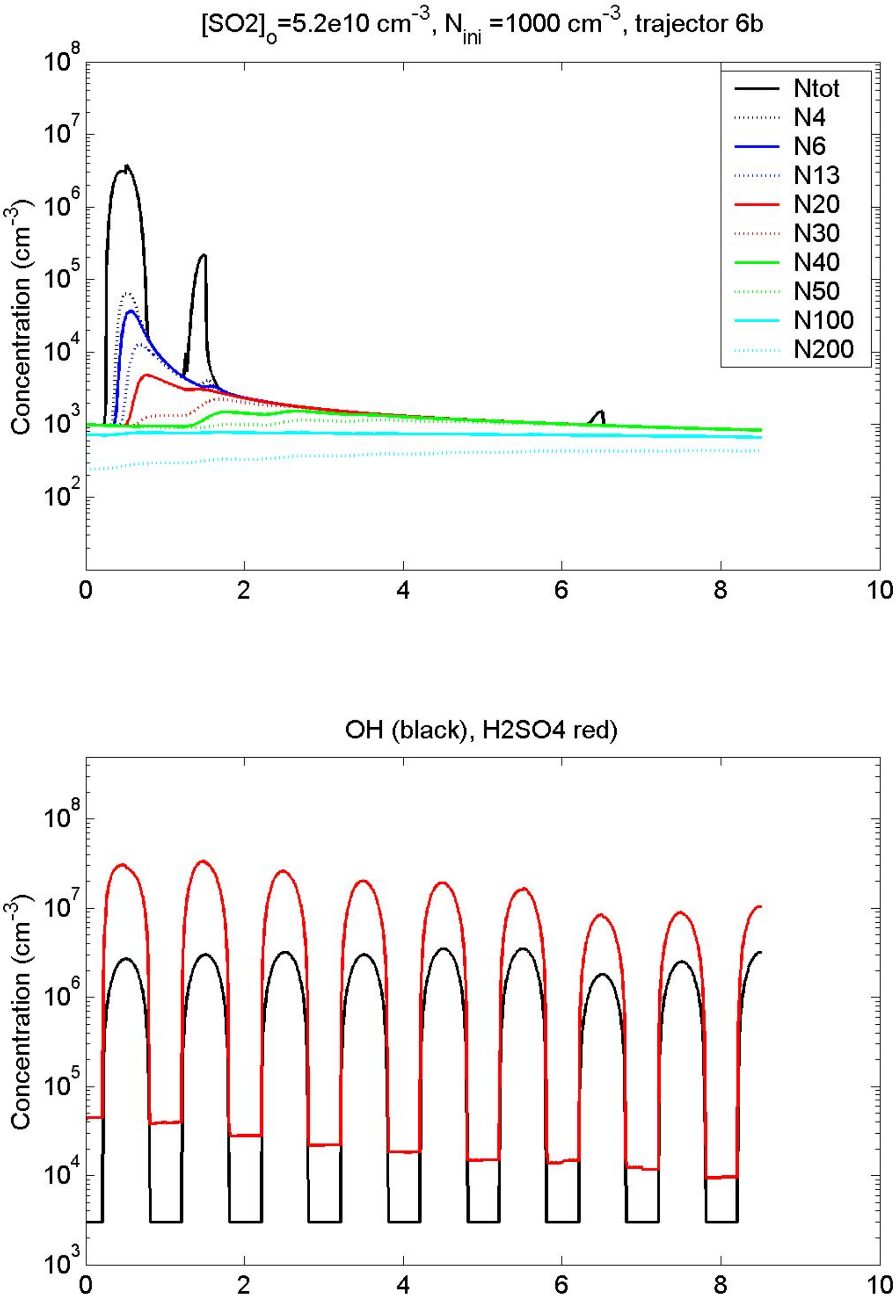

Figure 6.32: AEROFOR simulation scenario 4: initial particle concentration 1000 cm^{-3}. Upper panel: particle concentrations of particles of different size classes. Lower panel: modelled OH and H_2SO_4 concentrations.

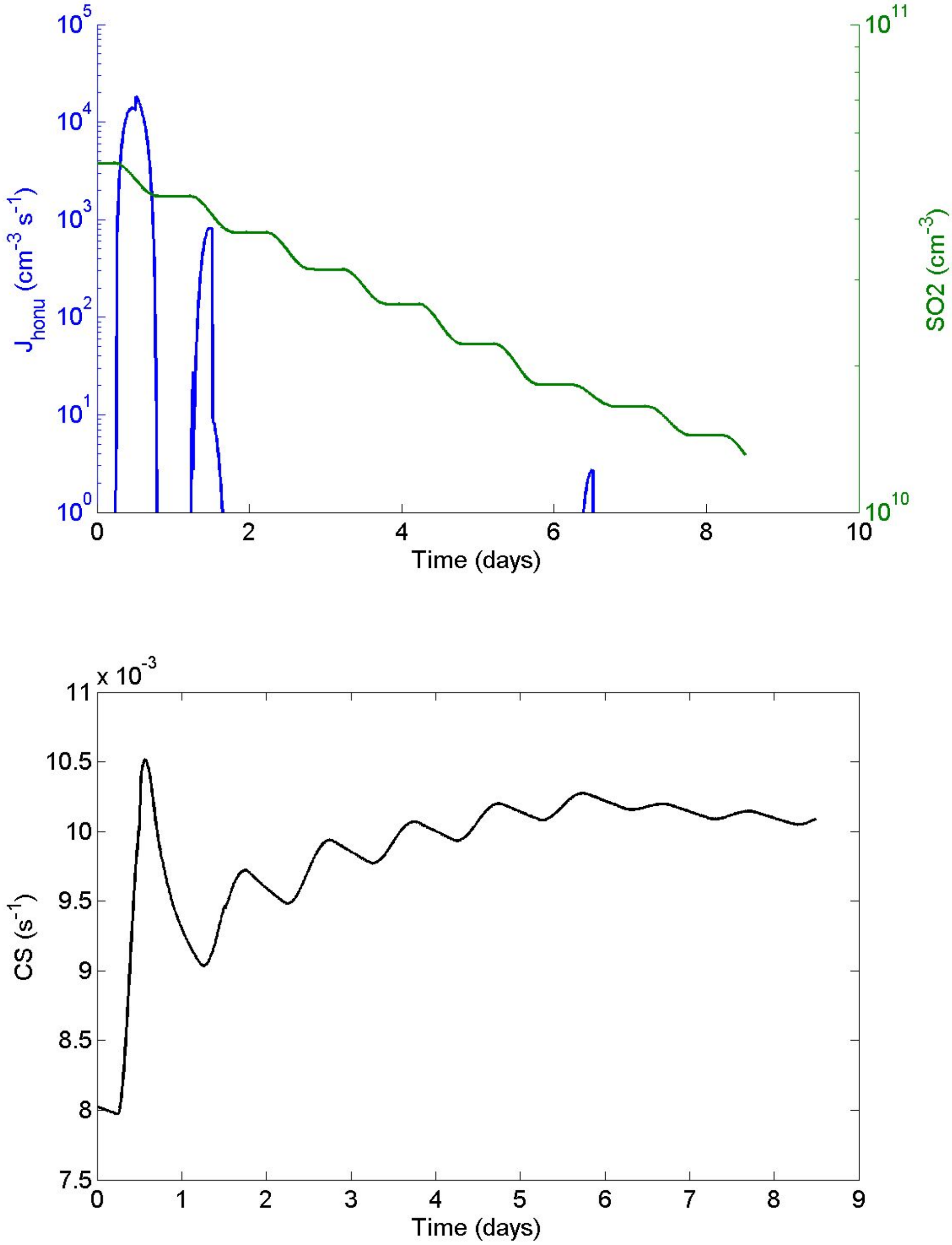

Figure 6.33: AEROFOR simulation scenario 4: initial particle concentration 1000 cm^{-3}. Upper panel: homogeneous nucleation rate J_{honu} and SO_2 concentration. Lower panel: condensation sink CS.

6.4 AMMA Flight 20060813, Biomass Burning

This flight started from the airport in Ouagadougou, Burkina Faso, right to the south over Ghana to the coast. Over the Atlantic ocean a profile down to an altitude of 4km was flown with an almost 180 degree turn back to Ouagadougou. During this profile a pollution plume has been detected in all trace gases and will be discussed now in detail in this section. The principle flight path can be seen in **Figure 6.34**.

6.4.1 Satellite Data and Air Mass Trajectories

Figure 6.35 shows a satellite image by the new instrument OMI (Ozone Monitoring Instrument) on satellite AURA. Depicted is the aerosol index (AI), which is a measure how much the backscattered UV wavelength of a polluted atmosphere (Mie-, Rayleigh-scattering and absorption) differs from that of a pure atmosphere (pure Rayleigh scattering). Positive AI

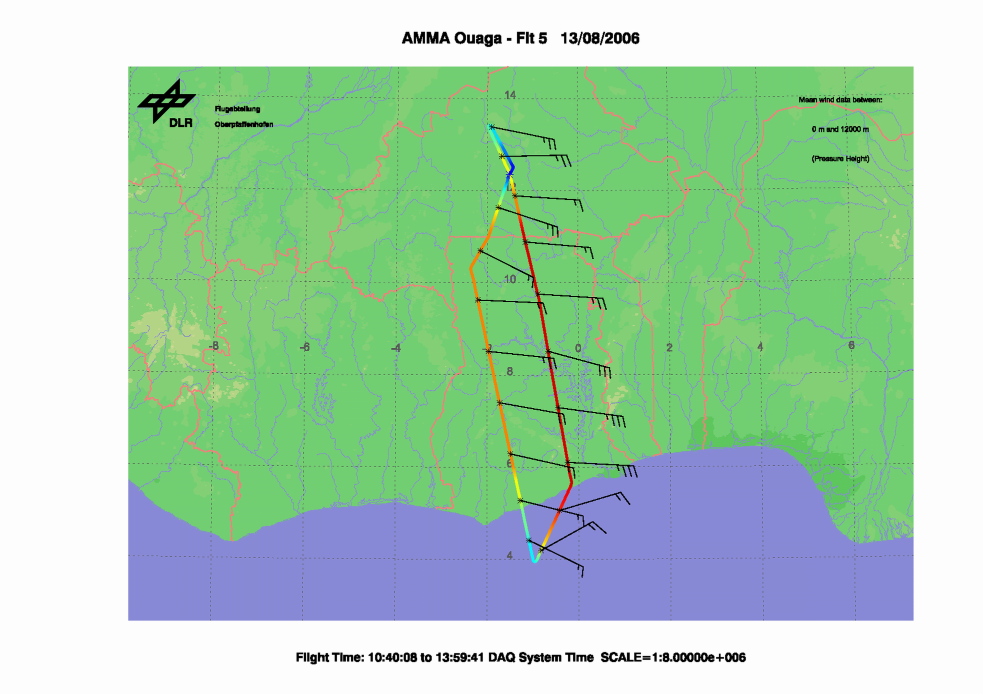

Figure 6.34: Flight path of AMMA flight 20060813. The colors from blue to red roughly indicate the altitude (0 to 11 km). Distance of the wind direction markers is 10 minutes. 1° Longitude corresponds to approximately 110 km, 1° Latitude to 111 km.

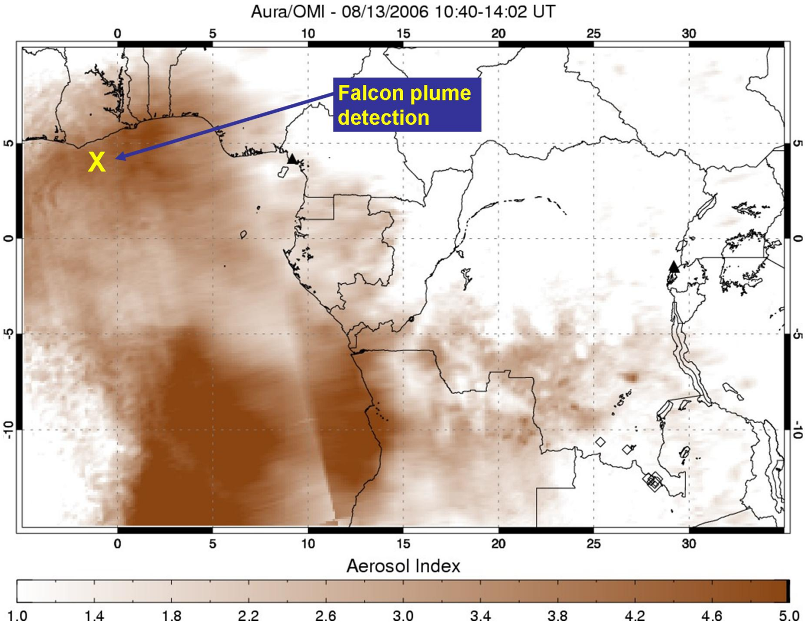

Figure 6.35: Aerosol Index (AI) measured by OMI on satellite AURA. The Falcon measurement area is marked by a cross. Positive AI values mean light absorbing aerosols, negative AI would mean pure scattering. (Figure by N. Krotkov (OMI team), private communication).

values mean absorbing aerosols, negative AI values mean pure scattering. As can be seen, a large plume of absorbing aerosol particles on the day of our aircraft measurements has been detected by AURA. The plume of absorbing particles covers an area of at least 4 million km^2 and is horizontally inhomogeneous distributed. The dive of the Falcon into the plume (marked in Figure 6.35 by a cross) took place in one of the denser plume regions.

The OMI instrument on Aura also delivers as a side product SO_2 column densities in Dobson units (DU). **Figure 6.36** is the SO_2 column graph for the flight day. It is interesting, that OMI did not see a strong SO_2 pollution. According to the OMI team, high aerosol concentrations unfortunately disturb the SO_2 measurements, which is expressed by negative DU values. More information about OMI can be found in [Krotkov et al., 2006].

An air mass trajectory overview graph for this flight has already been shown in chapter 5 (Figure 5.6). A more detailed self made analysis with the internet trajectory tool HYSPLIT lead to the following result. 6 trajectories have been calculated: shortly before the plume, while diving into the plume, 2 times inside the plume, while flying out and shortly after.

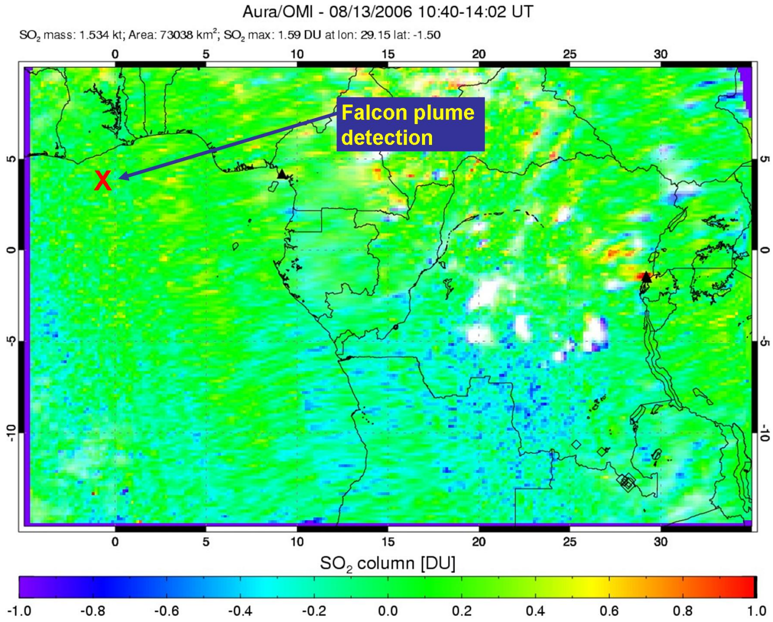

Figure 6.36: SO_2 column density (DU) on the AMMA biomass burning plume detection day measured by the ozone monitoring instrument (OMI) on satellite AURA. (Figure by N. Krotkov (OMI team), private communication).

The trajectories are plotted in **Figures 6.37-6.39** and the corresponding points in time are marked in the time series plot **Figure 6.42**. Moreover, **Figure 6.40** shows fires in Northern Africa for the time between the 1st and 10th of August 2006 detected by satellite MODIS. The fire region is located mostly south of the equator. Trajectory number 1, ending shortly before entering the plume, came straight from the east, a region without biomass burning. Trajectory 2 and 3 passed around 3 days before the measurements the coast of Nigeria, where some fires had been detected by MODIS. Trajectory 4 finally started 3-4 days before the measurement in the main biomass burning region south of the equator. The trajectory passed over the fire region in altitudes of about 3 km. Therefore it seems likely that pyroplumes may have injected pyrogenic trace substances (gases and aerosols) into the background air flow. Trajectories 5 and 6 again came from a more northern direction. However the trajectory model does not consider small scale convection or pyroplumes. Moreover, from the 6 trajectory graphs can be seen that the air mass situation was not very stable. A slight change in the final coordinates of the trajectory already resulted in a major change of the air mass direction.

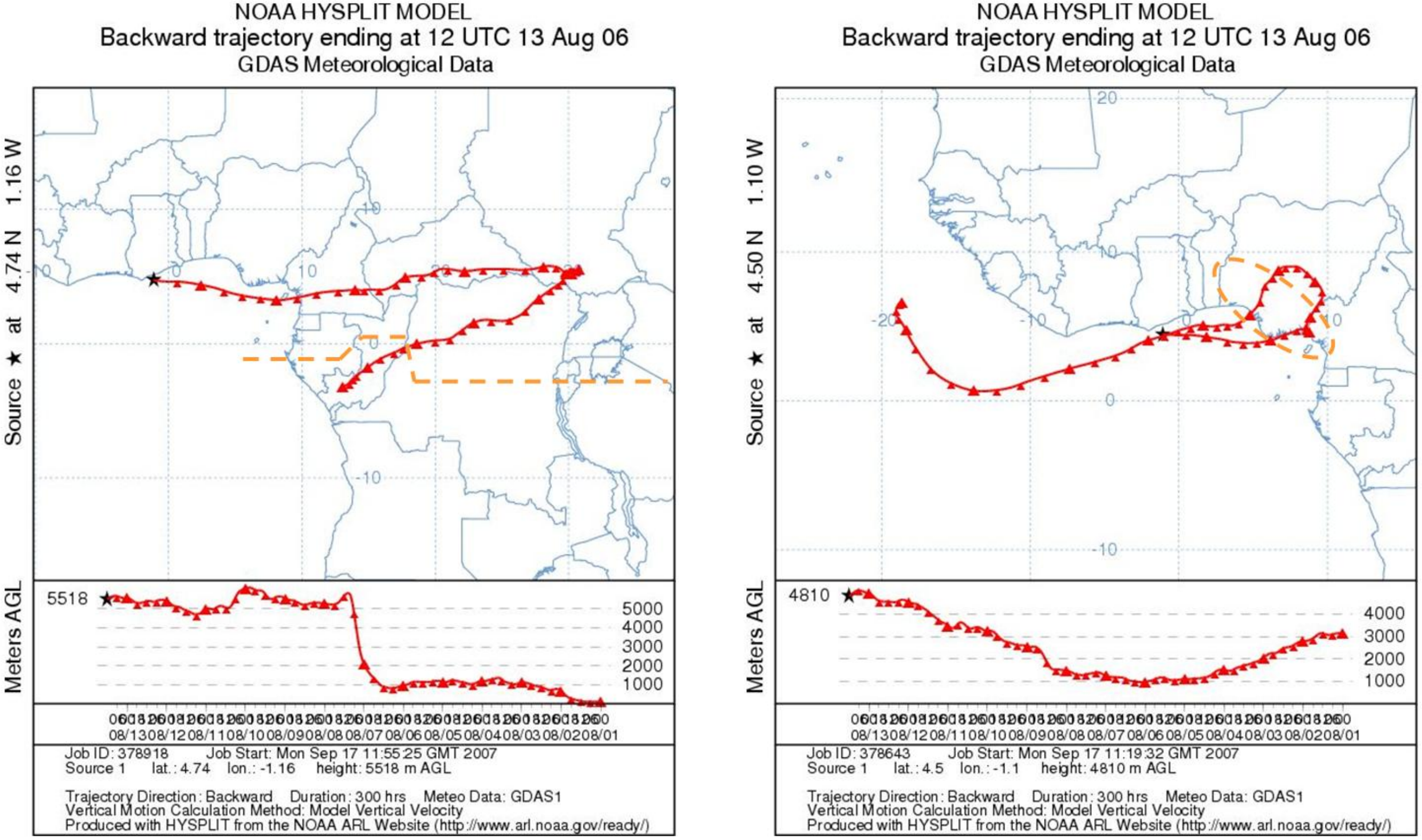

1 **2**

Figure 6.37: HYSPLIT trajectories for flight 20060813. 1: shortly before the plume, 2: while diving into the plume. South of the dashed line and inside the dashed ellipse has been biomass burning detected, view also Figure 6.40.

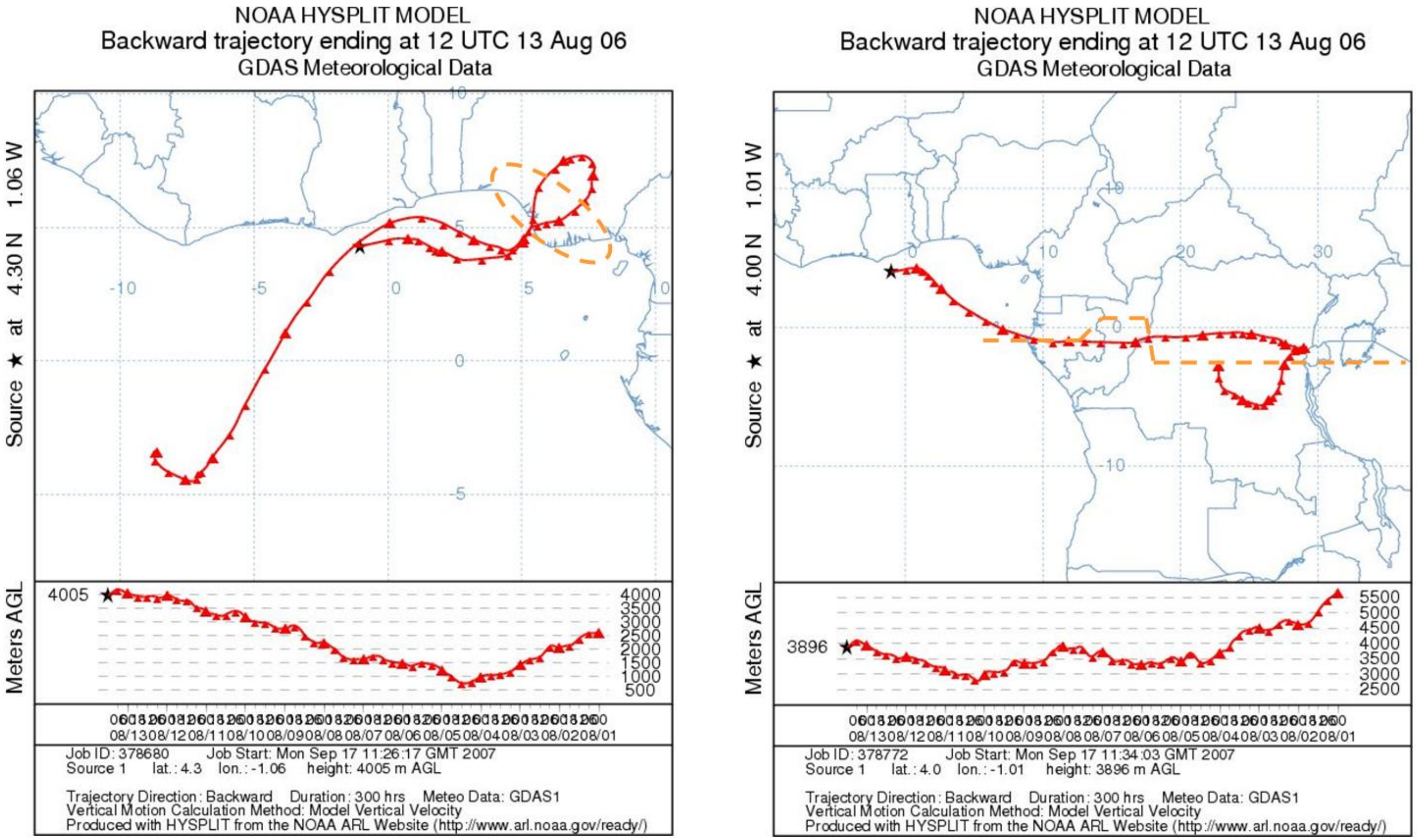

3 **4**

Figure 6.38: HYSPLIT trajectories for flight 20060813. 3 and 4: inside the plume. South of the dashed line and inside the dashed ellipse has been biomass burning detected, view also Figure 6.40.

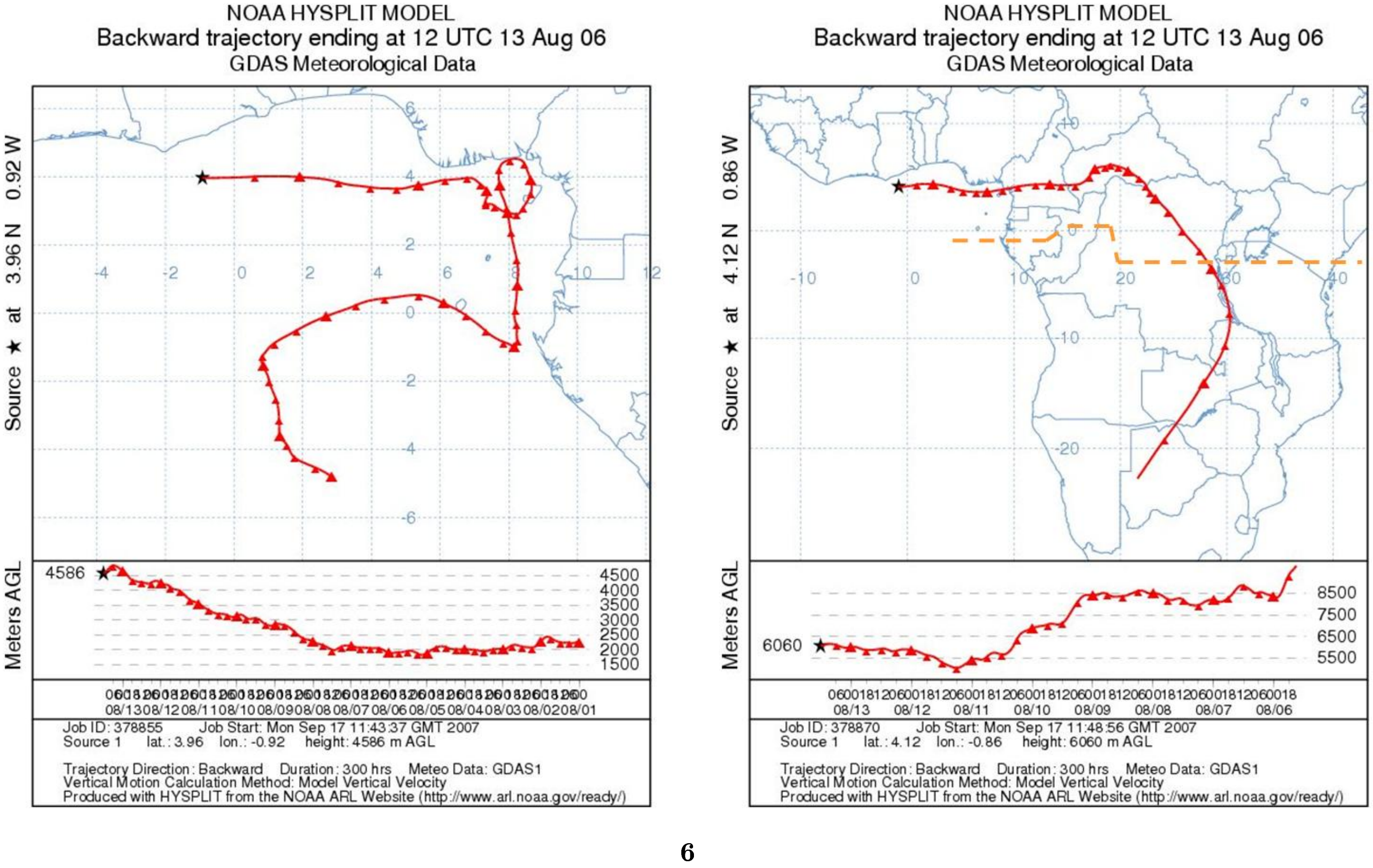

Figure 6.39: HYSPLIT trajectories for flight 20060813. 5: while flying out and 6: shortly after. South of the dashed line and inside the dashed ellipse has been biomass burning detected, view also Figure 6.40.

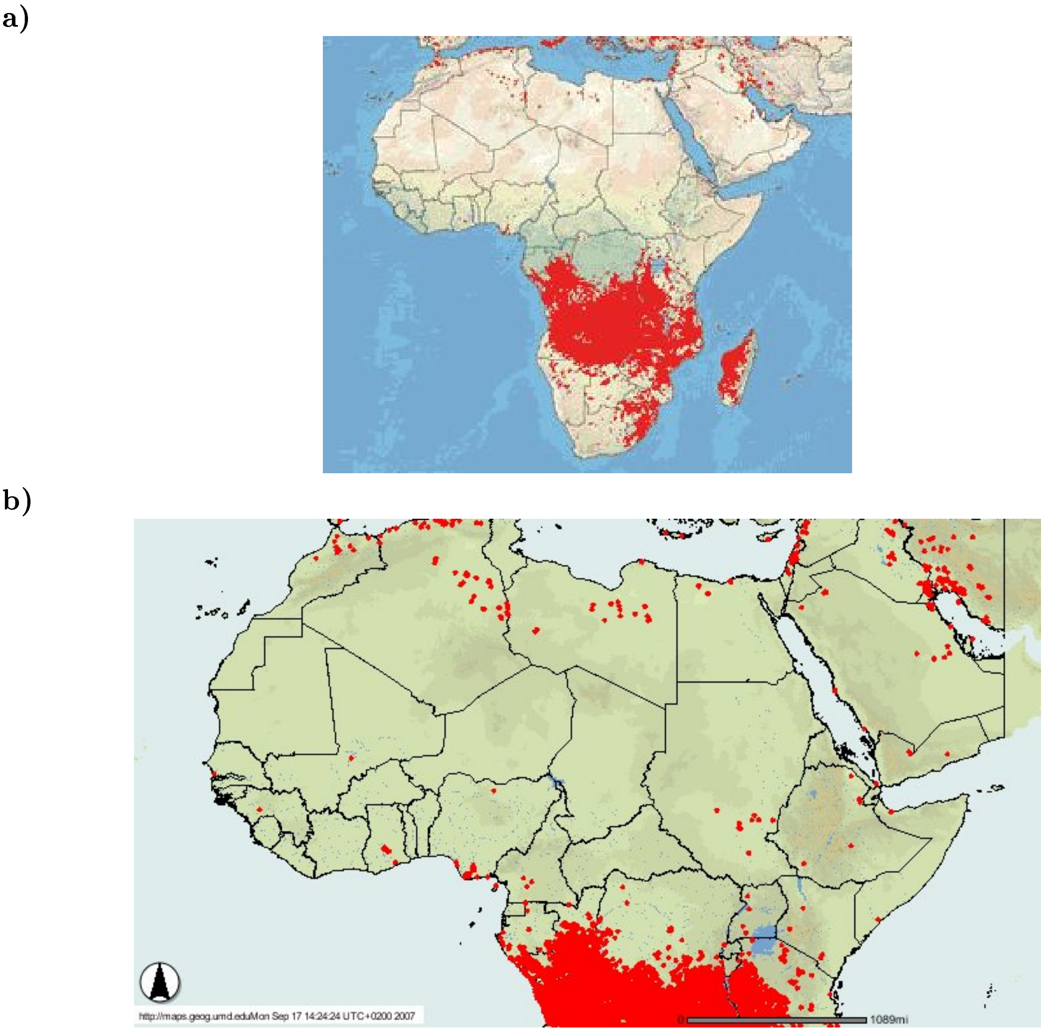

Figure 6.40: MODIS fire map for a) Africa in August 2006 and b) Northern Africa from the 1st to the 10th of August 2006.

Figure 6.41 shows two photographs of the plume taken from an experimentalist aboard the Falcon when the plane was above (upper photograph) and inside (lower photograph) the plume. Above the plume the sky was deep blue and the plume appeared as a haze which markedly reduced the visibility of the underlying planetary surface. Surface details are not visible. When the Falcon was at 3900 m, the lowest altitude of that flight step, the horizon is not visible any more, the pollution dust was completely dense.

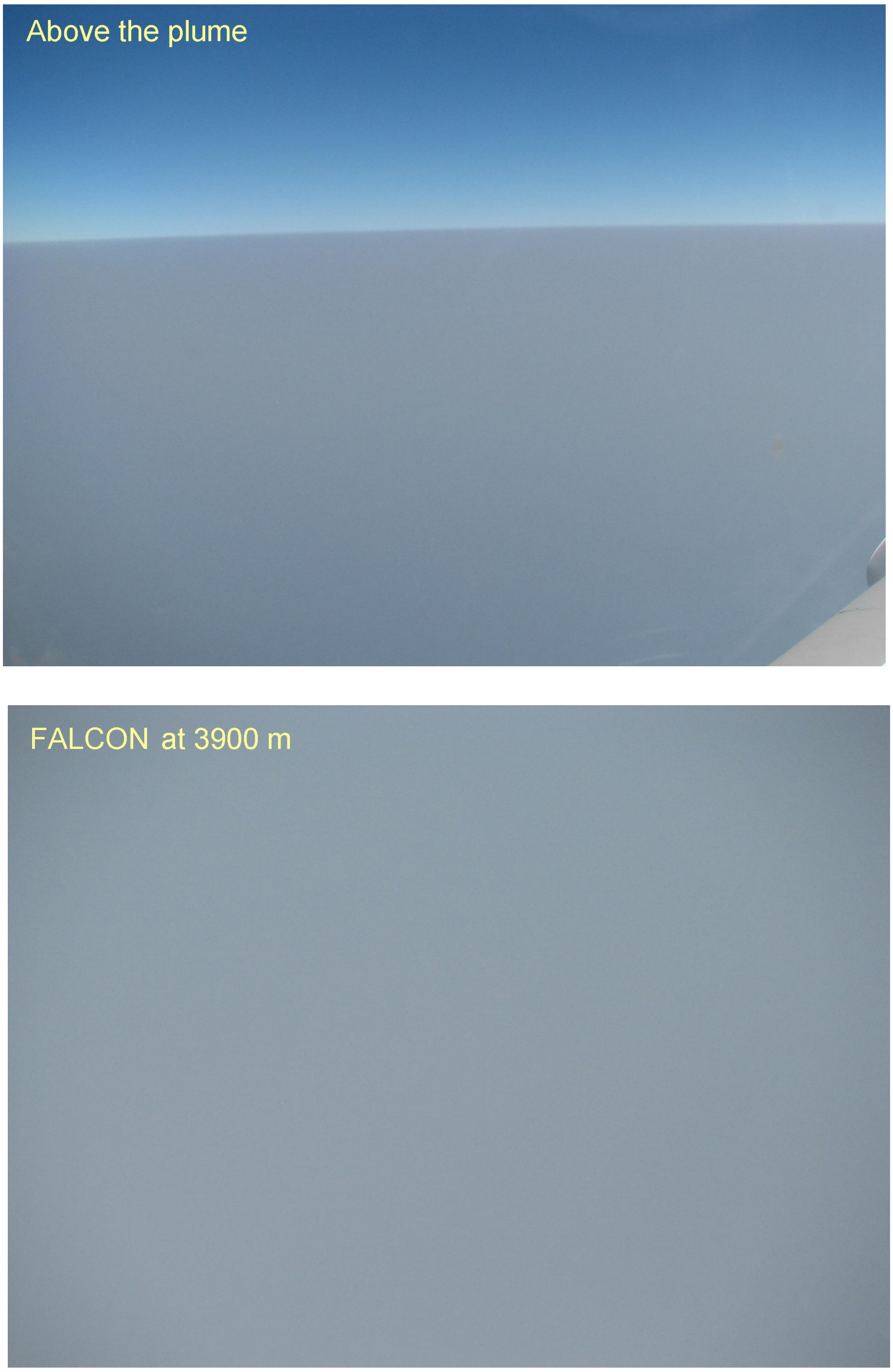

Figure 6.41: Photographs taken from an experimentalist aboard the Falcon above (upper photograph) and inside the plume (lower photograph).

6.4.2 Discussion of Time Series and Vertical Profiles

Figure 6.42 shows time series of the flight altitude and of measured trace gases SO_2, HNO_3, CO, CO_2, NO, NOy, HCHO and O_3 for the part of the flight, which was flown over the ocean off the southern coast of Ghana. A similar panel for the complete flight can be found in the appendix. At altitudes from about 5 to 3.9 km between 11:57 and 12:08 UTC the pollution plume was detected in all trace gases. The pollution was strongly developed with SO_2 peak values of more than 1 ppbv, which is usually a typical value only in the boundary layer of highly polluted regions. Two layers of the plume can be defined: a top layer, which is probed by diving into the plume between 5 and 4 km of altitude (here the SO_2 mole fraction is about 400 pptv) and a main layer at the lowest flight level around 3.9 km of altitude (with a SO_2 mole fraction of 1400 pptv).

NOy (the sum of odd nitrogen compounds) starts with 3 ppbv in the top layer, reaches up to 8 ppbv in the main layer and is closely correlated with SO_2. NO and HNO_3 behave differently. After diving into the plume they increase far more slowly reaching maximum mole fractions only at the end of the constant-level flight at 3900 m. HNO_3 then reaches nearly 9 ppbv which even exceeds the measured NOy (8 ppbv). This is actually not possible, as HNO_3 is a part of NOy, but it might be explained with HNO_3 store and release effects in the sampling line or with the missing calibration (view section 3.1.2.3). Anyhow the high HNO_3 mole fractions indicate that at least at the end of the constant flight-level at 3900 m NOy is composed mostly of HNO_3 while PAN (peroxyacetylnitrate) is only a minor NOy-component. The mole fraction ratio HNO_3/NO reaches a value of about 36 in the peak, which moreover indicates that most pyrogenic NO has been converted to HNO_3 during the 3-4 days travel of the plume from the fire region to the measurement site.

The time sequences of CO_2, O_3, and HCHO are correlated with SO_2, whereas CO behaves similar to NO and HNO_3. The secondary gas O_3 reaches a maximum mole fraction of about 135 ppbv which markedly exceeds the atmospheric background of about 50 ppbv. Hence the excess O_3 mole fraction is about 85 ppbv. This indicates very substantial ozone formation in the plume which is catalyzed by pyrogenic NO.

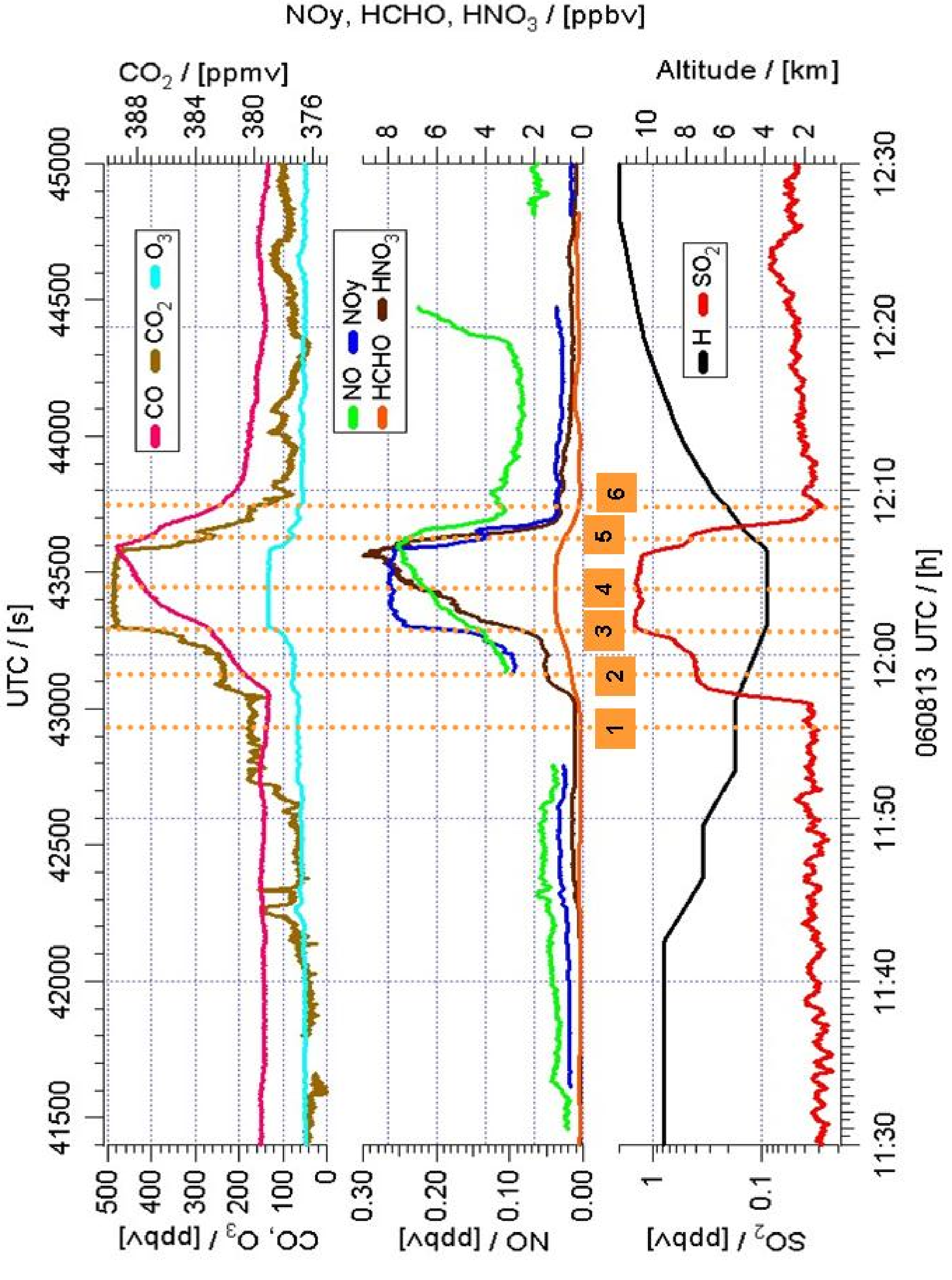

Figure 6.42: AMMA Fifth Local Flight center part. Between 11:57 and 12:08 UTC a biomass burning pollution plume has been detected. Lowest panel: SO$_2$ and flight altitude, middle panel: NO, NOy, HCHO and HNO$_3$ mole fractions, upper panel: CO, CO$_2$ and O$_3$. The SO$_2$ peak value in the plume was 1.3 ppbv.

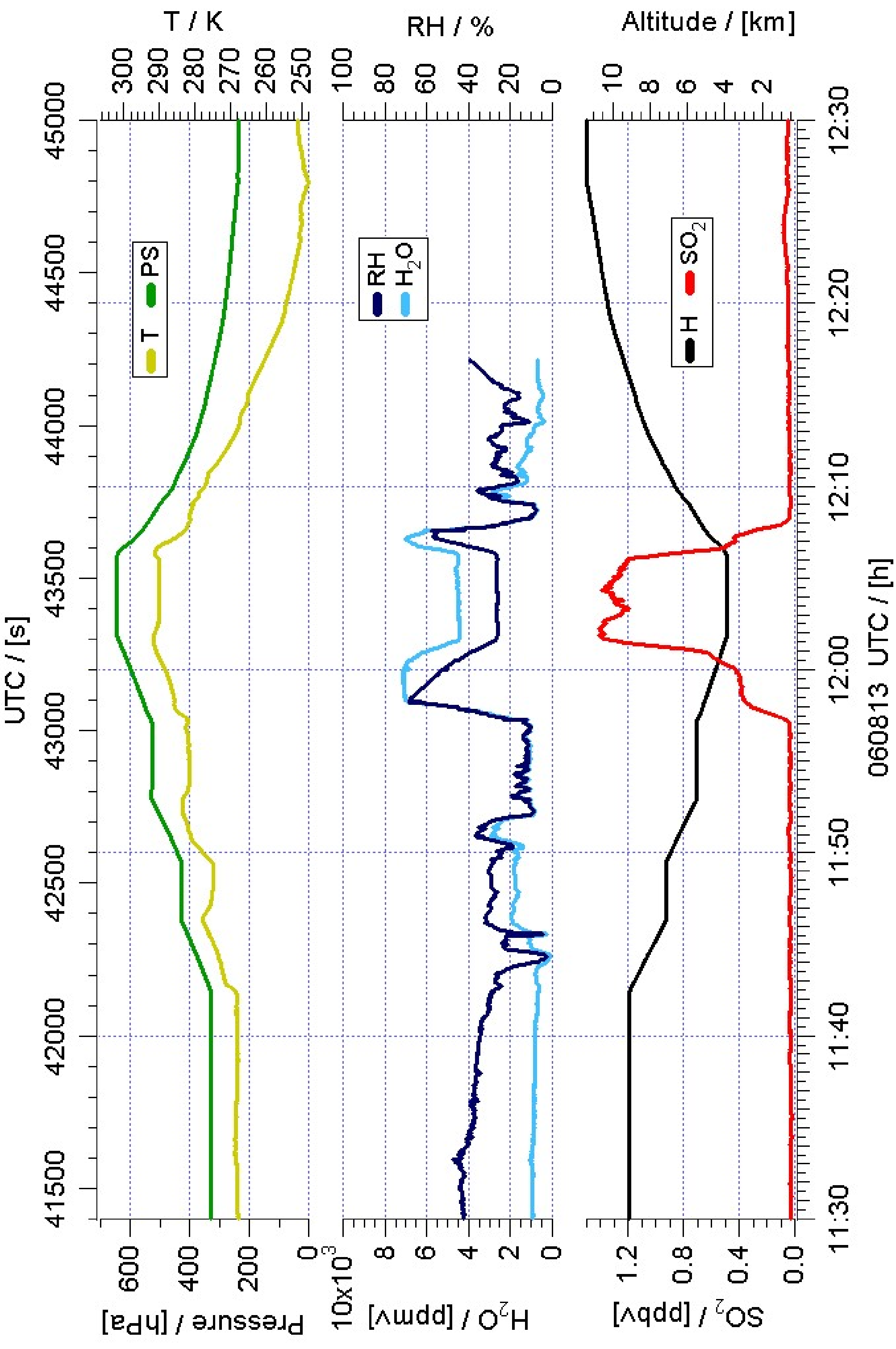

Figure 6.43: AMMA Fifth Local Flight center part. Lowest panel: SO$_2$ and flight altitude, middle panel: water vapor mixing ratio and relative humidity, upper panel: pressure and temperature.

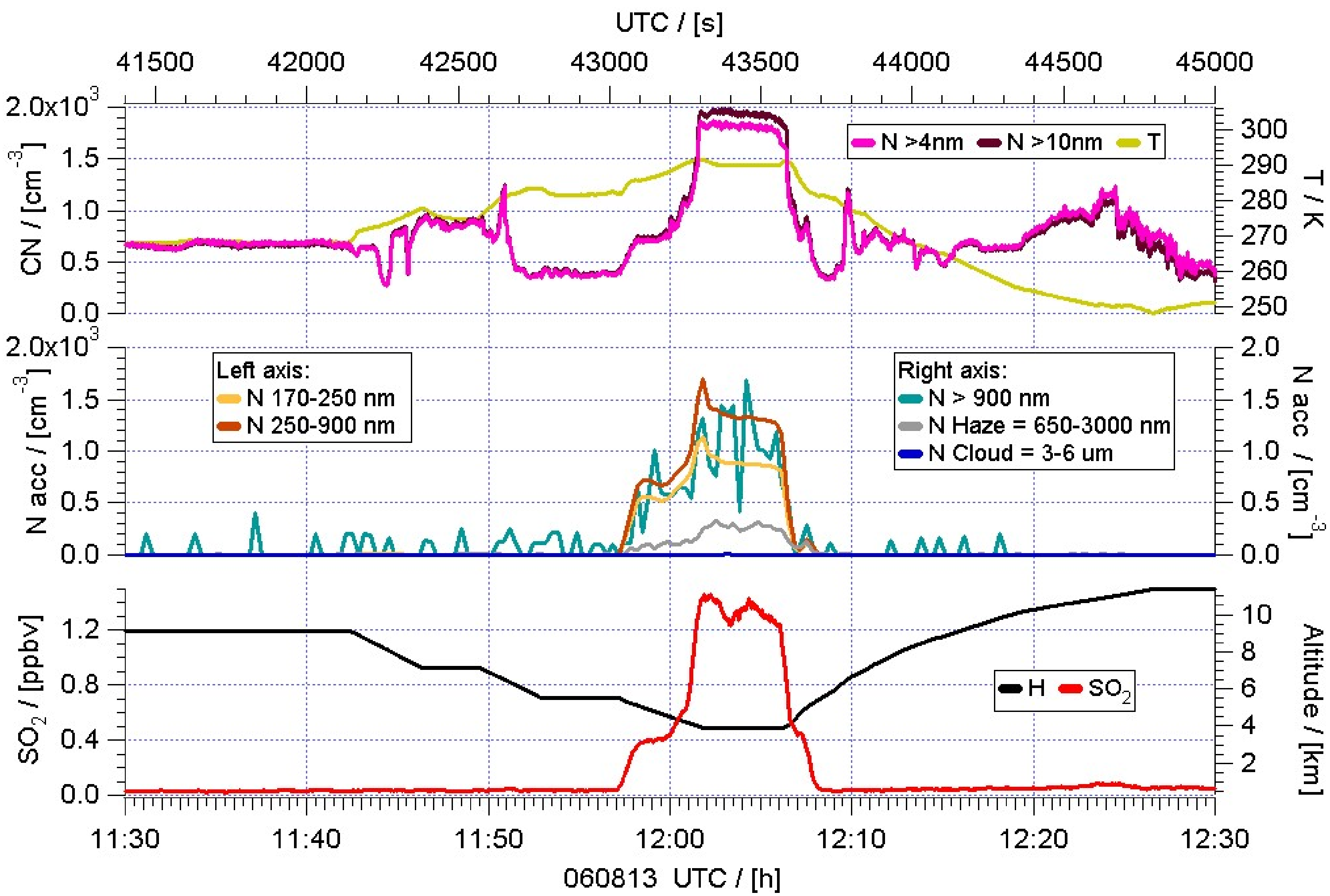

Figure 6.44: AMMA Fifth Local Flight center part. Lowest panel: SO_2 and flight altitude, middle panel and left axis: accumulation mode particles with 170-900 nm in diameter, right axis: accumulation mode particles with diameters >900 nm as well as haze and cloud particles, upper panel: particles with diameters larger than 4 and 10 nm, temperature.

Figure 6.43 shows time sequences of flight altitude, SO_2, water vapor, relative humidity, pressure and temperature. Water vapor starts to increase in the top plume layer below about 5500 m from 1000 to 7000 ppmv but decreases again to about 4500 ppmv in the main plume layer below 4200 m. Relative humidity is about 70% in the top plume layer and only 25% in the main plume layer. The temperature in the plume is with 290 K quite high for that altitude. Typical temperatures near the equator at that altitude are around 280 K [Seinfeld and Pandis, 1998]. The higher temperature might be due to long wave absorption inside the plume by e.g. soot particles.

Figure 6.44 depicts number concentrations N4 and N10 of aerosol particles with diameters larger than 4 and larger than 10 nm. Additionally in the second panel accumulation mode particles with diameters from 170 to 250 nm and from 250 to 900 nm (left axis) and particles with diameters larger than 900 nm, with diameters from 650 nm to 3 μm and from 3 to 6 μm (right axis) are plotted. Taking into account an error of 5%, N10 is identical to N4 which means that all particles had diameters larger than 10 nm, i.e. no nucleation mode particles existed. Even N250-900 (1400 cm^{-3}) is not much smaller than N10 (1900 cm^{-3}) inside the plume, so most particles had diameters larger than 250 nm. Particle concentrations are closely correlated with SO_2. This indicates either a common origin or SO_2 mediated particle formation. Inside this plume the first possibility is much more likely since gaseous H_2SO_4 formed by OH-induced SO_2 conversion would condense onto soot and preexistent aerosol particles rather than forcing nucleation leading to new particles.

Vertical profiles of the measured trace gases further strengthen the upper findings. **Figure 6.45** shows vertical profiles of SO_2, HNO_3, NOy and NO. The SO_2 and NOy profiles measured during descent and ascent are nearly identical. The HNO_3 and NO profiles are different, which was already visible in the time series data. They are higher during the climb out of the plume and hereafter. For HNO_3 this discrepancy may be due to store and release effects in the sampling line of the CIMS instrument. In other words, during interception of HNO_3 rich air some HNO_3 may attach to the inner surface of the sampling line and might be stored temporarily. This may also explain the slow HNO_3 increase during the constant-level flight at 3900 m. Here initially much HNO_3 may be lost by attachment to the sampling line and

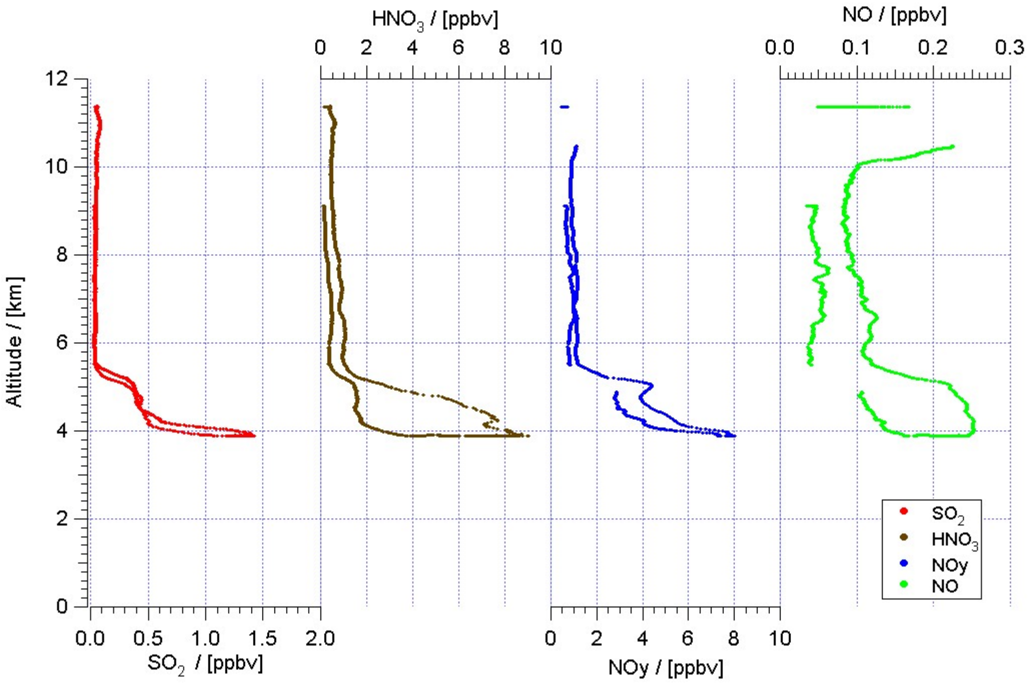

Figure 6.45: Vertical profiles of SO_2, NO, NOy and HNO_3 above and inside the plume.

HNO_3 loss may gradually have become less efficient due to surface HNO_3 saturation. After leaving the HNO_3 rich air the stored HNO_3 may have been released again. If so such a memory effect would lead to an overestimation of atmospheric HNO_3. Hence the descent HNO_3 profile should be more reliable than the ascent profile. By contrast for SO_2 which is much less sticky than HNO_3 a memory effect is not present. For NO such a store and release effect is not known so far but must be considered as one possible explanation of the higher ascent profile as well.

Figure 6.46 depicts vertical profiles of atmospheric mole fractions of SO_2, CO, excess CO_2 (named delta CO_2), ozone (O_3) and formaldehyde (HCHO). The vertical profile of the SO_2 mole fraction started to increase during descent below 5500 m from about 25 pptv to 400 pptv and below about 4200 m to 1400 pptv. Hence the SO_2 mole fraction was almost 100 times larger in the plume compared to the layer above the plume. The CO profile shows a similar behavior as the HNO_3 and NO profile: the mole fraction during ascent is higher than during descent with a maximum value of almost 500 ppbv.

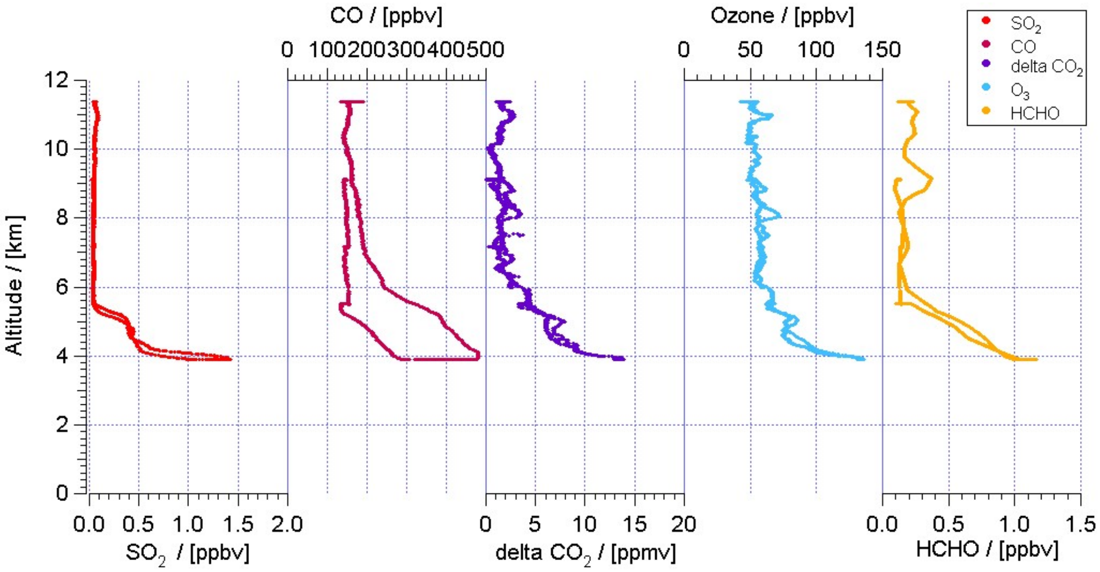

Figure 6.46: Vertical profiles of SO_2, CO, delta CO_2, ozone and formaldehyde above and inside the plume.

The excess CO_2 profile (CO_2 mole fraction minus a background mole fraction of 376 ppmv) exhibits a similar behavior as SO_2. It started to increase markedly during the descent below about 5500 m and finally increased very steeply below about 4200 m to about 14 ppmv. During ascent excess CO_2 decreased again to the atmospheric background value. The HCHO profile increases from a background of 0.2 ppbv to 1.2 ppbv, during ascent and descent behaving similar.

The SO_2 profile and also most of the other profiles show again nicely, that the biomass burning plume had a two-layer structure in the measurement area. The upper less polluted plume layer extended from 5500 to 4200 m and the lower severely polluted plume layer had its top around 4200 m.

In **Figure 6.47** additionally to the SO_2 profile particle profiles are shown: particles with diameters larger than 4 and larger than 10 nm as well as non volatile particles and accumulation mode particles with diameters between 170 and 250 nm and between 250 and 900 nm. The latter is not much smaller than N10 which indicates that most particles had diameters bigger than 250 nm. A fifths panel shows additionally the profiles of haze and cloud particles, which actually means particles with diameters from 650 to 3000 nm and from 3000

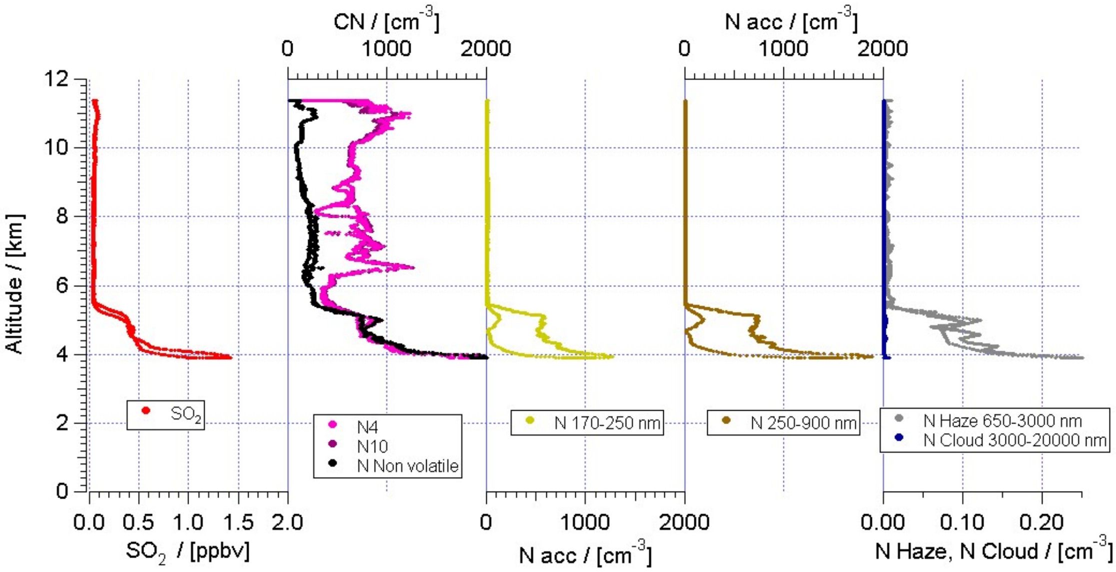

Figure 6.47: Vertical profiles of SO_2, N4, N10 and non volatile particles and accumulation mode particles with diameters between 170 and 250 nm and between 250 and 900 nm, additionally haze and cloud particles which means particles with diameters from 650 to 3000 nm and from 3000 to 20000 nm respectively.

to 20000 nm respectively. Their concentrations are low (<0.3 cm^{-3}). In fact most particles had diameters between 250 and 400 nm, whereas above 650 nm almost no particles have been detected.

Interestingly the fraction of non volatile particles reaches 100% in the plume (no difference between the black curve and the violet curves in **Figure 6.47**). At higher altitudes above 6 km this fraction is much lower (below 30%). This indicates that in the plume approximately 100% of the aerosol particles were soot and dust particles.

Figure 6.48 finally represents the profiles of relative humidity, water vapor and temperature. The top layer was with 70% relative humidity or 7000 ppmv water vapor much more humid than the main layer (30% RH and 4500 ppmv water vapor). The temperature profile shows inversions at both plume layer tops.

6.4.3 Formation of secondary HNO_3 and H_2SO_4

Figure 6.49 shows a simplified reaction scheme of HNO_3 and H_2SO_4 formation and loss in the plume. Pyrogenic NOx (NO + NO_2) undergoes photochemical conversion preferably to

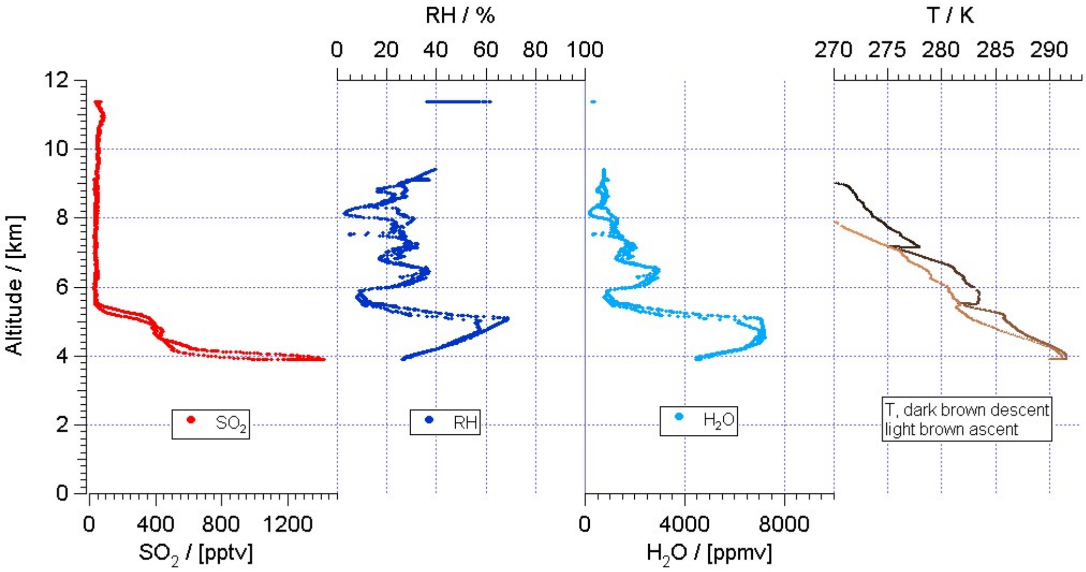

Figure 6.48: Vertical profiles of SO_2, relative humidity, water vapor mole fraction and temperature (temperature at descent is dark brown, ascent light brown).

HNO_3 and PAN (peroxyacetylnitrate, $CH_3C(O)O_2NO_2$) via reactions of NO_2 with OH and $CH_3C(O)O_2$ (peroxyacetyl radical). However PAN formation may be hindered by depletion of the PA radical via reaction with the abundant NO. This may explain the low inferred abundance of PAN compared to HNO_3. NO experiences conversion to NO_2 which photolyzes rapidly (within about 67 seconds) reforming NO. Thereby a rapid equilibrium of NO_2 and NO is established.

The reaction of NO_2 with OH leads to HNO_3. HNO_3 may be removed by cloud processes. These may include dissolution in cloud droplets followed by rain out. In addition dissolved HNO_3 may also react with pyrogenic ammonia (NH_3) which also dissolves in cloud droplets. This would lead to ammonium nitrate (NH_4NO_3) containing particles (mostly coated soot particles) residing after droplet water evaporation. Still another HNO_3 removal process may be uptake by haze particles in plume regions with high relative humidity (RH>70%).

Pyrogenic SO_2 reacts with OH leading to gaseous sulfuric acid, H_2SO_4, which experiences binary (H_2SO_4-H_2O) condensation on aerosols, preferably soot particles. In the plume at 3900 m the lifetime of a gaseous H_2SO_4 molecules with respect to collision with soot was only about 40 seconds, in the top layer about 70 seconds. This was estimated building on the total aerosol surface area density ($0.54{\cdot}10^{-5}$ cm^2/cm^3) inferred from the measured aerosol size distribution. The calculated condensation sink (with Fuchs-Sutugin-Correction) and therefore the inverse H_2SO_4 lifetime was 0.026 s^{-1} in the main layer and 0.015 s^{-1} in the top layer, which delivers the upper H_2SO_4 lifetimes.

The rate coefficient for the NO_2 reaction with OH ($8.9{\cdot}10^{-12}$ cm^3 s^{-1}) is approximately 10 times larger than the rate coefficient for the SO_2 reaction with OH ($9{\cdot}10^{-13}$ cm^3 s^{-1}). A major if not the dominant fraction (at least 50%) of NOx is NO_2. Therefore the OH-induced NOx conversion is at least about 5 times faster than OH-induced SO_2 conversion. The ratio NO/NO_2 is determined by NO conversion to NO_2 (mostly by reactions with ozone and organics) and the rapid photolysis of NO_2 reforming NO. Since O_3 and organics were markedly increased in the plume the abundance ratio NO/NO_2 was probably lowered. Considering NO_2 formation only via reaction of O_3 with NO (rate constant $1.9{\cdot}10^{-14}$ cm^3 s^{-1}) and NO_2 loss

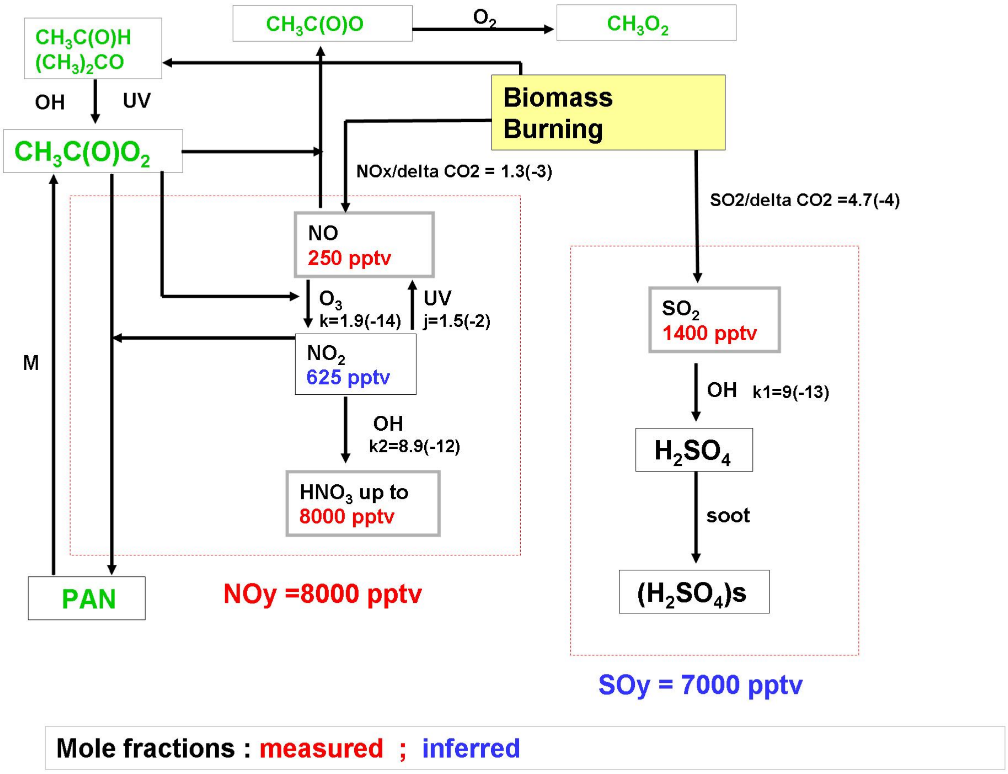

Figure 6.49: Highly simplified reaction scheme of NOy and SOy production and loss processes.

via photolysis (photolysis rate $j=1.5\cdot10^{-2}$ s^{-1}) one obtains an equilibrium ratio NO/NO_2 of about 0.4.

Figure 6.50 shows the molar ratios of SO_2, HNO_3, NO and NOy to CO_2, NOy or delta CO_2 and **Table 6.51** summarizes emission factors of several atmospheric compounds including CO, CO_2, SO_2, NO etc. The factors are given in g species per kg dry matter burned for different types of burning matter. In the following calculations the factors for tropical forest are taken into account. In the main plume layer at 3900 m the measured molar ratio NOy/delta CO_2 is $6\cdot10^{-4}$ and the measured ratio of NO/delta CO_2 is $0.2\cdot10^{-4}$ (view Figure 6.50). The molar emission ratio for tropical forest fires of NOy/delta CO_2 $\approx$ NO/delta CO_2 because NOy is emitted mostly as NO and its value is on average $1.3\cdot10^{-3}$. Hence the measured ratio NO/ delta CO_2 is only about 2% and the ratio NOy/delta CO_2 is only about 46% of the molar emission ratio. This indicates, considering the NO/NO_2 ratio of 0.4, that 93% of the emitted NOx has been converted in the plume and about 54% of the emitted gaseous NOy (emitted mostly as NO) experienced removal from the plume. Our measurements also indicate that at least at the end of the constant-level cruise at 3900 m in the plume most NOy was present as gaseous HNO_3. Therefore it is conceivable that the missing NOy was removed by interaction with clouds or haze. Due to its large solubility in cloud droplets HNO_3 can be removed by rain out. HNO_3 may also react with dissolved pyrogenic NH_3 forming ammonium nitrate as mentioned above. In addition gaseous HNO_3 may also be taken up by soot particles at large relative humidities.

At 3900 m in the plume the measured molar ratio SO_2/delta CO_2 is $1\cdot10^{-4}$. In comparison again the corresponding molar emission ratio for tropical forest fires is about $4.7\cdot10^{-4}$. Hence it seems that about 80% of the pyrogenic SO_2 experienced OH-induced conversion to gaseous H_2SO_4 which very rapidly condenses on aerosols, preferably on soot particles. This would correspond to a gaseous H_2SO_4 mole fraction of 5.6 ppbv or at 290 K and 640 hPa to a number concentration of condensed H_2SO_4 molecules of about $8.96\cdot10^{10}$ cm^{-3}.

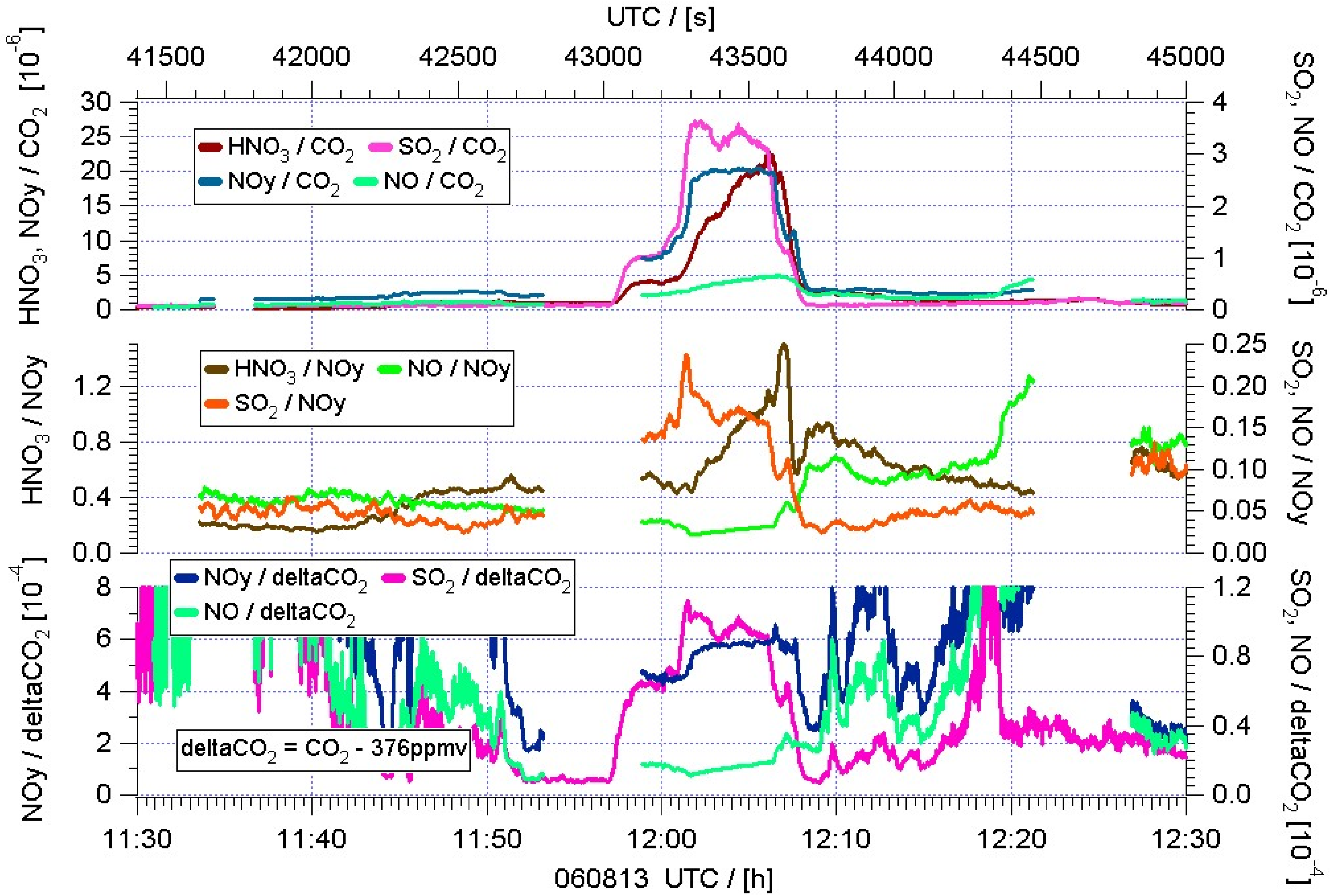

Figure 6.50: AMMA Fifth Local Flight center part. Lowest panel: ratios of several trace gases to delta CO_2, middle panel: ratios of several trace gases to NOy, upper panel: ratios of several trace gases to CO_2.

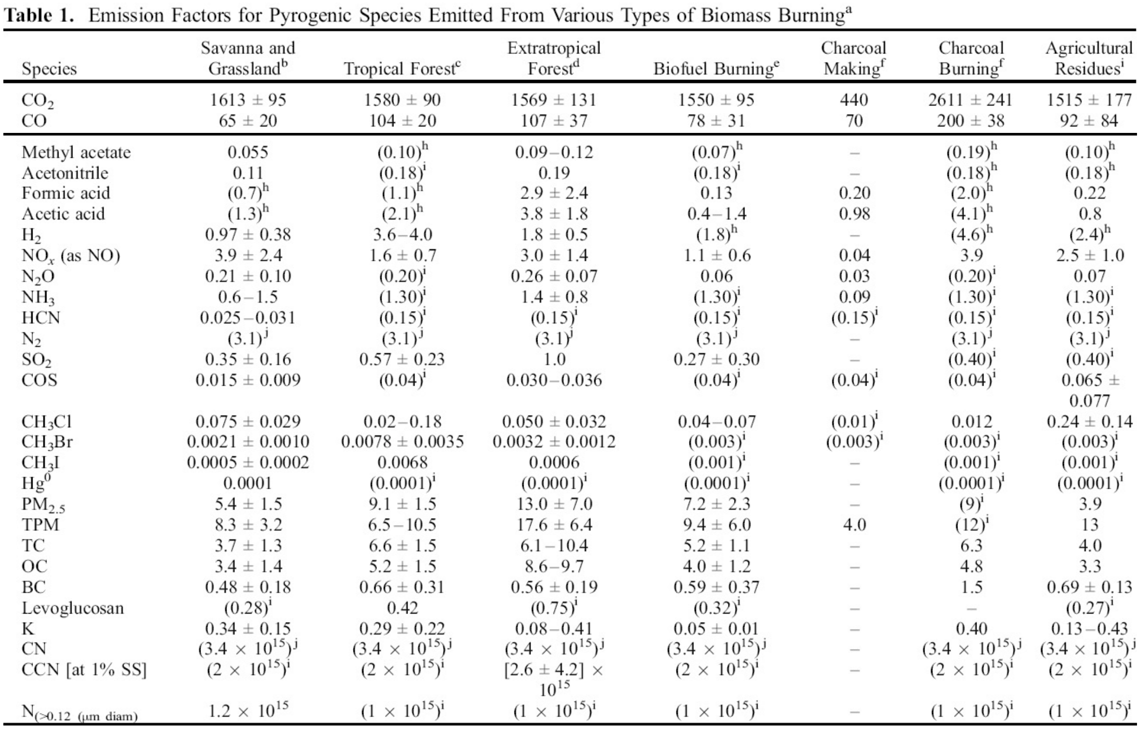

Table 1. Emission Factors for Pyrogenic Species Emitted From Various Types of Biomass Burning^{a}

Species	Savanna and Grassland^{b}	Tropical Forest^{c}	Extratropical Forest^{d}	Biofuel Burning^{e}	Charcoal Making^{f}	Charcoal Burning^{f}	Agricultural Residues^{i}
CO_2	1613 ± 95	1580 ± 90	1569 ± 131	1550 ± 95	440	2611 ± 241	1515 ± 177
CO	65 ± 20	104 ± 20	107 ± 37	78 ± 31	70	200 ± 38	92 ± 84
Methyl acetate	0.055	(0.10)^{h}	0.09–0.12	(0.07)^{h}	–	(0.19)^{h}	(0.10)^{h}
Acetonitrile	0.11	(0.18)^{i}	0.19	(0.18)^{i}	–	(0.18)^{h}	(0.18)^{h}
Formic acid	(0.7)^{h}	(1.1)^{h}	2.9 ± 2.4	0.13	0.20	(2.0)^{h}	0.22
Acetic acid	(1.3)^{h}	(2.1)^{h}	3.8 ± 1.8	0.4–1.4	0.98	(4.1)^{h}	0.8
H_2	0.97 ± 0.38	3.6–4.0	1.8 ± 0.5	(1.8)^{h}	–	(4.6)^{h}	(2.4)^{h}
NO_x (as NO)	3.9 ± 2.4	1.6 ± 0.7	3.0 ± 1.4	1.1 ± 0.6	0.04	3.9	2.5 ± 1.0
N_2O	0.21 ± 0.10	(0.20)^{i}	0.26 ± 0.07	0.06	0.03	(0.20)^{i}	0.07
NH_3	0.6–1.5	(1.30)^{i}	1.4 ± 0.8	(1.30)^{i}	0.09	(1.30)^{i}	(1.30)^{i}
HCN	0.025–0.031	(0.15)^{i}	(0.15)^{i}	(0.15)^{i}	(0.15)^{i}	(0.15)^{i}	(0.15)^{i}
N_2	(3.1)^{j}	(3.1)^{j}	(3.1)^{j}	(3.1)^{j}	–	(3.1)^{j}	(3.1)^{j}
SO_2	0.35 ± 0.16	0.57 ± 0.23	1.0	0.27 ± 0.30	–	(0.40)^{i}	(0.40)^{i}
COS	0.015 ± 0.009	(0.04)^{i}	0.030–0.036	(0.04)^{i}	(0.04)^{i}	(0.04)^{i}	0.065 ± 0.077
CH_3Cl	0.075 ± 0.029	0.02–0.18	0.050 ± 0.032	0.04–0.07	(0.01)^{i}	0.012	0.24 ± 0.14
CH_3Br	0.0021 ± 0.0010	0.0078 ± 0.0035	0.0032 ± 0.0012	(0.003)^{i}	(0.003)^{i}	(0.003)^{i}	(0.003)^{i}
CH_3I	0.0005 ± 0.0002	0.0068	0.0006	(0.001)^{i}	–	(0.001)^{i}	(0.001)^{i}
Hg^0	0.0001	(0.0001)^{i}	(0.0001)^{i}	(0.0001)^{i}	–	(0.0001)^{i}	(0.0001)^{i}
$PM_{2.5}$	5.4 ± 1.5	9.1 ± 1.5	13.0 ± 7.0	7.2 ± 2.3	–	(9)^{i}	3.9
TPM	8.3 ± 3.2	6.5–10.5	17.6 ± 6.4	9.4 ± 6.0	4.0	(12)^{i}	13
TC	3.7 ± 1.3	6.6 ± 1.5	6.1–10.4	5.2 ± 1.1	–	6.3	4.0
OC	3.4 ± 1.4	5.2 ± 1.5	8.6–9.7	4.0 ± 1.2	–	4.8	3.3
BC	0.48 ± 0.18	0.66 ± 0.31	0.56 ± 0.19	0.59 ± 0.37	–	1.5	0.69 ± 0.13
Levoglucosan	(0.28)^{i}	0.42	(0.75)^{i}	(0.32)^{i}	–	–	(0.27)^{i}
K	0.34 ± 0.15	0.29 ± 0.22	0.08–0.41	0.05 ± 0.01	–	0.40	0.13–0.43
CN	$(3.4 \times 10^{15})^{j}$	$(3.4 \times 10^{15})^{j}$	$(3.4 \times 10^{15})^{j}$	$(3.4 \times 10^{15})^{j}$	–	$(3.4 \times 10^{15})^{j}$	$(3.4 \times 10^{15})^{j}$
CCN [at 1% SS]	$(2 \times 10^{15})^{i}$	$(2 \times 10^{15})^{i}$	$[2.6 \pm 4.2] \times 10^{15}$	$(2 \times 10^{15})^{i}$	–	$(2 \times 10^{15})^{i}$	$(2 \times 10^{15})^{i}$
$N_{(>0.12\ (\mu m\ diam)}$	1.2×10^{15}	$(1 \times 10^{15})^{i}$	$(1 \times 10^{15})^{i}$	$(1 \times 10^{15})^{i}$	–	$(1 \times 10^{15})^{i}$	$(1 \times 10^{15})^{i}$

Figure 6.51: Biomass burning emission factors of several atmospheric compounds in g species per kg dry matter burned. (Table from [Andreae and Merlet, 2001]).

The OH concentration in the plume is difficult to predict. For cloud-free conditions the noon-time OH concentration in the atmosphere just above the plume is expected to be about $7{\cdot}10^6$ cm^{-3} and the diurnally averaged concentration OH_{av} is about $1{\cdot}10^6$ cm^{-3} [Logan et al., 1981]. For this OH_{av} one would obtain average half-lives for NOx and SO_2 of about 1.4 and 8 days respectively (view also section 2.1.2). Here a typical $NO_2/NO=2$ was assumed. Considering a plume age of 4 days the above NOx and SO_2 half-lives lead to $NOx(4)/NOx(0)\approx0.15$ and $SO_2(4)/SO_2(0)\approx0.75$. This would mean that only 85% of the initial NOx and only 25% of the initial SO_2 have been converted to HNO_3 and H_2SO_4. Consequently from the upper findings that about 93% of the NOx and 80% of H_2SO_4 must have been converted, follows that the OH concentration in the plume must be higher by a factor of ≈3 compared to the average value. This seems reasonable as the ozone mole fraction in the main layer (135 ppbv), which determines ozone formation, also exceeds the background (50 ppbv) by a factor of 2.7.

From the preceding discussion emerges the following picture of HNO_3 and H_2SO_4 formation in the plume. During the about 4 days travel of the plume from the fire region to the measurement site about 93% of the pyrogenic NOx experienced OH-induced conversion to gaseous HNO_3. About 46% of the HNO_3 remained in the gas-phase. The remaining 54% of the gaseous HNO_3 were removed by interaction with clouds or haze.

About 80% of the pyrogenic SO_2 experienced OH-induced conversion to gaseous sulphuric acid (calculated from the measured and emission factor ratio). The latter probably condensed very rapidly on the soot particles in the plume. The number concentration of condensed H_2SO_4 molecules is about $8.96 \cdot 10^{10}$ cm^{-3}. Considering a total aerosol surface area density of $0.54 \cdot 10^{-5}$ cm^2/cm^3 the above number of condensed H_2SO_4 plus 5 H_2O molecules associated with each H_2SO_4 molecule one obtains an H_2SO_4-H_2O coating of soot particles of about 32 monolayer on average (assuming a H_2SO_4-H_2O cluster diameter of 5 Å).

As the plume ages further the remaining 20% of the pyrogenic SO_2 will also experience gas-phase conversion to gaseous H_2SO_4 or liquid phase-conversion to sulphate. If so the H_2SO_4-H_2O coating of soot particles will further increase to about 40 monolayer. The uptake by soot of highly hydrophilic H_2SO_4 and eventually also HNO_3 tends to increase the hygroscopicity of soot. In other words this uptake increases the potential of a soot particle to become a cloud condensation nucleus (CCN). The more hygroscopic material present on the surface of a soot particle the lower the water vapor supersaturation required to activate a soot particle to become a CCN.

Additionally to this analyses a model simulation with AEROFOR is now planned, investigating formation and especially growth of secondary aerosol particles in the plume. The model results will be discussed thoroughly together with the upper data in the paper [Fiedler et al., 2008], which is in preparation.

Chapter 7

Comparison of Measured SO_2 with ECHAM-4 Model Results

The atmospheric general circulation model ECHAM is based on a numerical model developed by the European Center for Medium Range Weather Forecast (ECMWF). The name ECHAM is a combination of the EC from ECMWF and HAM from Hamburg, because ECHAM has been developed by the Max Planck Institute for Meteorology in Hamburg and the University of Hamburg. The most recent and well tested model development stage is ECHAM-4. The detailed model description of the ECHAM-4 version can be found in [Roeckner, 1996]. The ECHAM version used here includes cloud microphysics and an aerosol mass module [Lohmann et al., 2004].

In the applied configuration the model has a horizontal resolution of 3.75° x 3.75° at the ground level and up to 19 non-equidistant vertical layers, with the highest resolution in the boundary layer and with the top layer around 10 hPa (30 km).

Basic prognostic variables are vorticity, divergence of the wind field, surface pressure, temperature, water vapor, cloud water and optional tracer mixing ratios.

Time integration of the model equations is calculated with a time step of 30 min. The radiation scheme considers water vapor, ozone, CO_2, N_2O, CH_4, 16 CFCs, aerosols and clouds. Convection is parameterized. The cloud scheme considers cloud liquid water, cloud ice, the number concentrations of cloud droplets and ice crystals as prognostic variables.

Transport, dry and wet deposition and chemical interactions of certain trace constituents are calculated online as well in ECHAM-4. Therefore the standard ECHAM version is e.g.

coupled to a sulfur chemistry module. This sulfur module has been originally developed by [Feichter et al., 1996]. The module treats three sulfur species as prognostic variables: the gases dimethyl sulfide (DMS) and sulfur dioxide (SO_2) and sulfate (SO_4^{2-}) as aerosol. Advective, Convective and diffusive transport of these species are considered. The dry deposition flux is assumed to be proportional to the concentrations at the ground and to a prescribed deposition velocity. Precipitation scavenging of SO_2 and SO_4^{2-} is calculated explicitly.

Concerning DMS and SO_2 in the gas phase, the oxidation by OH is considered during daytime. At night, the reaction of DMS with nitrate is considered, but with the assumption of only one end product, namely SO_2. Dissolution of SO_2 within cloud water is calculated according to Henry's law. Moreover, in the aqueous phase, the oxidation of SO_2 by hydrogenperoxide (H_2O_2) and ozone (O_3) is taken into account.

As sources both natural and anthropogenic SO_2 emissions are considered, from biological sources and volcanoes and likewise from biomass burning, fossil fuel use and industry. At this point it is important, that all biogenic emissions from the ocean, soil or plants are assumed to occur as DMS, whereas all volcanic or anthropogenic emissions are assumed to occur as SO_2. For a more explicit description of the treatment of the sulfur cycle in ECHAM, the reader is referred to [Feichter et al., 1996, Feichter et al., 1997].

A detailed description of the model version employed by the DLR can be found in [Lauer et al., 2005, Lauer and Hendricks, 2006]. The model version which is explained in the mentioned papers has been actualized by emissions of aerosol and precursors of the year 2000 according to [Dentener et al., 2006] and a coarse particle mode (sea salt and dust particles) has been added. For the simulations analyzed here the model was run in a quasi-equilibrium mode fore a 10-year time period (see [Lauer and Hendricks, 2006]). Concerning convection e.g. that means, that not the actual existing convection is taken into account, but only a 10-year mean convection one would expect in that region at that time of the year.

Importantly, such an extensive model needs to be validated with measurement data, to check, if the modelled trace gas concentrations or other values are estimated correctly. So our SO_2 measurements can be of great help for a validation of the sulfur cycle module in ECHAM. So far ECHAM model results for SO_2 only exist for former ECHAM versions (e.g. ECHAM-3 [Feichter et al., 1996]) or for meridional and annually averaged cross sections [Lohmann et al., 2001]. Therefore a first comparison of SO_2 profiles calculated with ECHAM-4 and our measured profiles have been made and the results can be seen in **Figures 7.1**.

In **Figure 7.1**, left side, SO_2 mole fraction profiles of the 3 tropical measurement regions are depicted, TROCCINOX in the upper panel, SCOUT in the middle and AMMA in the lower panel. In red the measured data with its 25/75% percentile environment is plotted, in green the ECHAM mean, in blue the ECHAM median and ECHAM the 25/75% percentiles. The broken orange vertical line always marks the SO_2 measurement detection limit, which was slightly different for each campaign (13-33 pptv).

Obviously, the emissions at the ground and their dispersion seem to be estimated quite well by the model. Also the first decline of the mole fraction in the boundary layer up to an altitude of approximately 2 km fits the measurements. But, with increasing altitude, the modelled mole fractions decrease much more in the free troposphere than the measured mole fractions show. For SCOUT the deviation between model and measurement reaches almost a factor of 100 in the middle troposphere. This discrepancy can have several reasons. There might be either an overestimation of the free tropospheric sinks of SO_2 (e.g. SO_2 removal by cloud processes) or the vertical transport of SO_2 is underestimated. Nevertheless, the modelled upper tropospheric mole fraction of TROCCINOX again reproduces quite well the measurements, probably due to the impact of deep convection. Maybe the convective influence in Brazil was more dominantly treated in the model compared to the other places because of the central continental site in Brazil, where the profiles were taken. For SCOUT and AMMA both airports were closer to the Ocean coast, which will probably mean less convective influence being considered in the model.

Figure 7.1, right side, presents similar graphs, but for the INTEX campaign. Here it is interesting that the modelled SO_2 emission values at the ground level of OP and Santiago already differ a lot from the measurements, they are up to a factor of 10 times higher. The reason in this case could be the horizontal resolution of $3.75° \times 3.75°$. In this way strong European pollution sources even farther away from the measurement site might be taken

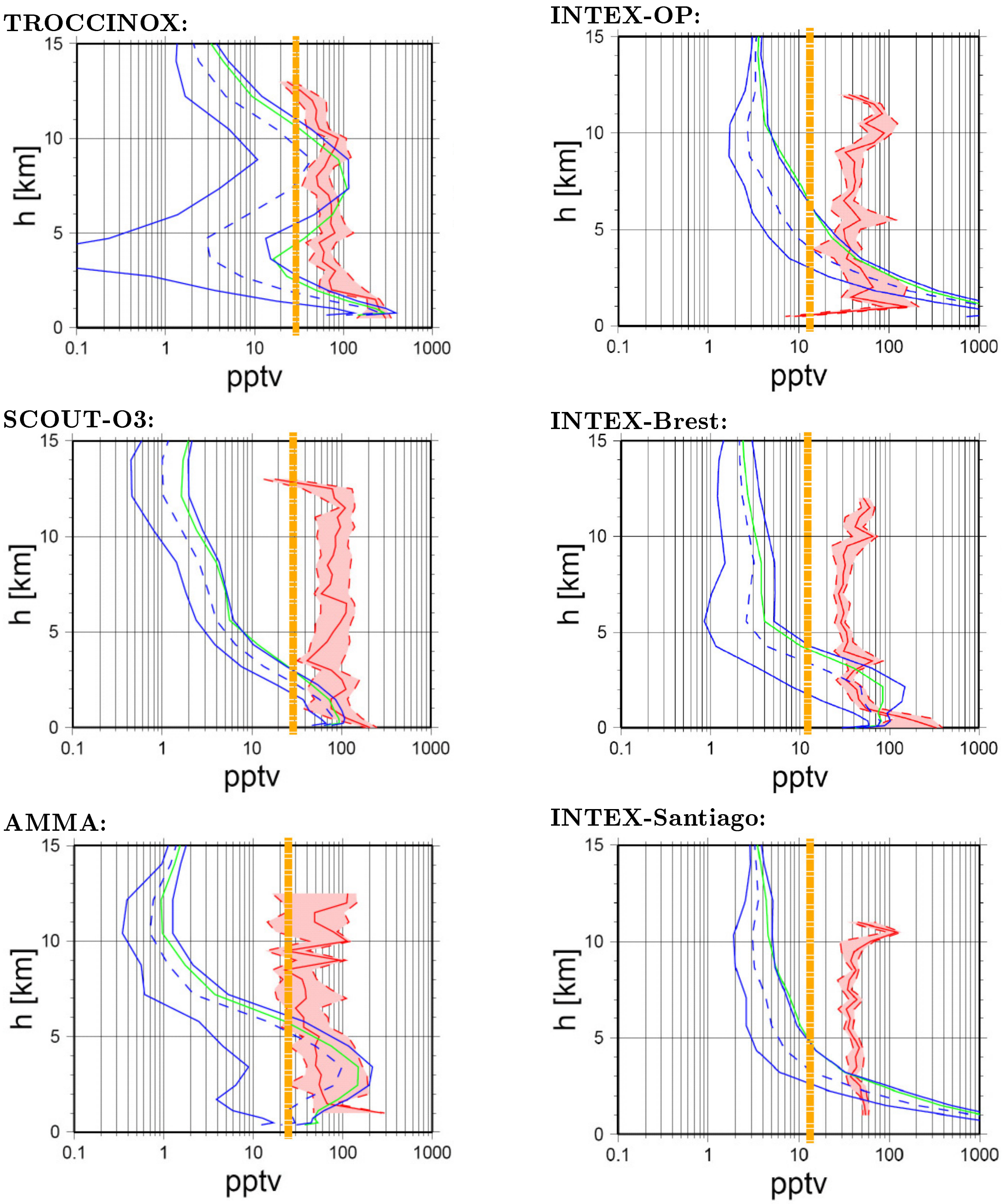
TROCCINOX:

INTEX-OP:

SCOUT-O3:

INTEX-Brest:

AMMA:

INTEX-Santiago:

Figure 7.1: Comparison of modelled SO_2 profiles (monthly averages) with our tropical (left side) and European (right side) measurements. Left side upper panel: TROCCINOX, middle panel: SCOUT, lower panel: AMMA. Right side upper panel: INTEX Oberpfaffenhofen, middle panel: INTEX Brest, lower panel: INTEX Santiago. In red the measured median and shaded the 25/75% percentile environment, broken blue lines the ECHAM median, green line the ECHAM mean and blue line the ECHAM 25/75% percentile environment. The vertical broken line marks the SO_2 measurement detection limit. (ECHAM calculations by V. Aquila, DLR).

into account, Brest might be a more remote area in that sense. In the middle troposphere the model nevertheless again strongly underestimates the measurement data. In the upper troposphere an increase of the mole fraction is not as pronounced as in the tropics, possibly due to weaker or no convection.

It has to be kept in mind as well, that the modelled SO_2 always is a monthly mean calculated from the 10 modelled years whereas our measurements were the mean result of 5-10 flights over a time scale of several days or weeks usually. Therefore in the measured profiles special pollution events will be probably more considered than in the model, even if major pollution events as e.g. the AMMA biomass burning plume data were not taken into account when calculating the mean and median profiles of the measurements.

Evidently, general circulation modelling of SO_2 is a very complex matter. The more variables one takes into account the more possibilities one has for discrepancies between model and measurement. And ECHAM is one of the most complex existing climate models. Nevertheless, this is a good example, how important actual measurements are to validate models and of course to assess SO_2 related aerosol particle processes which have a strong impact on climate. Still, the in our cases modelled upper tropospheric SO_2 seems generally to low to mediate new particle formation via H_2SO_4 /H_2O (binary) nucleation and new particle growth by H_2SO_4 /H_2O condensation. This is in conflict with the in situ measurements of upper tropospheric particles which often indicate the presence of small particles that must have been formed locally most likely by binary nucleation (see chapter 6). By contrast the measured SO_2 is mostly large enough to allow upper tropospheric new particle formation by binary nucleation.

Several ECHAM-4 comparison studies have already been done, not for SO_2 but concerning sulfate, black carbon and total aerosol. In those cases the agreement between model and measurements was quite fine, e.g. with [Schwarz, 2006, Dibb et al., 1998, Dibb et al., 2000]. A possible explanation for our results now could be that the SO_2 in the model is transformed quite early at low altitudes into sulfate aerosol, which then nevertheless can be transported far up into the upper troposphere, lower stratosphere (UTLS) so that the aerosol concentrations again fit to measurements. Also nucleation has been modelled as a typical feature of the

UTLS, e.g. [Lauer and Hendricks, 2006]. Hence the SO_2 lifetime seems to be too short somewhere on the way up, but this point needs to be analyzed more clearly by the modelers.

This was a first comparison of the DLR ECHAM-4 version with SO_2 measurements. A more detailed analysis of the discrepancies will still follow and also a comparison of the measurements to the newest ECHAM version ECHAM-5 is planned.

Chapter 8

Conclusions and Perspectives

In this work aircraft based measurements of atmospheric sulfur dioxide, SO_2, have been carried out during four campaigns in South America (TROCCINOX), Australia (SCOUT-O3), Europe (INTEX/MEGAPLUME) and Africa (AMMA). The altitude range of the measurements was 0-12 km.

The measurement method was chemical ionization mass spectrometry (CIMS) with permanent online isotopically labelled calibration. The method has been described thoroughly and the measured data has been presented. Next, the mean and median data of the different regions have been compared in general and typical SO_2 polluted air mass situations have been described. Hereby it was found that the mean upper tropospheric SO_2 mole fractions in the tropics (70-90 pptv) were significantly higher than the European mole fractions (30-40 pptv), which is probably a result of deep convective transport in the tropics. A detailed analysis of four SO_2 pollution plume cases followed. The SO_2 measurements of the different plume events have been analyzed in the light of simultaneously measured trace gas, particle and meteorological data. FLEXPART or HYSPLIT air trajectory analyses have been employed for a determination of the air mass origin and thus for a determination of the pollution origin. Further going evaluations, e.g. with the aerosol nucleation model AEROFOR, have been made.

Long-range transport of middle American SO_2 pollution over the Atlantic Ocean (SCOUT) as well as SO_2 pollution from East Asia (INTEX) have been detected. SO_2 has a half-life with respect to the reaction with OH of about 8 days in the upper troposphere. This means, if the SO_2 is lifted up fast and without much loss due to e.g. cloud processes, that long range transport is very likely. Moreover, as the AEROFOR model shows, the measured SO_2 mole fractions are often sufficient to explain new particle formation and successive growth up to cloud condensation nuclei size. Therefore the detected SO_2 might have even an impact on climate.

During TROCCINOX SO_2 pollution from copper smelters/volcanoes in southern Peru/ northern Chile has been found at the measurement site over Brazil. Again the measured concentrations are sufficient for new particle formation.

The AMMA campaign in Africa delivered one example of biomass burning pollution. High mole fractions have been measured in all trace gases. Emission factors and molar ratios of several compounds including SO_2 HNO_3, NO and NOy have been discussed. An estimation of a H_2SO_4 concentration derived from the measured SO_2 mole fraction lead to a probable coating of soot aerosol particles with about 32 monolayers of H_2SO_4-H_2O clusters. The uptake of H_2SO_4 and HNO_3 by soot particles tends to increase the hygroscopicity of the soot. This increases the probability of a soot particle to become a cloud condensation nucleus, which again means an impact on climate.

For the future several other measurement campaigns are planned: an aircraft campaign in Greenland with the objective to investigate pollution transport from North America to the Arctic region, a measurement campaign at MAN Nuremberg, to investigate Diesel engine exhaust, a campaign at the CERN, Genf, to investigate ion-induced nucleation and a campaign to study chemical reactions that occur during lightnings at the Technical University of Munich.

For all these campaigns SO_2 and also H_2SO_4 measurements are of great importance. Therefore a mass spectrometer system for H_2SO_4 measurements on aircrafts has to be implemented. So far, our H_2SO_4 measurement system was in use only at the ground. Further developments of the measurement system are conceivable and desired: a calibration method for HNO_3 (this will be already discussed in [Nau, 2008]), the construction of a measurement system for OH, NH_3, PAN and all this as small as possible for the employment during aircraft missions.

The DLR will soon start missions using a new research aircraft called HALO (High Altitude and Long Range Aircraft). On this plane the new measurement systems shall already be implemented.

So there will be obviously enough to do in the area of atmospheric mass spectrometric trace gas measurements in the future.

Appendix A

Data Compilation

A.1 TROCCINOX

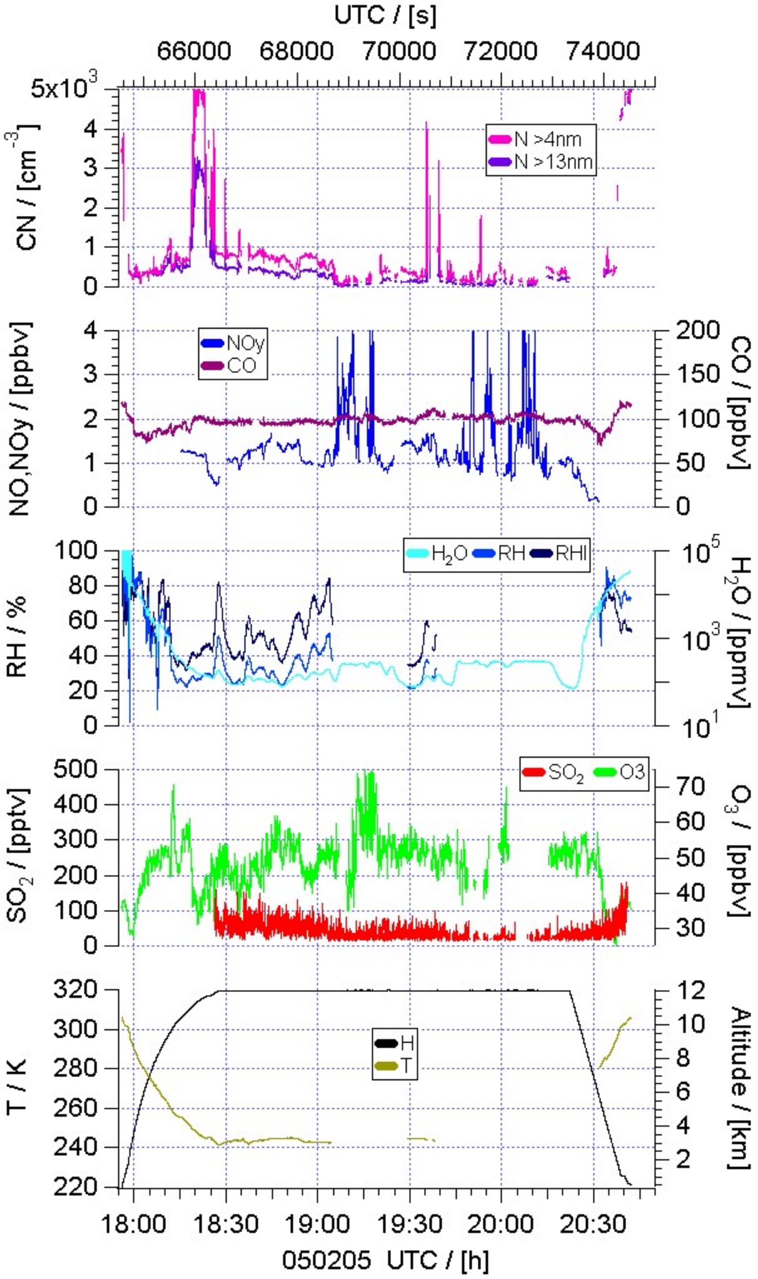

Figure A.1: TROCCINOX First Local Flight: Convective Systems.

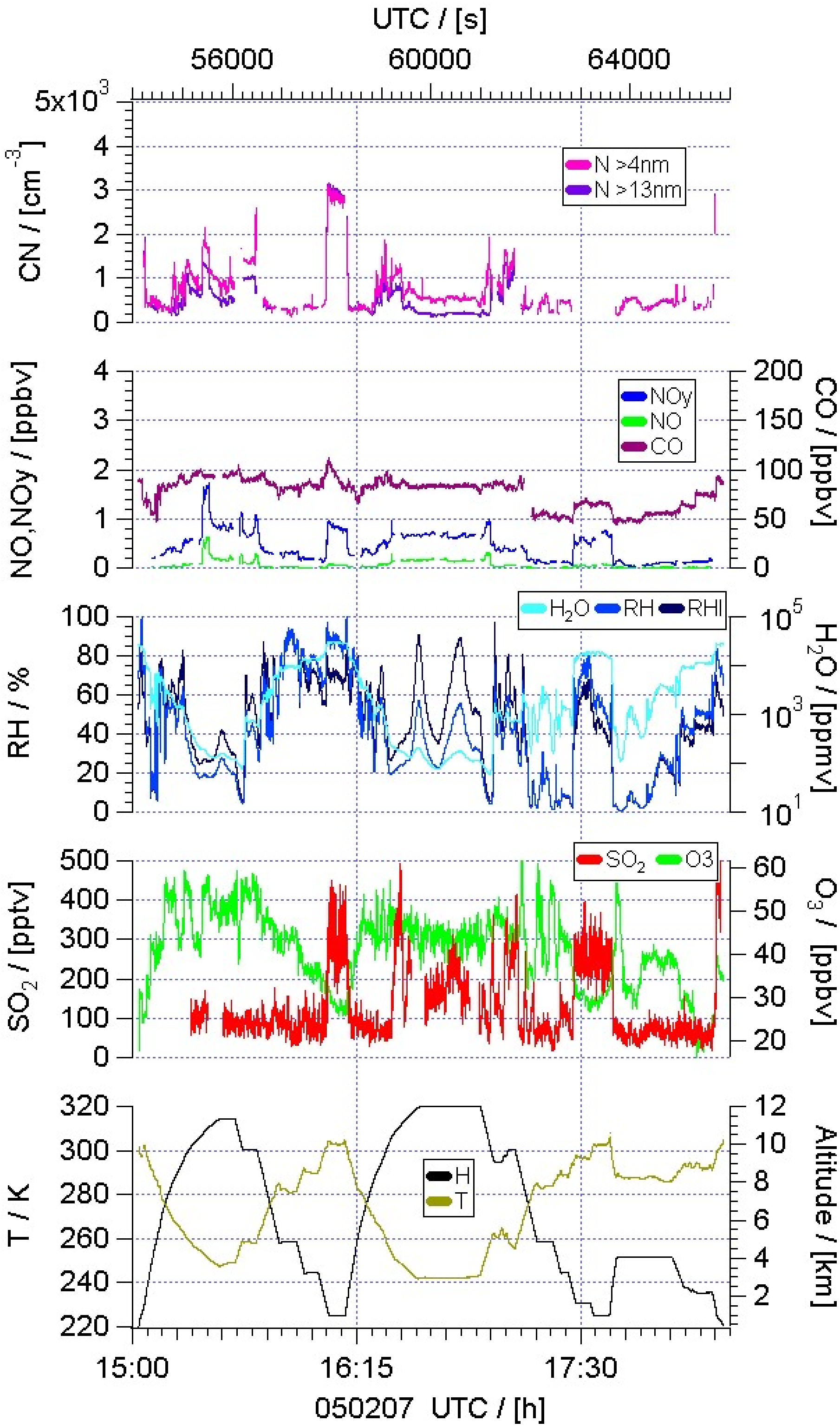

Figure A.2: TROCCINOX Second Local Flight: NW and SE Profiles.

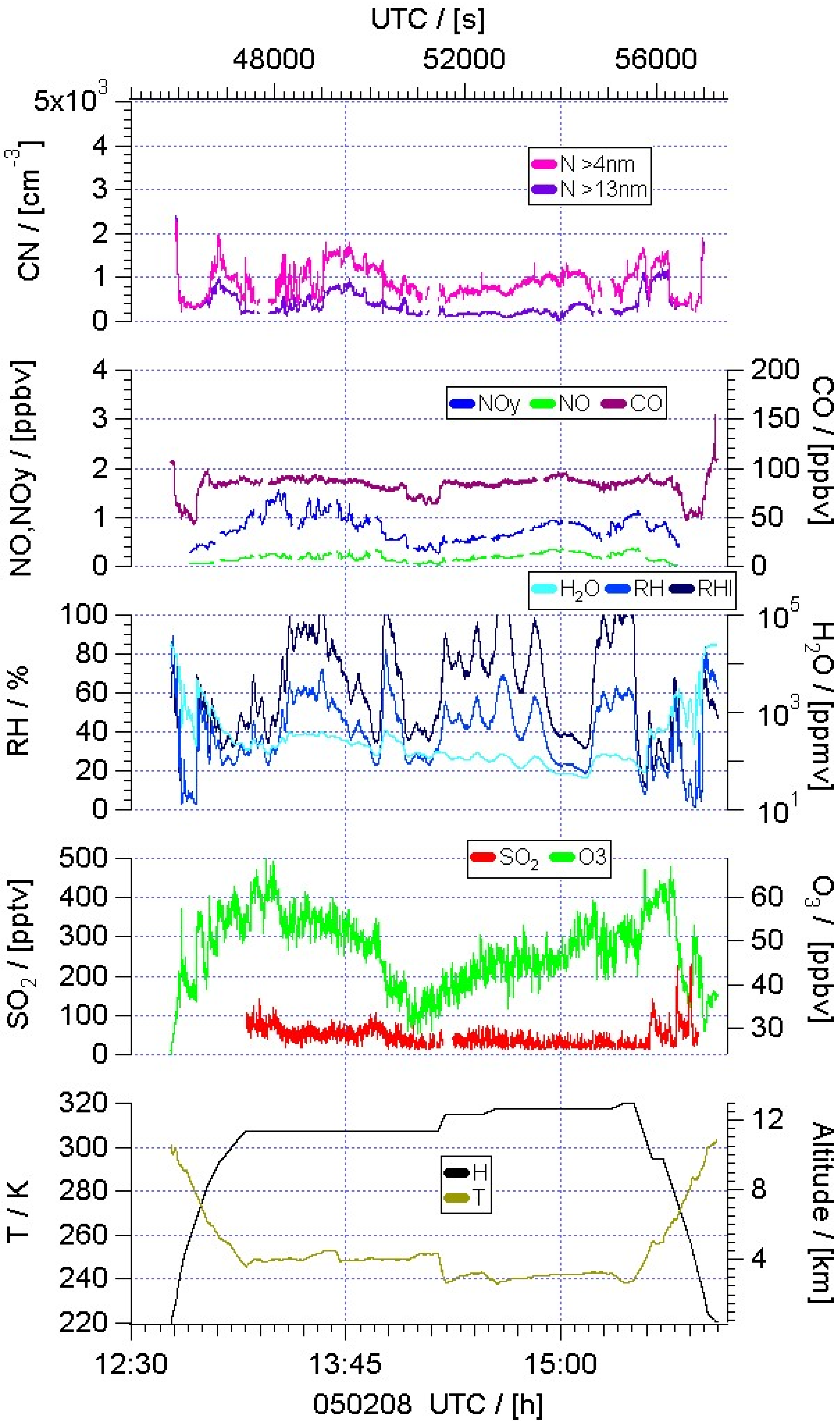

Figure A.3: TROCCINOX Third Local Flight: W-E survey.

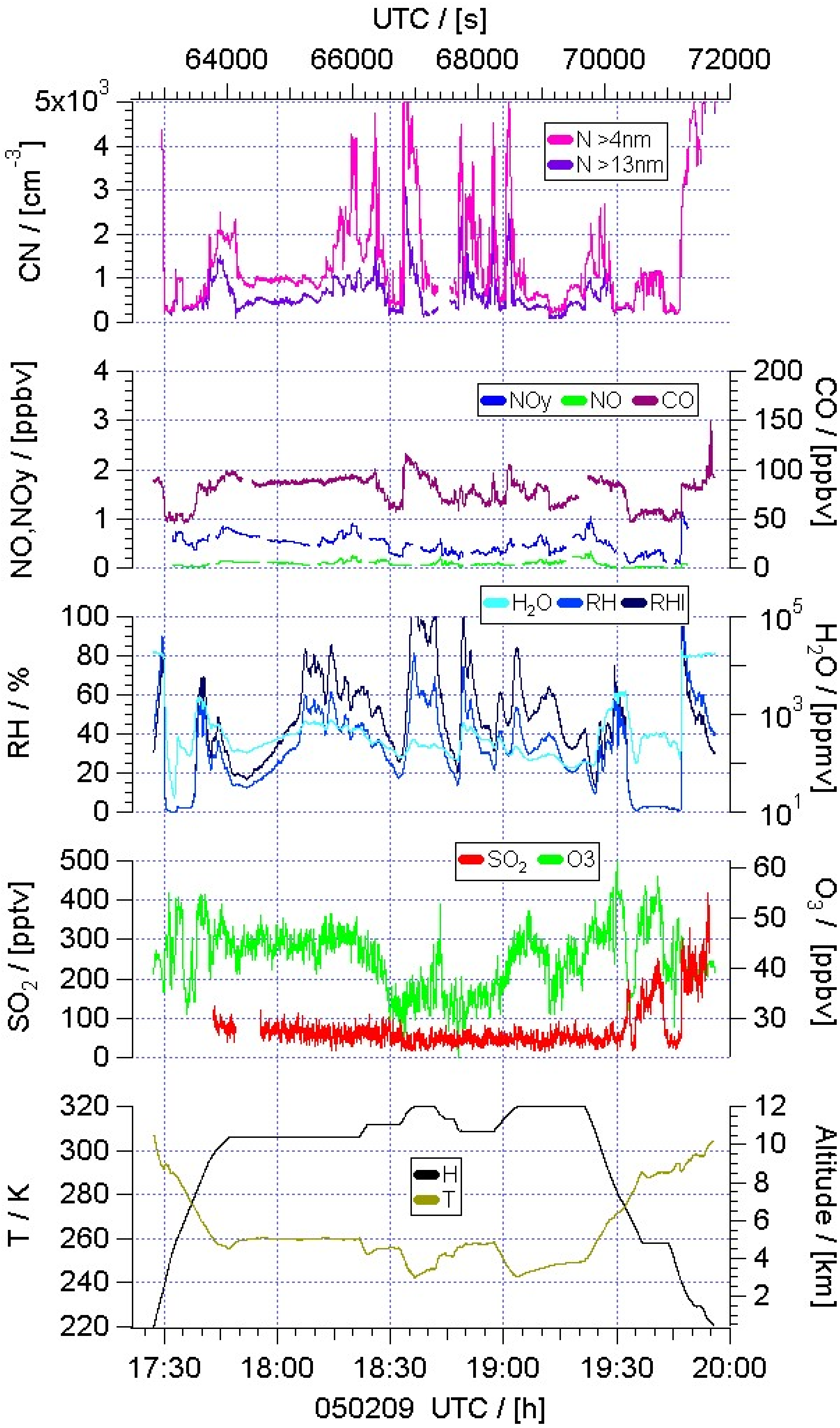

Figure A.4: TROCCINOX Fourth Local Flight: South survey.

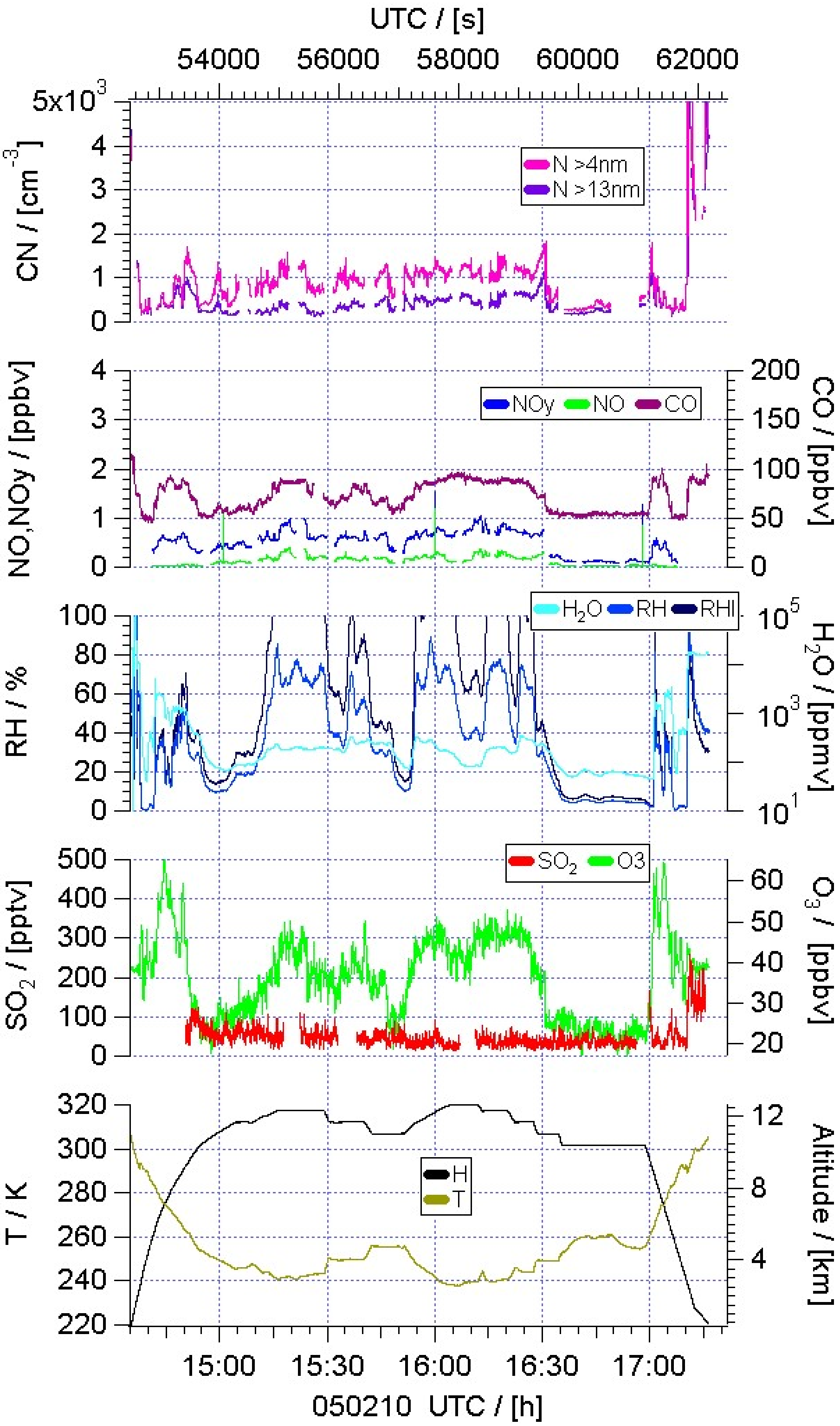

Figure A.5: TROCCINOX Fifth Local Flight: Stacked levels.

A.2 SCOUT-O3

A.2.1 Transfer

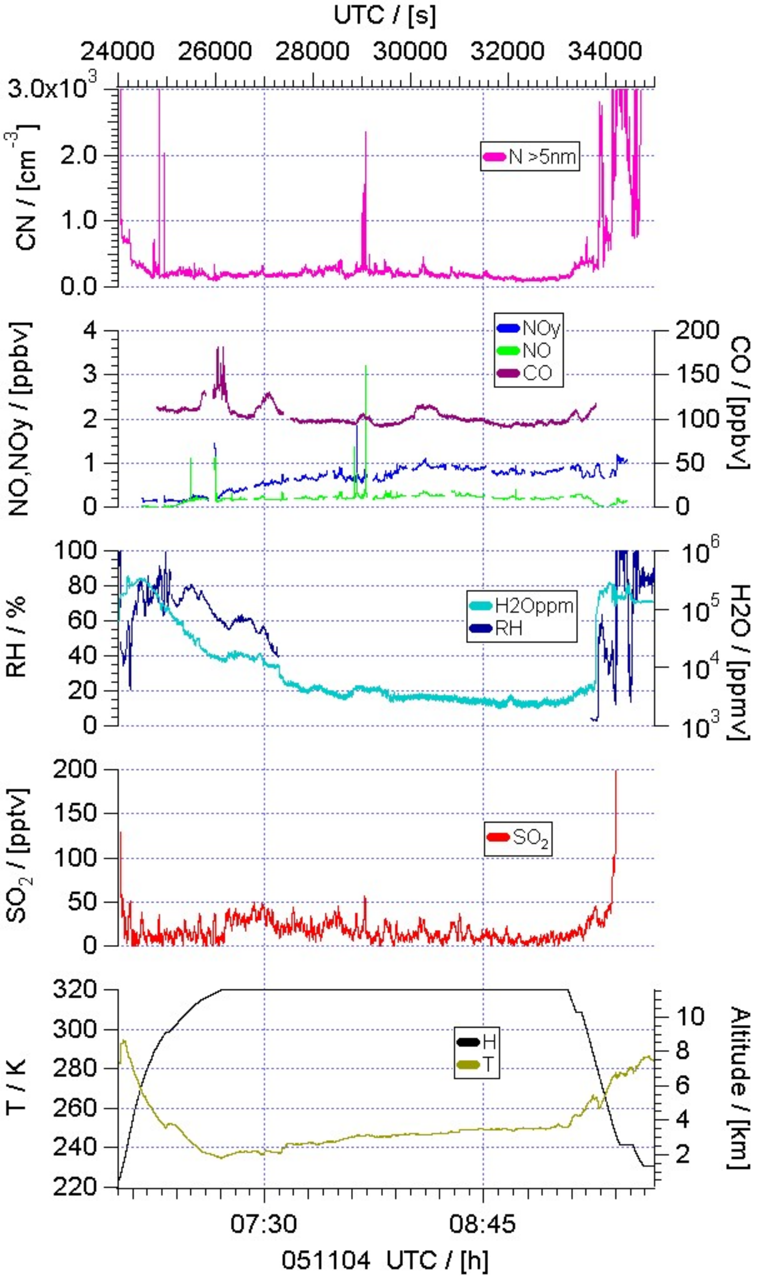

Figure A.6: SCOUT-O3 First Transfer Flight: Oberpfaffenhofen-Larnaca.

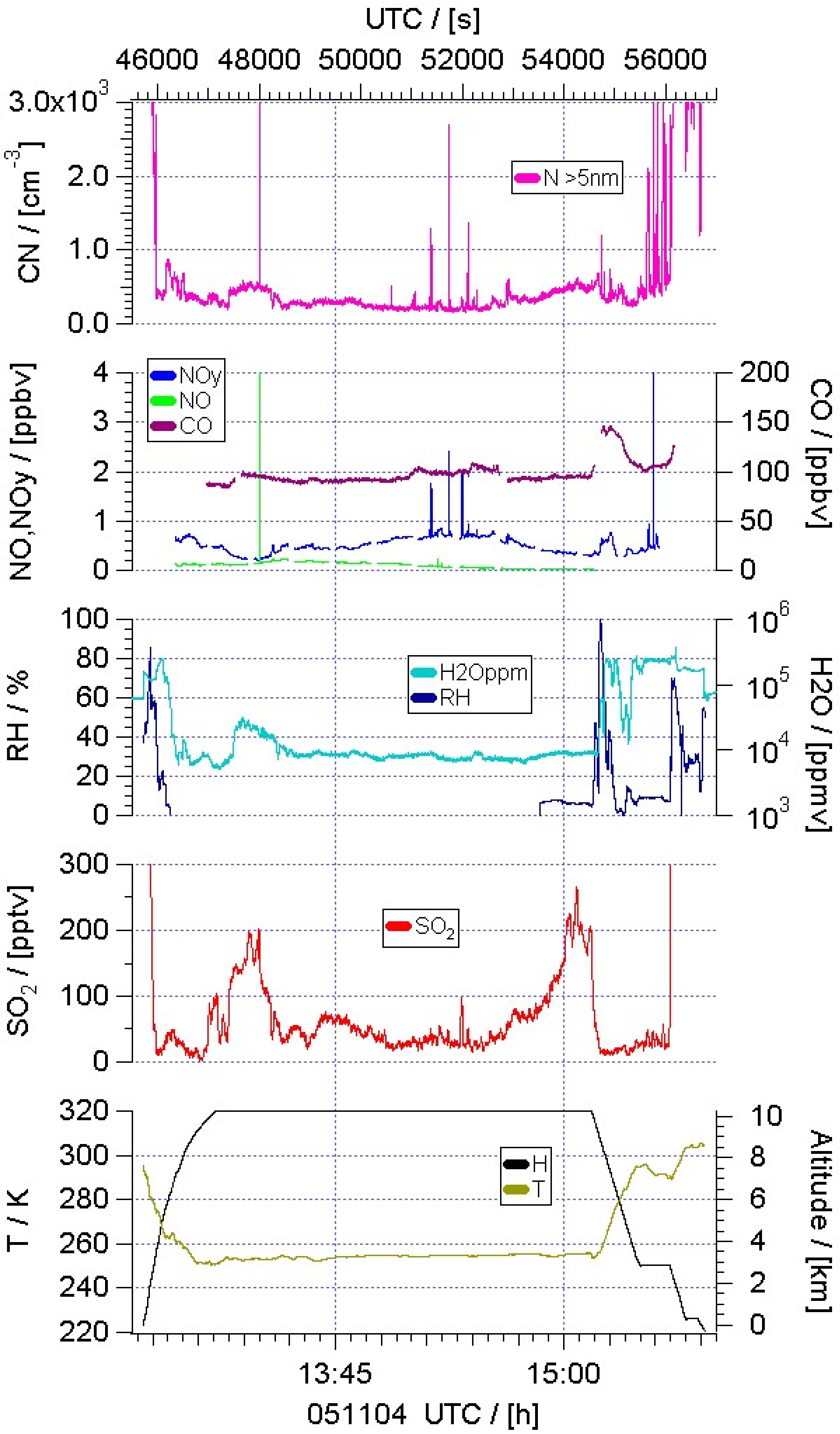

Figure A.7: SCOUT-O3 Second Transfer Flight: Larnaca-Dubai.

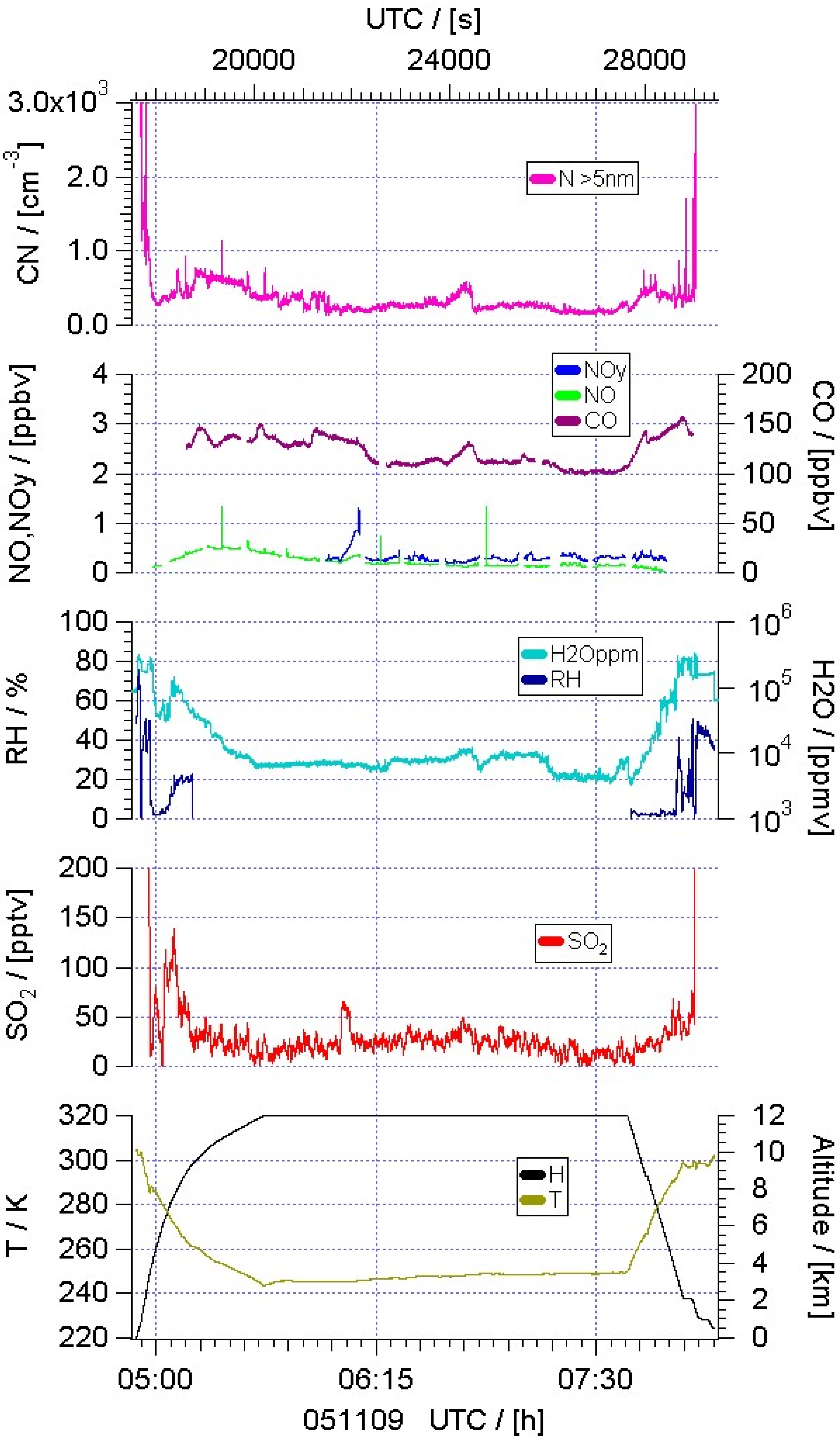

Figure A.8: SCOUT-O3 Third Transfer Flight: Dubai-Hyderabad.

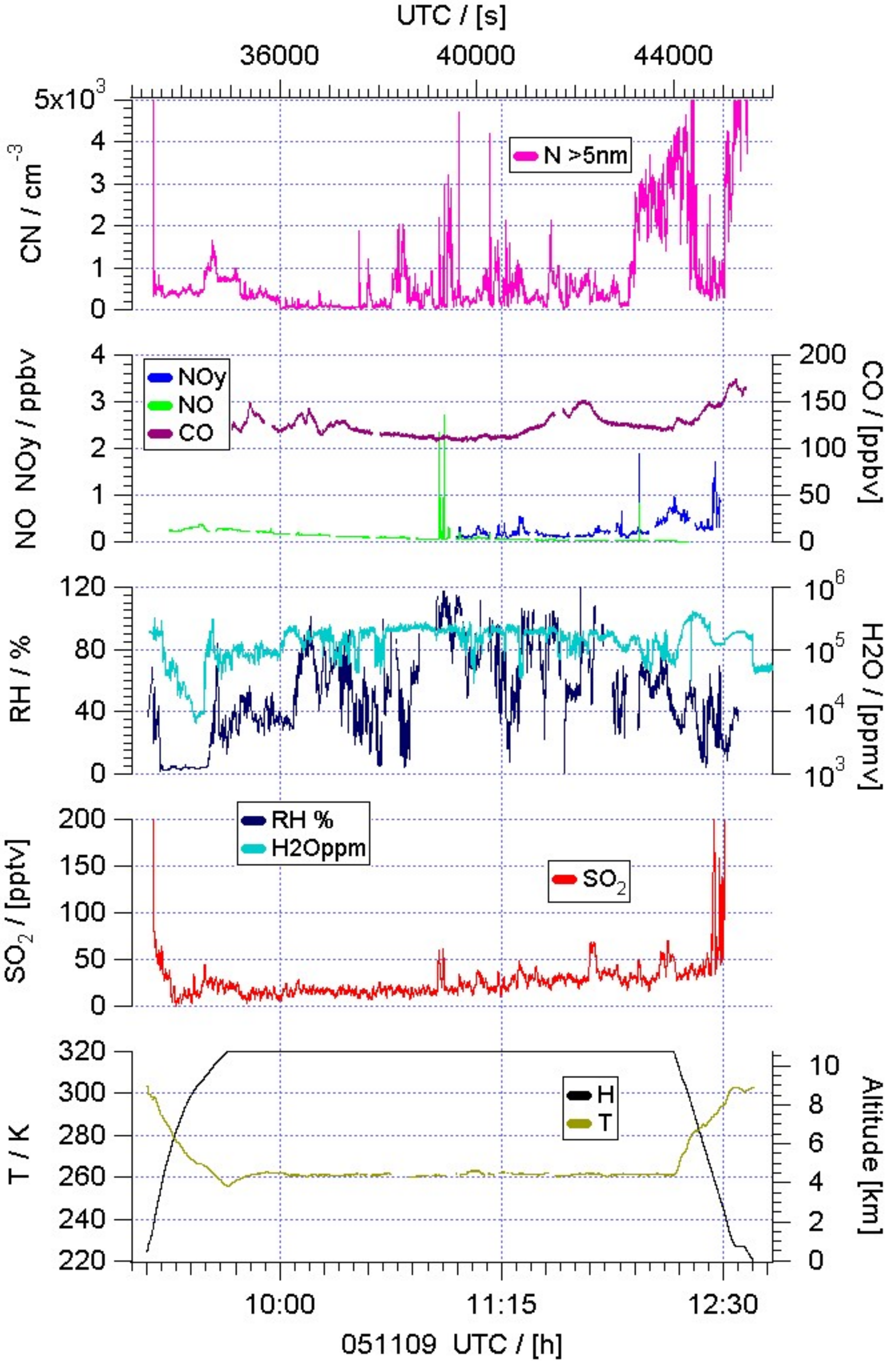

Figure A.9: SCOUT-O3 Fourth Transfer Flight: Hyderabad-Utapao.

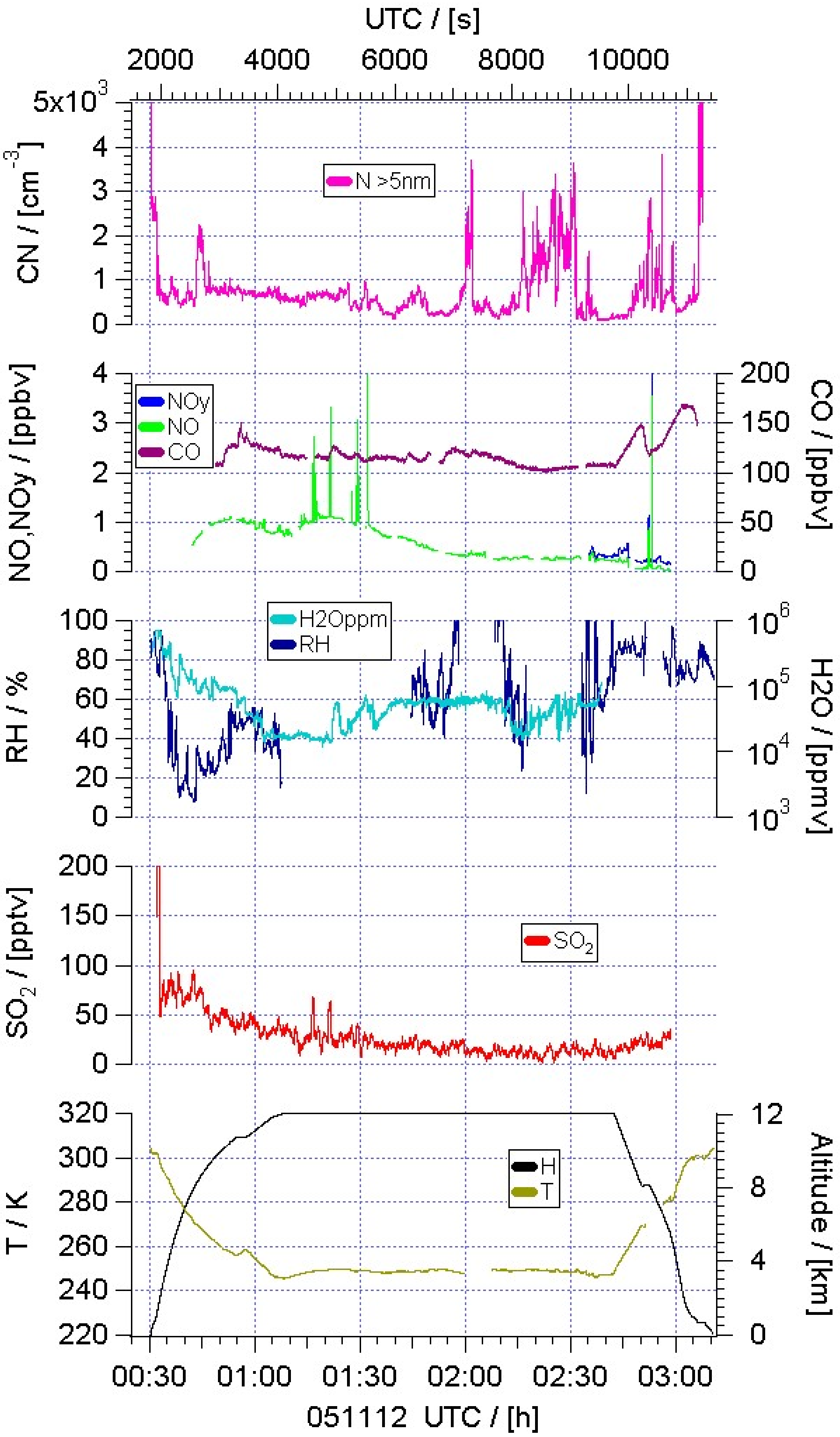

Figure A.10: SCOUT-O3 Fifth Transfer Flight: Utapao-Brunei.

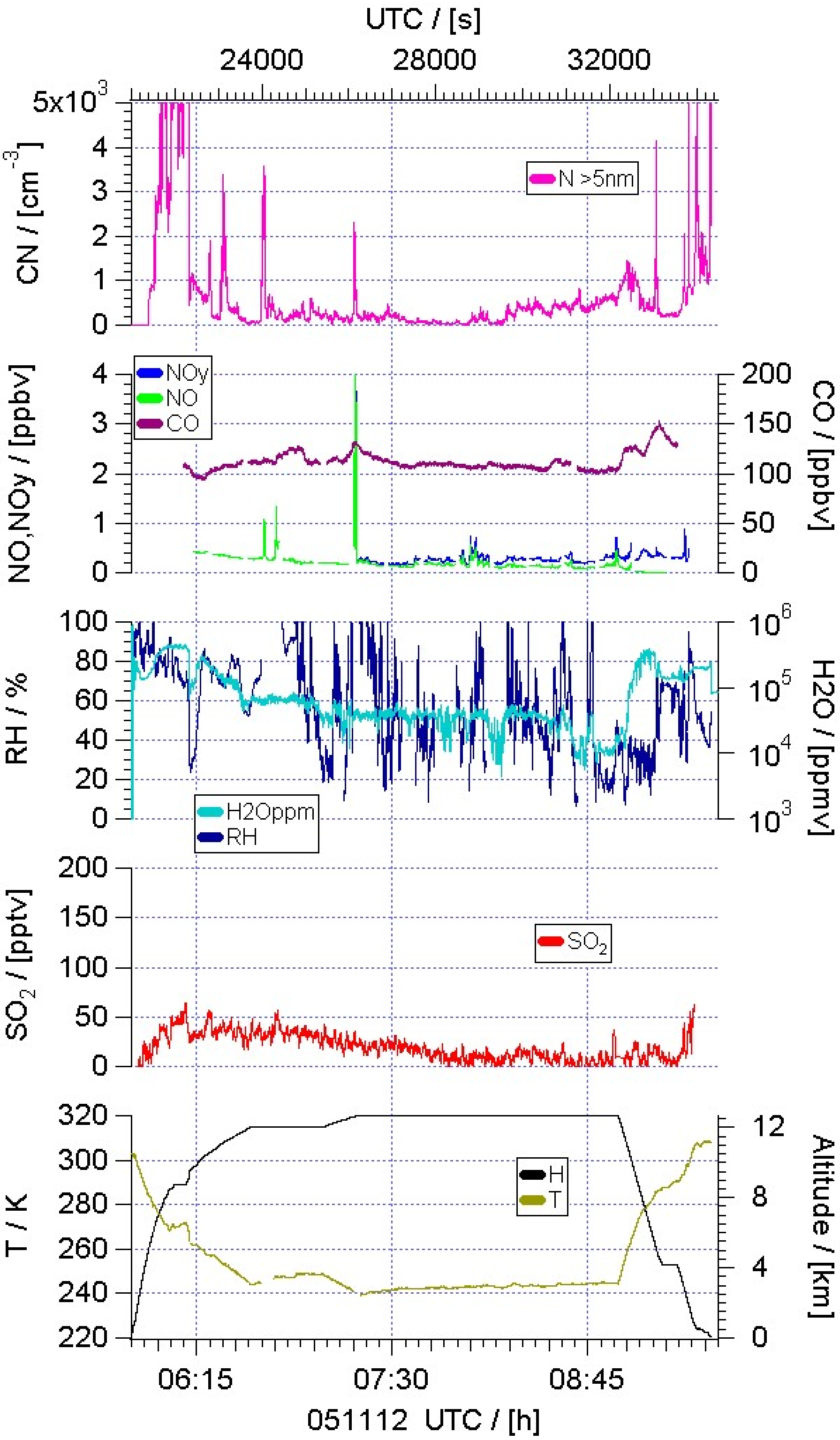

Figure A.11: SCOUT-O3 Sixth Transfer Flight: Brunei-Darwin.

A.2.2 Local Flights

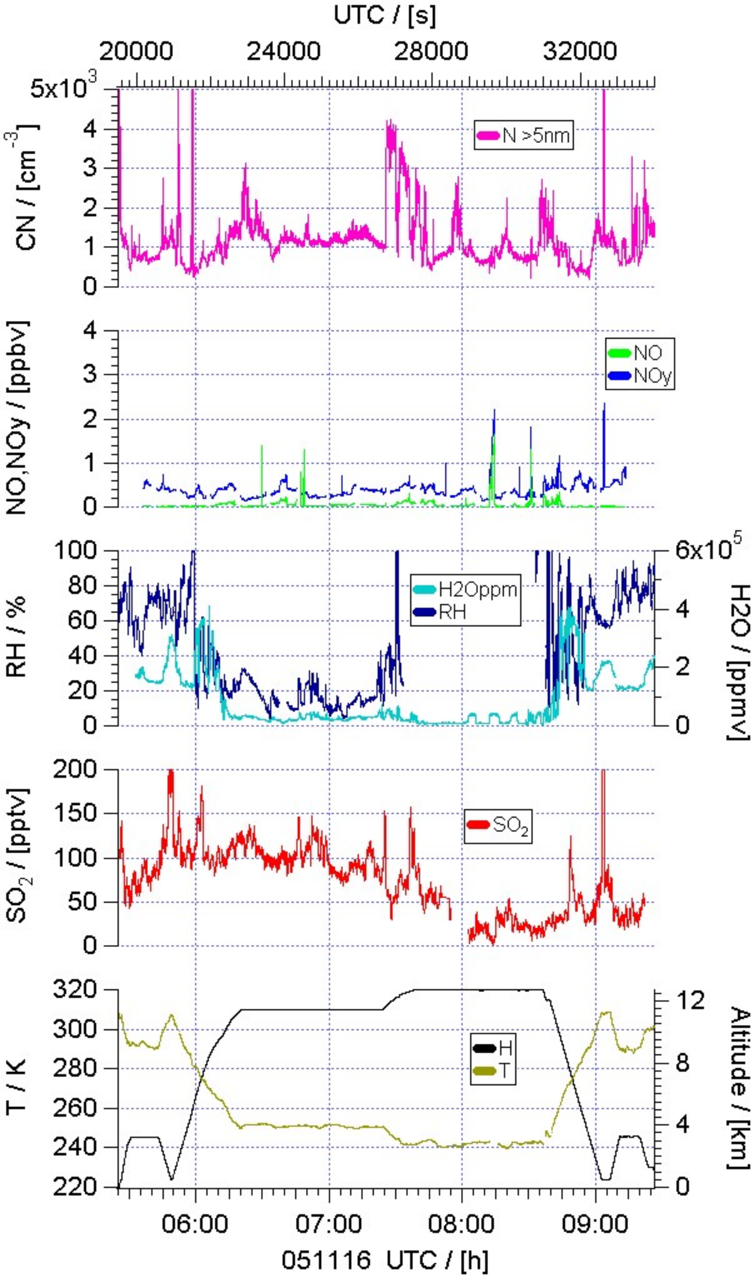

Figure A.12: SCOUT-O3 First Local Flight: Hector outflow.

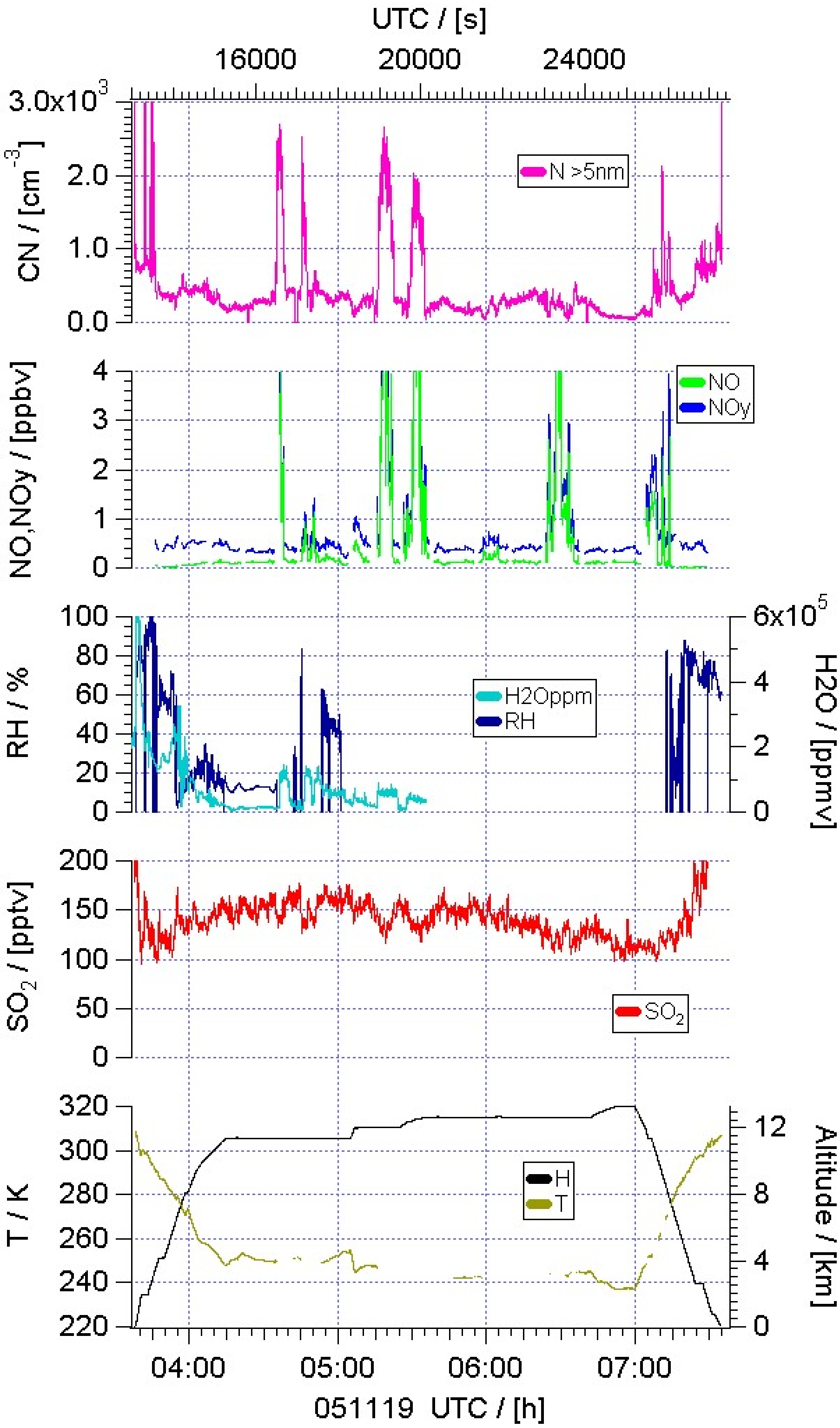

Figure A.13: SCOUT-O3 Second Local Flight: Hector outflow.

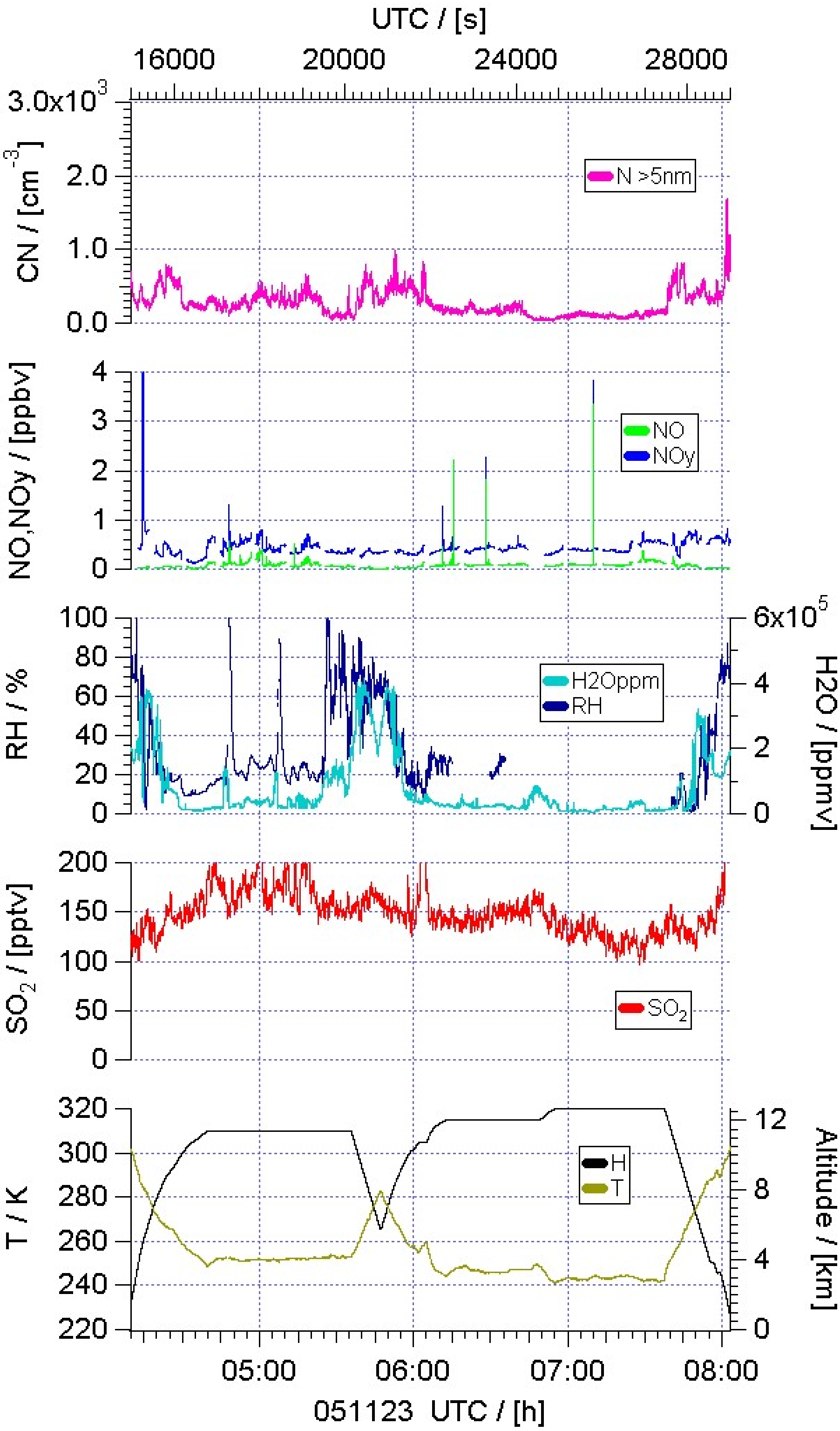

Figure A.14: SCOUT-O3 Third Local Flight: North-East survey.

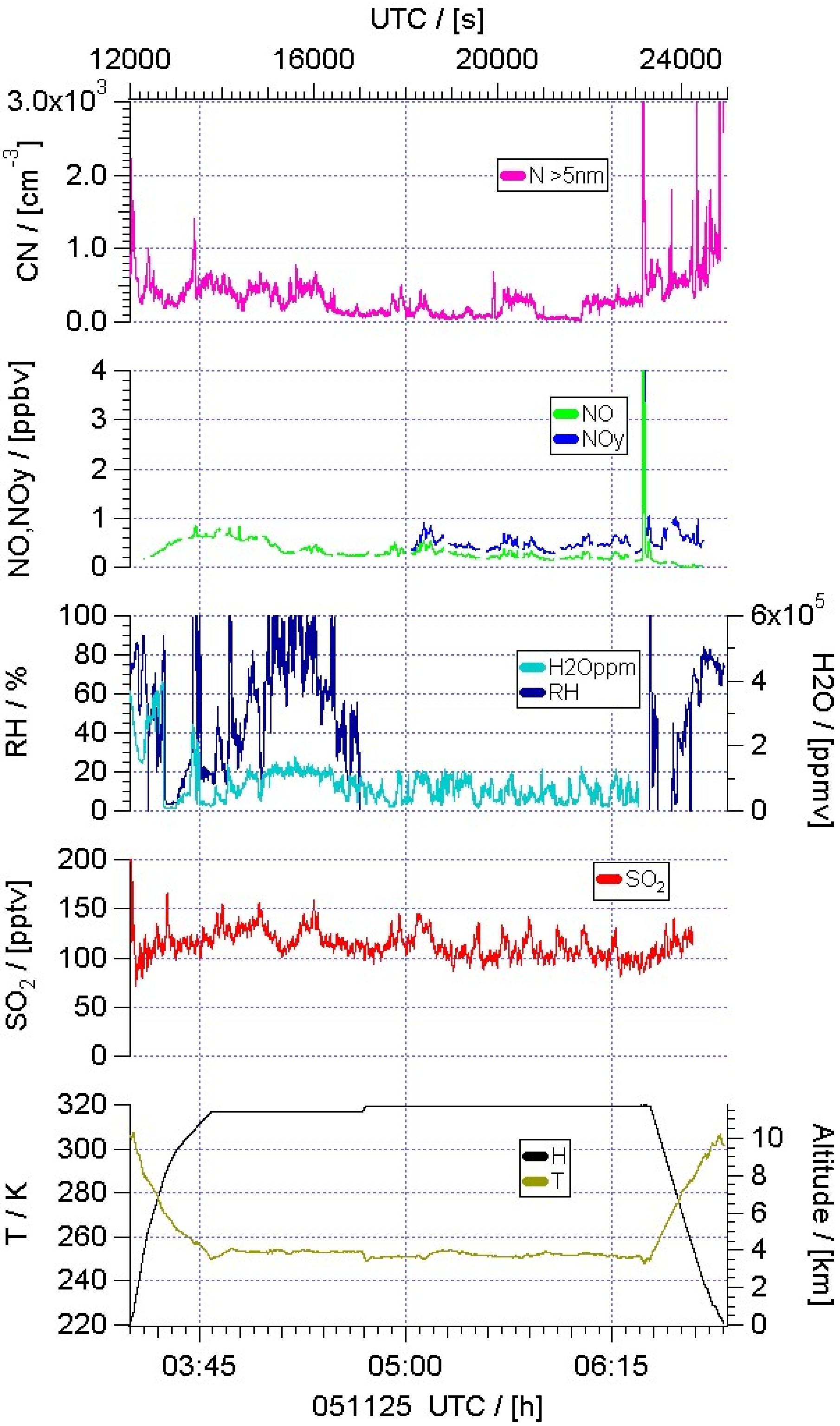

Figure A.15: SCOUT-O3 Fourth Local Flight: Hector outflow.

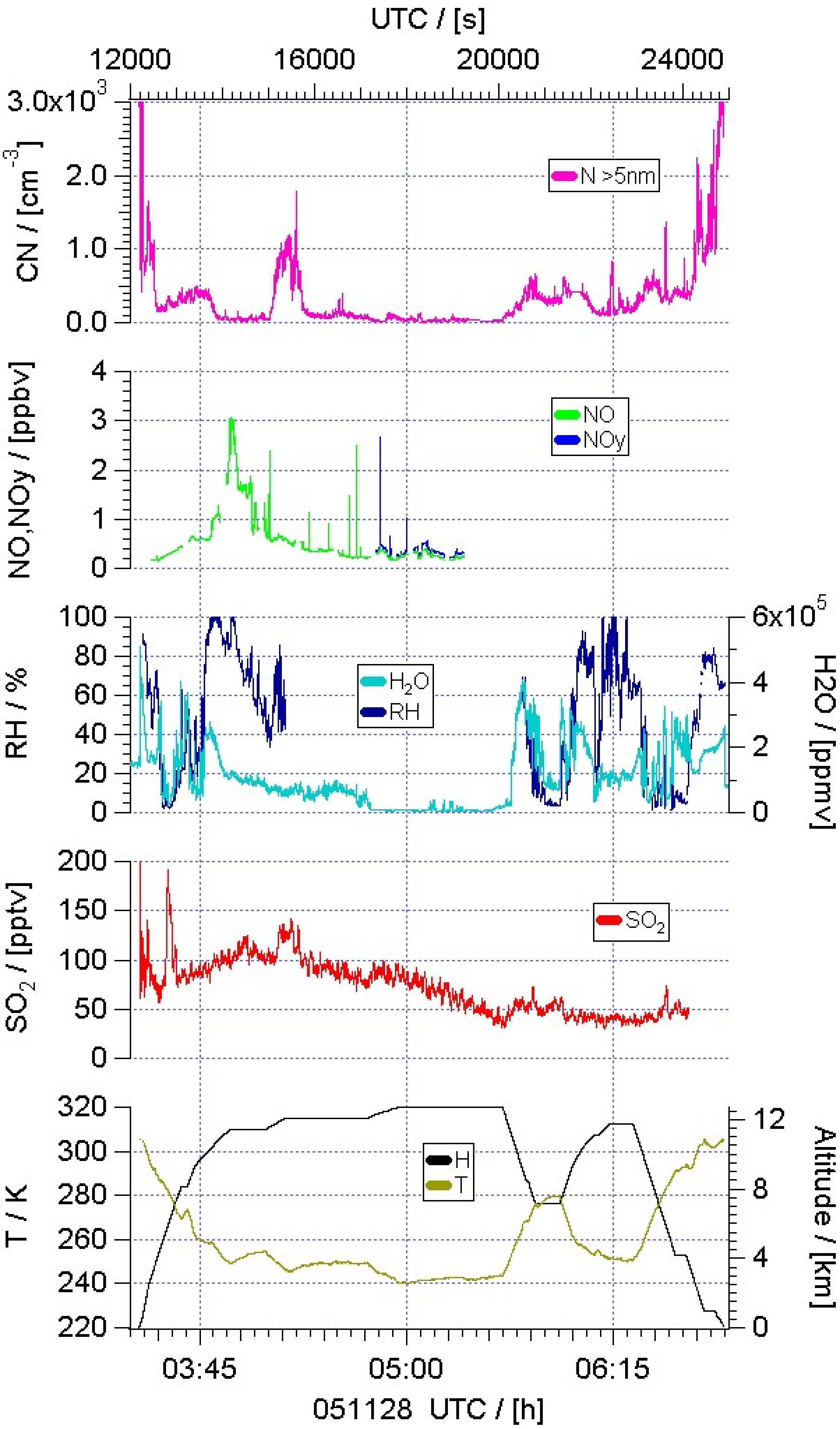

Figure A.16: SCOUT-O3 Fifth Local Flight: Hector outflow.

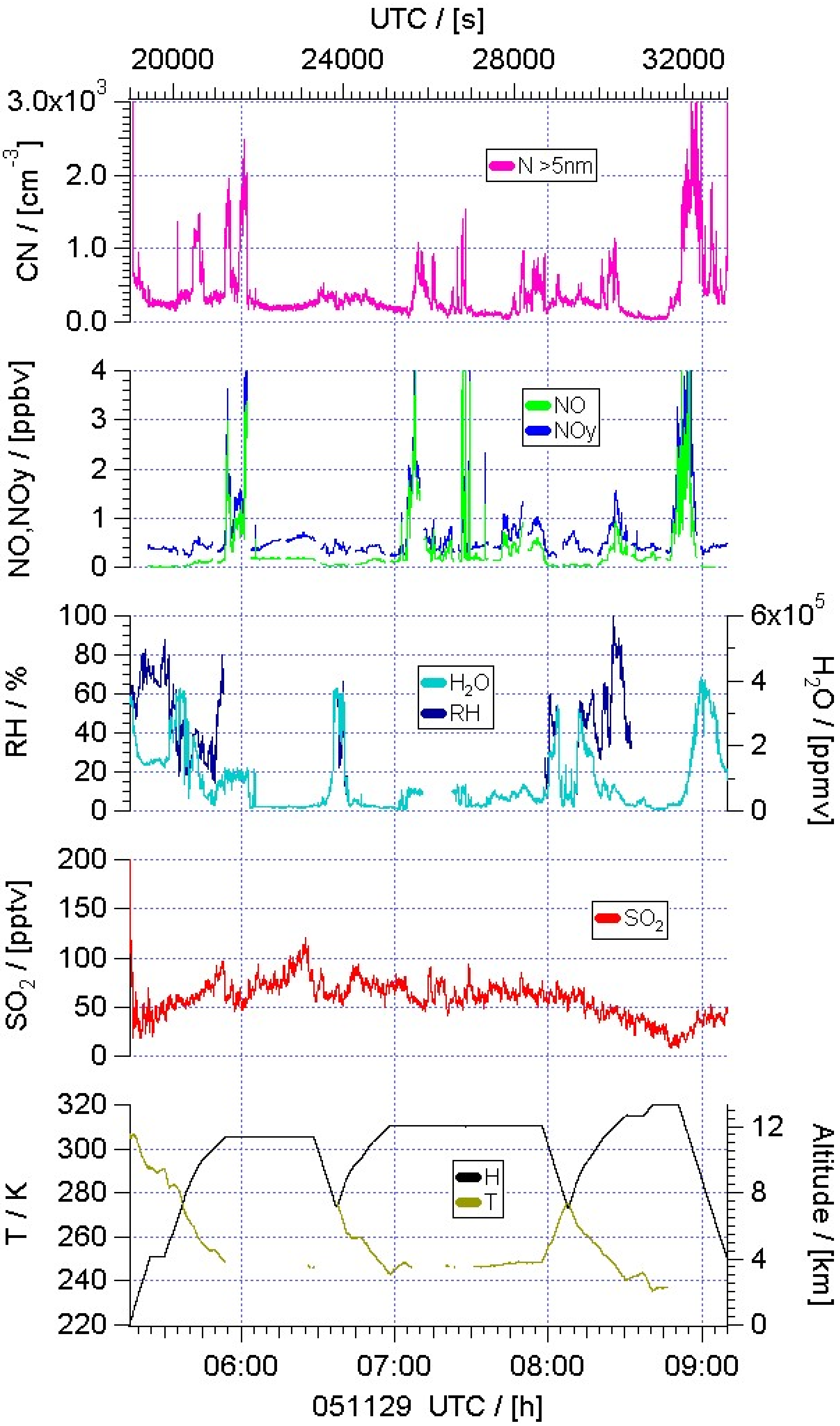

Figure A.17: SCOUT-O3 Sixth Local Flight: North-South survey.

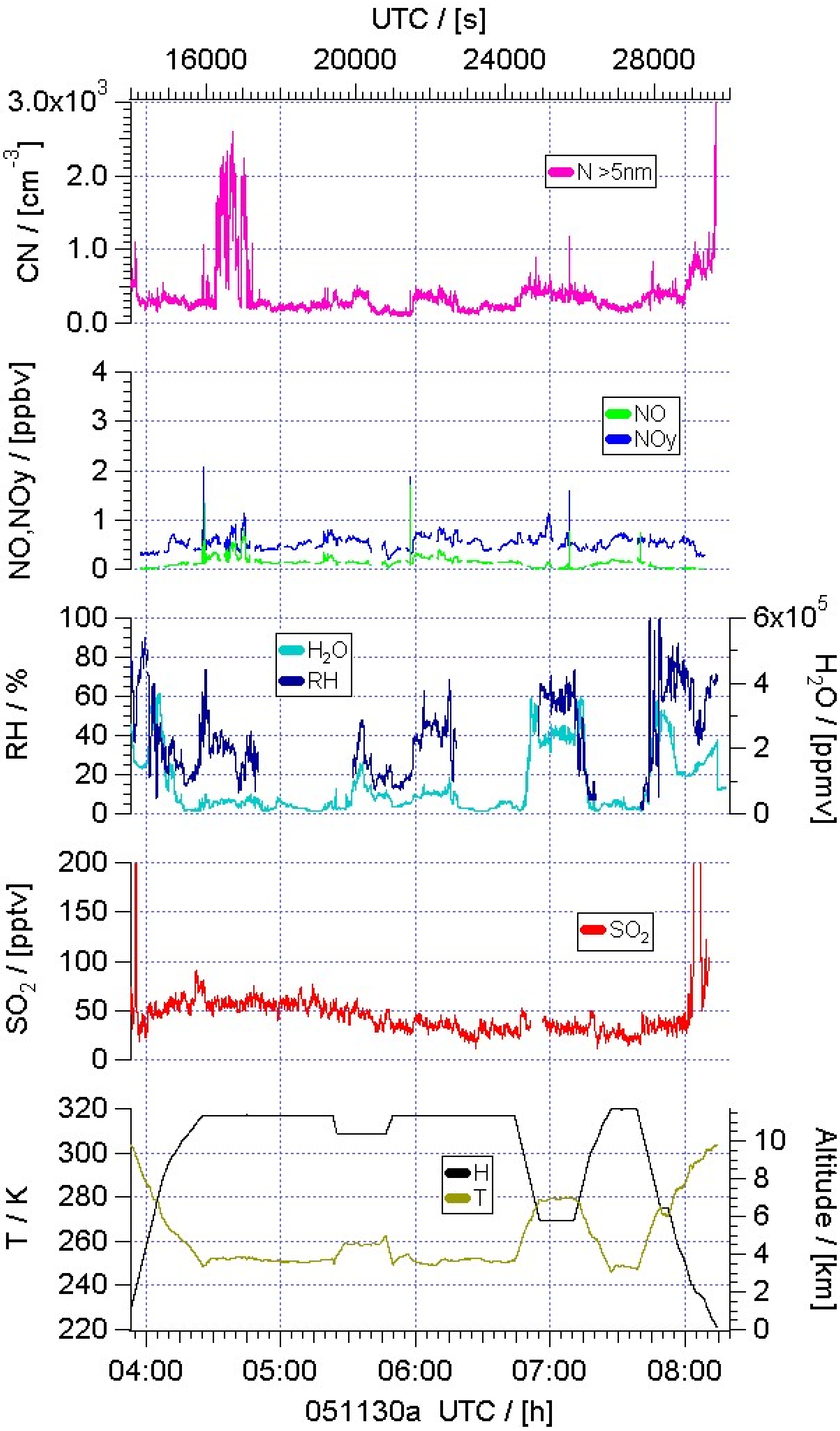

Figure A.18: SCOUT-O3 Seventh Local Flight: Fresh Hector outflow.

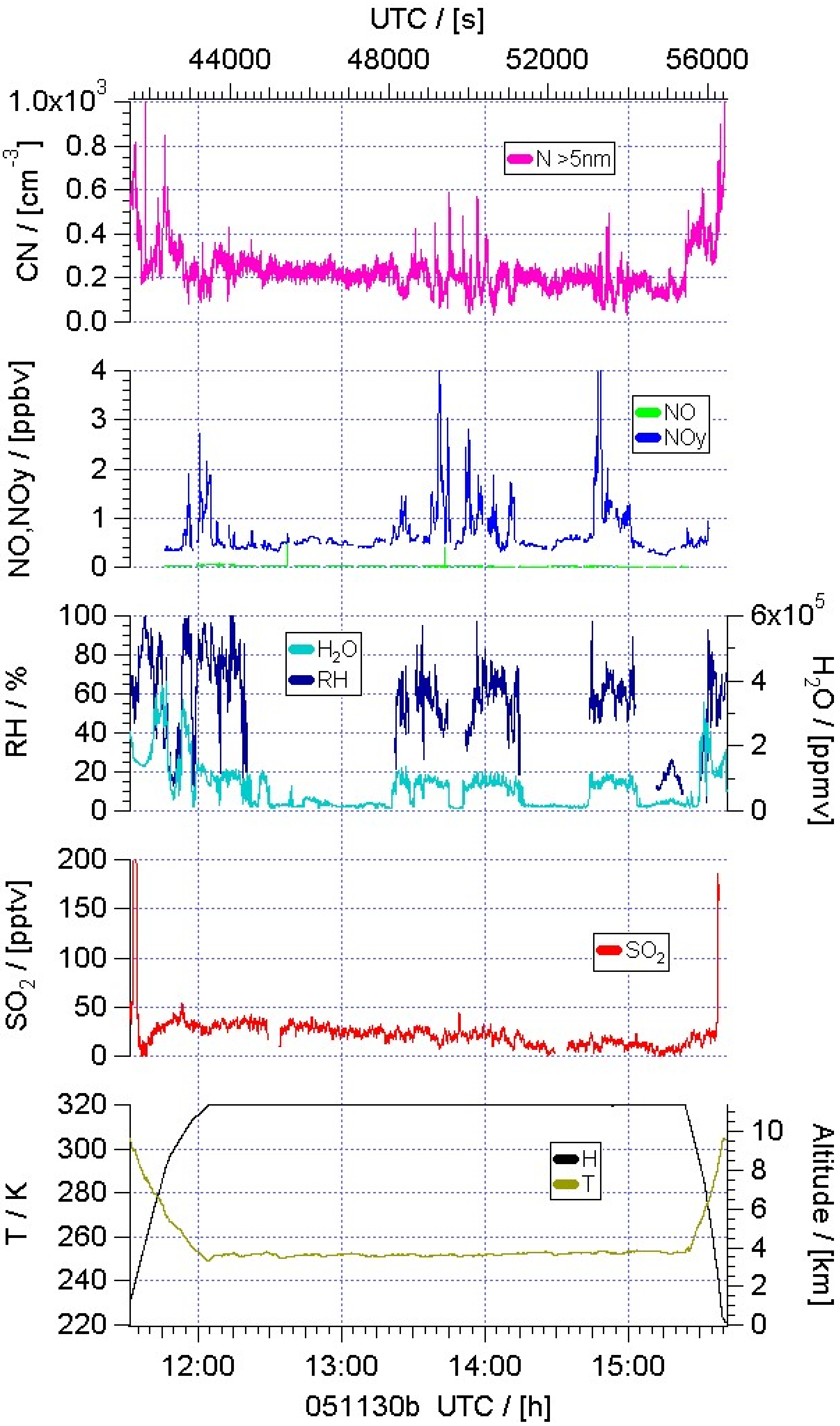

Figure A.19: SCOUT-O3 Eighth Local Flight: Aged Hector outflow.

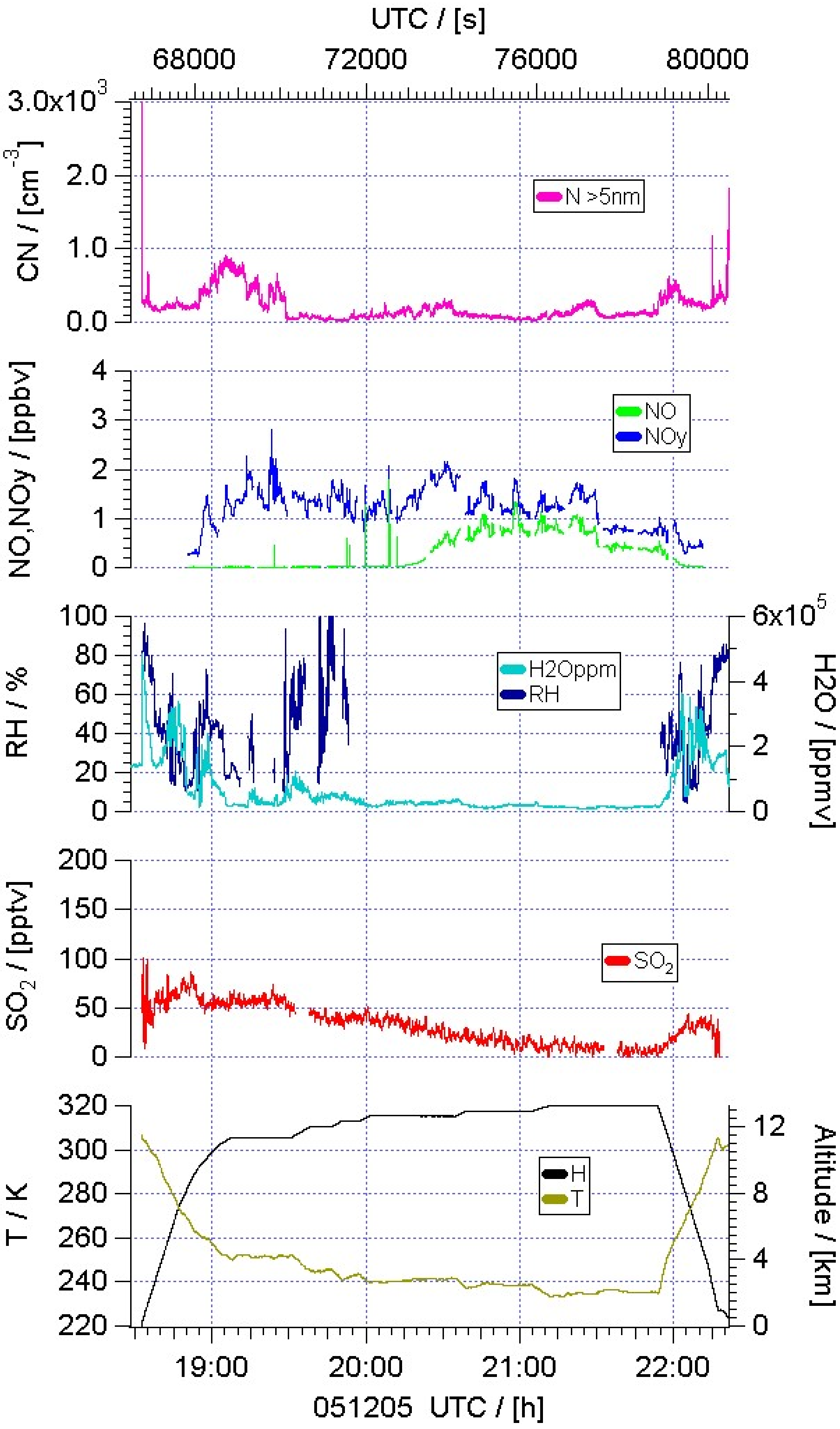

Figure A.20: SCOUT-O3 Ninth Local Flight: South survey.

A.2.3 Backtransfer

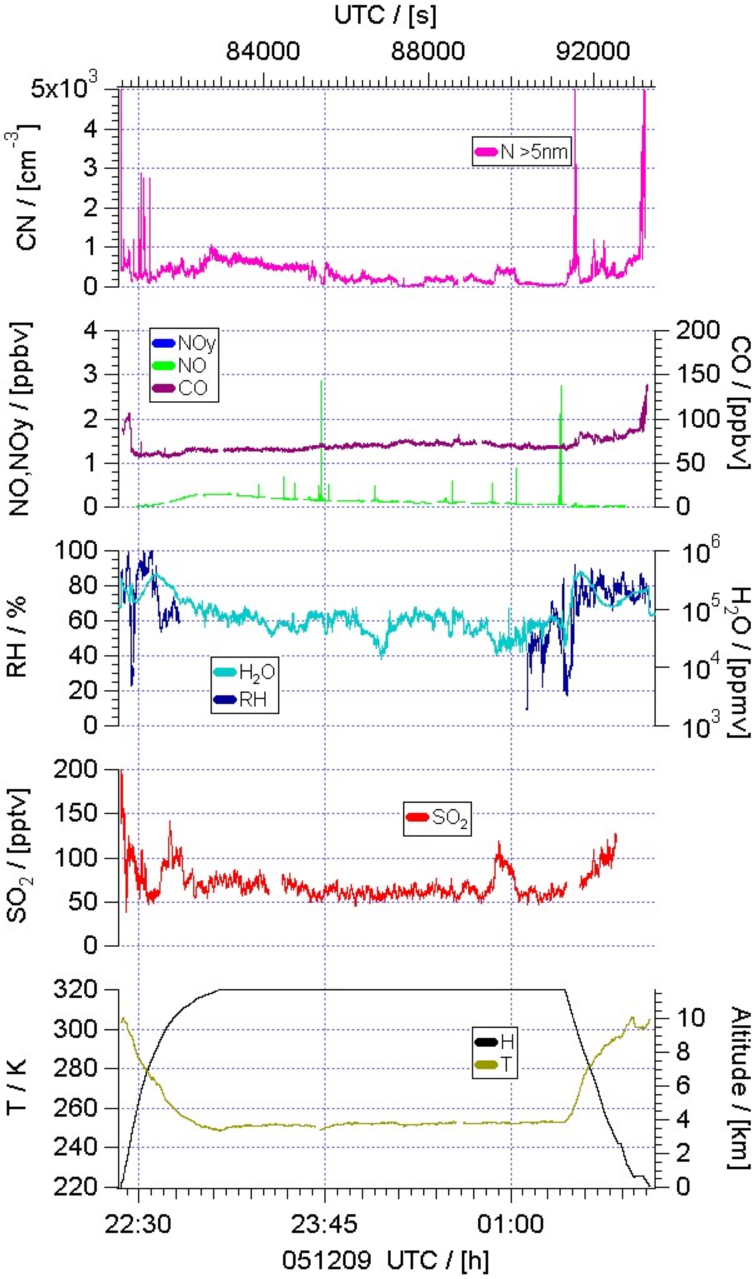

Figure A.21: SCOUT-O3 First Back Transfer Flight: Darwin-Brunei.

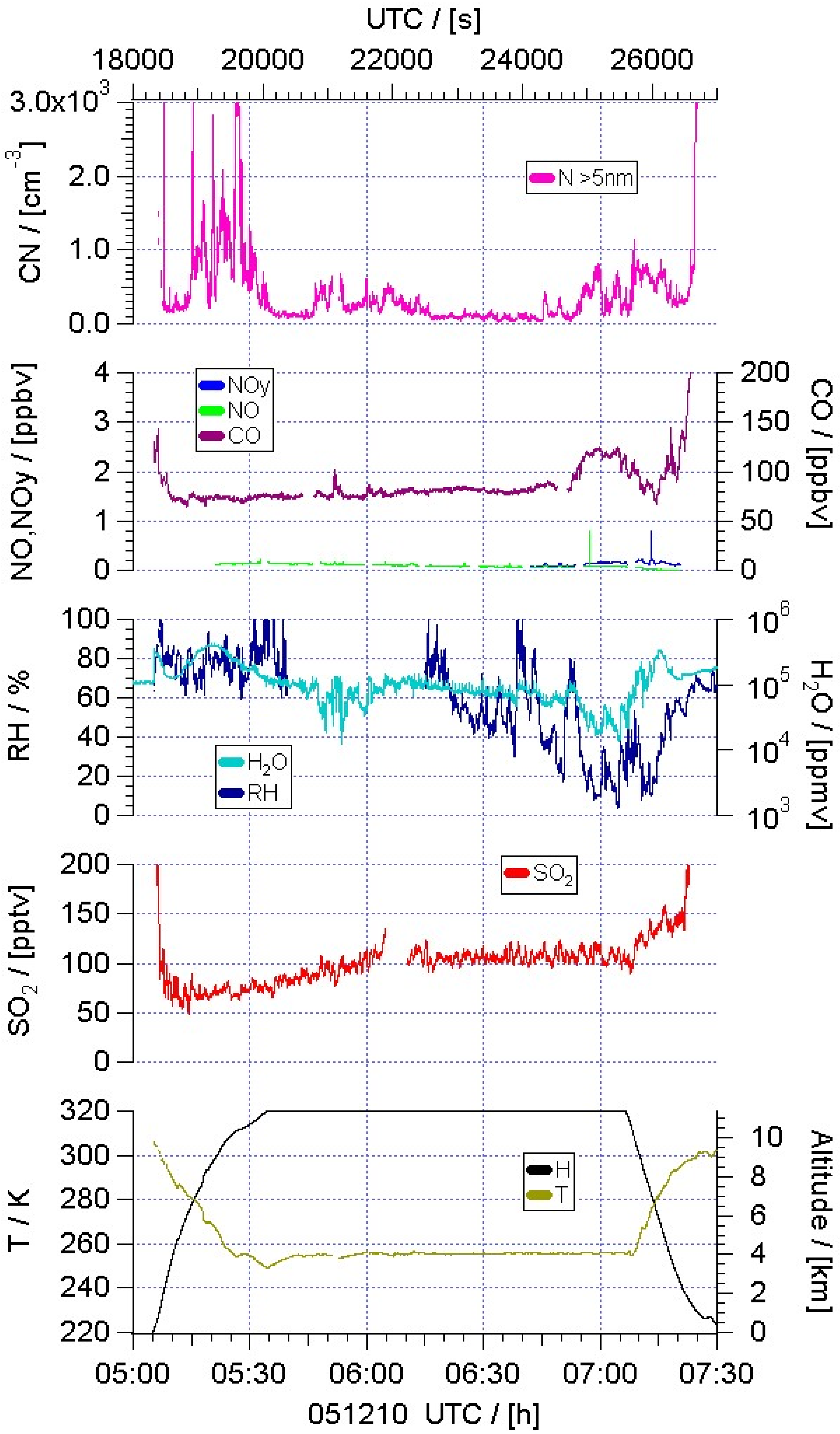

Figure A.22: SCOUT-O3 Second Back Transfer Flight: Brunei-Utapao.

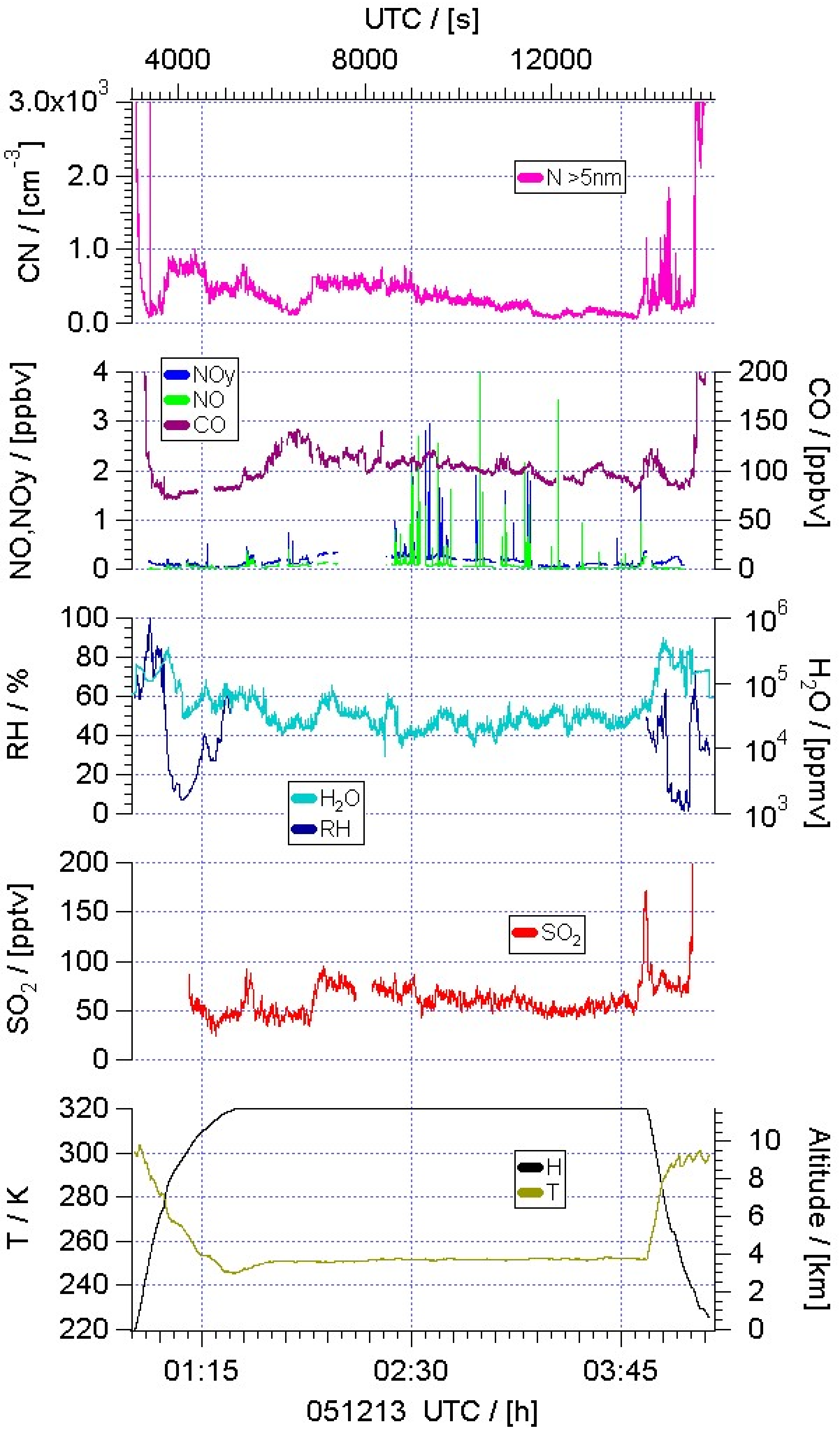

Figure A.23: SCOUT-O3 Third Back Transfer Flight: Utapao-Hyderabad.

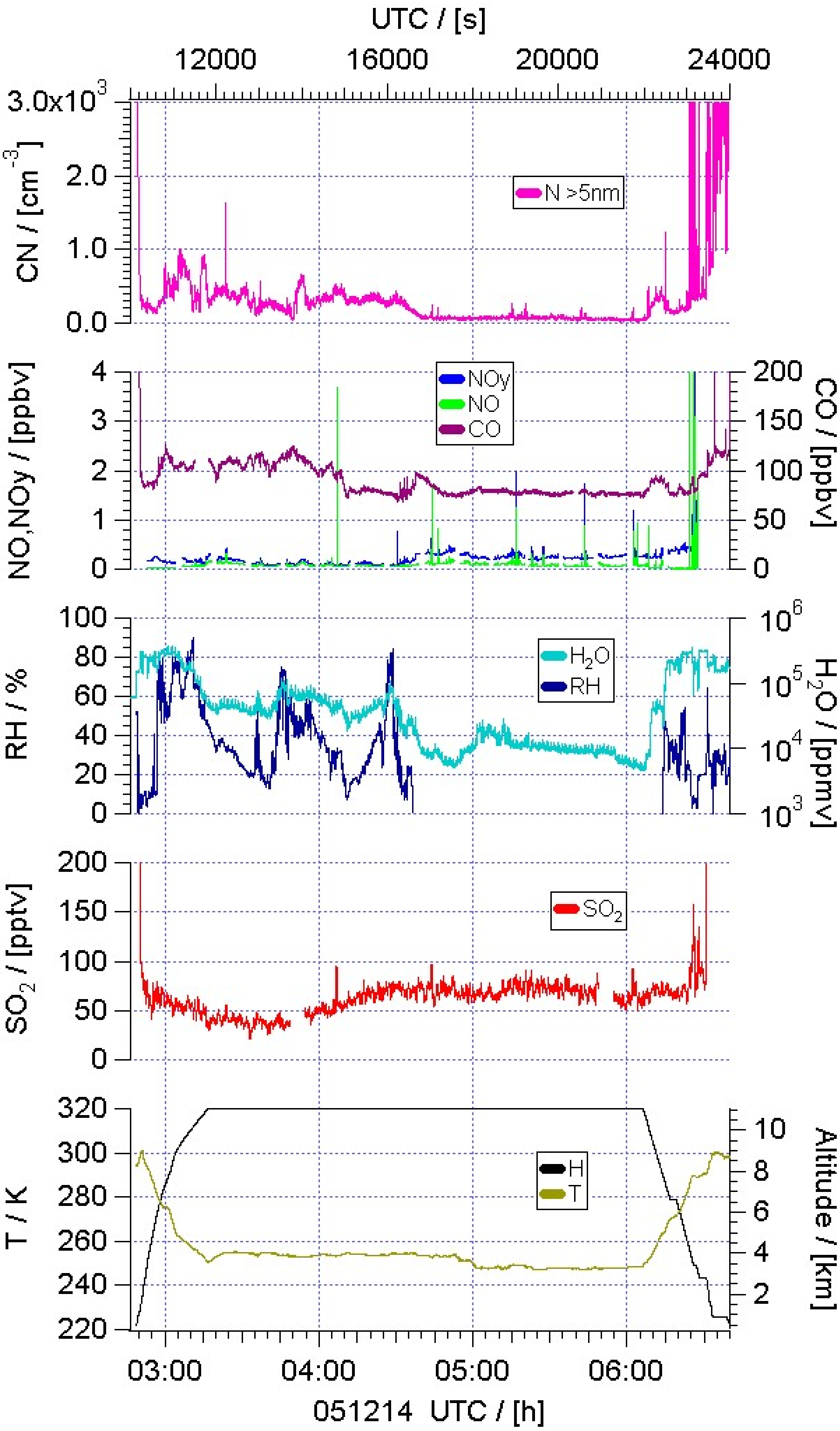

Figure A.24: SCOUT-O3 Fourth Back Transfer Flight: Hyderabad-Dubai.

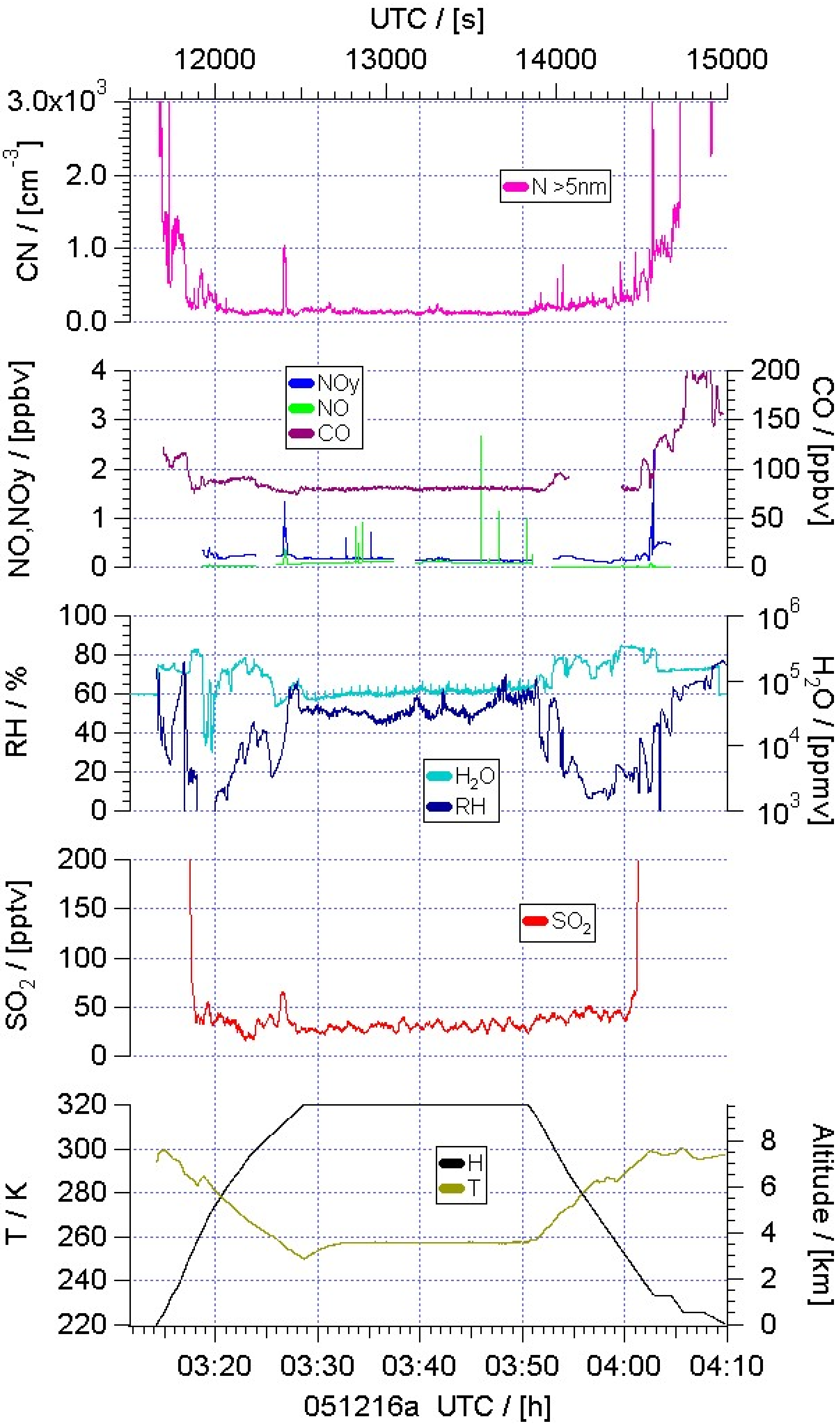

Figure A.25: SCOUT-O3 Fifth Back Transfer Flight: Dubai-Bahrain.

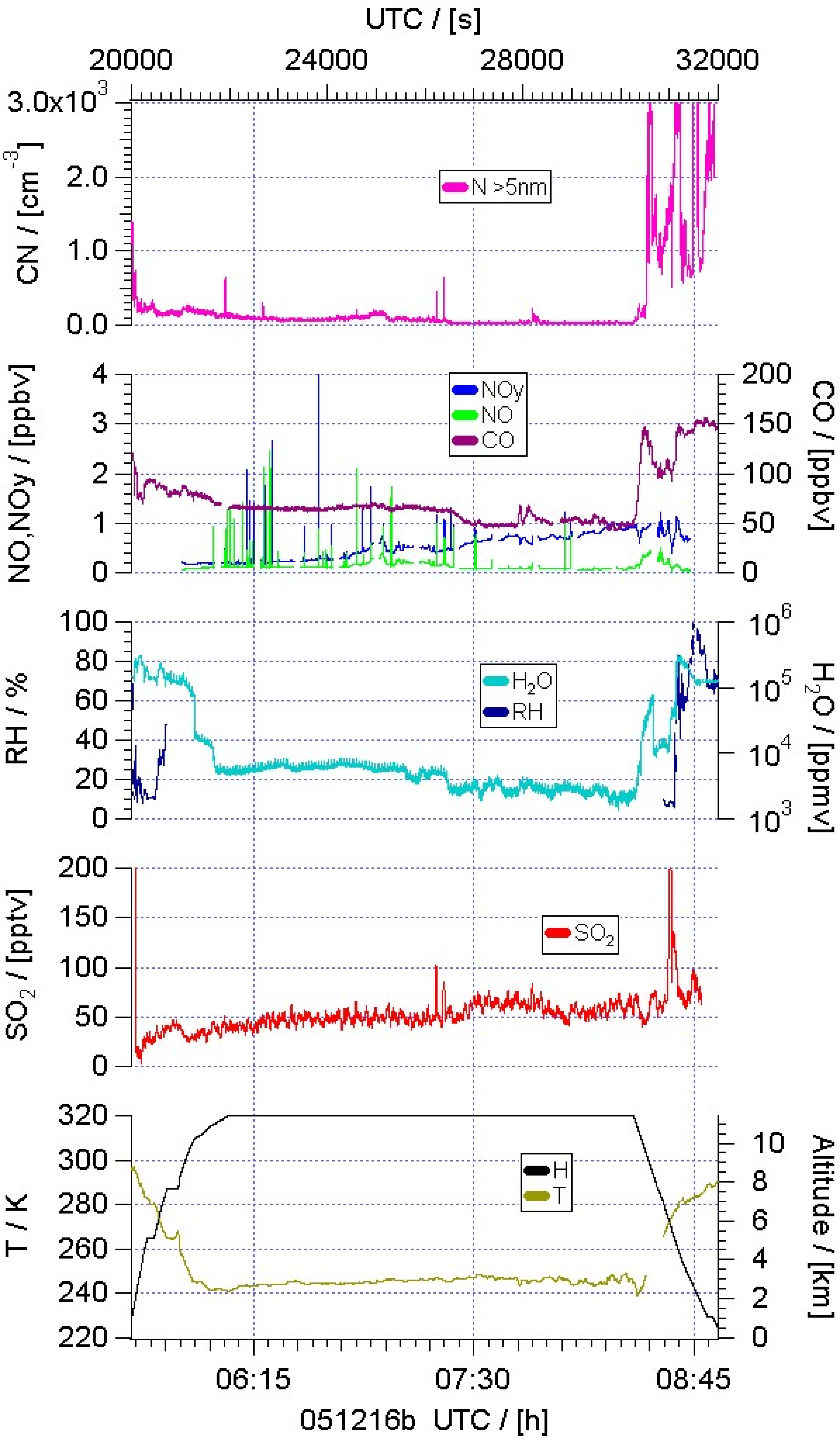

Figure A.26: SCOUT-O3 Sixth Back Transfer Flight: Bahrain-Larnaca.

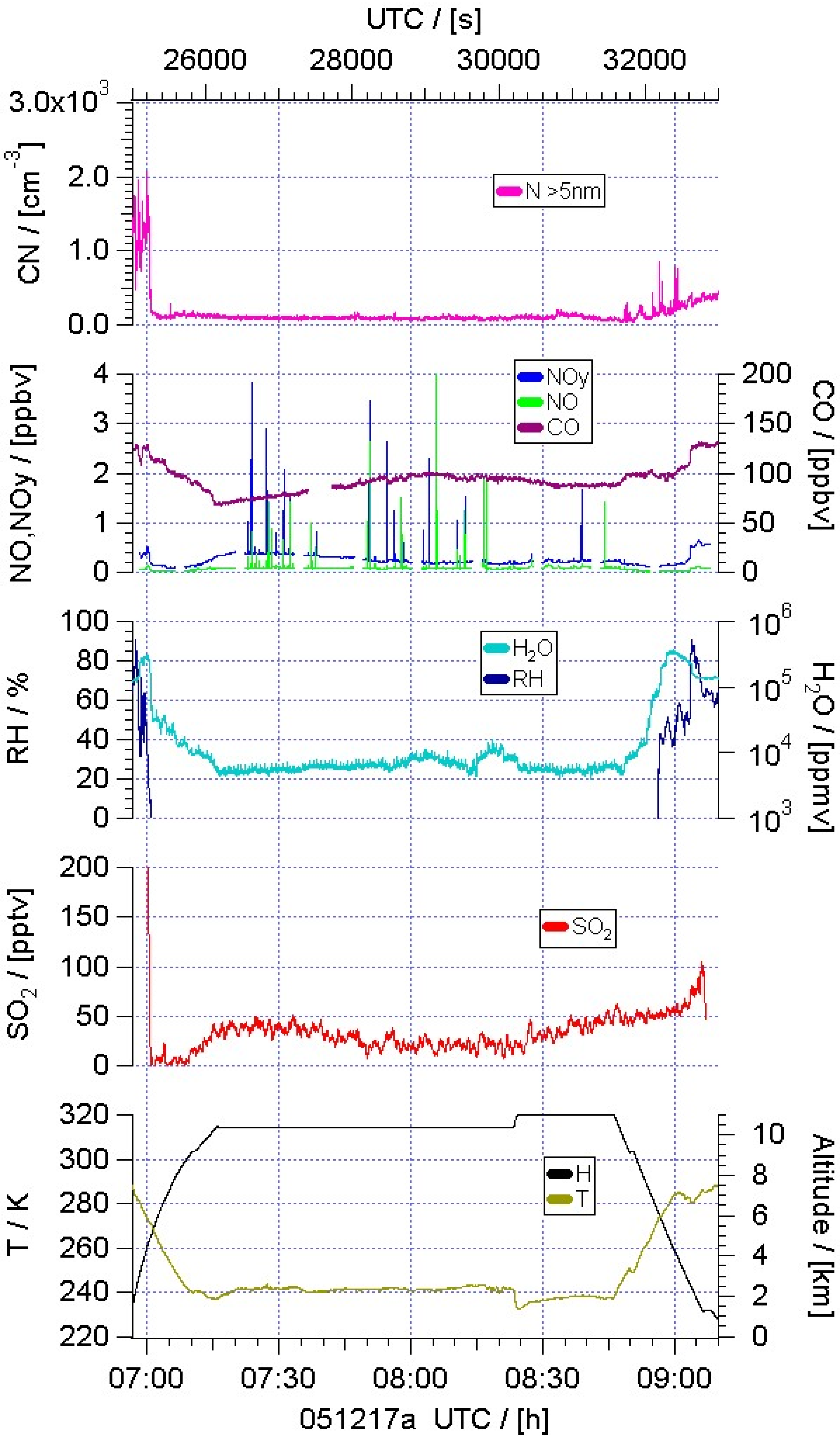

Figure A.27: SCOUT-O3 Seventh Back Transfer Flight: Larnaca-Brindisi.

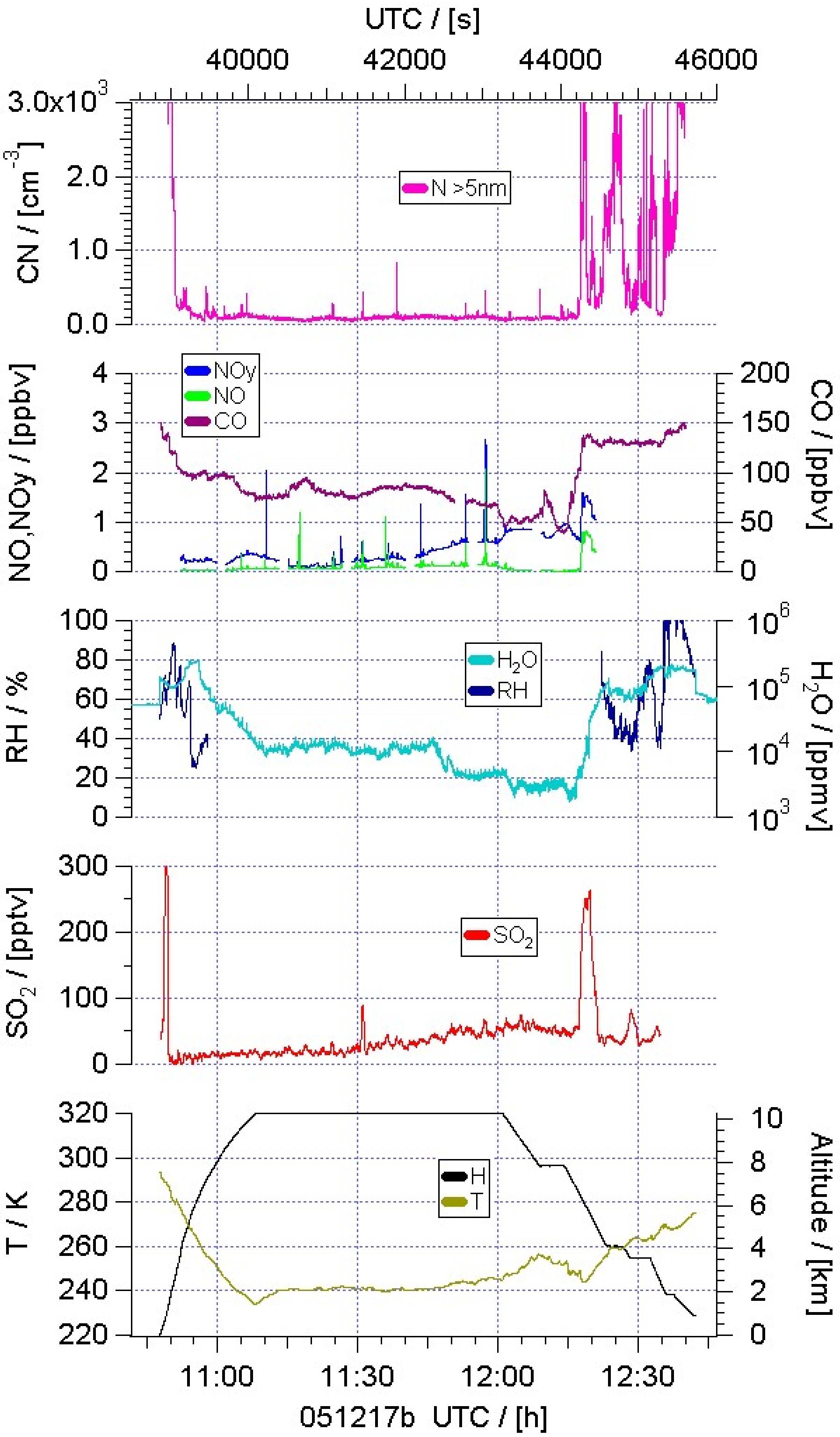

Figure A.28: SCOUT-O3 Eighth Back Transfer Flight: Brindisi-Munich.

A.3 INTEX, SHIPS, MEGAPLUME

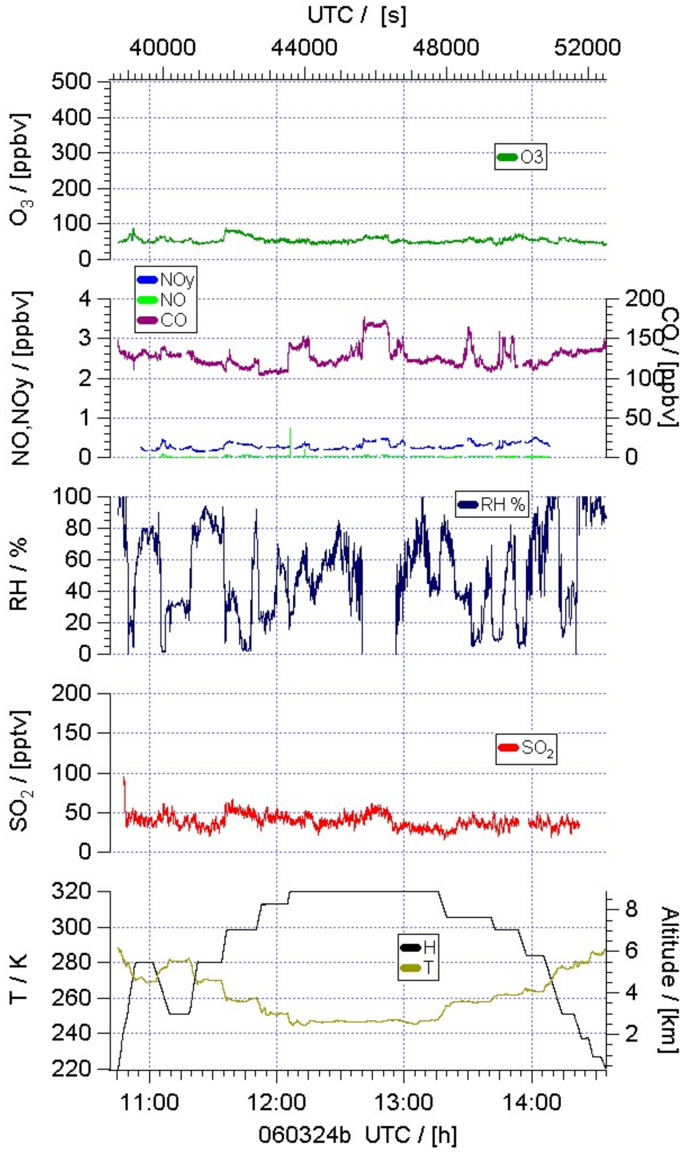

Figure A.29: MEGAPLUME Flight Santiago-Santiago: Asian and American pollution plumes.

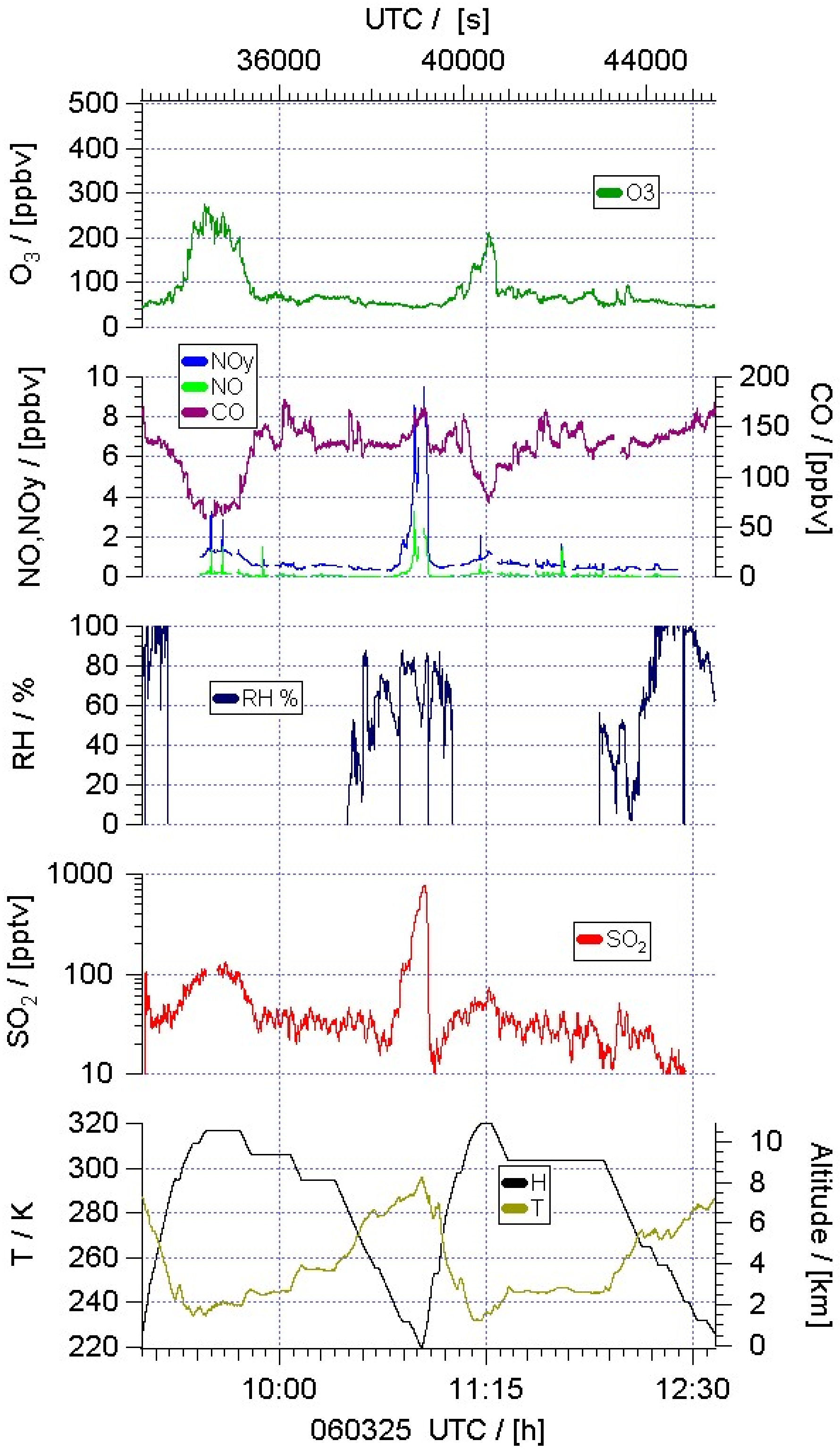

Figure A.30: MEGAPLUME Flight Oberpfaffenhofen-Oberpfaffenhofen: Asian emissions.

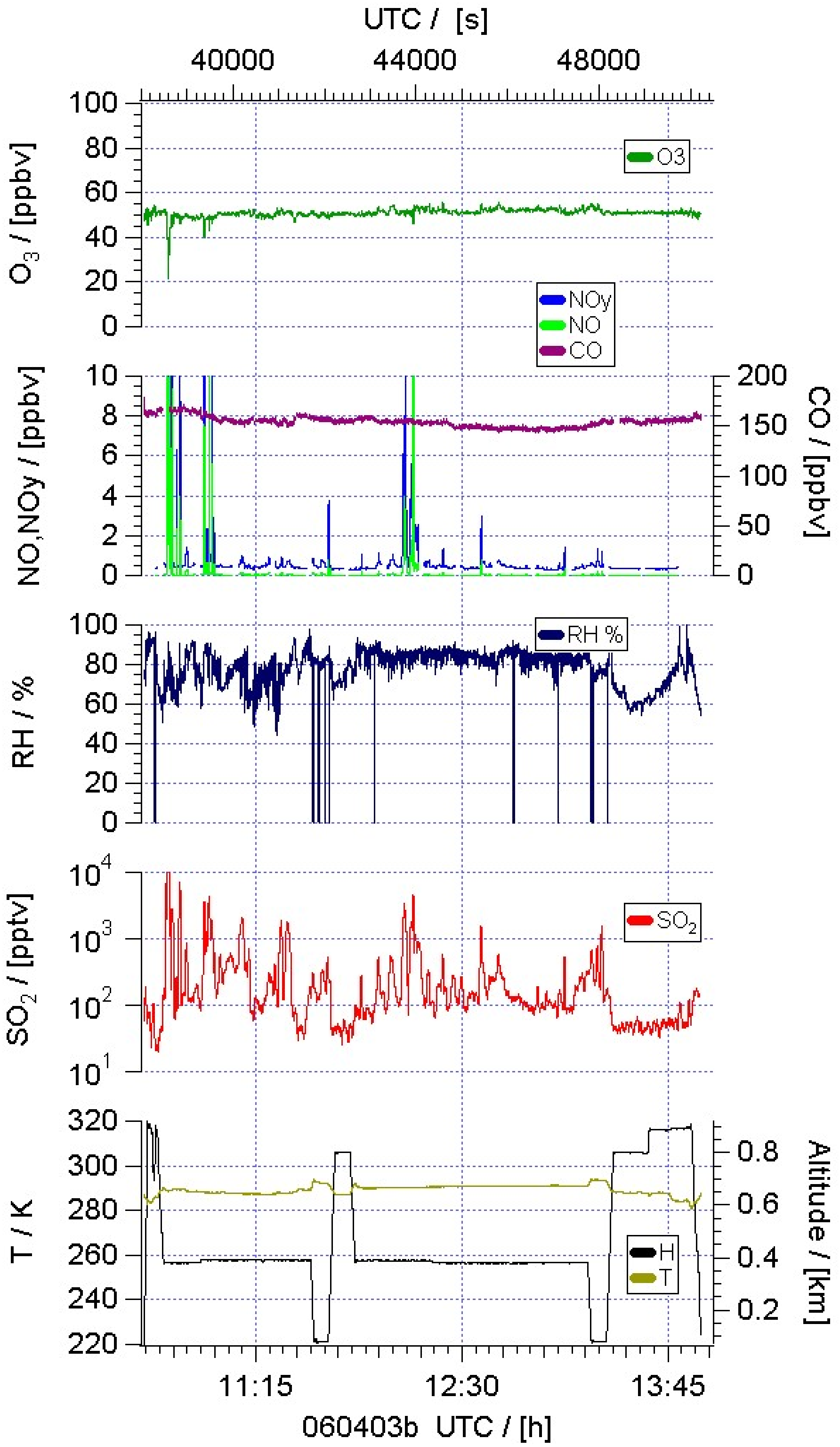

Figure A.31: SHIPS Flight Brest-Brest: Atlantic ship emissions.

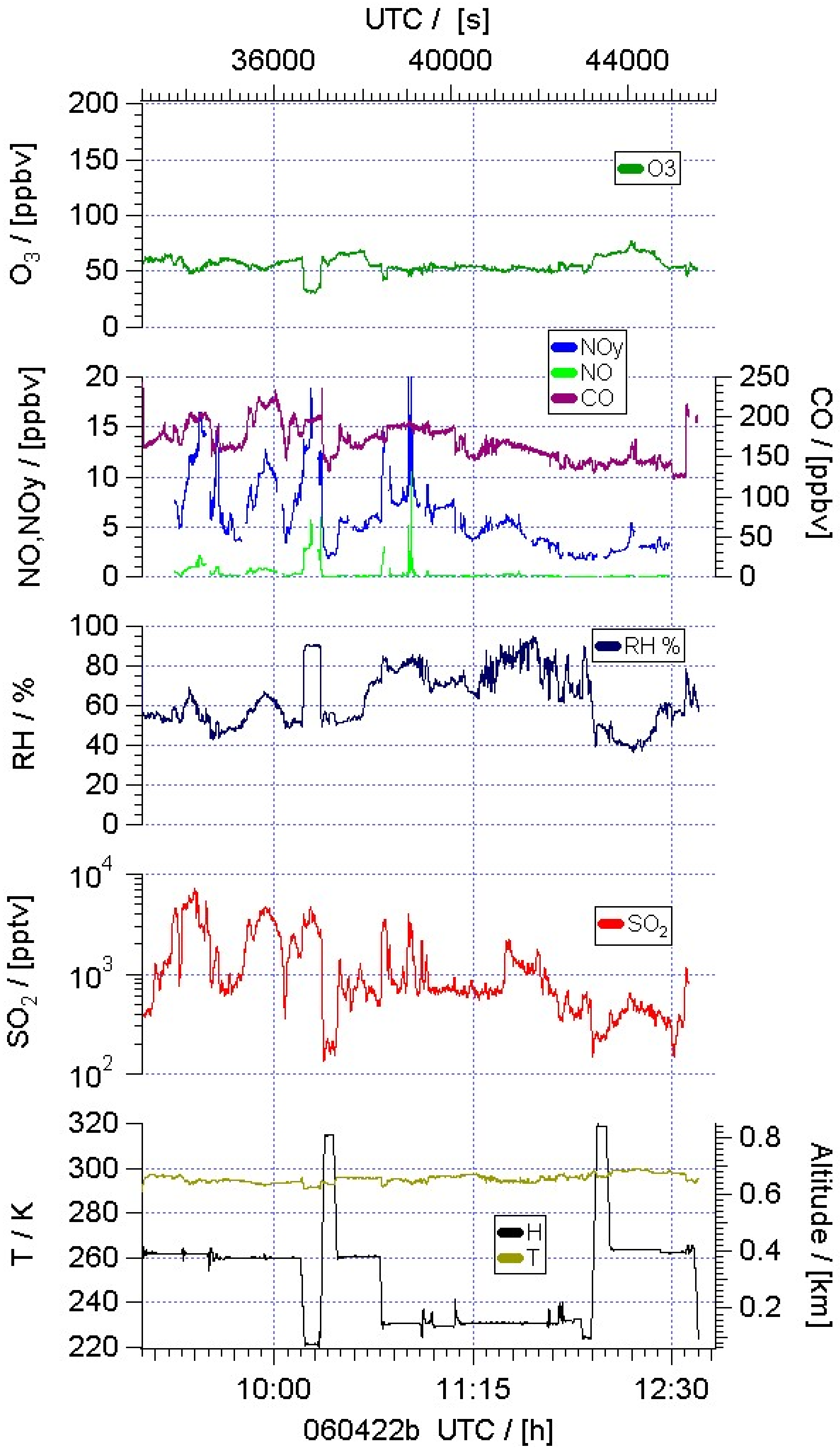

Figure A.32: SHIPS Flight Brest-Brest: Atlantic ship emissions.

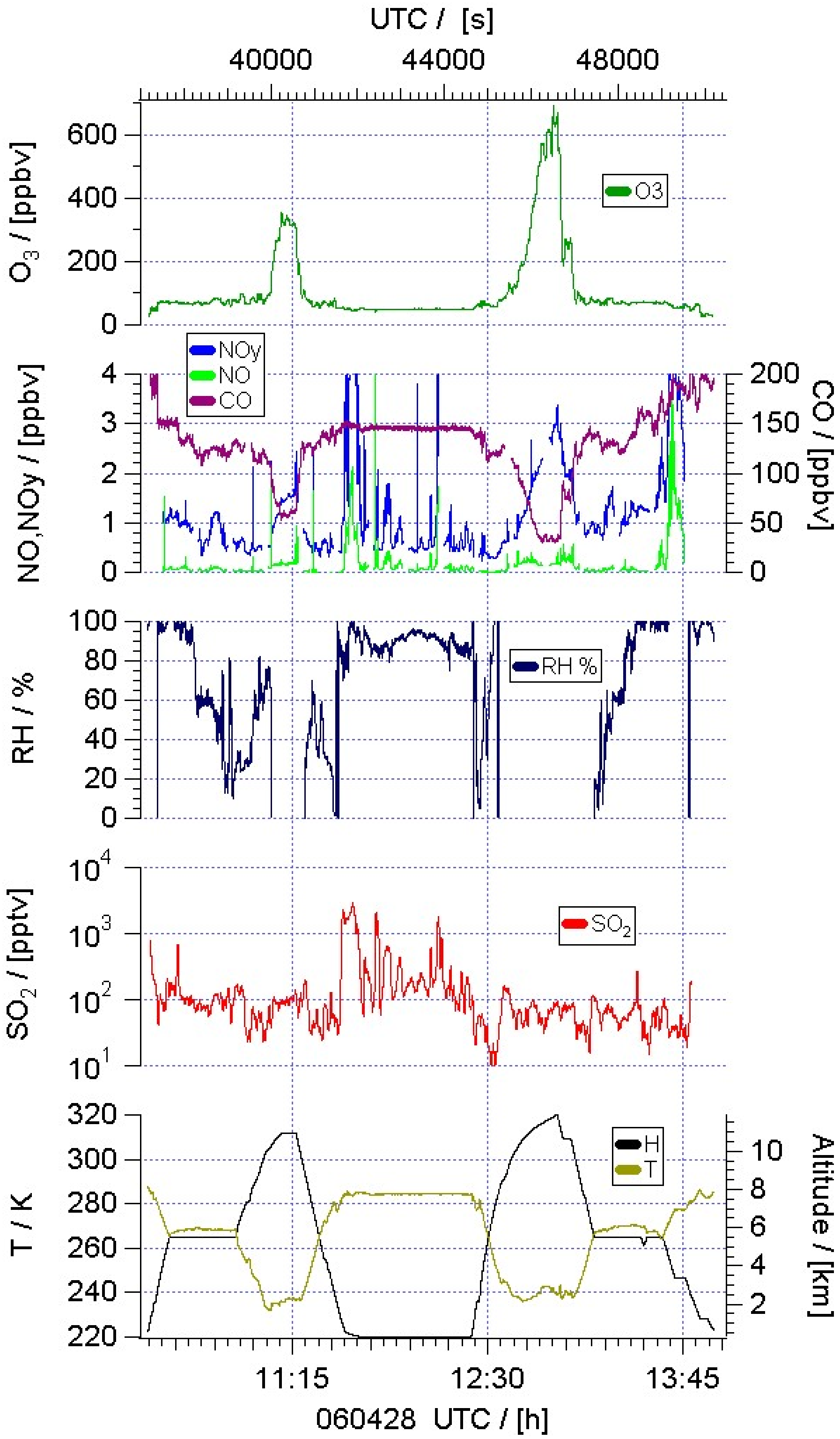

Figure A.33: INTEX Flight Oberpfaffenhofen-Oberpfaffenhofen: North American pollution and ship exhaust.

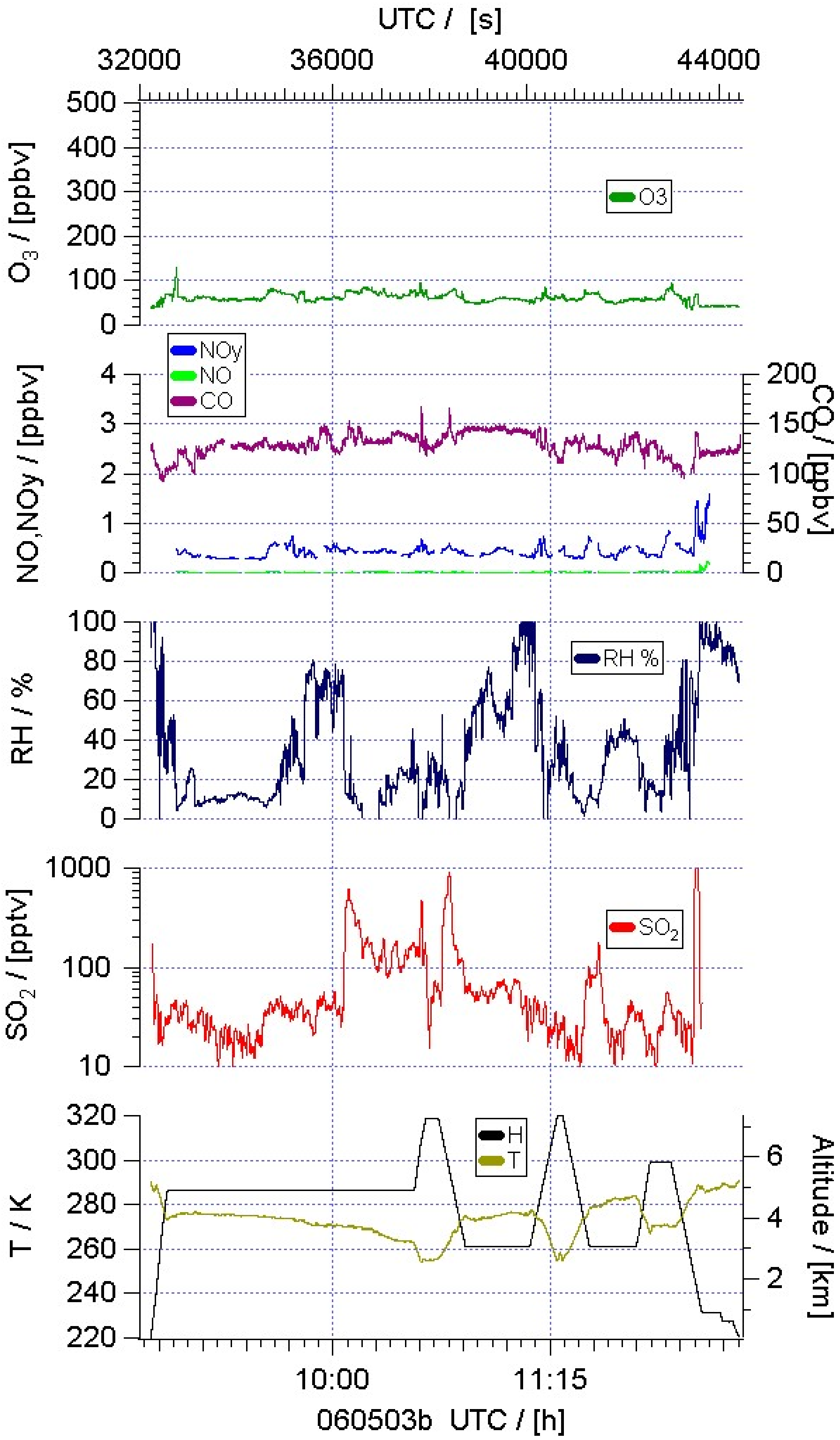

Figure A.34: INTEX Flight Brest-Brest: North American and Asian pollution.

A.4 AMMA

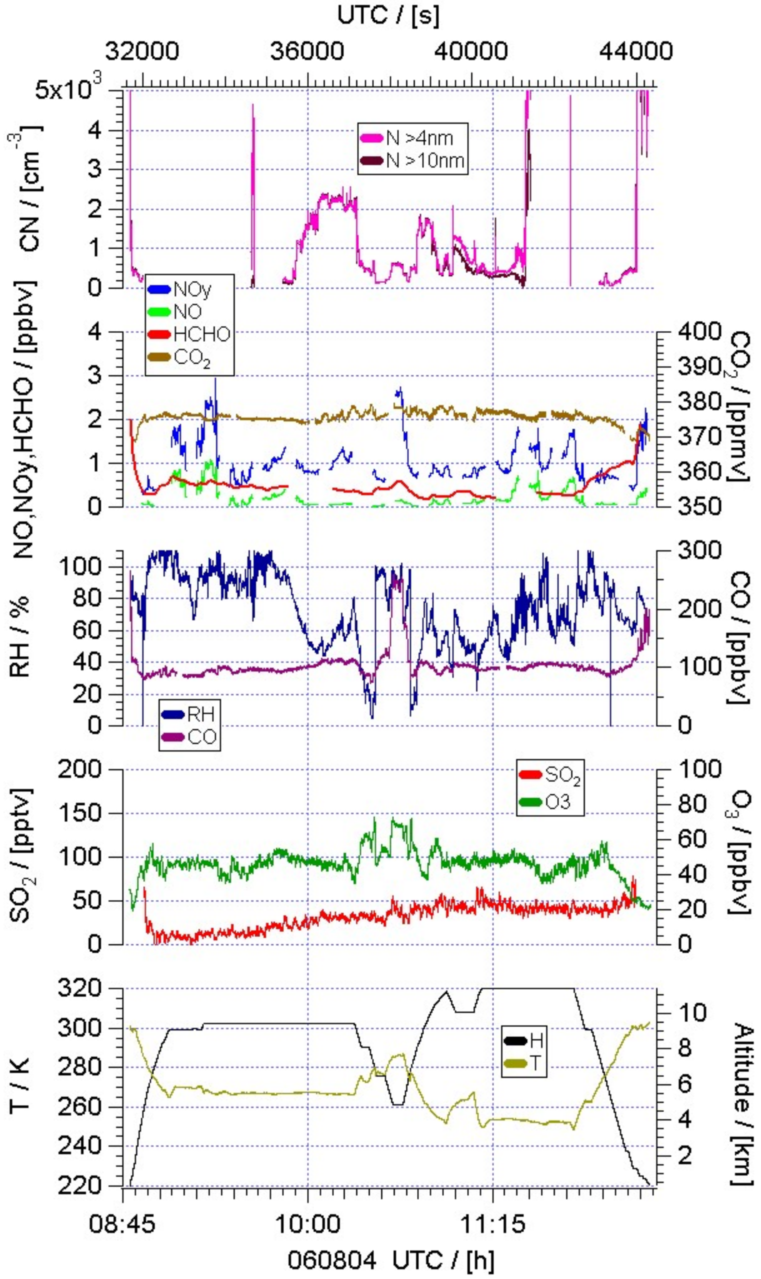

Figure A.35: AMMA First Local Flight: Long Range Transport.

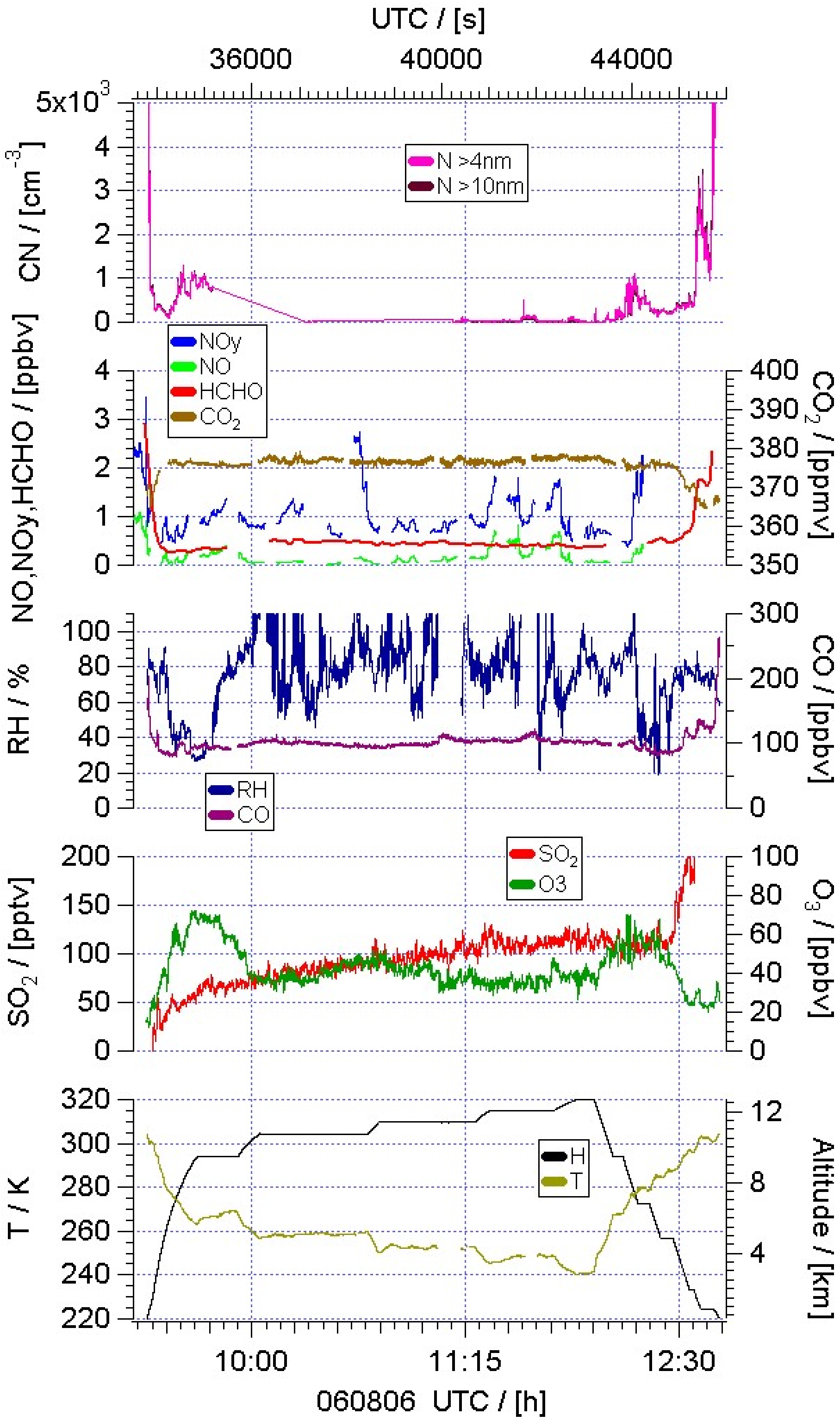

Figure A.36: AMMA Second Local Flight: MCS Outflow.

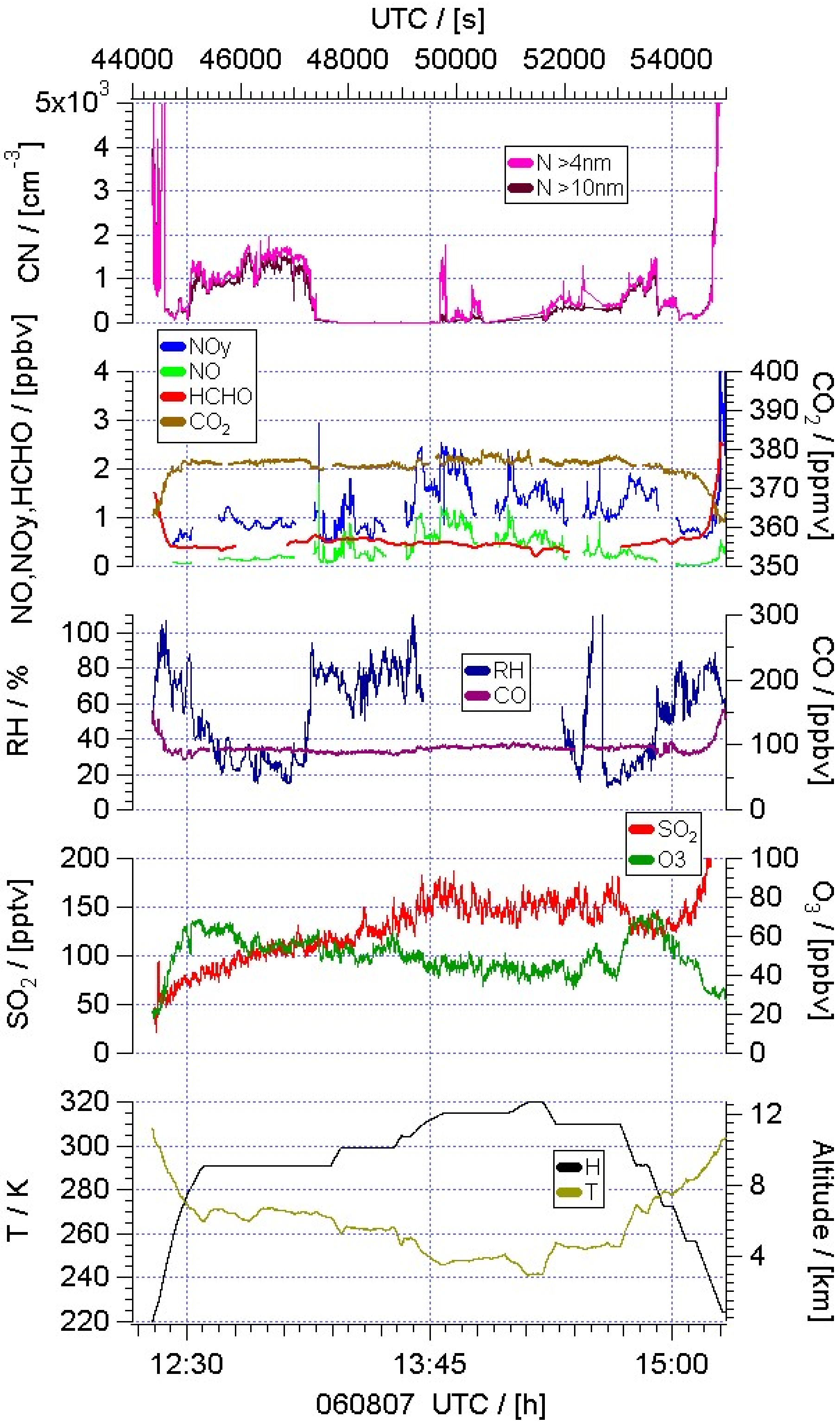

Figure A.37: AMMA Third Local Flight: MCS.

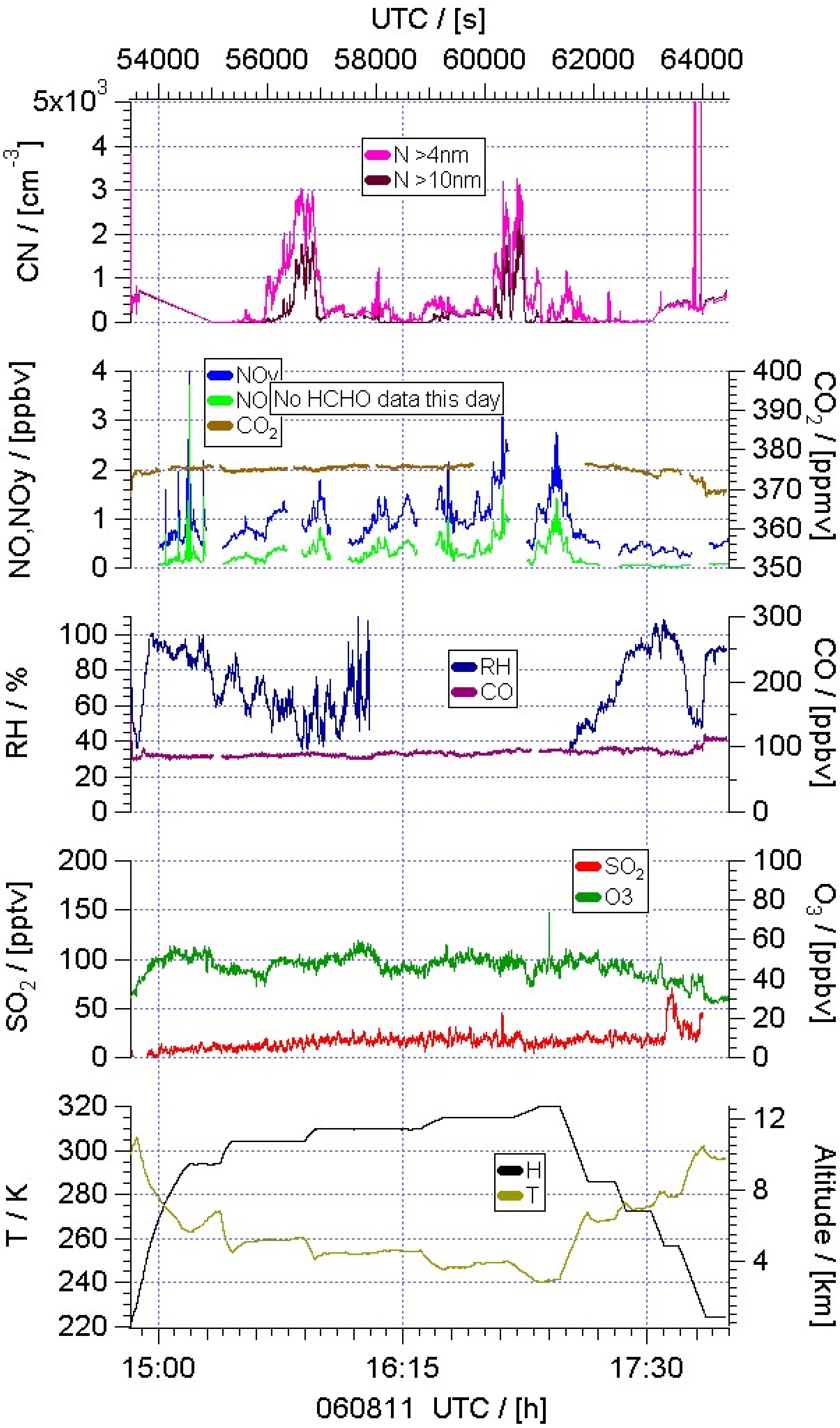

Figure A.38: AMMA Fourth Local Flight: MCS outflow.

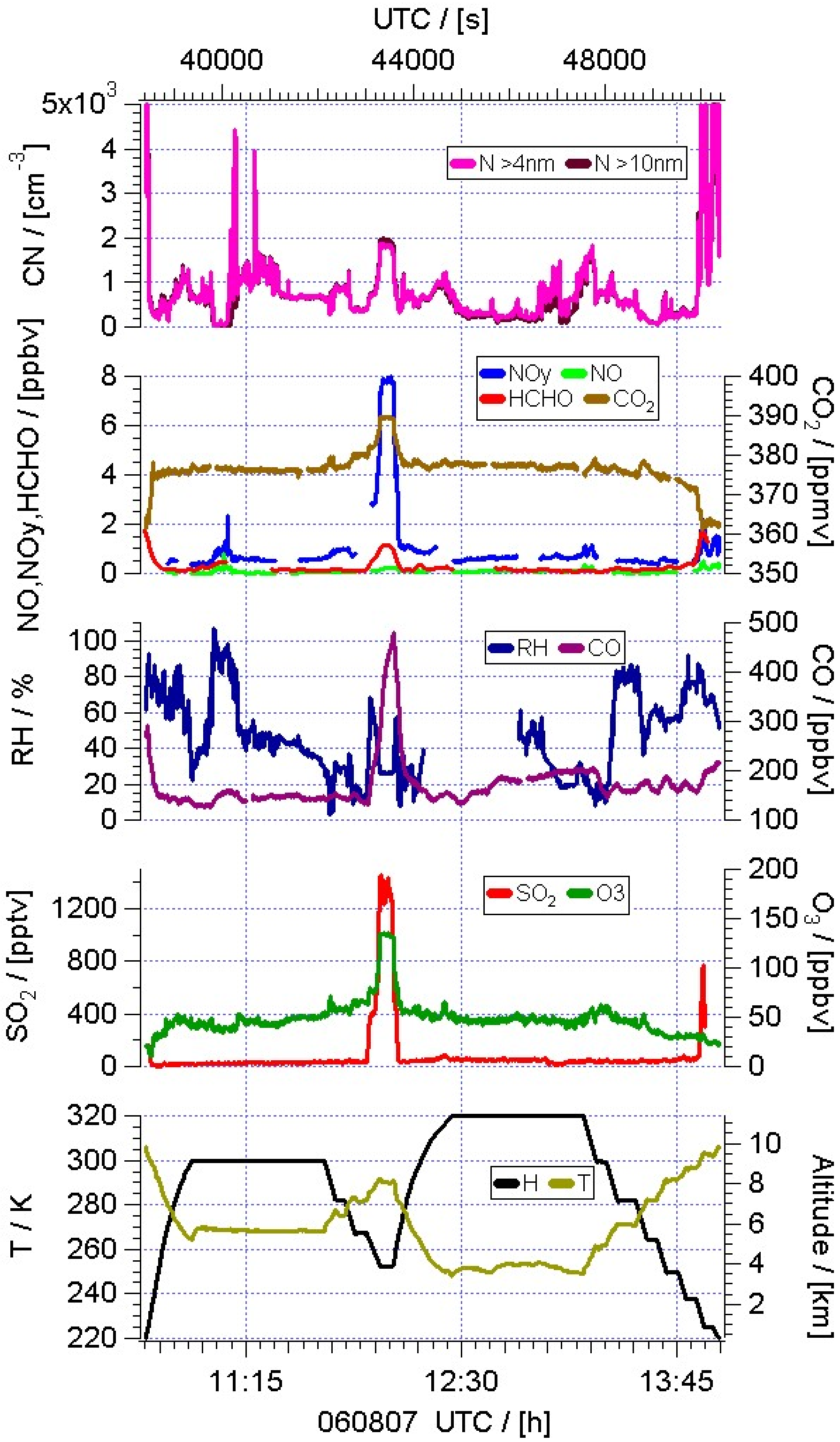

Figure A.39: AMMA Fifth Local Flight: Long Range Transport. Mind the changed axes scaling compared to previous figures.

List of Figures

List of Tables

List of Abbreviations

General Abbreviations:

Å	Angström, 1Å= 10^{-10} m
ACE1	First Aerosol Characterization Experiment
ACIMS	Active Chemical Ionization Mass Spectrometry
AEROFOR	Aerosol Formation and Dynamics Model
AI	Aerosol Index
amu	Atomic mass unit
AMMA	African Monsoon Multidisciplinary Analysis
CCN	Cloud Condensation Nuclei
CERN	Centre Europeen de la Recherche Nucleaire
CIMS	Chemical Ionization Mass Spectrometry
CNRS	Centre National de la Recherche Scientifique
CS	Condensation Sink
DLR	Deutsches Zentrum für Luft- und Raumfahrt
DU	Dobson Unit = 10^{-3} cm
ECHAM	Atmospheric General Circulation Model
ECMWF	European Center for Medium Range Weather Forecast
EDGAR	Emission Database for Global Atmospheric Research
ETH	Eidgenössische Technische Hochschule, Zürich

FLEXPART	Lagrangian Particle Dispersion Model
FZJ	Forschungs-Zentrum Jülich
HALO	High Altitude and Long Range Aircraft
HYSPLIT	Air Trajectory Model
INTEX	Intercontinental Chemical Transport Experiment
IPCC	International Panel on Climate Change
ITOP	International Transport of Ozone and Precursors
KNMI	Royal Netherland Meteorological Institute
LAGRANTO	Air Trajectory Model
MAN	Maschinenfabrik Augsburg/Nürnberg
MCS	Mesoscale Convective System
MEGAPLUME	Long-range transport of megacity air pollution plumes
MPI-K	Max-Planck-Institute for Nuclear Physics
NILU	Norwegian Institute for Air Research
OMI	Ozone Monitoring Instrument
PACIMS	Passive Chemical Ionization Mass Spectrometry
PEM	NASA Pacific Exploratory Mission
ppmv	Parts per million by volume = 10^{-6} mol/mol
ppbv	Parts per billion by volume = 10^{-9} mol/mol
pptv	Parts per trillion by volume = 10^{-12} mol/mol
ppqv	Parts per quadrillion by volume = 10^{-15} mol/mol
SCOUT-O3	Stratospheric-Climate Links with Emphasis on the Upper Troposphere and Lower Stratosphere
slpm	Standard liters per minute
TM5	Air Trajectory Model
TROCCINOX	Tropical Convection, Cirrus and Nitrogen Oxides Experiment
UTC	Universal Time Code
UTLS	Upper troposphere, lower stratosphere

Chemical Substances:

CO	Carbon Monoxide
$\mathbf{CO_2}$	Carbon Dioxide
DMS	Dimethyl Sulfide CH_3SCH_3
HCHO	Formaldehyde
$\mathbf{H_2O}$	Water Vapor
$\mathbf{H_2O_2}$	Hydrogen Peroxide
$\mathbf{H_2SO_4}$	Sulfuric Acid
$\mathbf{HNO_3}$	Nitric Acid
HONO	Nitrous Acid
$\mathbf{NH_3}$	Ammonia
$\mathbf{NH_4NO_3}$	Ammonium Nitrate
NO	Nitrogen Oxide
NOx	$NO + NO_2$
NOy	sum of odd Nitrogen compounds, i.e. sum of NO, NO_2, PAN, HNO_3 and some minor odd Nitrogen compounds
$\mathbf{N}\boldsymbol{x}$	Particles with diameters larger than x nm.
$\mathbf{O_3}$	Ozone
OH	Hydroxyl radical
OCS	Carbonyl Sulfid
PAN	Peroxyacetyl Nitrate $CH_3C(O)O_2NO_2$
RH	Relative Humidity
$\mathbf{SO_2}$	Sulfur Dioxide

Bibliography

[Andreae et al., 2005] Andreae, M., Jones, C., and Cox, P. (2005). Strong present-day aerosol cooling implies a hot future. *Nature*, 435:1187–1190.

[Andreae and Merlet, 2001] Andreae, M. and Merlet, P. (2001). Emission of trace gases and aerosols from biomass burning. *Global Biogeochemical Cycles*, 15:955–966.

[Arnold et al., 2007] Arnold, F., Schuck, T., Pirjola, T., Nau, R., Schlager, H., Fiedler, V., Minikin, A., and Stohl, A. (2007). Upper troposphere SO_2 pollution over South America: Impact on aerosol and cloud condensation nuclei formation. *paper in preparation*.

[Bandy et al., 1993] Bandy, A., Thornton, D., and Driedger, A. (1993). Airborne measurements of sulfur dioxide, dimethyl sulfide, carbon disulfide and carbonyl sulfide by isotope dilution gas chromatography/mass spectrometry. *J. Geophys. Research*, 98:23423–23433.

[Clegg and Abbatt, 2001] Clegg, S. and Abbatt, J. (2001). Uptake of Gas-Phase SO_2 and H_2O_2 by Ice Surfaces: Dependence on Partial Pressure, Temperature, and Surface Acidity. *J. Phys. Chem. A*, 105:6630–6636.

[Crutzen, 2006] Crutzen, P. (2006). Albedo Enhancement by Stratospheric Sulfur Injections: a Contribution to Resolve a Policy Dilemma? *Climatic Change*, 77:211–219.

[Dentener et al., 2006] Dentener, F., Kinne, S., Bond, T., Boucher, O., Cofala, J., Generoso, S., Ginoux, P., Gong, S., Hoelzemann, J., Ito, A., Marelli, L., Penner, J., Putaud, J., Textor, C., Schulz, M., van der Werf, G., and Wilson, J. (2006). Emissions of primary aerosol and precursor gases in the years 2000 and 1750 prescribed data-sets for AeroCom. *Atmos. Chem. Phys.*, 6:43214344.

[Dibb et al., 1998] Dibb, J., Talbot, R., and Loomis, M. (1998). Tropospheric sulfate distribution during SUCCESS: Contributions from jet exhaust and surface sources. *Geophys. Res. Let.*, 25:1375–1378.

[Dibb et al., 2000] Dibb, J., Talbot, R., and Scheuer, E. (2000). Composition and distribution of aerosols over the North Atlantic during the Subsonic Assessment Ozone and Nitrogen Oxide Experiment (SONEX). *J. Geophys. Res.*, 105:3709–3717.

[Feichter et al., 1996] Feichter, J., Kjellström, E., Rodhe, H., Dentener, F., Lelieveld, J., and Roelofs, G. (1996). Simulation of the tropospheric sulfur cycle in a global climate model. *Atmos. Environ.*, 30:1693–1707.

[Feichter et al., 1997] Feichter, J., Lohmann, U., and Schult, I. (1997). The atmospheric sulfur cycle in ECHAM-4 and its impact on the shortwave radiation. *Climate Dynamics*, 13:235–246.

[Ferek and Hegg, 1993] Ferek, R. and Hegg, D. (1993). Measurements of dimethyl sulfide and SO_2 during GTE/CITE 3. *J. Geophys. Res.*, 98.

[Fiedler, 2004] Fiedler, V. (2004). The Atmospheric Aerosol Precursor Gas Sulphuric Acid: Mass Spectrometric Measurements in the Atmospheric Boundary Layer in Finland and Germany. Diplomarbeit, Universität Heidelberg.

[Fiedler et al., 2008] Fiedler, V., Arnold, F., Schlager, H., Minikin, A., and Ludmann, S. (2008). Acidic trace gases in an aged tropical biomass burning plume: Aircraft based CIMS measurements and implications for soot activation. *paper in preparation*.

[Fiedler et al., 2005] Fiedler, V., Dal Maso, M., Boy, M., Aufmhoff, H., Hoffmann, J., Schuck, T., Birmili, W., Hanke, M., Uecker, J., Arnold, F., and Kulmala, M. (2005). The contribution of sulphuric acid to atmospheric particle formation and growth: a comparison between boundary layers in Northern and Central Europe. *Atmos. Chem. Phys.*, 5:1773–1785.

[Finlayson-Pitts and Pitts, 2000] Finlayson-Pitts, B. J. and Pitts, J. N. J. (2000). *Chemistry of the upper and lower atmosphere.* Academic Press, San Diego, London, first edition.

[Flood, 1934] Flood, H. (1934). *Z. Phys. Chemie A*, 170:280.

[Froger et al., 2007] Froger, J., Remy, D., Bonvalot, S., and Legrand, D. (2007). Two scales of inflation at Lastarria-Cordon del Azufre volcanic complex, central Andes, revealed from ASAR-ENVISAT interferometric data. *Earth and Planetary Science Letters*, 255:148–163.

[Frost et al., 2006] Frost, G., McKeen, S., Trainer, M., Ryerson, T., Neuman, J., Roberts, J., Swanson, A., Holloway, J., Sueper, D., Fortin, T., Parrish, D., Fehsenfeld, F., Flocke, F., Peckham, S., Grell, G., Kowal, D., Cartwright, J., Auerbach, N., and Habermann, T. (2006). Effects of changing power plant NO_x emissions on ozone in the eastern United States: Proof of concept. *J. of Geophys. Res.*, 111:12306.

[Garrett et al., 2002] Garrett, T., Radke, L., and Hobbs, P. (2002). Aerosol Effects on Cloud Emissivity and Surface Longwave Heating in the Arctic. *Journal of the Atmospheric Sciences*, 59:769–778.

[Georgii and Jost, 1964] Georgii, H.-W. and Jost, D. (1964). Untersuchung über die Verteilung von Spurengasen in der freien Atmosphäre. *Pure and Appl. Geophysics*, 59:217–224.

[Gregory et al., 1993] Gregory, G., Davis, D., Beltz, N., Bandy, A., Ferek, R., and Thornton, D. (1993). An Intercomparison of Aircraft Instrumentation for Tropospheric Measurements of Sulfur Dioxide. *J. Geophys. Res.*, 98:23325–23352.

[Hanke, 1999] Hanke, M. (1999). *Development of a Novel Method for Measuring Atmospheric Peroxy Radicals : Calibration, Aircraft-Borne Measurements and Speciated Measurements of* HO_2 *and* RO_2. PhD thesis, Universität Heidelberg.

[Harshvardhan et al., 2002] Harshvardhan, Schwarz, S., Benkovitz, C., and Guo, G. (2002). Aerosol influence on cloud microphysics examined by satellite measurements and chemical transport modelling. *Journal of the Atmospheric Sciences*, 59:714–725.

[IPCC, 2007] IPCC (2007). *Intergovernmental Panel On Climate Change Report*. IPCC.

[Jaeschke et al., 1976] Jaeschke, W., Schmitt, R., and Georgii, H.-W. (1976). Preliminary Results of Stratospheric SO_2-Measurements. *Geophysical Research Letters*, 3:517–519.

[Junge, 1961] Junge, C. (1961). Vertical profiles of condensation nuclei in the stratosphere. *J. Meteorol.*, 18:501–509.

[Kim, 2000] Kim, C.S., J. P. (2000). Respiratory dose of inhaled ultrafine particles in healthy adults. *Phil. Trans. R. Soc. Lond. A.*, 358:2693–2705.

[Kolb et al., 1994] Kolb, C., Jayne, J., Worsnop, D., Molina, M., Meads, R., and Viggiano, A. (1994). Gas phase reaction of sulphur trioxide with water vapor. *J. Am. Chem. Soc.*, 116:10314–10315.

[Krotkov et al., 2006] Krotkov, N. A., Carn, S., Krueger, A., Bhartia, P., and Yang, K. (2006). Band Residual Difference algorithm for retrieval of SO_2 from the Aura Ozone Monitoring Instrument (OMI). *IEEE Trans. Geosci. Remote Sens.*, 44(5):12591266.

[Kulmala, 2003] Kulmala, M. (2003). How Particles Nucleate and Grow. *Science*, 302:1000–1001.

[Laakso et al., 2003] Laakso, L., Grönholm, T., Rannik, U., Kosmale, M., Fiedler, V., Vehkamäki, H., and Kulmala, M. (2003). Ultrafine particle scavenging coefficients calculated from 6 years field measurements. *Atmospheric Environment*, 37:3605–3613.

[Lauer and Hendricks, 2006] Lauer, A. and Hendricks, J. (2006). Simulating aerosol microphysics with the ECHAM/MADE GCM. Part II: Results from a first multiannual simulation of the submicrometer aerosol. *Atmos. Chem. Phys.*, 6:5495–5513.

[Lauer et al., 2005] Lauer, A., Hendricks, J., Ackermann, I., Schell, B., Hass, H., and Metzger, S. (2005). Simulating aerosol microphysics with the ECHAM/MADE GCM. Part I: Model description and comparison with observations. *Atmos. Chem. Phys.*, 5:3251–3276.

[Logan et al., 1981] Logan, J., Prather, M., Wofsy, S., and McElroy, M. (1981). Tropospheric Chemistry: A Global Perspective. *J. Geophys. Res.*, 86:7210–7254.

[Lohmann et al., 2004] Lohmann, U., Kärcher, B., and Hendricks, J. (2004). Sensitivity studies of cirrus clouds formed by heterogeneous freezing in the ECHAM GCM. *J. Geophys. Res.*, 109:D16204.

[Lohmann et al., 2001] Lohmann, U., Leaitch, W., Barrie, L., Law, K., Yi, Y., Bergmann, D., Bridgeman, C., Chin, M., Christensen, J., Easter, R., Feichter, J., Jeuken, A., Kjellström, E., Koch, D., Land, C., Rasch, P., and Roelofs, G. (2001). Vertical distributions of sulfur species simulated by large scale atmospheric models in COSAM: Comparison with observations. *Tellus B*, 53:646–672.

[Lovejoy et al., 1996] Lovejoy, E., Hanson, D., and Huey, L. (1996). Kinetics and products of the gas phase reaction of SO_2 with water. *J. Phys. Chem.*, 100:19911–19916.

[March and Hughes, 1989] March, R. and Hughes, R. (1989). *Quadrupole Storage Mass Spectrometry.* John Wiley & Sons, New York.

[Maroulis et al., 1980] Maroulis, P., Torres, A., Goldberg, A., and Bandy, A. (1980). Atmospheric SO_2 Measurements on Project Gametag. *J. Geophys. Research*, 85:7345–7349.

[Mathieu, 1868] Mathieu, E. (1868). Memoire sur le mouvement vibratoire d´une membrane de forme elliptique. *J. Math. Pures Appl.*, 13:137.

[McLachlan, 1947] McLachlan, N. (1947). *Theory and Applications of Mathieu Functions.* Clarendon, Oxford.

[Meixner and Jaeschke, 1981] Meixner, F. and Jaeschke, W. (1981). The determination of low atmospheric SO_2 concentrations with a chemiluminescence technique. *Int. J. Environ. Anal. Chem.*, 10:51–67.

[Menon and Saxena, 1998] Menon, S. and Saxena, V. (1998). Role of sulfates in regional cloud-climate interactions. *Atmos. Research*, 47-48:299–315.

[Möhler and Arnold, 1992] Möhler, O. and Arnold, F. (1992). Gaseous sulphuric acid and sulfur dioxide measurements in the arctic troposphere and lower stratosphere: Implications for hydroxyl radical abundances. *Geophysical Research Letters*, 19:1763–1766.

[Möhler et al., 1992] Möhler, O., Reiner, T., and Arnold, F. (1992). The formation of SO_5^- by gas phase ion-molecule reactions. *Journal of Chemical Physics*, 97:8233–8239.

[Nau, 2004] Nau, R. (2004). Das atmosphärische Aerosol-Vorläufergas SO_2: Messungen mit einem flugzeuggetragenem Massenspektrometer. Diplomarbeit, Universität Heidelberg.

[Nau, 2008] Nau, R. (2008). *Weiterentwicklung eines flugzeuggetragenen CIMS-Instruments; Spurengasmessungen in der Atmosphäre und in einem Blitzlabor.* PhD thesis, Universität Heidelberg.

[Neumann and Döring, 1940] Neumann, K. and Döring, W. (1940). *Z. Phys. Chemie A*, 186:203.

[Olivier et al., 1994] Olivier, J., Bouwman, A., van der Maas, C., and Berdowski, J. (1994). Emission database for global atmospheric research (edgar). *Environmental Monitoring and Assessment*, 31:93–106.

[Paul and Raether, 1955] Paul, W. and Raether, M. (1955). Das elektrische Massenfilter. *Zeitschrift für Physik*, 140:161–273.

[Paul et al., 1958] Paul, W., Reinhard, H., and von Zahn, U. (1958). Das elektrische Massenfilter als Massenspektrometer und Isotopentrenner. *Zeitschrift für Physik*, 152:143–182.

[Paul and Steinwedel, 1953] Paul, W. and Steinwedel, H. (1953). Ein neues Massenspektrometer ohne Magnetfeld. *Zeitschrift für Naturforschung*, pages 448–450.

[Pirjola, 1998] Pirjola, L. (1998). Effects of the increased UV radiation and biogenic VOC emissions on ultrafine sulphate aerosol formation. *J. of Aerosol Science*, 29.

[Pirjola and Kulmala, 1998] Pirjola, L. and Kulmala, M. (1998). Modelling the formation of H_2SO_4-H_2O particles in rural, urban and marine conditions. *Atmospheric Research*, 46:321–347.

[Ramanathan et al., 2001] Ramanathan, V., Crutzen, P., Kiehl, J., and Rosenfeld, D. (2001). Aerosol, climate, and the hydrological cycle. *Science*, 294:2119–2124.

[Reiner and Arnold, 1993] Reiner, T. and Arnold, F. (1993). Laboratory flow reactor measurements of the reaction SO_3 + H_2O + M → H_2SO_4 + M: Implications for gaseous H_2SO_4 and aerosol formation in the plume of jet aircraft. *Geophysical Research Letters*, 20:2659–2662.

[Reiner and Arnold, 1994] Reiner, T. and Arnold, F. (1994). Laboratory investigations of gaseous sulfuric acid formation via SO_3 + H_2O + M → H_2SO_4 + M: Measurements of the rate constant and products identification. *J. Chem. Phys.*, 101:7399–7407.

[Reiner et al., 1998] Reiner, T., Möhler, O., and Arnold, F. (1998). Improved atmospheric trace gas measurements with an aircraft-based tandem mass spectrometer: Ion identification by mass-selected fragmentation studies. *Journal of Geophysical Research*, 103:31309–31320.

[Reiss, 1950] Reiss, H. (1950). The kinetics of phase transition in binary systems. *J. Chem. Phys.*, 18:840–848.

[Roeckner, 1996] Roeckner, E. (1996). The atmospheric general circulation model ECHAM-4: Model description and simulation of present-day climate. *Max-Planck-Institut für Meteorologie, Report*, 218.

[Schuck, 2006] Schuck, T. (2006). *Flugzeugmessungen troposphärischen Schwefeldioxids und Schwefelsäuremessungen im Abgas von Dieselmotoren.* PhD thesis, Universität Heidelberg.

[Schuck et al., 2007] Schuck, T., Arnold, F., Nau, R., Fiedler, V., Speidel, M., and Schlager, H. (2007). First aircraft-based measurements of sulfur dioxide in the upper troposphere over South America. *paper in preparation.*

[Schwarz, 2006] Schwarz, J. e. a. (2006). Single-particle measurements of midlatitude black carbon and light-scattering aerosols from the boundary layer to the lower stratosphere. *J. Geophys. Res.*, 111:D16207.

[Seeley et al., 1997] Seeley, J. V., Morris, R. A., and Viggiano, A. A. (1997). Rate constants for the reaction of $CO_3^-(H_2O)_{n=0-5}$+ SO_2: Implications for CIMS detection of SO_2. *Geophysical Research Letters*, 24:1379–1382.

[Seinfeld and Pandis, 1998] Seinfeld, J. and Pandis, S. (1998). *Atmospheric Chemistry and Physics*. John Wiley & Sons, Inc., first edition.

[Seinfeld and Pandis, 2006] Seinfeld, J. and Pandis, S. (2006). *Atmospheric Chemistry and Physics*. John Wiley & Sons, Inc., second edition.

[Speidel et al., 2007] Speidel, M., Nau, R., Arnold, F., Schlager, H., and Stohl, A. (2007). Sulfur dioxide measurements in the lower, middle and upper troposphere: Deployment of an aircraft-based chemical ionization mass spectrometer with permanent in-flight calibration. *Atmos. Environ.*, 41:2427–2437.

[Stauffer, 1976] Stauffer, D. (1976). *Journal of Aerosol Science*, 7:319.

[Stieb et al., 2002] Stieb, D. M., Judek, S., and Burnett, R. T. (2002). Meta-analysis of time-series studies of air pollution and mortality: Effects of gases and particles and their influence of cause of death, age and season. *J. Air and Waste Manage. Assoc.*, 52:470–484.

[Stockwell and Calvert, 1983] Stockwell, W. and Calvert, J. (1983). The Mechanism of the HO-SO_2 reaction. *Atmos. Environ.*, 17:2231–2235.

[Stohl et al., 2002] Stohl, A., Eckhardt, S., Forster, C., James, P., Spichtinger, N., and Seibert, P. (2002). A replacement for simple back trajectory calculations in the interpretation of atmospheric trace substance measurements. *Atmos. Environ.*, 36:4635–4648.

[Stohl et al., 2005] Stohl, A., Forster, C., Frank, A., Seibert, P., and Wotawa, G. (2005). Technical note: The Lagrangian particle dispersion model FLEXPART version 6.2. *Atmos. Chem. Phys.*, 5:2461–2474.

[Sunyer et al., 2003a] Sunyer, J., Atkinson, R., Ballester, F., Le Tertre, A., Ayres, J., Forastiere, F., Forsberg, B., Vonk, J., Bisanti, L., Anderson, R., Schwartz, J., and Katsouyanni, K. (2003a). Respiratory effects of sulphur dioxide: a hierarchical multicity analysis in the APHEA 2 study. *Occupational and Environmental Medicine*, 60.

[Sunyer et al., 2003b] Sunyer, J., Ballester, F., Tertre, A., Atkinson, R., Ayres, J., Forastiere, F., Forsberg, B., Vonk, J., Bisanti, L., Tenias, J., Medina, S., Schwartz, J., and Katsouyanni, K. (2003b). The association of daily sulfur dioxide air pollution levels with hospital admissions for cardiovascular diseases in Europe (The Aphea-II study). *European Heart Journal*, 24:752–760.

[Thornton et al., 1997] Thornton, D., Bandy, A., and Blomquist, B. (1997). Transport of sulfur dioxide from the Asian Pacific Rim to the North Pacific troposphere. *J. Geophys. Research*, 102:28489–28499.

[Thornton et al., 1999] Thornton, D., Bandy, A., Blomquist, B., Driedger, A., and Wade, T. (1999). Sulfur dioxide distribution over the Pacific Ocean 1991-1996. *J. Geophys. Research*, 104:5845–5854.

[Thornton et al., 1986] Thornton, D., Driedger, A., and Bandy, A. (1986). Determination of parts-per-trillion levels of sulfur dioxide in humid air. *Anal. Chem.*, 58:2688–2691.

[Tu et al., 2004] Tu, F., Thornton, D., Bandy, A. R., Carmichael, G., Tang, Y., Thornhill, K., Sachse, G., and Blake, D. (2004). Long-range transport of sulfur dioxide in the central Pacific. *J. Geophys. Research*, 109:8.

[Tu et al., 2003] Tu, F., Thornton, D., Bandy, A. R., Kim, M., Carmichael, G., Tang, Y., Thornhill, K., and Sachse, G. (2003). Dynamics and transport of sulfur dioxide over the Yellow Sea during TRACE-P. *J. Geophys. Research*, 108:8790.

[Uecker, 2002] Uecker, J. (2002). *Messung der atmosphärischen Radikale OH, HO_2, RO_2 sowie des Ultraspurengases H_2SO_4 - Weiterentwicklung, Kalibration und Einsatz einer hochempfindlichen massenspektrometrischen Analysemethode.* PhD thesis, Universität Heidelberg.

[Umann et al., 2005] Umann, B., Arnold, F., Schaal, C., Hanke, M., Uecker, J., Aufmhoff, H., Balkanski, Y., and Van Dingenen, R. (2005). Interaction of mineral dust with gas phase nitric acid and sulfur dioxide during the MINATROC II field campaign: First estimate of the uptake coefficient γ_{HNO_3} from atmospheric data. *J. Geophys. Research*, 110:D22306.

[van Aardenne et al., 2001] van Aardenne, J., Dentener, F., Olivier, J., Klein Goldewijk, C., and Lelieveld, J. (2001). A 1°x1° resolution data set of historical anthropogenic trace gas emissions for the period 1890-1990. *Global Biogeochemical Cycles*, 15:909–928.

[Volmer, 1939] Volmer, M. (1939). Kinetik der Phasenbildung. *Verlag Von Theodor Steinkopff, Dresden und Leipzig.*

[Wayne, 2000] Wayne, R. P. (2000). *Chemistry of Atmospheres.* Oxford University Press.

[West and Gaeke, 1956] West, P. and Gaeke, G. (1956). Fixation of sulfur dioxide as disulfitomercurate(ii) and subsequent colorimetric estimation. *Analytical Chemistry*, 28:1816–1819.

[Wichmann and Peters, 2000] Wichmann, H.-H. and Peters, A. (2000). Epidemiological evidence of the effects of ultrafine particle exposure. *Phil. Trans. R. Soc. Lond. A.*, 358:2751–2769.

[Wollny, 1998] Wollny, A. (1998). Flugzeugmessungen atmosphärischer Spurengase mittels Ionen-Molekül-Reaktions-Massenspektrometrie: Methodische Untersuchungen zur Reaktionskinetik. Master's thesis, Universität Heidelberg.

Acknowledgments

Last but not least I would like to thank everyone who was somehow involved in this thesis:

- Prof. Dr. Frank Arnold, who gave me the possibility of this thesis. Thanks for the helpful discussion and hints, often at interesting meeting points like the Munich Main Station Mongdratzerl Restaurant.

- Dr. Hans Schlager for being my supervisor at the DLR Oberpfaffenhofen.

- Prof. Dr. Klaus Pfeilsticker for preparing the expertise.

- Prof. Dr. W. Krätschmer and Prof. Wegner from the University of Heidelberg for being examiners in the PhD exam.

- All colleagues from Heidelberg: Sabrina, Tanja, Anna, Tina, Uli, Heinfried, Rainer, Michael and our technicians Ralph and B. Preissler for the help- and joyful time there.

- Prof. Liisa Pirjola from the Helsinki Polytechnic for the fast model calculations and the nice dinners, ”Kiitos paljon”.

- My officemate Ingo for always supporting me with different kinds of distractions.

- All campaign colleagues from the DLR Oberpfaffenhofen, whose data I was allowed to use for the analyses in this thesis: Andreas, Bernadette, Anke, Paul, Michael, Hans.

- All other colleagues from the DLR Oberpfaffenhofen: Thomas, Kati, Erik, Jan, Andreas, Christiane, Sebastian, Dominik, Heidi, Helmut, Simon, Kasper and many others, which I have probably forgotten, for the always friendly atmosphere.

- Oliver for the amusing and helpful proof reading.

- My parents for always supporting me, ”Danke für jegliche Hilfe und Unterstützung”.